

https://dspace.org/

Muon-spin spectroscopy studies of hydrogen-related defects relevant to doping of diamond

Madhuku, Morgan

2009-03-05T11:35:42Z
http://hdl.handle.net/10539/6624

Downloaded from a DSpace repository. https://dspace.org/

MUON-SPIN SPECTROSCOPY STUDIES OF HYDROGEN-RELATED DEFECTS RELEVANT TO DOPING OF DIAMOND

Morgan Madhuku

A thesis submitted to the Faculty of Science,
University of the Witwatersrand, Johannesburg,
in fulfilment of the requirements for the degree of
Doctor of Philosophy
School of Physics

Johannesburg, 2007

I declare that this thesis is my own, unaided work. It is being submitted for the Degree of **Doctor of Philosophy** at the University of the Witwatersrand. It has not been submitted before for any degree or examination in any other university.

_____

Morgan Madhuku

Date _____

Abstract

This study focused on investigation of the behaviour of hydrogen-related defects in diamond. Diamond represents a material with potential in electronics, particularly for high power and high temperature electronic devices operating under radiation and in corrosive environments. However, the production and characterization of high-quality diamond for electronic devices is a great challenge. The main objective is to understand the origin of structural imperfections and impurities and to reduce or control these in order to improve the electronic and optical properties of diamond. The presence of hydrogen is known to influence these properties. Therefore, very significant experimental and computational effort is expended in trying to understand and predict the behaviour of hydrogen in diamond and in other semiconducting materials, and the recent discovery of its ability to act as a shallow dopant to enhance conductivity in some materials has generated much interest. However, most of the experimental information on hydrogen in diamond has hitherto been obtained from studies of the light hydrogen pseudo-isotope, muonium. In this thesis, we employ transverse field muon spin rotation (TF-μSR) and longitudinal field muon spin relaxation (LF-μSR) to investigate two specific aspects of muonium (and hence hydrogen) in diamond: Firstly, the high temperature stability of bond-centred muonium (Mu_{BC}) is investigated in a search for its possible ionization. The Mu_{BC} state in diamond is easily observed and there is a very pleasing correlation between theoretical and experimental hyperfine parameters. Curiously, despite its predicted stability, the bond-centred hydrogen (H_{BC}) state has not yet been observed in diamond. As one proceeds with LF-μSR measurements above room temperature, one encounters firstly the expected increase in the Mu_{BC} population corresponding to the well known $Mu_T \rightarrow Mu_{BC}$ transition, but observed here for the first time in diamond in longitudinal field. At still higher temperatures (setting in near 1 000 K), the Mu_{BC} population decreases, a result which is consistent with Mu_{BC} ionization. There is also an indication, from the TF-μSR measurements, that this is correlated with the increase in the population of the diamagnetic (μ_D^+) species. Secondly, the muonium states in high-purity type IIa diamond grown by high-pressure and high-temperature (HPHT) synthesis are investigated in a search for the origin

of the missing fraction (MF) observed in many previous muonium studies in diamond. The pure synthetic diamond gave similar fractions of the muonium states as pure natural samples. There is still a small missing fraction.

For my family, who offered me unconditional love

and support throughout the course of this thesis.

Acknowledgements

There are a number of people without whom this thesis might not have been written, and to whom I am greatly indebted:

- my supervisors, **Dr. S. H. Connell** and **Dr. I. Z. Machi**. With their enthusiasm, their inspiration, and their great efforts to explain things clearly and simply, they helped to make physics fun for me. Throughout my thesis-writing period, they provided encouragement, sound advice, good teaching, and lots of good ideas. I would have been lost without them;

- all our foreign collaborators, especially: **Prof. S. F. J. Cox**, **Dr. P. J. C. King** and **Dr. J. S. Lord** (ISIS, Rutherford Appleton Laboratory);

- all our local collaborators, especially: **Dr. J. M. Keartland** (University of the Witwatersrand), **Prof. K. Bharuth-Ram** (University of KwaZulu-Natal), and **Mr. D. Gxawu** (Durban University of Technology);

- **Prof. S. F. J. Cox** and **Prof. K. Bharuth-Ram** for their invaluable time going through this thesis;

- **Mr. S. Ballestrero** and **Dr. Ian Korir** for their help with the Geant4 simulation and programming in general;

- **Mr. M. Rebak** for expertly preparing all the diamond samples used in this work;

- **Dr. J. M. Keartland** and **Ms. T. Baisitse** (National Laser Centre) for their invaluable assistance in characterising the diamond samples;

- my many student colleagues for providing a stimulating and fun environment in which to learn and grow, especially: I. Korir, A. Dacosta, K. G. Sekonya, T. Sibiya, L. Mkhonza, N. Makau, G. Amolo, M. Dalton and C. Lee;

- the administrative staff at iThemba LABS-Gauteng, especially: **Mrs. D. Monyamane**, **Ms. M. Lunga** and **Mr. K. Radebe**;

- my parents, brothers and sisters for their unfailing support and encouragement;

- my dearly beloved wife, Hamundidi Catherine for her tireless devotion to making my life better. Her constant concern for every aspect of my life and how I might improve them have made this thesis possible. My children Zvifumiso and Namatwai for their love and everlasting patience.

- I would like to acknowledge financial support from the National Research Foundation (NRF), iThemba LABS, and the University of the Witwatersrand.

It is impossible to remember all, and I apologise to those I have inadvertently left out. Lastly, thank you all and thank God!

Contents

Chapter

1 Introduction **1**

1.1 Problem Area 1

1.1.1 The search for shallow molecular donors in diamond 2

1.1.2 Research approach and organisation of the thesis 7

1.2 Hydrogen and other Dopants in Diamond 9

1.2.1 Preliminary remarks 9

1.2.2 Nitrogen and other n-type dopants in diamond 11

1.2.3 Electrical activity and diffusion of isolated hydrogen in diamond 19

1.2.4 Hydrogen-related complex formation in diamond 22

2 Theoretical Aspects of Muon Spin Spectroscopy **28**

2.1 Preliminary Remarks 28

2.2 Shallow-donor Muonium States 36

2.3 Muon Production and Decay 38

2.4 Principles of the μSR Studies 44

2.4.1 Extraction of information from longitudinal field μSR spectra . 52

2.4.2 Extraction of information from transverse field μSR spectra . . 53

2.5 Muonium Formation in Diamond 57

2.5.1 Tetrahedral Muonium (Mu_T^0) in diamond 60

2.5.2 Bond-centred Muonium (Mu^0_{BC}) in diamond 61
2.5.3 Muonium charge-state and site transitions in diamond 63

3 Sample Preparations 67

3.1 Preliminary Remarks 67
3.2 Diamond View 68
3.3 Fourier Transform InfraRed (FTIR) Spectroscopy Measurements 70
3.3.1 Principles of Infrared Spectroscopy 70
3.3.2 Interferometry 73
3.3.3 Analysis of FTIR spectra 75
3.4 Electron Paramagnetic Resonance (EPR) Measurements 78
3.4.1 Preliminary remarks 78
3.4.2 Principles of EPR Spectroscopy 80
3.4.3 EPR spectra 83

4 Experimental Arrangements for Muon(ium) Studies in Natural Type Ia And Synthetic Type HPHT-IIa Diamond 86

4.1 Preliminary Remarks 86
4.2 Experimental Details 87
4.2.1 The EMU Spectrometer in Fly-past Mode 89
4.2.2 Sample Mounting 91
4.3 Geant4 Simulation of the Fly-Past and Alpha Correction 96
4.3.1 Field-dependent alpha value in fly-past mode 96
4.3.2 Geant4 simulation 99
4.4 Data Analysis Approach 104

5 Experimental Results of Muon(ium) Studies in Natural Type

Ia and Synthetic Type HPHT-IIa Diamond 107

5.1 Preliminary Remarks 107

5.2 The Longitudinal Field Technique - Data Reduction and Analysis . . . 108

5.3 Thermal Ionisation of Muonium in Natural Type Ia Diamond 112

5.3.1 Results From Longitudinal Field Measurements 112

5.3.2 Results From Transverse Field Measurements 127

5.4 Muonium Studies in High-purity Type IIa Diamond grown by HPHT Synthesis 132

5.4.1 Results From Longitudinal Field Measurements 132

5.4.2 Results From Transverse Field Measurements 136

6 Discussion: Ionization of Mu_{BC} in Natural Type Ia and Muonium States in Synthetic Type IIa Diamond 144

6.1 Muonium dynamics in natural type Ia diamond above 300 K 144

6.2 The gap-level of Mu_{BC} in diamond: Mathematical model 147

6.3 Muonium states in high-purity type IIa HPHT diamond 153

7 Concluding Remarks on Major Findings 155

7.1 Natural type Ia single crystal diamond 155

7.2 Synthetic type IIa diamond 156

Appendix

A CAXBD97 decomposition spreadsheet fits 158

B Detector construction 163

Bibliography 166

List of Tables

Table

1.1 Physical characteristics of Si and the major WBG semiconductors. 4

1.2 Main figures of merit for WBG semiconductors compared with Si. 4

2.1 Correlation of the spin density on the central muon with experimental donor-level depth 38

2.2 Properties of the positive muon [126]. m_e is the mass of the electron and m_p is the mass of the proton; μ_N is the nuclear magneton. 57

2.3 Comparison of hydrogen and muonium [33] 58

2.4 Comparison of the hyperfine coupling constants of Mu^0_T and Mu^0_{BC} at 0 K [33] 63

2.5 Comparison of the absolute fractions of tetrahedral interstitial Mu^0_T, bond-centred Mu^0_{BC}, diamagnetic μ^+, Mu_X, and MF in some published experiments . 66

5.1 F_{MuBC} and F_d fractions in natural type Ia diamond samples determined by fitting to equation 5.11. 126

5.2 Prompt diamagnetic fractions in natural type Ia diamond samples determined by fitting to T20 histograms 130

5.3 Muonium fractions F_{MuT}, F_{MuBC}, F_d, and MF at a temperature of 5 K in this study determined by theoretical fitting to equation 5.18. 136

5.4 Prompt muonium fractions in high-purity type IIa HPHT diamond samples determined by fitting to T20 and T2 histograms. 141

6.1 Comparison of F_{MuT}, F_{MuBC}, F_d, and MF in the present study and other published experiments (see Table 2.5) 153

List of Figures

Figure

1.1 Crystal structure of diamond. Diamond has a face-centred cubic (fcc) structure. 3

1.2 Infrared spectrum of Type IaB diamond. (1) region of nitrogen impurities absorption, (2) B2 peak, (3) self absorption of diamond lattice, (4) hydrogen peaks. This figure is taken from Ref. [61] 13

1.3 Schematic diagrams of some of the most important nitrogen-related defects that occur in natural diamonds. The diagrams were taken from Ref. [63]. . . . 14

1.4 The classification scheme for diamonds. N is the chief determiner: when present we have type I; when it is essentially absent we have type II 17

1.5 An illustration of the most important interstitial sites in diamond structure materials. C atoms are shown as black circles, and ideal interstitial sites as small white circles. The T site lies equidistant from 4 carbon sites, the H site lies midway between two T sites, the C site is midway between an atom site and a T site along < 001 > and the bond-centred (BC) site is the mid-point between two atom sites. The anti-bonded (AB) configuration is less well specified, and is usually taken to mean somewhere between an atom site and a T site along < 111 >. This figure is taken from Ref. [28]. 20

1.6 The < 100 > aligned boron-hydrogen defect and the first nearest neighbour carbon atoms. The arrows indicate the direction in which the important relaxations of the atoms take place. This figure is taken from Ref. [96]. 23

1.7 Optimized structure of the N-H-N defect. This defect is made up from the A-centre with a hydrogen atom placed in the bond-centre between two N atoms; d = 2.20 Å, α = 117.0°, and β = 100.0° Insertion of H between two Ns elongates the N-N distance by about 3 %. This figure is taken from Ref. [4]. . 25

1.8 Calculated formation energies (E_{form}) of various N- and H-related defects in diamond, as a function of $\Delta\mu = \mu_H - \mu_N$, where μ_H and μ_N are chemical potentials of H and N, respectively. The formation energy of the N-H-N defect is lower than those of V as well as other H-related defects. This figure is taken from Ref. [4]. 26

1.9 A schematic representation of four possible locations of hydrogen in impurity-hydrogen complexes. BC and AB refer to bond-centred and anti-bonding sites, respectively. The black, white and grey atoms represent carbon, hydrogen and impurity sites, respectively. This figure is taken from Ref. [28]. 27

2.1 μSR time spectra for the four compounds CdS, CdSe, CdTe, and ZnO. The beating pattern originates from the splitting of precession frequencies, with a period related to the hyperfine constants of the paramagnetic muonium, i.e., of the undissociated donor. This figure is taken from Ref. [111] 37

2.2 Decay of the positive pion in a co-ordinate system where the pion is at rest. Directions of spin and momentum for the decay particles are indicated. 39

2.3 Production of surface (or 'Arizona'-type) muons from pions which have been stopped near the surface of the production target. This figure is taken from Ref. [128]. 41

2.4 Conservation of angular and linear momentum when the positron energy is close to the maximum value E_{max} and the two neutrinos are emitted in approximately the same direction. 42

2.5 The angular distribution of positrons from positively charged muons for various positron energies. This figure is taken from Ref. [133]. 43
2.6 Muon energy spectrum. 44
2.7 The histogram shows an exponential decay corresponding to the muon lifetime and periodic maxima and minima as the spins are aligned towards and away from the counter. 46
2.8 From the raw collected histograms the exponential decay due to the finite muon lifetime is divided out and the so-called asymmetry spectrum is obtained, which contains the information about the precessing and relaxing muon spins in the total local field. 47
2.9 F-B polarization asymmetry measured in a longitudinal magnetic field. 48
2.10 Muon spin polarization asymmetry measured in a longitudinal magnetic field. . 49
2.11 The two types of experimental geometry: the transverse and longitudinal setups are illustrated in the upper and lower panel, respectively. The muon beam momentum and the initial muon beam polarization have been taken as parallel but in reality, these two vectors are antiparallel. The arrows originating from the sample sketch the muon spin direction: the dashed one at $t = 0$ and the solid one at t. This figure is taken from Ref. [137]. 50
2.12 Schematic diagram of the history of energetically introduced positive muon in condensed matter; energy loss and depolarization mechanisms. This diagram is taken from Ref. [141]. 59
2.13 The configuration diagram for three charge states of muonium and hydrogen in silicon showing (a) the experimental energy parameters for muonium, and (b) the correspondence with the deep donor and acceptor levels. This figure is taken from Ref. [82]. 66

3.1 The DiamondView^{TM} fluorescent imager with associated PC. 68

3.2 Diamond View images of the four natural type Ia diamond samples used in this study, showing some inclusions and growth zones. 69

3.3 Schematic absorption spectrum. 72

3.4 Optical schematic of a simple Michelson interferometer. The beam from the source is collimated and the wavefront is divided at the beam splitter. One arm of the interferometer consists of a fixed mirror, while the other arm contains a movable mirror. The beams are recombined at the beam splitter after having been reflected and transmitted once, and then proceed to the sample area and detector. 73

3.5 Infrared absorption spectra of the four natural type Ia diamond samples used in this study. The combined sample contained about 150 ppm of A-centres and 56.2 ppm of B-centres. 76

3.6 Infrared absorption spectra of the natural type Ia diamond samples used by Ref. [124]. These samples contained about 650 ppm of A-centres and 400 ppm of B-centres. 77

3.7 Illustrations of the geometries of the paramagnetic P1, P2, and N3 centres in diamond. The positions of the unpaired electrons are shown in the diagrams. These diagrams are taken from Ref. [185]. 80

3.8 An illustration of the formation of the paramagnetic N2 centre by a translational slip in diamond. N1 and N2 are nitrogen atoms, while C1 and C2 are carbon atoms. This diagram is taken from Ref. [185] 81

3.9 (a) Schematic representation of a single electron spin in a steady magnetic field $\mathbf{H}_0$ (b) Corresponding energy-level scheme 82

3.10 Room-temperature EPR spectrum of sample w001. The resonance lines of P1 and P2 centres are indicated. 84

3.11 Room-temperature EPR spectrum of sample w002. The resonance lines of P1 and P2 centers are identical to Figure 3.10. 84

3.12 Room-temperature EPR spectrum of sample w003. The resonance lines of P1 and P2 centers are indicated. 85

3.13 Room-temperature EPR spectrum of sample w008. The resonance lines of P1 and P2 centers are identical to Figure 3.12. 85

4.1 General layout of the European Muon Facility at ISIS. The data presented in this study were collected using the EMU spectrometer. This diagram is taken from Ref. [192] 87

4.2 A schematic view of the EMU spectrometer. This diagram is taken from Ref. [192] 89

4.3 Schematic of the EMU spectrometer in fly-past mode showing the detector rings, muon beam, beam pipe window and sample position. 90

4.4 Schematic diagram of how the vacuum pumps were connected to the sample area. The vacuum was maintained in the order of 10^{-5} torr using this arrangement. 92

4.5 Picture of the reflector furnace showing two halogen bulbs mounted opposite each other around a sample space. 93

4.6 Picture of the reflector furnace showing the sample space enclosed by titanium shields. 93

4.7 Wiring diagram for the furnace, showing the 0-5V trip line and the type K trip thermocouples which are attached to the cruciform and beam snout. This diagram is taken from Ref. [194]. 94

4.8 A schematic of the electrical and mechanical connections on the furnace. This diagram is taken from Ref. [194]. 95

4.9 Field dependent asymmetry in a small silver sample. 97

4.10 Field dependent value of alpha in a small silver sample. This was done by varying alpha in the analysis code UDA until a constant asymmetry was found. 98

4.11 Diamond data corrected using a field-dependent alpha value plotted together with normalised (to Ag) and un-normalised diamond data. 99

4.12 A Geant4 generated detector geometry showing the detector rings, muon beam pipe, particle gun, and beam stop. 101

4.13 Variation of positron asymmetry with fly-past for (a) 1 million, (b) 2 million, and (c) 3 million events per data point. The three graphs are plotted together in (d) for comparison. 103

4.14 Variation of signal asymmetry with fly-past for the individual detector rings for (a) 1 million events, (b) 2 million events. Note the marked reduction in asymmetry for the inner detector rings. 104

4.15 An LF histogram collected using the ISIS EMU spectrometer. The time zones for the young and old muons used in this analysis are indicated. 106

5.1 Theoretically simulated polarisation for the Mu_T state in diamond, in longitudinal field ranging from 0 to 6000 G. The hyperfine constant of Mu_T in diamond is given in Table 2.4. 110

5.2 Theoretical polarisations for the Mu^0_{BC} state in a diamond (simulations due to James Lord [198]). The polarisation is orientation-dependent. The hyperfine constants of Mu^0_{BC} in diamond are given in Table 2.4. 111

5.3 An LF histogram collected using the ISIS EMU spectrometer at an applied field of 2 G. The data are for natural type Ia diamond at 303 K. 112

5.4 An LF histogram collected using the ISIS EMU spectrometer at an applied field of 1047.5 G. The data are for natural type Ia diamond at 689 K. 113

5.5 Longitudinal field repolarisation curves for young and old muons in the single crystal natural type Ia diamonds used in this study at 303 K. It was below these temperatures when Machi et al. [124] discovered Mu_X in natural type Ia single crystal diamonds with aggregated nitrogen defects, and their repolarisation curves are reproduced in Figure 5.6 for comparison. 113

5.6 Longitudinal field repolarisation curves for young and old muons in single crystal natural type Ia diamond at 300 K. These data are from Mach et al. [124] who discovered Mu_X in single crystal natural type Ia diamonds with aggregated nitrogen defects. 114

5.7 Longitudinal field repolarisation curves for young and old muons in the single crystal natural type Ia diamonds used in this study, in the temperature range 303-361 K and in the magnetic field range 2-4500 G. There were no significant differences observed between young and old muons in this temperature regime. The same trend was observed up to about 1000 K. 115

5.8 Longitudinal field repolarisation curves for young and old muons in the temperature range 910-1200 K. Note the differences between young and old muons above 1000 K. This difference between young and old muons beyond 1000 K is due to the spin relaxation. 116

5.9 A TF histogram collected using the ISIS EMU spectrometer at an applied field of 2 G. There are no oscillations in the histogram. The data, which are for natural type Ia diamond at 303 K show that tetrahedral interstitial muonium (Mu_T) was relaxing rapidly in the sample at this temperature. 119

5.10 Mu_{BC} [111] theory fitted with the sum of three Lorentzians to show how good a job it does replicating the full simulation. 120

5.11 Mu_{BC} theoretical fitting to the data in the magnetic field range 2 - 1000 G. These data are for single crystal natural type Ia diamond from 303 - 361 K. . . 121

5.12 Mu_{BC} theoretical fitting to the data in the magnetic field range 2 - 1000 G. These data are for single crystal natural type Ia diamond from 396 - 476 K. . . 122

5.13 Mu_{BC} theoretical fitting to the data in the magnetic field range 2 - 1000 G. These data are for single crystal natural type Ia diamond from 522 - 629 K. . . 123

5.14 Mu_{BC} theoretical fitting to the data in the magnetic field range 2 - 1000 G. These data are for single crystal natural type Ia diamond from 689 - 829 K. . . 124

5.15 Mu_{BC} theoretical fitting to the data in the magnetic field range 2 - 1000 G. These data are for single crystal natural type Ia diamond from 910 - 1200 K. . 125

5.16 Temperature dependence of the Mu_{BC} fractions in (a) young and (b) old muons obtained by theoretical fitting to equation 5.11. There is a decrease in the Mu_{BC} populations above 1 000 K. These data are for natural type Ia single crystal diamond. 126

5.17 A TF histogram collected using the ISIS EMU spectrometer at an applied field of 20 G. The oscillations in the signal are due to the precession of the muon spin in the transverse field. The data, which are for natural type Ia diamond at 303 K, were used to determine both the alpha value as well as the promptly formed diamagnetic fraction for the sample. 127

5.18 A TF histogram collected using the ISIS EMU spectrometer at an applied field of 20 G. The oscillations in the signal are due to the precession of the muon spin in the transverse field. The data, which are for natural type Ia diamond at 476 K, were used to determine both the alpha value as well as the promptly formed diamagnetic fraction for the sample. 128

5.19 A TF histogram collected using the ISIS EMU spectrometer at an applied field of 20 G. The oscillations in the signal are due to the precession of the muon spin in the transverse field. The data, which are for natural type Ia diamond at 756 K, were used to determine both the alpha value as well as the promptly formed diamagnetic fraction for the sample. 128

5.20 A TF histogram collected using the ISIS EMU spectrometer at an applied field of 20 G. The oscillations in the signal are due to the precession of the muon spin in the transverse field. The data, which are for natural type Ia diamond at 1200 K, were used to determine both the alpha value as well as the promptly formed diamagnetic fraction for the sample. 129

5.21 Variation of (a) prompt diamagnetic fraction and (b) spin relaxation rate with temperature in the natural type Ia diamond sample used in this study. There is an increase in the population of the diamagnetic fraction above 1 000 K. . . . 131

5.22 A typical LF histogram collected at the ISIS EMU spectrometer. The data are for synthetic type HPHT IIa diamond taken at 290 K for an applied field of 56.80 G. 133

5.23 Longitudinal field repolarisation curve for high-purity type IIa HPHT diamond at a temperature of 5 K. A missing fraction of about 12 % was observed. . . . 134

5.24 Longitudinal field repolarisation curve for high-purity type IIa HPHT diamond at a temperature of 290 K. No thermal ionization of Mu_{BC} was observed from 5 - 290 K. 135

5.25 A TF histogram collected using the ISIS EMU spectrometer at an applied field of 20 G. The data, which are for high-purity type IIa HPHT diamond at 5 K, were used to determine both the alpha value as well as the prompt diamagnetic fraction for the sample. 137

5.26 A TF histogram collected using the ISIS EMU spectrometer at an applied field of 20 G. The data, which are for high-purity type IIa HPHT diamond at 100 K, were used to determine both the alpha value as well as the prompt diamagnetic fraction for the sample. 138

5.27 A TF histogram collected using the ISIS EMU spectrometer at an applied field of 20 G. The data, which are for high-purity type IIa HPHT diamond at 290 K, were used to determine both the alpha value as well as the prompt diamagnetic fraction for the sample. 138

5.28 A TF histogram collected using the ISIS EMU spectrometer at an applied field of 2 G, showing the presence of the isotropic muonium state in the sample. The data, which are for high-purity type IIa HPHT diamond at 5 K, were used to determine the promptly formed isotropic muonium fraction for the sample. . 139

5.29 A TF histogram collected using the ISIS EMU spectrometer at an applied field of 2 G, showing the presence of the isotropic muonium state in the sample. The data, which are for high-purity type IIa HPHT diamond at 100 K, were used to determine the promptly formed isotropic muonium fraction for the sample. 139

5.30 A TF histogram collected using the ISIS EMU spectrometer at an applied field of 2 G, showing the presence of the isotropic muonium state in the sample. The data, which are for high-purity type IIa HPHT diamond at 290 K, were used to determine the promptly formed isotropic muonium fraction for the sample. 140

5.31 Variation of (a) prompt diamagnetic fraction and (b) spin relaxation rate with temperature in the high-purity type IIa HPHT diamond samples used in this study. 142

5.32 Variation of (a) prompt isotropic muonium fraction and (b) spin relaxation rate with temperature in the high-purity type IIa HPHT diamond samples used in this study. 143

6.1 Variation of (a) bond-centred muonium (LF data) and (b) diamagnetic muonium (TF data) with temperature. The decrease in the Mu_{BC} fraction and the corresponding increase in the diamagnetic fraction above 1 000 K are interpreted as due to the thermal ionization of Mu_{BC}. 145

6.2 F_{MuBC} variation with temperature fitted with equation 6.17 in order to estimate the ionization energy of the Mu_{BC} state. This model gives an ionization energy of about 1.80 eV while a double Arrhenius fit gives a value of about 0.60 eV. . 152

A.1 CAXBD97 decomposition spreadsheet fits to the FTIR spectrum of sample W001 to determine the nitrogen concentrations in the sample. This sample contains 76.2 ppm of A-centres and 29.8 ppm of B-centres. 159

A.2 CAXBD97 decomposition spreadsheet fits to the FTIR spectrum of sample W002 to determine the nitrogen concentrations in the sample. This sample contains 23.8 ppm of A-centres and 8.8 ppm of B-centres. 160

A.3 CAXBD97 decomposition spreadsheet fits to the FTIR spectrum of sample W003 to determine the nitrogen concentrations in the sample. This sample contains 32.8 ppm of A-centres and 4.1 ppm of B-centres. 161

A.4 CAXBD97 decomposition spreadsheet fits to the FTIR spectrum of sample W008 to determine the nitrogen concentrations in the sample. This sample contains 17.2 ppm of A-centres and 13.5 ppm of B-centres. 162

Chapter 1

Introduction

”If we knew what it was we were doing, it would not be called research, would it ?”

Albert Einstein.

1.1 Problem Area

Hydrogen has a significant influence on the electronic properties of many semiconductors and insulators, whether introduced intentionally or inadvertenly. For example, it is commonly used to passivate unwanted electrical activity associated with impurities or defects in silicon. However, in other semiconductors hydrogen can itself be the source of free carriers [1]. In the light of current attempts to develop diamond material for electronic applications, it is important to know, and possibly predict, the form which incorporated hydrogen will take. Hence, very significant experimental and computational effort is expended in trying to understand and predict the behaviour of hydrogen in diamond and in other semiconducting materials. For various reasons, studies of various hydrogen states in semiconductors, using conventional spectroscopic techniques, have not been successful. To the contrary, investigations using positive muons - particles that behave as light isotopes of hydrogen when implanted into solids - have been surpassingly fruitful in disentangling the nature of these states.

Ri et al. [2] have studied the behaviour of hydrogen in CVD polycrystalline diamond

film using the longitudinal field muon spin relaxation (LF-μSR) technique and observed a missing fraction (muon spin polarization that is not recovered during longitudinal field repolarization) (MF) of 24 %. In an effort to trace the origin of the MF in nitrogen-rich diamonds Machi et al. [3] have discovered a new paramagnetic muonium centre, Mu_X, with less than axial symmetry and associated with aggregated nitrogen in the form of A-and/or B- centres[1] . A model structure involving hydrogen and nitrogen that gives rise to a shallow donor level has been proposed [4]. This defect is made up from the A centre with a hydrogen atom placed in the bond centre between the two N atoms. This shows that the study of hydrogen and hydrogen-related defects in diamond is still an open area. It is therefore important to ascertain whether the electronic states of hydrogen in diamond lie deep in the band gap, or whether they are shallow. This study has also investigated the muonium states in high-purity diamond in an effort to establish whether the missing fraction observed in many previous studies is related to defect or intrinsic processes. Understanding the origin of the missing fraction would lead to some clarification of the hydogen-related properties of diamond.

The primary objectives of this study were therefore to, firstly, investigate the donor level of interstitial hydrogen in diamond through its chemical analogue, and, secondly, investigate whether the missing fraction observed in many previous studies is related to defect or intrinsic processes.

1.1.1 The search for shallow molecular donors in diamond

Diamond[2] represents a material with many extreme properties, making it ideal for use as a semiconductor in applications that require high-frequency, high-temperature, high-power, and high-irradiation tolerant devices. These properties include: high electric

[1] For a description of these nitrogen defects see Section 1.2.2

[2] essentially diamond is carbon, a group IV element with the electronic configuration $1s^2 2s^2 2p^2$, which crystallise in the so-called diamond structure when the *s* and *p* atomic orbitals hybridise forming tetrahedral sp^3 bonds.

breakdown field strength, high carrier mobility, the highest room temperature thermal conductivity of any material, low dielectric constant, and wide band gap [5, 6]. The crystal structure of diamond is equivalent to a face-centred cubic (fcc) lattice, with a basis of two identical carbon atoms (Figure 1.1). Table 1.1 shows some of these characteristics for the most popular wide-bandgap (WBG) semiconductors compared to those of Si.

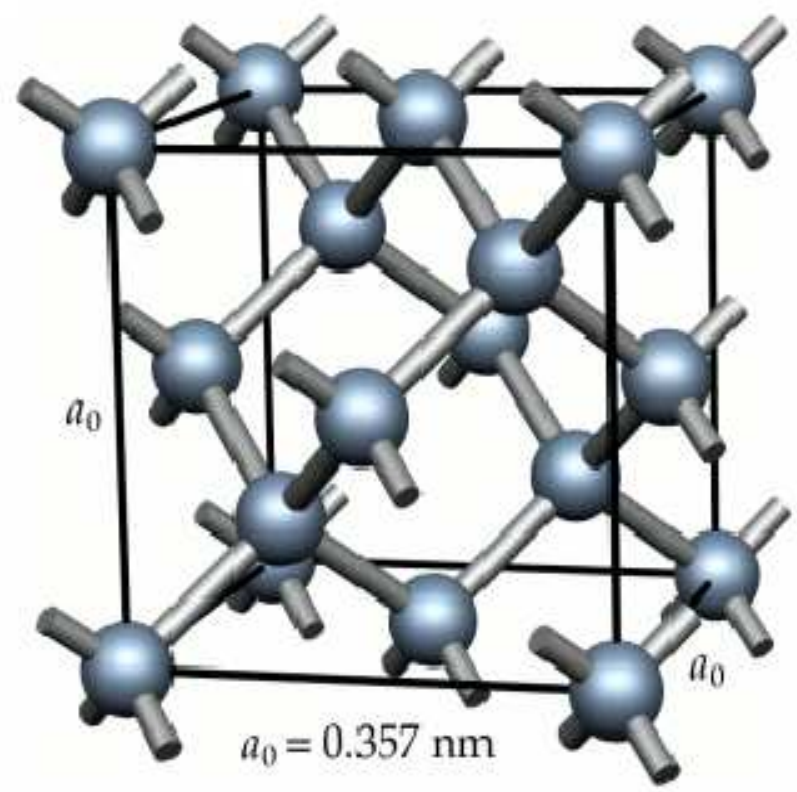

Figure 1.1: Crystal structure of diamond. Diamond has a face-centred cubic (fcc) structure.

For a comparison of the possible power electronics performances of these materials, some commonly known figures of merit (FoM), normalized with respect to Si, are listed in Table 1.2. The FoM values for diamond are at least 40-50 times more than those for any other semiconductor in the table.

Table 1.1: Physical characteristics of Si and the major WBG semiconductors.

Property	Si	GaAs	6H-SiC	4H-SiC	GaN	**Diamond**
Bandgap, E_g(eV)	1.12	1.43	3.03	3.26	3.45	**5.45**
Dielectric constant, ϵ_r	11.9	13.1	9.66	10.1	9	**5.5**
Electric breakdown field, E_c (kV/cm)	300	400	2,500	2,200	2,000	**10,000**
Electron mobility, μ_n (cm^2/V.s)	1,500	8,500	500	1,000	1,250	**2,200**
Hole mobility, μ_p(cm^2/V.s)	600	400	101	115	850	**850**
Thermal Conductivity, λ (W/cm.K)	1.5	0.46	4.9	4.9	1.3	**22**
Saturated electron drift velocity, v_{sat}(x 10^7 cm/s)	1	1	2	2	2.2	**2.7**

Table 1.2: Main figures of merit for WBG semiconductors compared with Si.

	Si	**GaAs**	**6H – SiC**	**4H – SiC**	**GaN**	**Diamond**
JFM	1.0	1.8	277.8	215.1	215.1	**81,000**
BFM	1.0	14.8	125.3	223.1	186.7	**25,106**
FSFM	1.0	11.4	30.5	61.2	65.0	**3,595**
BSFM	1.0	1.6	13.1	12.9	52.5	**2,402**
FPFM	1.0	3.6	48.3	56.0	30.4	**1,476**
FTFM	1.0	40.7	1,470.5	3,424.8	1,973.6	**5,304,459**
BPFM	1.0	0.9	57.3	35.4	10.7	**594**
BTFM	1.0	1.4	748.9	458.1	560.5	**1,426,711**

JFM: Johnson's figure of merit, a measure of the ultimate high-frequency capability of the material

BFM: Baliga's figure of merit, a measure of the specific on-resistance of the drift region of a vertical field effect transistor (FET)

FSFM: FET switching speed figure of merit

BSFM: Bipolar switching speed figure of merit

FPFM: FET power-handling-capacity figure of merit

FTFM: FET power-switching product

BPFM: Bipolar power handling capacity figure of merit

BTFM: Bipolar power switching product

However, the exploitation of diamond as an electronic material is compromised by the non-existence of diamond of adequate structural quality and its lack of a suitable shallow donor for the production of n-type material. The recent breakthrough [7] in the synthesis of single crystal diamond via plasma-assisted chemical vapour deposition has enlivened the quest to develop diamond devices capable of electronic functionality at temperatures where silicon based electronics are inadequate. Boron has been successfully both grown into and implanted into diamond and forms p-type material with a hole activation energy of 0.37 eV [8] but finding a suitable n-type counterpart to make the p-n technologies of the conventional semiconductor industry applicable to diamond-based devices remains notoriously difficult, with solubility and hydrogen-related problems being contributing factors to the problem. Nitrogen forms a very deep donor with an activation energy of 1.7 eV [9]. Phosphorus yields an donor level with an activation energy of 0.6 eV [10, 11], however, it readily complexes with the vacancy, and activation levels are very low. Other possibilities for elemental dopants have been theoretically and experimentally considered, but they are yet to be reliably established. Several molecular dopant systems in diamond have been predicted [12, 13, 14, 15, 16, 17]. There is therefore an active interest for research which enhances the understanding of factors leading to improved diamond quality and developing shallow n-type dopants. In this regard, hydrogen plays an important role since it is known to influence the electronic and optical properties of the material [18, 19].

The presence of hydrogen in conventional semiconductors plays an important role in their electrical and optical properties. For example, hydrogen terminates dangling bonds [20, 2] at vacancies, dislocations, or grain boundaries, which improves the elec-

tronic properties of the material [21, 22]; passivates shallow and deep levels through the formation of hydrogen-dopant complexes, which prevents the doping control of semiconductors [21, 20, 23, 2]; and introduces extended defects in semiconductors [21, 2]. Hydrogen is a key and an ubiquitous impurity in diamond, but unlike other group IV materials, there is little detailed information about any hydrogen defect [24]. Therefore the electronic structure and dynamics of isolated hydrogen in diamond need to be well understood [20, 25, 3, 26, 27, 24, 28, 2] before diamond can be exploited in a range of new applications, as anticipated. However, it is extremely difficult to obtain direct information on isolated interstitial hydrogen in diamond due to its very high mobility, combined with its propensity to form complexes with other defects and impurities [29, 30, 26, 31]. Isolated hydrogen atomic states commonly form deep-level defects in semiconductors, with donor and acceptor states involving different locations. Despite concerted efforts to study hydrogen centres using conventional techniques like electron paramagnetic resonance (EPR) (which in principle can be used to study paramagnetic hydrogen centres), optical absoption and infrared spectroscopy, information on such centres remains sparse. Most of the experimental information on hydrogen in diamond has hitherto been obtained from muon spin rotation, relaxation or resonance (μSR) experiments [18, 30, 26]. Muonium (Mu) is a pseudo isotope of hydrogen which consists of an electron bound to a positive muon (μ^+). The positive muon is a spin $\frac{1}{2}$ particle with a lifetime of 2.2μs and a mass of approximately $\frac{1}{9}$ of the proton mass [32].

The electronic structures of analogous hydrogen and muonium centres are expected to be identical apart from differing dynamical effects arising from the smaller mass of the muon [33, 34, 35]. Using muonium as an analogue [3] for hydrogen has therefore been

[3] However, it should be noted that when employing muonium as a light hydrogen isotope one should always bear in mind that hydrogen and muonium are introduced into a semiconductor in very different ways. Hydrogen is incoporated during the process of sample preparation and reaches thermal and chemical equilibrium long before measurements start, whereas muonium is observed a few nanoseconds after the injection of very energetic muons into the sample and only those states reached on the microsecond timescale of the muon lifetime can be studied [36].

a promising method of obtaining a great deal of spectroscopic information concerning the behaviour of hydrogen in diamond.

The production and characterization of high-quality diamond, especially for electronic devices, is a great challenge. One main aim is to understand the origin of structural imperfections and impurities and to reduce or control these in order to improve the electronic and optical properties. The presence of hydrogen is, as indicated earlier, known to influence these properties. The hydrogen concentration in a diamond sample depends on the type and quality of the diamond. Average hydrogen concentrations have been found to vary from 10^{17} atoms/cm^3 up to about 10^{19} atoms/cm^3 in the bulk of polycrystalline diamond layers [37]. In addition, several hydrogen-related defects have been identified [38, 39, 40]. However, there is insufficient information about the quantity and spatial distribution of these defects, and possibly there are other types of hydrogen-related defects which are yet to be identified. Furthermore, it is not yet known whether most of the hydrogen being detected in diamond is concentrated at grain boundaries, inclusions, and other extended defects or whether hydrogen is distributed homogeneously throughout the bulk at defects of atomic dimensions.

1.1.2 Research approach and organisation of the thesis

The aim of this thesis is to study the electronic properties of hydrogen-related defect systems relevant to the doping of diamond. The main interest is the gap-level of hydrogen in nitrogen-rich diamond because of the theoretical prediction that it is a shallow donor [4]. The methods used for sample characterisation are fourier transform infrared spectroscopy (FTIR) and electron paramagnetic resonance (EPR). Our main experimental techniques are longitudinal-field muon spin relaxation (LF-μSR) and transverse-field muon spin rotation (TF-μSR). These spectroscopy techniques employ a short-lived subatomic particle called a *muon*, with spin and charge exquisitively sensitive to local

magnetic and electronic probes of matter. As an experimental model for isolated hydrogen, μSR studies of semiconductors are the primary source of detailed information on the site migrations and dynamics of the charge states and how muonium diffuses and interacts with charge carriers.

It is worthwhile to consider, briefly, the merits of the two different muon techniques which were available for this study: transverse field μSR and longitudinal field μSR. Transverse field μSR is able to provide accurate measurements of hyperfine parameters by direct observation of muonium precession lines [31]. However, muonium species can only be observed by this method when they are formed rapidly in comparison to the period of the precession signal, and the species must live long enough and have slow enough relaxation rate for a precession to be observed. Longitudinal field μSR does not have the requirement that the muonium species should be formed promptly, and is sensitive to states produced as a result of conversion of another species. It can be used to identify a muonium species by field-dependence of the muon polarisation, but provides the least accurate method of hyperfine parameter measurement [31].

This thesis is divided into seven chapters. The role of hydrogen and hydrogen-related complexes in the doping of diamond is dealt with in Section 1.2. To clarify the motivations of the study, special emphasis is given to the recently published articles on the electrical activity of hydrogen and hydrogen-related defects in diamond. In Chapter 2, aspects of muon spin rotation/relaxation relevant to this thesis are described, and an introduction to muon spin spectroscopic theory, which forms the foundation for the interpretation of μSR measurements, is provided. A description of the characterisation of the samples by means of infrared absorption and electron paramagnetic resonance is given in Chapter 3. Chapter 4 describes the experimental arrangements and sample mounting. A Monte Carlo simulation, using the GEANT4 toolkit, is described as a way

of correcting for artifacts observed in experiments where not all the muons are stopped by the sample. The variation of asymmetry with the amount of fly-past is considered. The results of muonium studies in natural type Ia and synthetic type IIa diamond are presented in Chapter 5. In Chapter 6 the results of the thesis are discussed, with the main focus on the observed thermal ionization of bond-centred muonium in natural type Ia diamond and the muonium states in high-purity synthetic type IIa diamond. Some general trends are discussed and the possible muonium dynamics in the diamond samples used are examined in detail. The major findings of this study are summarised in Chapter 7.

1.2 Hydrogen and other Dopants in Diamond

1.2.1 Preliminary remarks

Since the operation of carrier-transporting heterojunction devices is predicated on ambipolar (p- and -n type) doping, the failure to successfully dope certain classes of materials is an important bottleneck for the technological utilization of these materials in electronic devices. The problem has been especially severe in wide-bandgap semiconductors where in many instances n- or p-type doping is very difficult, if not impossible, significantly limiting the range of applications of these materials [41]. For example, whereas diamond can be doped p-type, its n-type doping is rather difficult [42]; conversely, while ZnO [43, 44, 45] and other main-group oxides [46] can be readily doped n-type, their p-type doping is problematic.

The issue of doping in itself deals with a complex problem of enhancing conductivity. A number of factors can contribute to the final measured conductivity. For example, the mobility of the carriers depends on their lifetime, which is greatly affected by defect scattering and/or non-radiative centres present in the host, and the effective mass [47]. The carrier concentration is the most important factor [47] because without enough

carriers the device made of the material would lose its functionality. There are several scenarios that can give rise to lack of free charge carriers [42, 47]:

(i) structural instability associated with the dopant,
(ii) dopants being on the wrong lattice positions or forming undesired clusters,
(iii) self-compensation by creation of intrinsic defects,
(iv) exceptionally low dopant solubility, and
(v) too large impurity ionization energy.

Hydrogen is a common impurity in all semiconductors. It can be incorporated during the growth of the crystal and it is present at virtually every stage of the processing of devices [48]. An interest in the properties of hydrogen as an impurity in semiconductors has been driven largely by the impact that hydrogenation has on the electrical characteristics of devices. For example, hydrogen has been shown to neutralise the electrical activity of both n-type and p-type dopants [49, 50, 28] and produce a variety of defect and impurity states, which prevent the doping control of semiconductors [20].

The understanding of the interaction of hydrogen with dopants in diamond and the role that hydrogen plays in passivating these dopants is very important because the deposition of both polycrystalline and monocrystalline diamond films has to be done within a very active hydrogen plasma [51]. Detailed information on the structure of hydrogen-related defects in diamond and other wide-band gap semiconductors is therefore an essential pre-requisite for understanding the influence of hydrogen on electrical and optical properties, and ultimately exploiting the full potential of these materials.

In this Section, the role of hydrogen in the doping of diamond is presented. We describe several potential n-type dopants at substitutional and interstitial sites and provide reasons on why these have failed to give rise to electrical conductivity at room temperature.

The electrical activity and diffusion of isolated hydrogen in silicon with comparison to some theoretical calculations for diamond are reviewed. The Section ends with a description of the electronic structures of some of the known hydrogen-related defects in diamond. Of particular interest here are the hydrogen-nitrogen complexes because of the theoretical prediction that an N-H-N complex may give rise to a shallow donor level in diamond.

1.2.2 Nitrogen and other n-type dopants in diamond

In order to achieve n-type diamond by chemical doping due to donor impurities it is imperative to identify the element that can be introduced and driven into the required lattice site in the diamond crystal to form a donor level in the gap which may give rise to electrical conductivity at room temperature. Thus, an impurity atom must be identified which, when in the required charge state and on the correct lattice site, has an energy level close enough to the conduction band minimum. In classical semiconductors, n- and p- type doping is usually attained by substituting a fraction from the host lattice atoms with impurity atoms of neighbouring groups of the periodic Table of elements. Elements of group III are used as acceptors and those of group V as donors to dope Si and Ge. According to the simple theoretical model of hydrogen-like impurities [52], a donor atom in the lattice is similar to a hydrogen atom; it is a positive ion, keeping, by Coulomb force, its extra electron, which is not used for covalent bonding by the host lattice. The strength of the interaction between the electron and the ion is determined by the charge carrier effective mass and the screening ability of the host lattice. Also, there is need for thermodynamic plausibility in the occupation of the state at room temperature, i.e. the atomic size of the impurity must suit the desired lattice location [42]. However, it is not sufficient for an impurity atom to have the required energy level in the gap; it must also have low formation energy to enable its existence in the crystal [53]. The formation energy of a substitutional dopant X in a charge state q can

be calculated from [53, 28]:

$$E_X^f(q) = E_X^{tot}(q) - E_{bulk}^{tot} - \mu_X + qE_F, \tag{1.1}$$

where E_X^{tot}(q) is the total energy of X in the charge state q in diamond, E_{bulk}^{tot} is the total energy of X in charge state q from the computation (DFT, etc.), μ_X is the chemical potential for X. The Fermi energy E_F is measured from the top of the valence band.

Several potential n-type dopants in diamond have been investigated. These include, among others, Li and Na, on interstitial sites; N, P, and As, when singly ionised, on substitutional sites; and O and S, in the singly ionised charge state, on substitutional sites [42].

Nitrogen: Nitrogen, a group V, light element, at a substitutional site (N_{sub}) is a natural candidate to act as a donor in diamond. Nitrogen is the dominant impurity in diamonds [54, 55, 56] and was first identified in 1959 by Kaiser and Bond of Bell Telephone [57]. Previously, all lattice defects in diamond were thought to be the result of structural anomalies; later research revealed nitrogen to be present in most diamonds and in many different configurations. The light absorption and other material properties of diamond are highly dependent upon nitrogen content and aggregation state. Although all aggregate configurations cause absorption in the infrared and ultraviolet, diamonds with high levels of nitrogen are usually colourless. It is the interactions between different aggregate configurations which cause colour rather than the aggregates themselves [58]. Nowadays one commonly distinguishes, according to the production method, natural, High pressure high temperature (HPHT), and Chemical vapour deposition (CVD) diamonds. Natural diamonds are traditionally subdivided into the following four types, according to the dominant type of nitrogen defects present:

- **Type Ia diamond**. More than 95 % of all natural diamonds belong to type Ia, where the dominant defect encountered is aggregated, diamagnetic nitrogen (up to 3000 ppm) [59, 60]. This type is further divided into two subtypes: In the IaA subtype, nitrogen is present in the form of nearest-neighbour substitutional pairs ($[N_{sub} - N_{sub}]^0$ or the A- centre). Its IR spectrum consists of a major peak at 1282 cm^{-1} and another one at 1212 cm^{-1} [56]. It occurs as a complex of four substitutional nitrogen atoms bordering a lattice vacancy ($[4N_{sub} - V]^0$ or the B- centre) in the IaB subtype, and gives rise to a characteristic infrared spectrum with the major peak at 1175 cm^{-1}, but is optically inactive [56]. Figure 1.2 shows the infrared spectrum of Type IaB diamond.

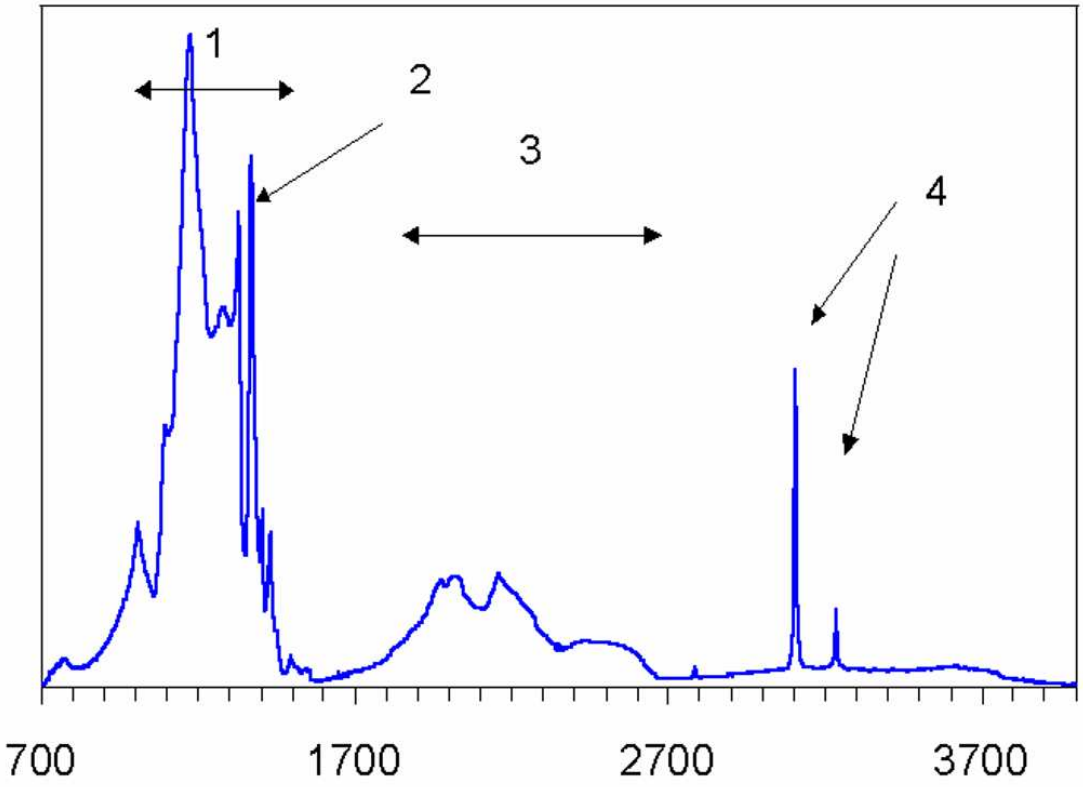

Figure 1.2: Infrared spectrum of Type IaB diamond. (1) region of nitrogen impurities absorption, (2) B2 peak, (3) self absorption of diamond lattice, (4) hydrogen peaks. This figure is taken from Ref. [61]

- **Type Ib diamond**. In the rare natural type Ib, the dominant defect is the single-substitutional nitrogen (up to 800 ppm) donor centre, variably labelled as N_{sub}; P1 [55]; or C centre [62]. The P2 centre comprises three adjacent substitutional nitrogen atoms situated around a vacancy, each of which has two unbonded electrons [63]. Most HPHT and many CVD diamonds can be ranked into this class [59]. Figure 1.3 shows the schematic diagrams of some of the most important nitrogen defects.

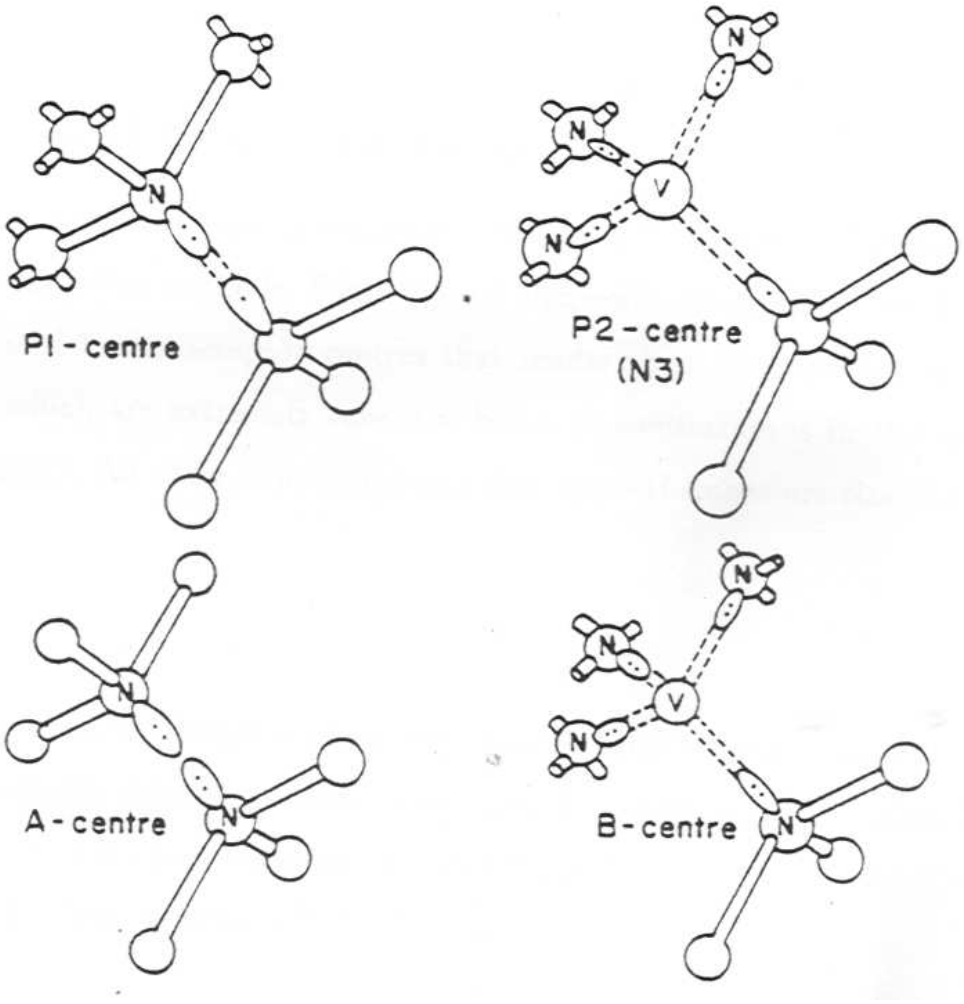

Figure 1.3: Schematic diagrams of some of the most important nitrogen-related defects that occur in natural diamonds. The diagrams were taken from Ref. [63].

- **Type IIa diamond** - artificial class, in which the nitrogen impurity level is

below the IR absorption detectivity. In practice, it means presence of less than a few ppm of single and aggregated nitrogen and of large variety of other defect centres [59]. In other words, natural IIa diamonds should not be considered as high-purity material. To the contrary, synthetic IIa diamonds can be of exceptional purity (< 1-10 ppb) [59].

- **Type IIb diamond**. Diamonds containing boron as a substitutional impurity are termed Type IIb. They are extremely rare in nature and are found only in the Premium mine (South Africa) [59]. The boron acts as an acceptor; that is, because the substituting boron atoms have one less available electron than the carbon atoms they replace, each boron atom creates an electron hole in the band gap that can accept an electron from the valence band. This allows red light absorption, and due to the relatively small energy ($\simeq$ 0.4 eV) needed for the electron to leave the valence band, holes are created in the latter even via thermal heat at room temperatures. These holes can move in an electric field and render the diamond electrically conductive (i.e., a p-type semiconductor). Very little substitutional boron is required for this to happen. In contrast, type Ia, Ib and IIa crystals exhibit no measurable conductivity at ambient conditions [60].

The above classification is summarised in figure 1.4. In addition to the central role of being the basis for the rough classifications of diamonds, nitrogen plays an important role in establishing the Fermi level in diamond [64].

The various complexes which nitrogen forms in the diamond crystal have been identified, and the amount of nitrogen incorporated in substitutional sites and the nitrogen bonding configuration in diamond have been investigated. Nitrogen can enter in substitutional positions at concentrations up to 10^{19} cm^{-3} [52]. Although N_{sub} has a low

formation energy and a high solubility in diamond [65, 24] it acts as a very deep donor, with observed activation energy of about 1.7 eV [66, 67, 5]. In fact, the level is so deep that N-doped diamonds are good insulators at room temperature. The A-centre has a much deeper donor level at $\approx$ 4.0 eV below the conduction band minimum, while the B-centre has no level [68]. Hence, doping diamond with nitrogen is not expected to yield useful conductivities at room temperature.

Phosphorus: An obvious candidate to be considered as a shallow n-type dopant in diamond is phosphorus, in analogy to P-doped n-type Si. However, contrary to the case of n-Si doped with phosphorus, P doping of diamond turned out to be problematic, [4] [52] and this has only recently been solved [42]. The phosphorus content can reach 50 ppm in the < 111 >- oriented homoepitaxial CVD films [60]. Hall measurements on phosphorus-doped films demonstrate n-type conductivity with an activation energy of 0.55 eV [69], rather high for room-temperature conduction. Sternschulte et al. [66] have used cathodoluminescence at low temperatures to study diamond samples doped with phosphorus either during high-pressure/high-temperature (HPHT) synthesis or during chemical vapour deposition (CVD) growth and found the donor level to be at around 0.62 eV below the conduction band. This donor level is relatively deep for room temperature operation [16]. Furthermore, the electron mobility of P-doped diamond ($\sim$ 200 cm^2/Vs) [70] is lower than the hole mobility of the B-doped counterpart ($\sim$ 2000 cm^2/Vs) [4].

Sulphur: Sulphur has attracted attention due to the suggestion that it can be used to form n-type diamond (μ = 597 cm^2/Vs and E_a = 0.38eV) [71]. The reality of the situation is still controversial, with accidental boron contamination apparently responsible for some of the observations [72, 53, 42]. There are also inconsistencies in

[4] Different theoretical calculation methods gave inconsistent results, and the experimental results were also contradictory.

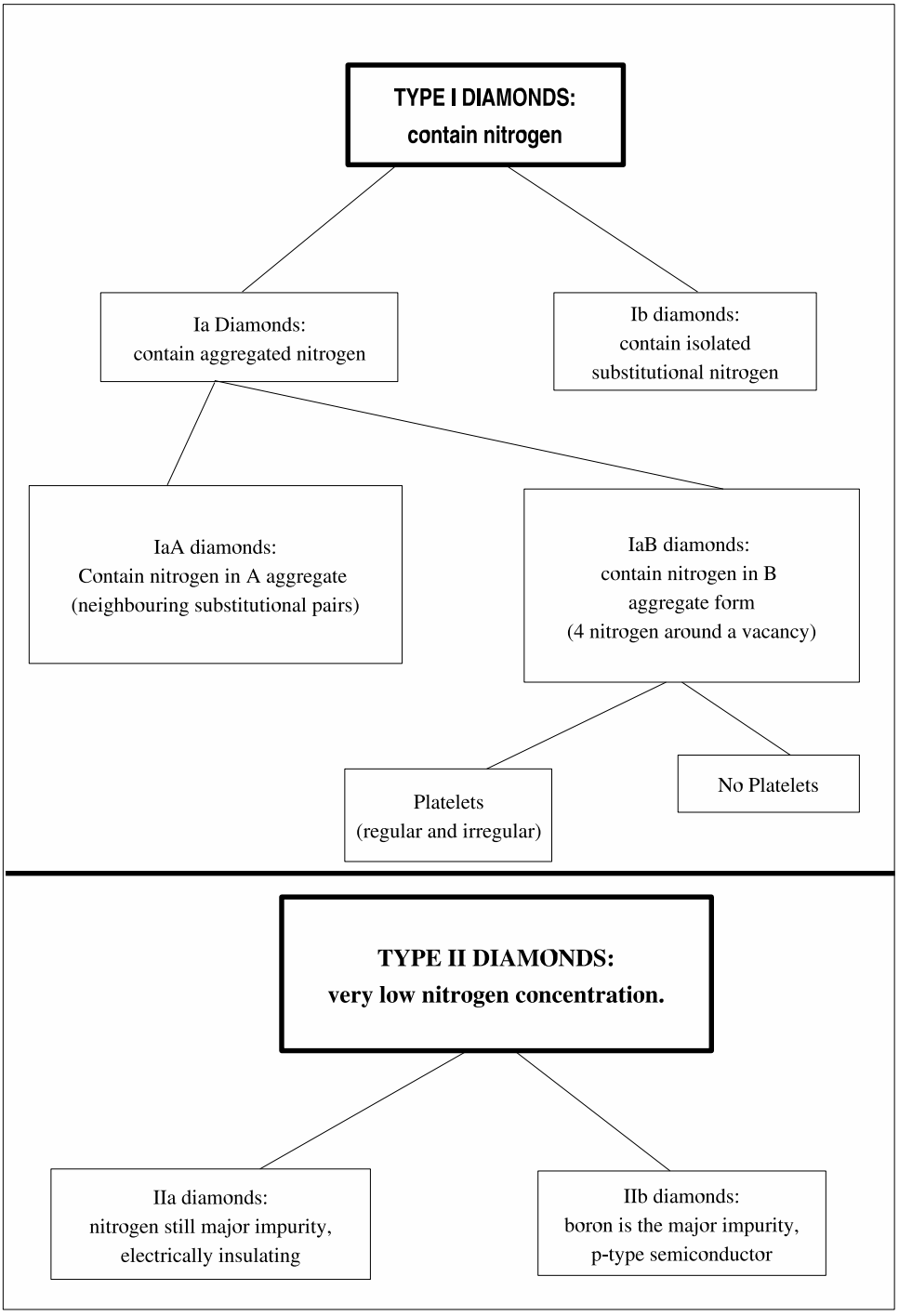

Figure 1.4: The classification scheme for diamonds. N is the chief determiner: when present we have type I; when it is essentially absent we have type II

the theoretical location of the sulphur donor levels, with them lying either very close to the conduction band[53], or more likely being rather deep [23, 73, 74, 75]. Saada et al. [53] have performed first principle calculations on the energetics of substitutional sulphur in diamond and came up with 0.15 and 0.5 eV as the expected energy levels for sulphur in the neutral and singly ionised charge-states respectively. However, the probability of finding S in the S^0 and S^+ state is low, and the S^{2+} state, which is most likely the state for sulphur in diamond, has no electron to donate to conduction [42].

Lithium and Sodium: Impurity atoms can enter interstitial sites of the diamond lattice in the tetrahedral or hexagonal voids of the lattice. It was shown theoretically [76] that for small ions in the diamond lattice, for which the repulsive energy is small, the hexagonal sites and the tetrahedral sites are equilibrium sites and saddle points respectively. For large ions, the repulsive energy will dominate the picture, and the tetrahedral site will be the equilibrium position.

The most promising interstitial dopants for diamond are lithium (Li) and sodium (Na). The ionic radius of Li is 0.060 nm and that of Na is 0.095 nm; their atomic radii, however, are quite large: r(Li) = 1.52 Åand r(Na) = 1.66 Å[52]. In reference [65], Kajihara et al. have carried out ab initio calculations to investigate the possibility of obtaining shallow donor levels from interstitial Li and Na in diamond. The calculations predicted shallow donor levels of 0.1 eV and 0.3 eV below the conduction band minimum for Li and Na respectively. However, experiments on Li and Na doping have not confirmed the theoretical results. Moreover, the solubilities of these dopants are too low to contribute significantly to conductivity.

Other donors: The donor levels of elements such as As, Sb, Se, and Te have also been theoretically investigated (see [5]). As and Sb have been predicted to have

shallow donor levels close to the effective-mass value of 0.218 eV below the conduction band. However, these predictions are yet to be put to an experimental test.

1.2.3 Electrical activity and diffusion of isolated hydrogen in diamond

Due to the absence of any unambiguous data pertaining to the electrical activity of hydrogen in bulk diamond, it is necessary to briefly review what is believed to be the case for silicon. The assignment of the electrical levels of single interstitial hydrogen in silicon has been controversial [77, 78, 79, 80, 81], but, as with many other materials [81], the various charge states of hydrogen correspond to different geometries and produce so-called negative-U centres. Interstitial hydrogen in semiconductors generally can be found at two sites and in three charge states, H^+, H^0, and H^- [82] -respectively, the interstitial proton, the trapped atom or its derivative neutral centres, and the hydride ion where appropriate. H^- is either non-bonded or weakly anti-bonded to a Si atom and is highly mobile, whereas H^0 and H^+ are located at a Si-Si bond centre [28]. The donor and acceptor levels of bond-centred (BC) and tetrahedral (T)-site hydrogen have been calculated to lie around 0.2 eV below the conduction band and mid-gap, respectively [77, 78]. The solubility of hydrogen in silicon is activated with an energy around 1.8 eV [24]. In addition, there are numerous complexes containing hydrogen, such as vacancies, interstitials [83], and impurities. Many of these have been characterised by local mode spectroscopy.

The situation regarding diamond is very different. Muon implantation experiments [33] and theory [84, 29, 85, 27] both indicate that H^0 is metastable at a tetrahedral interstitial site, with its lowest energy configuration consisting of hydrogen at or around the bond-centre. The lowest energy configuration of H^+ was theoretically found to be in a puckered bond-centre site with a C-H-C bond angle of 100° and the lowest energy site for H^- was calculated to be the BC site [24]. Theoretically, the energy of hydrogen in

various sites in diamond varies considerably. In particular, the relative energies of the T and BC sites vary between 0.5 eV and 2.7 eV [28]. The interstitial sites are depicted in figure 1.5.

Bond-centred hydrogen in diamond has been calculated to possess a donor level, which

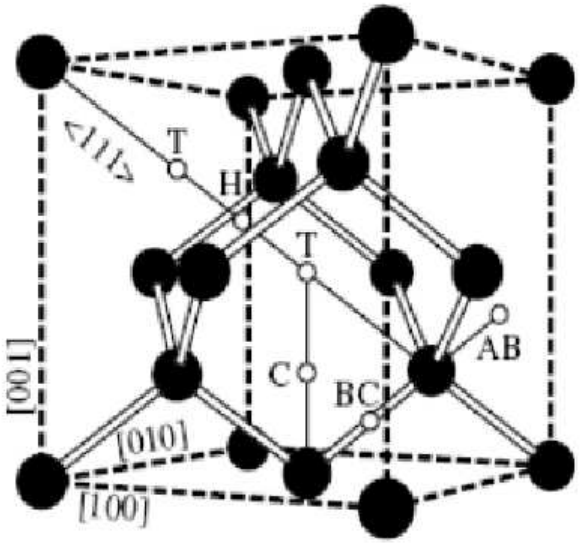

Figure 1.5: An illustration of the most important interstitial sites in diamond structure materials. C atoms are shown as black circles, and ideal interstitial sites as small white circles. The T site lies equidistant from 4 carbon sites, the H site lies midway between two T sites, the C site is midway between an atom site and a T site along < 001 > and the bond-centred (BC) site is the mid-point between two atom sites. The anti-bonded (AB) configuration is less well specified, and is usually taken to mean somewhere between an atom site and a T site along < 111 >. This figure is taken from Ref. [28].

varies considerably depending on the theoretical methods being employed. Comparison of the ionization energy and electron affinity of bond-centred hydrogen with phosphorus and boron, respectively, place the donor and acceptor levels at E_c - 3 eV and E_c - 1.8 eV, respectively [86, 24]. Application of the formation energy calculation using DFT methods has yielded various donor levels at E_v + 2.6 eV [24] and E_v + 1.2 eV [23], and acceptor levels at E_c - 2.3 eV [24] and E_v + 3.0 eV [23]. Total energy differences in cluster calculations with a quantum confinement correction yields a donor level of E_c - 3.8 eV [73]. Consequently, the evident conclusion is that bond-centred hydrogen

possesses a donor level below the band gap and an acceptor level around mid-gap. This has implications for both n- and p-type material. In n-type material bond-centred hydrogen will be negatively charged and compensate the donor, while on the contrary in p-type material the hydrogen will be positively charged, but still compensating the dopant. The passivation of p-type diamond by hydrogen has been confirmed experimentally [20, 87, 15, 88, 89].

The diffusion of hydrogen in diamond is mainly controlled by [90]:

- H solubility in diamond, which is related to H formation energy in diamond,
- H migration energy in diamond, and
- the height of the surface barrier for H to enter into the crystal, prior to bulk diffusion.

The main characterisation methods used for the study of diffusion of hydrogen in diamond are [90]:

(i) SIMS (secondary-ion mass spectroscopy) measurements, to study the hydrogen profile in the layer[5] .

(ii) Optical measurements like IR spectroscopy, to detect hydrogen-related complexes,

(iii) nuclear method combined with channeling to determine the location of D or H in the crystal and to get hydrogen concentration profiles in the near surface region,

(iv) micro-scanning heavy ion elastic recoil detection analysis (ERDA) to measure the hydrogen concentration profile in the near-surface region,

[5] Deuterium is usually introduced instead of hydrogen because of the higher sensitivity of the SIMS to D than H: the detection limit for deuterium being approximately 5 x 10^{16} cm^{-3}

(v) electrical measurements to study the activation or deactivation of specific dopants and defects caused by pairing with hydrogen.

In diamond layers that contain native defects or impurities, only a very small fraction of hydrogen diffuses as an interstitial due to the presence of many traps like dangling bonds, grain boundaries or vacancies, or by shallow acceptors or donors, and other impurities. There are a number of possible migration trajectories for bond-centred hydrogen, and different theoretical studies have indicated qualitatively different expectations. The simplest are processes that involve only metastable or symmetry defined structures, such as BC $\rightarrow$ T and BC $\rightarrow$ H [28]. If it is energetically favourable, the hydrogen atom would possibly migrate many steps along the open channels via T $\rightarrow$ H $\rightarrow$ T hops. Alternatively, it moves from the bond centre to a C_{2v} symmetry site close to the C site in Figure 1.5 [28].

1.2.4 Hydrogen-related complex formation in diamond

The race is on to find an alternative to phosphorus. This has led to a number of suggestions, many of which rely on the principles of co-doping. This essentially combines properties of more than one defect which conspire to yield the desired electrical (or indeed optical) properties. For example, the combination of two donors (D) and a single acceptor (A) in close proximity such as D-A-D will give rise to a single donor, but this may be shallower than that of an isolated single donor, D. Some of the suggestions along these lines are boron-hydrogen; hydrogen-nitrogen; hydrogen-phosphorus; and hydrogen-sulphur complexes. Diamond is the intellectual model wide band gap material for both experimental and theoretical investigations of these hydrogen-intrinsic defect complexes [91].

Hydrogen-Boron complexes: The most clear evidence for hydrogen-related defects in diamond comes from the passivation of boron acceptors by in-diffused deuterium [20, 51, 92, 87]. It has been suggested [51] that neutral hydrogen atoms entering boron-doped diamond will become ionized, providing their electrons to firstly compensate holes arising from the few ionized boron acceptors, and secondly to ionize neutral boron atoms. The resulting B^- and H^+ ions are expected to attract each other via a Coulomb interaction and form neutral boron-hydrogen (BH_1) pairs [24, 93].

Passivated boron in silicon adopts a structure with hydrogen in the bond-centred location [94, 95], but there is no direct experimental data to establish the site of the hydrogen atom for diamond [28]. Local-density-functionary theory [96] showed that the hydrogen lies close to < 100 > from the B site (Fig. 1.6), while semi-empirical cluster calculations [97] suggest that the hydrogen atom is in a puckered bond-centred location such that $\angle BHC = 113°$.

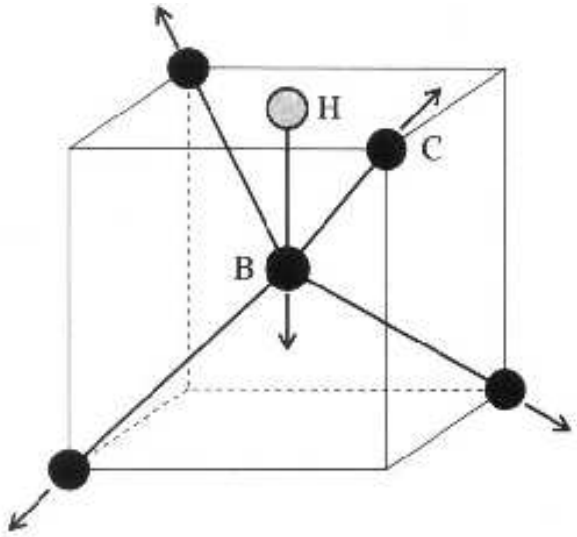

Figure 1.6: The < 100 > aligned boron-hydrogen defect and the first nearest neighbour carbon atoms. The arrows indicate the direction in which the important relaxations of the atoms take place. This figure is taken from Ref. [96].

Recently, Teukam et al. [15] (see also Ref. [98]) reported on experimental evidence that high-conductivity n-type diamond, with a shallow activation energy only 0.23 eV below the conduction band, can be achieved by deuteration of particularly selected homo-epitaxially grown < 100 > boron-doped diamond layers. The authors interpret their results using a model based on the formation of some unknown deuterium-boron complexes, which are supposed to be the origin of the electron shallow donors. However, Dai et al. [99, 100] have explained this phenomenon of conversion from *p*-type to *n*-type conductivity through deuteration by the transformation from the type of one-hydrogen-boron complexes (BH_1) into that of two- or three-hydrogen-boron (BH_2 or BH_3) complexes. Thus, it is of great importance to understand these possible deuterium-boron complexes responsible for the conductivity-type conversion in research and development of the electronic diamond devices.

Hydrogen-Nitrogen complexes: The nitrogen-hydrogen pair in diamond locates hydrogen at the bond centre [97]. Semi-empirical calculations have shown that the hydrogen atom lies closer to the carbon neighbour, with the overall N-H-C separation being dilated by around 0.26 Å relative to the already dilated N-C bond, with the C-H and N-H distances being 1.06 and 1.20 Å, respectively [97]. In the semi-empirical cluster calculations [97] the binding energy of this structure was found to be 1.49 eV. This is comparable to the binding energy of the boron-hydrogen pair calculated using the same approximations [97], and similar to the binding energy of the N-H defect found from LDA-DFT methods [24] at 4.2 and 3.5 eV for the reactions N-H $\rightarrow N^0 + H^0$ and N-H $\rightarrow N^+ + H^-$, respectively, assuming a formation energy of bond-centred hydrogen at 2.6 eV.

A model structure involving hydrogen and nitrogen that gives rise to a shallow donor level was proposed [4]. This defect is made up from the A centre with a hydrogen atom

placed in the bond centre between the two N atoms, as shown in Figure 1.7.

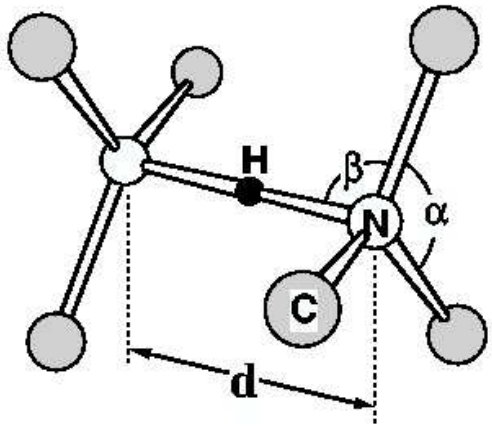

Figure 1.7: Optimized structure of the N-H-N defect. This defect is made up from the A-centre with a hydrogen atom placed in the bond-centre between two N atoms; d = 2.20 Å, $\alpha = 117.0°$, and $\beta = 100.0°$ Insertion of H between two Ns elongates the N-N distance by about 3 %. This figure is taken from Ref. [4].

The A-centre defect is a prime site for bond-centred hydrogen since it has a very long N-N separation comparable to the dilation seen when H lies between two carbon atoms [28]. The dilation induced by the addition of the H to the A centre is just 3 %. Using the substitutional N centre as an empirical marker, the N-H-N defect is calculated to yield a donor level at around E_c - 0.6 eV [4] which is comparable to substitutional phosphorus [66, 101]. The formation energy of the complex is calculated to be in the 4-5 eV range [28] (see Figure 1.8).

A new muonium centre (Mu_X) has been discovered by Machi et al. [3] in N-rich diamond. They propose that Mu_X is a muonium sitting between two N atoms in an A centre. This observation suggests a possibility of the N-H-N defects having a real existence in N-rich diamond. Since H is much heavier than a muonium, H should be trapped in the middle of the A centre for a much longer period than the muonium.

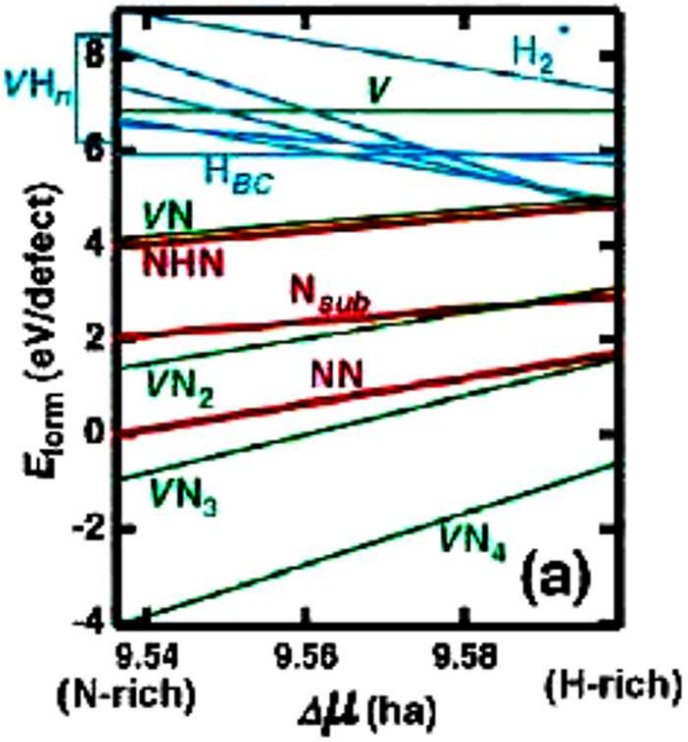

Figure 1.8: Calculated formation energies (E_{form}) of various N- and H-related defects in diamond, as a function of $\Delta\mu = \mu_H - \mu_N$, where μ_H and μ_N are chemical potentials of H and N, respectively. The formation energy of the N-H-N defect is lower than those of V as well as other H-related defects. This figure is taken from Ref. [4].

Hydrogen-phosphorus complexes: Density functional calculations show that hydrogen binds to phosphorus in an anti-bonding site[74, 102], bonded to the phosphorus atom, rather than the anti-bonding to a neighbouring host atom as is the case for the P-H pair in silicon [103]. The binding energy is estimated to be 2.56 eV [74, 102], 3.1 eV [24] and 2.45 eV [23] for separation into neutral components, and 1.0 eV [24] and 1.85 eV [23] for breaking down into charged components, P^+ and H^-.

Hydrogen-Sulphur complexes: The general consensus is that substitutional sulphur generates a donor level that is too deep for semiconductor applications, but that the interaction of other impurities, including hydrogen, may bring the donor level into

a more accessible location. The S-H pair is lowest in energy when hydrogen lies at the AB1 site [102, 74, 104] (Figure 1.9), just as found with phosphorus. The binding energy of the S-H pair in the neutral charge state is 2.56 eV from LDA-DFT supercell calculations [74, 102]. The S-H_{AB} pair remains a deep donor in these calculations (E_c - 1.07 eV).

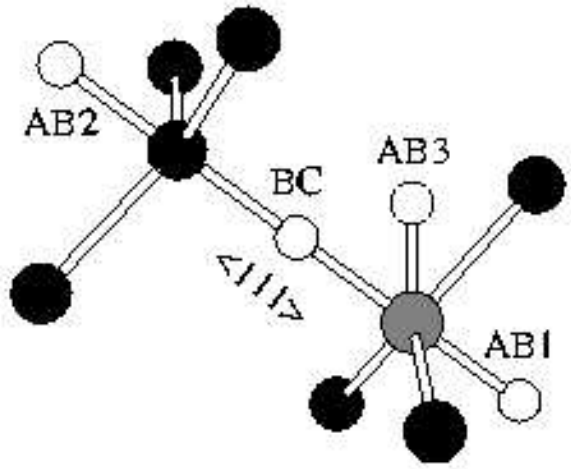

Figure 1.9: A schematic representation of four possible locations of hydrogen in impurity-hydrogen complexes. BC and AB refer to bond-centred and anti-bonding sites, respectively. The black, white and grey atoms represent carbon, hydrogen and impurity sites, respectively. This figure is taken from Ref. [28].

Miyazaki et al. [105, 75] have found, using GGA-DFT methods, that there are several forms of combinations of sulphur, hydrogen and vacancy; namely, H-S, SVH_3 and SVH_4H_{AB}; that generate shallow donors, ranging from 0.5-0.6 eV below the conduction band minimum. However, the main problems with these structures as dopants are the absolute formation energy (4 eV and greater) and the fact that alternative structures, such as vacancy-hydrogen complexes, are more stable for a wide range of hydrogen chemical potentials [28]. Furthermore, there are many more structures with deep levels that can be formed from the same constituents, and under any thermally annealed conditions it seems unlikely that the beneficial complexes would survive [28].

Chapter 2

Theoretical Aspects of Muon Spin Spectroscopy

"You do not really understand something unless you can explain it to your grandmother."

Albert Einstein.

In this chapter μSR (Muon Spin Rotation, Relaxation) techniques used to obtain the data presented in this thesis will be introduced. The theory of muon spin spectroscopy is introduced in Section 2.1. Section 2.3 describes properties of the muon and the fundamentals of muon decay. Section 2.4 deals with the μSR signals observed under the longitudinal field (LF) and transverse field (TF) geometries. In our experiments the LF and TF techniques were used to obtain the necessary information about the localisation and mobility of the muon in a diamond lattice. Section 2.5 describes the properties and behaviour of muonium in a diamond lattice compared to that of hydrogen. It also looks at the electronic structure and dynamics of the two muonium centres, namely tetrahedral muonium (Mu_T) and bond-centred muonium (Mu_{BC}), observable in diamond.

2.1 Preliminary Remarks

The magnetic interactions of a muonium atom in its ground state in the presence of an external field B, in the absence of extraneous interactions, are given by the Hamiltonian [106]

$$\mathcal{H}_{MU} = A\vec{\mathbf{S}}_\mu \cdot \vec{\mathbf{S}}_e + g_\mu \mu_\mu \vec{\mathbf{S}}_\mu \cdot \vec{\mathbf{B}} + g_e \mu_B \vec{\mathbf{S}}_e \cdot \vec{\mathbf{B}}. \tag{2.1}$$

The electron spin $\vec{\mathbf{S}}_e$ and the muon spin $\vec{\mathbf{S}}_\mu$ are coupled through the Fermi contact interaction

$$\mathcal{H}_{hf} = \frac{2}{3}\mu_0 g_e \mu_B g_\mu \mu_\mu |\Psi_{1s}(0)|^2 \vec{\mathbf{S}}_\mu \cdot \vec{\mathbf{S}}_e \tag{2.2}$$

with a hyperfine coupling constant A proportional to $|\Psi_{1s}(0)|^2$, the electron density at the muon site, that is

$$A = h\nu_0 = -\frac{8}{3} g_e g_\mu \pi \mu_B^e \mu_B^\mu |\Psi(0)|^2, \tag{2.3}$$

where the operators for the magnetic moments of the electron and the muon are

$$\begin{aligned} \vec{\mu}_e &= -g_e \mu_B \vec{\mathbf{S}}_e, \\ \vec{\mu}_\mu &= -g_\mu \mu_\mu \vec{\mathbf{S}}_\mu. \end{aligned} \tag{2.4}$$

For muonium atoms in a solid, the local symmetry to which the electron wavefunction adapts itself has to be taken into account, and the hyperfine coupling will be given by a tensor **A** instead of the hyperfine constant A. Bond centred muonium is axially symmetric and if $\hat{\mathbf{z}}'$ is chosen to be along its major axis, then the only non-zero elements of **A** for this state are $A_{\hat{x}'\hat{x}'} = A_{\hat{y}'\hat{y}'} = A_\perp$ and $A_{\hat{z}'\hat{z}'} = A_\parallel$. Tetrahedral muonium, Mu_T is isotropic and $A_\perp = A_\parallel = A$. The spin eigenfunctions $|n\rangle = \sum_i a_{ni}|\chi\rangle$ of the Hamiltonian 2.1 can be evaluated in the non-diagonal basis $|\chi\rangle = |M_e, M_\mu\rangle$:

$$\begin{aligned} |\chi_1\rangle &= |\tfrac{1}{2}, \tfrac{1}{2}\rangle & |\chi_2\rangle &= |\frac{1}{2}, -\frac{1}{2}\rangle \\ |\chi_3\rangle &= |-\tfrac{1}{2}, \tfrac{1}{2}\rangle & |\chi_4\rangle &= |-\frac{1}{2}, -\frac{1}{2}\rangle, \end{aligned} \tag{2.5}$$

where M_e and M_μ are the electron and muon magnetic quantum numbers respectively. The energy eigenvalues E_n are obtained by solving the secular equation:

$$\begin{vmatrix} \kappa - E & \delta & \gamma & \alpha \\ \delta^* & -\kappa - E & \beta & -\gamma \\ \gamma^* & \beta^* & -\kappa - E & -\delta \\ \alpha^* & -\gamma^* & -\delta^* & \kappa - E \end{vmatrix} = 0 \tag{2.6}$$

where

$$\begin{gathered} \alpha = \tfrac{1}{4}\left[A_{xx} - A_{yy} - i(A_{xy} + A_{yx})\right] \\ \beta = \tfrac{1}{4}\left[A_{xx} + A_{yy} + i(A_{xy} - A_{yx})\right] \\ \gamma = \tfrac{1}{4}(A_{xz} - iA_{yz}) \qquad \delta = \tfrac{1}{4}(A_{zx} - iA_{zy}) \qquad \kappa = \tfrac{1}{4}A_{zz} \end{gathered} \tag{2.7}$$

with corresponding complex conjugate quantities $\alpha^*, \beta^*, \gamma^*, and\ \delta^*$. Since the Hamiltonian $\mathcal{H}_{hf}$ is invariant under a rotation of the co-ordinate system, a co-ordinate system (x', y', z') in which **A** is diagonal, can be chosen. It follows then, from equation 2.7, that $\gamma = \delta = 0$ and the secular equation 2.6 reduces to

$$\left[((\kappa - E)^2 - \alpha^2)(-\kappa - E)^2 - \beta^2\right] = 0 \tag{2.8}$$

with solutions

$$\begin{aligned} E_{1,3} &= \kappa \pm \alpha = \frac{1}{4}\left[A_{z'z'} \pm (A_{x'x'} - A_{y'y'})\right] \\ E_{2,4} &= -\kappa \pm \beta = -\frac{1}{4}\left[A_{z'z'} \mp (A_{x'x'} + A_{y'y'})\right]. \end{aligned} \tag{2.9}$$

An analytic solution for E can always be obtained even though the secular equation is of the fourth order in E. Thus, the isotropic Hamiltonian, equation 2.2, with $A_{xx} = A_{yy} = A_{zz} = \hbar\omega_0$, possesses the eigenvalues

$$E_1 = E_2 = E_3 = +\frac{1}{4}\hbar\omega_o \qquad , \qquad E_4 = -\frac{3}{4}\hbar\omega_o, \tag{2.10}$$

and an axially isotropic Hamiltonian with $A_{x'x'} = A_{y'y'} \neq A_{z'z'}$ leads to eigenvalues of

$$\begin{aligned} E_1 = E_3 &= \tfrac{1}{4}A_{z'z'} \\ E_2 = -\tfrac{1}{4}A_{z'z'} + \tfrac{1}{2}A_{x'x'} \qquad & E_4 = -\tfrac{1}{4}A_{z'z'} - \tfrac{1}{2}A_{x'x'}. \end{aligned} \tag{2.11}$$

If the Zeeman interaction of the μ^+ and the electron in an external magnetic field, B, is included, the secular equation 2.6 assumes the form

$$\begin{vmatrix} \kappa + \frac{1}{2}\hbar(\omega_e^z - \omega_\mu^z) - E & \delta - \frac{1}{2}\hbar\omega_\mu^- & \gamma + \frac{1}{2}\hbar\omega_e^- & \alpha \\ \delta^* - \frac{1}{2}\hbar\omega_\mu^+ & -\kappa + \frac{1}{2}\hbar(\omega_e^z + \omega_\mu^z) - E & \beta & -\gamma + \frac{1}{2}\hbar\omega_e^- \\ \gamma^* + \frac{1}{2}\hbar\omega_e^+ & \beta^* & -\kappa - \frac{1}{2}\hbar(+\omega_e^z + \omega_\mu^z) - E & -(\delta + \frac{1}{2}\hbar\omega_\mu^-) \\ \alpha^* & -\gamma^* + \frac{1}{2}\hbar\omega_e^+ & -(\delta^* + \frac{1}{2}\hbar\omega_\mu^+) & \kappa - \frac{1}{2}\hbar(\omega_e^z - \omega_\mu^z) - E \end{vmatrix} \tag{2.12}$$

This equation has analytic solutions if the field **B** is applied along any of the principal axes of the hyperfine Hamiltonian, and if this Hamiltonian is isotropic, then the famous Breit-Rabi equations, which describe the the energy splitting of atomic hydrogen or muonium in an external magnetic field, are retained:

$$\begin{aligned} E_1 &= \tfrac{1}{4}A + \tfrac{1}{2}\hbar(\omega_e - \omega_\mu) = \tfrac{1}{4}A(1 + 2dx) \\ E_2 &= -\tfrac{1}{4}A + \left[\tfrac{1}{4}A^2 + \tfrac{1}{4}\hbar^2(\omega_e + \omega_\mu)^2\right]^{\frac{1}{2}} = \tfrac{1}{4}A\left[-1 + 2(1 + x^2)^{\frac{1}{2}}\right] \\ E_3 &= \tfrac{1}{4}A - \tfrac{1}{2}\hbar(\omega_e - \omega_\mu) = \tfrac{1}{4}A(1 - 2dx) \\ E_4 &= \tfrac{1}{4}A - \left[\tfrac{1}{4}A^2 + \tfrac{1}{4}\hbar^2(\omega_e - \omega_\mu)^2\right]^{\frac{1}{2}} = \tfrac{1}{4}A\left[1 - 2(1 + x^2)^{\frac{1}{2}}\right] \end{aligned} \tag{2.13}$$

where

$$x = B(g_e\mu_B + g_\mu\mu_N)/A \tag{2.14}$$

(for muonium in vacuum $x \approx B/1585$ G) and

$$\begin{aligned} d &= (1 - g_\mu \mu_N / g_e \mu_B)/(1 + g_\mu \mu_N / g_e \mu_B) \\ &= \frac{\gamma'_e - \gamma_\mu}{\gamma'_e + \gamma_\mu} = 0.990, \end{aligned} \tag{2.15}$$

where $\gamma'_e = g_e \mu_B$ and $\gamma_\mu = g_\mu \mu_N$.

Once the muonium eigenfunctions and energy eigenvalues have been obtained, the time evolution of the muon spin polarization can be determined. As indicated in Section 2.4 the motion of the muon spin in MuSR is monitored by measuring the directions of emitted positrons as functions of the time after creation of the muons.

The evolution of the muon spin motion with time under the influence of the magnetic moment of the bound electron and external field can be calculated using the density matrix formulation. A good treatment of this formulation is provided by [107, 108]. With the basis states (2.6) valid for the ground state of muonium, a spin operator ρ can be defined, that is,

$$\rho = \sum_{ij} |i\rangle \rho_{ij} \langle j|, \tag{2.16}$$

which has the property that $\mathrm{Tr}\,\rho = 1$ and $\rho_{ij} = \langle i|\rho|j\rangle = \rho_{ij}$ where ρ is the **spin density matrix**. The muon and electron spin polarizations can be represented by the Pauli spin matrices σ_μ and σ_e respectively, and therefore the spin density operator becomes

$$\rho = \frac{1}{4}\left(1 + \mathbf{P}_\mu \cdot \sigma_\mu + \mathbf{P}_e \cdot \sigma_e + \sum P_{ij} \sigma_\mu^i \sigma_e^j\right), \tag{2.17}$$

where the muon, electron and mixed-term polarizations, respectively, are

$$\begin{aligned} \mathbf{P}_\mu &= Tr\left(\rho \sigma_\mu\right) \\ \mathbf{P}_e &= Tr\left(\rho \sigma_e\right) \\ P_{ij} &= Tr\left(\rho \sigma_\mu^i \sigma_e^j\right) \end{aligned} \tag{2.18}$$

The time evolution $\mathbf{P}_\mu(t)$ as expressed in the Heisenberg representation is

$$\mathbf{P}_\mu(t) = Tr[\rho(0)\sigma_\mu(t)] \tag{2.19}$$

where

$$\sigma_\mu(t) = exp\,(i\mathcal{H}t/\hbar)\,\sigma_\mu exp\,(-i\mathcal{H}t/\hbar)\,. \tag{2.20}$$

When muonium is formed in a MuSR experiment, the muons are spin polarized, say, along the $\hat{z}$ axis. The spin state of the μ^+ is hence represented by the function

$$\chi_\mu^+ = |+\frac{1}{2}\rangle_\mu. \tag{2.21}$$

Conversely, the electrons picked during the muonium formation are unpolarized. Their spin states are therefore represented, with respect to the chosen z axis, by

$$\chi_e^+ = |+\frac{1}{2}\rangle_e \qquad \chi_e^- = |-\frac{1}{2}\rangle_e \tag{2.22}$$

with a population of 50% in each case. Upon formation of muonium, the combined spin state is then given by

$$\chi_{\mu^+e^-}^+ = |\frac{1}{2}\rangle_e|\frac{1}{2}\rangle_\mu = |\frac{1}{2},\frac{1}{2}\rangle \qquad \chi_{\mu^+e^-}^- = |-\frac{1}{2}\rangle_e|\frac{1}{2}\rangle_\mu = |-\frac{1}{2},\frac{1}{2}\rangle. \tag{2.23}$$

The second state is not an eigenstate of the hyperfine Hamiltonian equation and hence the spin arrangement, $|-\frac{1}{2}\rangle_e|+\frac{1}{2}\rangle_\mu$, is unstable in zero applied magnetic field. Put differently, the spin polarisation vector of those μ^+ in this initial spin arrangement will become time dependent, and will evolve in time. However, the configuration $|+\frac{1}{2}\rangle_e|+\frac{1}{2}\rangle_\mu$ is an eigenstate of the hyperfine Hamiltonian, and consequently the muon polarisation

in this state will not display any time dependence. If an external field is applied, a complex time dependence of the muon's spin polarisation $\mathbf{P}_\mu$ evolves.

In order to calculate the time evolution of $\mathbf{P}_\mu(t)$, the spin density matrix formalism is employed. The initial condition is characterised by a non-zero polarisation, $\mathbf{P}_\mu(0)$, of the μ^+ and zero electron polarisation $\mathbf{P}_e(0) = 0$ and $\mathbf{P}_{ij}(0) = 0$. Therefore at time $t = 0$ the spin density operator 2.17 becomes

$$\rho(0) = \frac{1}{4}[1 + \mathbf{P}(0)\sigma_\mu]. \tag{2.24}$$

The time evolution of the muon polarization can then be obtained by inserting equations 2.19 and 2.24 into the general equation of motion, $i\hbar\dot{\rho}(t) = [\mathcal{H}, \rho(t)]$. With the eigenfunctions $|n\rangle = \sum_i a_{ni}|\chi\rangle$ of $\mathcal{H}$ as a basis, this gives

$$\begin{aligned} \mathbf{P}_\mu(t) &= \tfrac{1}{4}\textstyle\sum_{k,n,m}\langle k|n\rangle\langle n|1 + \mathbf{P}_\mu(0)\sigma_\mu|m\rangle\langle m|\sigma_\mu(t)|k\rangle \\ &= \tfrac{1}{4}\textstyle\sum_{n,m}\langle n|1 + \mathbf{P}_\mu(0)\sigma_\mu|m\rangle\langle m|\sigma_\mu|n\rangle exp(i\omega_{mn}t) \end{aligned} \tag{2.25}$$

where $\omega_{nm} = (E_m - E_n)/\hbar$. Since $\langle n| = \sum_j \langle\chi|a_{jn}^{-1} = \sum_j \langle\chi|a_{nj}^*$ and the matrix (a_{ij}) represents a unitary transformation, equation 2.25 finally becomes

$$\mathbf{P}_\mu(t) = \frac{1}{4}\sum_{n,m,i,j,k,l} a_{nj}^* a_{mi} a_{mk}^* a_{nl}\langle\chi_j|\mathbf{P}_\mu(0)\sigma_\mu|\chi_i\rangle\langle\chi_k|\sigma_\mu|\chi_l\rangle exp(i\omega_{mn}t). \tag{2.26}$$

Equation 2.26 can be employed to find the solution for $\mathbf{P}_\mu(t)$ for anisotropic hyperfine interaction in zero field; isotropic hyperfine interaction in zero field; isotropic hyperfine interaction in transverse applied field; and anisotropic hyperfine interaction in transverse applied field.

In a LF-μSR experiment in which the applied field and μ^+ polarisation are parallel and the μ^+ is polarised in the z direction, equation 2.26 is easily evaluated and yields

$$|\mathbf{P}_\mu(t)| = P_z(t) = 1 - \frac{1}{2}\left[1 - \cos\omega_0(1+x^2)^{\frac{1}{2}}t\right]/(1+x^2) \tag{2.27}$$

with $\omega_0 = A/\hbar$ and x given by equation 2.14. The evaluation of $P_z(t)$ for the Mu_T state is characterised by a time independent term called the residual polarisation, and is given by

$$P_z = \frac{(1+2x^2)}{(2+2x^2)} \tag{2.28}$$

In zero field, P_z is reduced to 50 % of the initial polarisation and approaches 100 % upon increasing the applied field to large values (see Figure 5.1). This is a consequence of the decoupling of electron and muon spin in strong magnetic fields (Paschen-Back effect) and is usually referred to as the ”quenching of depolarisation”.

In a TF-μSR experiment in which the μ^+ are polarised in the x direction perpendicular to the applied field (z direction) equation 2.25 yields

$$P_x(t) = \frac{1}{4}\left[(1+\delta)\cos\omega_{12}t + (1-\delta)\cos\omega_{14}t + (1+\delta)\cos\omega_{34}t + (1-\delta)\cos\omega_{23}t\right] \tag{2.29}$$

$$P_y(t) = \frac{1}{4}\left[-(1+\delta)\sin\omega_{12}t + (\delta-1)\sin\omega_{14}t + (\delta-1)\sin\omega_{23}t + (1+\delta)\sin\omega_{34}t\right] \tag{2.30}$$

$$P_z(t) = 0 \tag{2.31}$$

where $\omega_{ij} = \frac{(E_i - E_j)}{\hbar}$ and $\delta = x(1+x^2)^{-\frac{1}{2}}$.

The time evolution of the muon’s polarisation is therefore characterised by four frequencies corresponding to possible transitions among the hyperfine states of muonium obeying the selection rules $\Delta F = 0, 1$; $\Delta m_F = 1$ at low fields and $\Delta m_e = 0$, $\Delta m_\mu = 1$

at very high fields. At these fields the terms with ω_{14} and ω_{23} involving the electronic transitions $\Delta m_e = 1$ vanish due to the effective decoupling of μ^+ spin and electron spin in the Paschen-Back limit.

2.2 Shallow-donor Muonium States

Tetrahedral and bond-centred muonium have fairly localised or compact electronic wavefunctions, albeit of quite different symmetry. They are both, in the nomenclature of semiconductor defects, deep states. The binding or ionization energy of the electron, for Mu^0_{BC} in Si, defines a donor level that lies several hundred meV below the conduction-band minimum [80]. The binding energy for Mu^0_T cannot be measured directly but, given the hyperfine constants, must be a substantial fraction of a Rydberg, i.e., at least several electron volts [109].

There is a third category of muonium states, discovered only recently, for which the ionization energies and temperatures are low and the hyperfine parameters are tiny. They have all the characteristics of the classic shallow-donor states exemplified, in silicon for instance, by impurities such as interstitial lithium or dopants such as substitutional phosphorus. For such states, the paramagnetic electron of the unionized donor occupies a very much more extended orbital and is bound only weakly to the charge defect. Muonium states which appear to qualify for this shallow-donor category have been reported in CdS, CdSe, CdTe, ZnO, GaN and InN [110, 111, 112, 113, 82, 114, 115] (see Figure 2.1), and also inferred shallow states in GaAs and GaP [116, 117, 36]. This is the first experimental evidence of muonium (and hence hydrogen) forming shallow donor states in semiconductors and is of very real interest to the semiconductor physics community. For all these materials, the contact terms A^* representing electronic spin density on the muon, are some four orders of magnitude smaller than the hyperfine constant of vacuum-state muonium ($A_0 = 4.5$ GHz). It is this factor which is suggestive of weakly

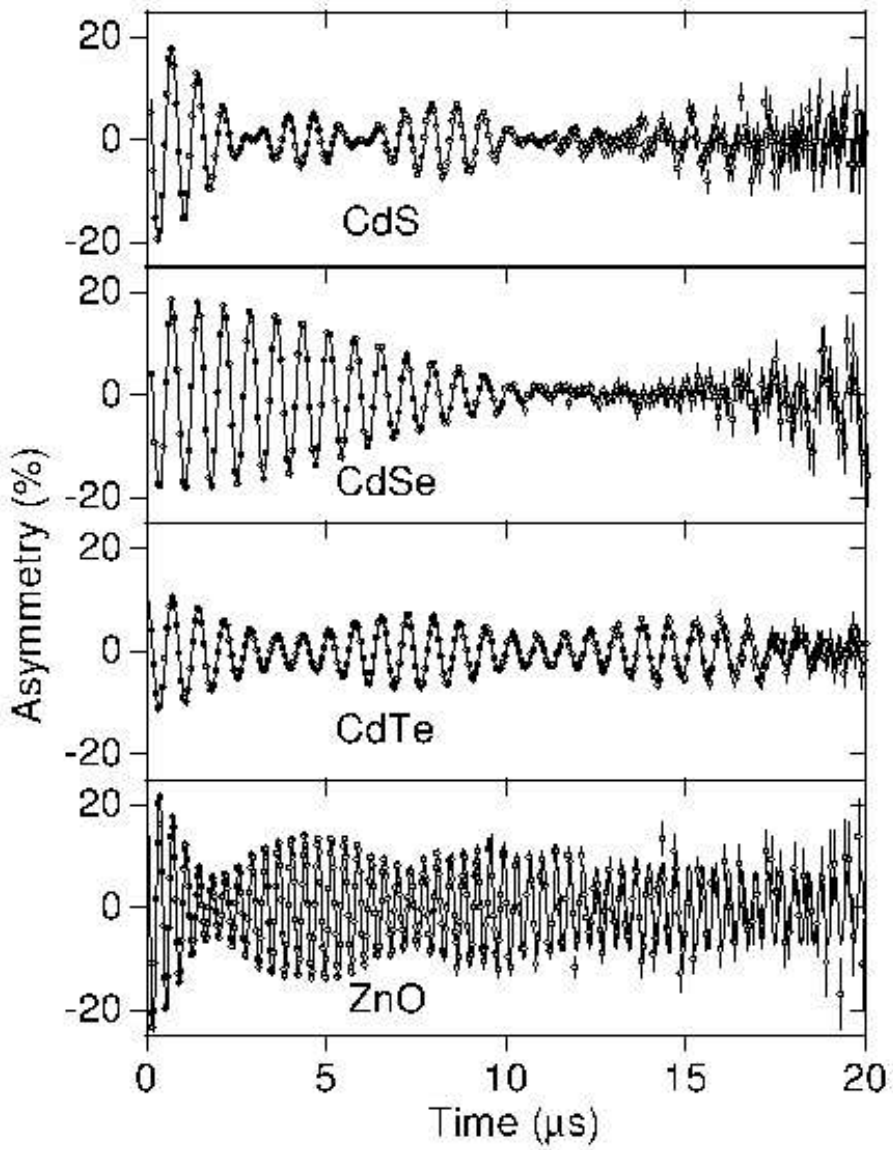

Figure 2.1: μSR time spectra for the four compounds CdS, CdSe, CdTe, and ZnO. The beating pattern originates from the splitting of precession frequencies, with a period related to the hyperfine constants of the paramagnetic muonium, i.e., of the undissociated donor. This figure is taken from Ref. [111]

bound electrons with extended wavefunctions. The effective Bohr radii inferred from these spin densities are comparable with values calculated within the effective-mass model [111]; ionization temperatures and activation energies deduced from the temperature dependence of signal amplitudes are also consistent with the shallow-donor

interpretation [110, 112, 111]. This interpretation can be reinforced by noting a relationship between central spin density and ionisation energy. In the usual notation, the effective-mass expressions [118]: $a^* = (a_0\varepsilon)/(m^*/m_e)$, $R^* = R_0(m^*/m_e)/(\varepsilon^2)$ and $A^* = A_0(a_0/a^*)^3$ can be combined to give

$$R^* = \frac{R_0}{\varepsilon}\left(\frac{A^*}{A_0}\right)^{\frac{1}{3}} \tag{2.32}$$

where $R_0 = 13.6eV$. These values are compared in Table 2.1 with the experimental binding energies. For diamond $\varepsilon = 5.70$, and taking $m^* = m_e$ yields $R^* \approx 0.42$ eV as the expected shallow-donor ionization energy for a hydrogenic impurity in diamond.

Table 2.1: Correlation of the spin density on the central muon with experimental donor-level depth

	A^* / A_0	R^* (meV)	E_d (meV)
CdS	0.55 x 10^{-4}	59	26± 6
CdSe	0.19 x 10^{-4}	37	20± 4
CdTe	0.58 x 10^{-4}	52	16± 4
ZnO	1.1 x 10^{-4}	79	58±6

2.3 Muon Production and Decay

The muon is found in nature and it is a member of a class of fundamental particles called leptons that include the more familiar electron (e), as well as the tau (τ) and the muon, electron and tau neutrinos and their corresponding antiparticles. All leptons are point-like particles with no internal structure [119]. The muon was initially identified in cosmic rays in 1936 [120, 121, 122, 123]. Major advances in muon science and their application followed from the first artificial production of pions by particle accelerators about 1957. High- energy proton beams (typical energy 500 MeV) are fired into a target

of graphite or other light element to produce positive pions (π^+)[1] via the two reactions

$$p + p \rightarrow p + n + \pi^+ \tag{2.33}$$
$$p + n \rightarrow n + n + \pi^+$$

and the pion[2] then decay quickly to muons:

$$\pi^+ \rightarrow \mu^+ + \nu_\mu, \qquad (\tau_\pi = 26\ ns) \tag{2.34}$$

where ν_μ is a muon neutrino. Since the neutrino is produced with negative helicity (its spin is aligned anti parallel with its momentum) and the pion has zero spin it therefore follows that in order to conserve angular momentum, μ^+ must also have negative helicity in the rest frame of the pion [35, 124]. This is shown in Figure 2.2.

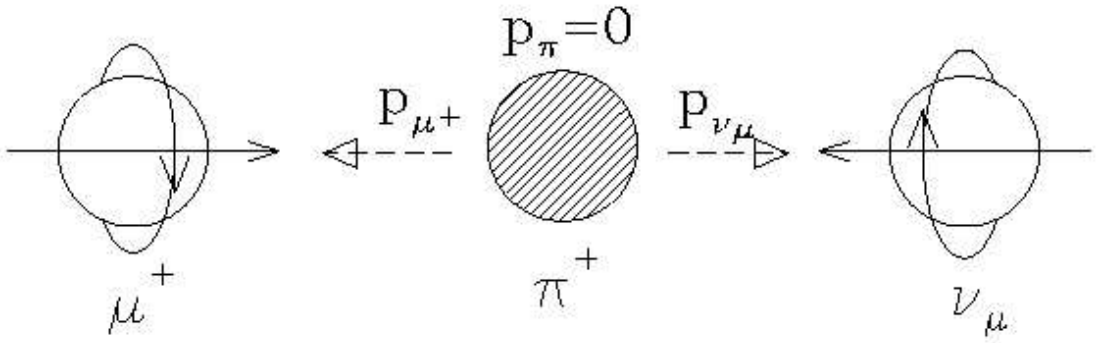

Figure 2.2: Decay of the positive pion in a co-ordinate system where the pion is at rest. Directions of spin and momentum for the decay particles are indicated.

Two types of μ^+ beams are available for μSR measurements, according to the value of the pion momentum at the decay time. The first type of muon beam is formed by the

[1] In fact, the pions are created in one of three charge states(π^+, π^- *or* π^0) during the high-energy nuclear collisions.

[2] The pion decay is a two-body decay and is an example of parity- violating weak interaction, the result being a neutrino with negative helicity and a muon which in the pion rest frame is 100 % polarised anti-parallel to the muon momentum (from π^+ and μ^+).

π^+ decaying in flight (usually in a long superconducting solenoid). In this way, typical muon beams with a polarization of ~80% and energies of ~40-50 MeV are produced after momentum selection by bending magnets. Incomplete polarisation arises because muons in the beam include some emitted at non-zero angles with respect to the pion beam direction[125]. Although such a high-energy beam requires the use of suitable moderators and samples with sufficient thickness, it guarantees a homogeneous implantation of the muons in the sample volume [126].

The second type of muon beam is often called the Surface or Arizona beam. Here, muons are produced from π^+ decaying at rest near the surface of the production target (see Figure 2.3). Such muons are 100 % spin-polarised (all spinning in the same direction), have a maximum momentum of 29.8 MeV/c [127] and a kinetic energy of about 4 MeV [35]. These muons are formed into a muon beam and guided to the experimental set-up by a beam transport system that is several metres long and consists primarily of quadrupole lenses and bending magnets. An essential advantage of Arizona muons is their complete polarisation and the high stopping density [125]. The latter property has the possibility that thin samples can be used.

The implantation range R of surface muons in a sample has an associated range width or straggling, ΔR, arising partly from the statistical nature of the muon energy loss processes and partly from the momentum spread of the incident muons. R and ΔR are given by the following expressions [129]

$$\begin{aligned} R &= \mathbf{a}\mathbf{p}^{3.5} \\ \Delta R &= \mathbf{a}\left[0.008 + 12.25\left(\frac{\Delta \mathbf{p}}{\mathbf{p}}\right)^2\right]^{\frac{1}{2}} \mathbf{p}^{3.5} \end{aligned} \tag{2.35}$$

where **p** is the momentum in MeV/c. For surface muons of **p** = 26.5 MeV/c, Rρ is typically 110 mg/cm^2 (where ρ is the sample density) and ΔR = 20 % of R. The muons

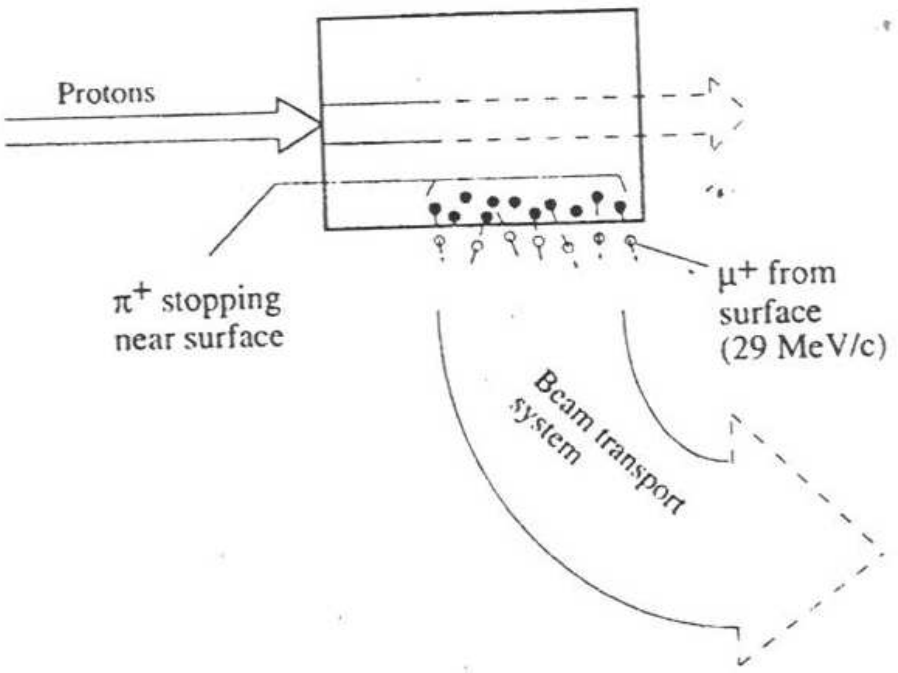

Figure 2.3: Production of surface (or 'Arizona'-type) muons from pions which have been stopped near the surface of the production target. This figure is taken from Ref. [128].

therefore stop in the bulk material and not at the surface.

The muons[3] are themselves unstable particles, and decay radioactively with a lifetime of 2.197 μs according to the scheme

$$\mu^+ \rightarrow e^+ + \nu_e + \bar{\nu}_\mu \tag{2.36}$$

The muon decay is a three body process and involves the weak interaction. Muon decay also violates parity[4] [130] with the result that positron emission occurs preferentially along the instantaneous spin direction of the parent muon [127] as shown in Figure 2.4. The maximum momentum of the decay positron is given by the relation

[3] negative muons decay to electrons, positive muons to positrons. The lifetime of the negative muon depends on the atomic number Z of the material into which it is planted. It is 2.2μs for carbon and 0.07μs for lead [35].

[4] The fact that neutrinos are left- handed and not "right- handed" is also an example of parity violation

$$m_\mu c^2 = \left[P_{e^+}^2 + m_{e^+}^2 c^4\right]^{\frac{1}{2}} + P_{e^+} c \qquad ; \qquad P_{e^+}^{max} = 52.827\ MeV/c \tag{2.37}$$

This maximum occurs when both the neutrino and anti-neutrino are emitted in the same direction, opposite to that of the decay positron. For this case the spins of the neutrino (negative helicity) and anti-neutrino (positive helicity) cancel, leaving the positron to balance the spin of the positive muon.

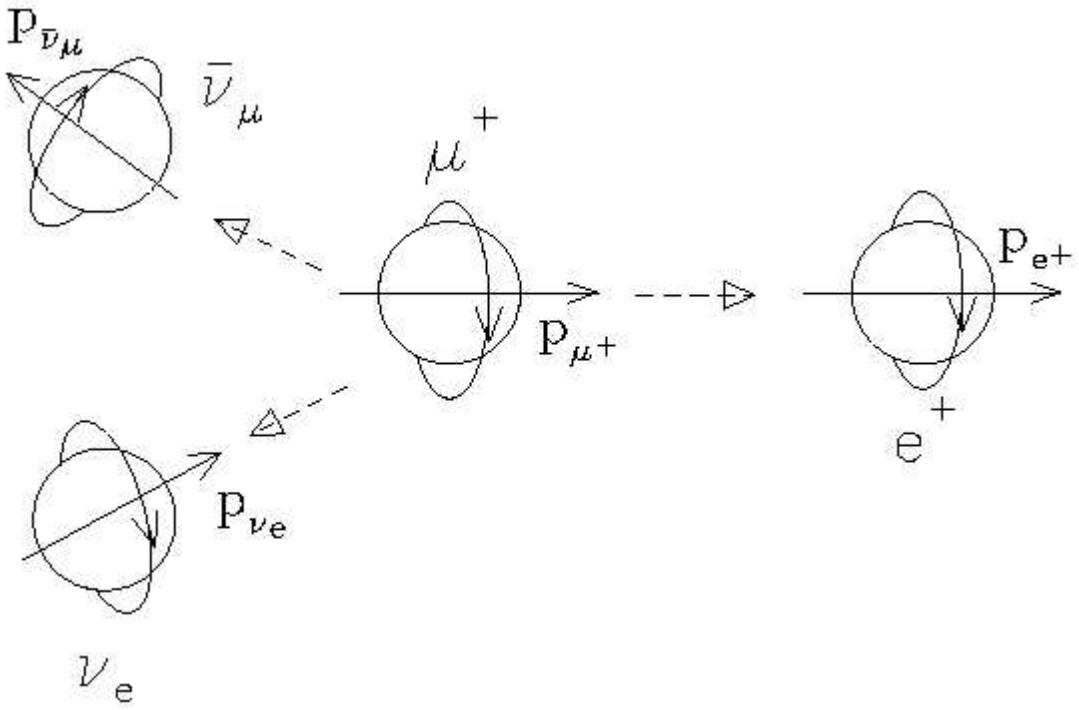

Figure 2.4: Conservation of angular and linear momentum when the positron energy is close to the maximum value E_{max} and the two neutrinos are emitted in approximately the same direction.

The probability with which the positron is emitted in a certain direction within a certain energy range can be calculated by integrating over the neutrinos' momenta, because they usually cannot be observed. The double differential distribution $W(\theta, \epsilon)$ of the decay positrons with respect to the spin of the muon is given by [131, 132]

$$d^2W = W(\theta,\epsilon)d\epsilon\, d(\cos\theta) = (3-2\epsilon)\epsilon^2\tau_\mu\left[1 + \frac{2\epsilon - 1}{3-2\epsilon}\cos\theta\right]d\epsilon\, d(\cos\theta), \tag{2.38}$$

where ϵ = E/E$_{max}$ is the reduced positron energy, θ is the angle between the positron trajectory and the μ^+ spin, as shown in Figure 2.5 and τ_μ is the muon mean lifetime.

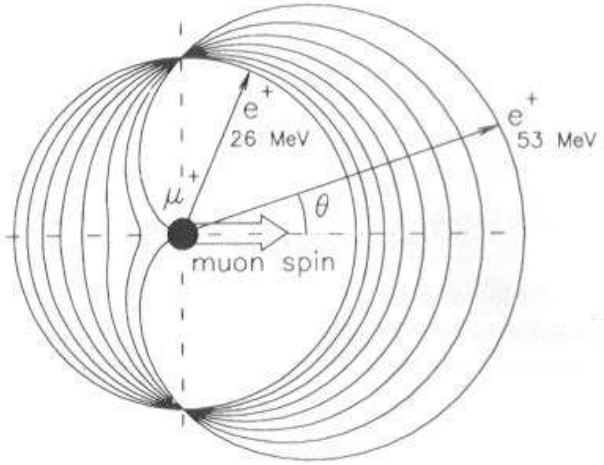

Figure 2.5: The angular distribution of positrons from positively charged muons for various positron energies. This figure is taken from Ref. [133].

The angular distribution of the positron is strongly anisotropic, with respect to the muon spin, because of parity violation in muon decay via the weak interaction. The energy spectrum of the positrons follows from Equation 2.38 by only integrating over $\cos\theta$

$$dW(\epsilon) = W(\epsilon)d\epsilon = \left[\frac{2(3-2\epsilon)\epsilon^2}{\tau_\mu}\right] d\epsilon. \tag{2.39}$$

The asymmetry factor preceding the cosine function in Equation 2.38 depends on the positron energy and for an ensemble of muons with polarisation P the asymmetry is

$$\mathbf{A}(\epsilon) = \frac{2\epsilon - 1}{3 - 2\epsilon} P. \tag{2.40}$$

For decay positrons in the same plane as the muon spin gives

$$\frac{dN_{e^+}}{d\theta} \sim (1 + \mathbf{A}(\epsilon)\cos\theta). \tag{2.41}$$

A(ϵ) is an intrinsic asymmetry parameter in the positrons angular distribution (see Fig. 2.6), determined by the weak decay mechanism, with a theoretical value of $\frac{1}{3}$ if all emitted positrons are detected with the same efficiency irrespective of their energy. It is usually $\simeq 0.23$ due to the finite solid angle of the detectors, energy dependent efficiency of detection, and possible reduced beam polarization [134]. This anisotropic

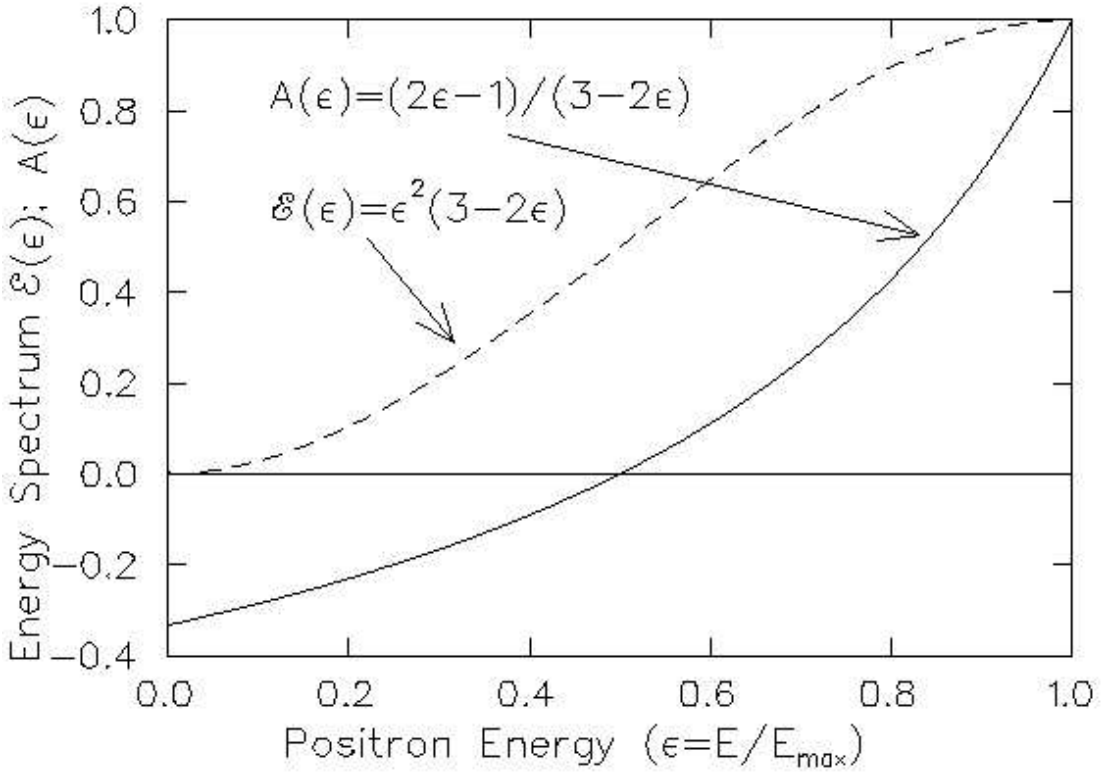

Figure 2.6: Muon energy spectrum.

emission constitutes the basics of the μSR technique. Hence by measuring the positron distribution, it is possible to determine the original μ^+ spin direction.

2.4 Principles of the μSR Studies

Once the muons are implanted within a sample their local magnetic environment dictates the subsequent evolution of their spin vectors. If the muons experience a unique off-axis magnetic field (either internal or applied) the spins precess about the field at

the Larmor frequency. If the muons adopt equivalent sites within the lattice, or within the molecules of the sample, and experience there identical fields, they will precess in phase and the magnitude of their initial polarisation will be preserved during the rotation. However, any spatial or temporary, site to site, variation of the magnetic field results in a depolarization or a relaxation of the muon spin ensemble. It is instructive at this point to define what is meant by depolarization **vis-á-vis** relaxation. The term **depolarization** encompasses all varieties of spin dynamics, including interactions in which the phase coherence of the spin ensemble could in principle be recovered at some later time (e.g., by spin echo techniques); whereas **relaxation** applies to those interactions which result in a strictly irreversible loss of ensemble polarization, such as in a diffusing magnetic probe [135]. In the case of a bare μ^+, spin relaxation occurs via the interaction of the μ^+ spin with the local magnetic field distribution. In the case of muonium, however, the μ^+ is strongly coupled to the electron so that in weak magnetic fields the fraction of muonium that forms in the polarized triplet state behaves magnetically like a polarized spin-one object with a magnetic moment of the order of the electron's and is thus about 103 times more sensitive to local magnetic fields than a bare μ^+ [135]. The depolarization or relaxation of the μ^+ spin in a muonium atom can also be induced by random local magnetic fields, random anisotropic hyperfine distortions, chemical reactions, spin exchange, and superhyperfine interactions [135].

The precessional motion and/or depolarisation of the muon spins can be monitored because of the propensity of the muon decay positron to be emitted preferentially along the spin direction of the muon. In a μSR experiment the information[5] on the distribution of local magnetic environments over all muon sites is thus delivered to the exper-

[5] In μSR one observes a spin-precession signal superposed on a lifetime. This provides three pieces of useful information [136]: from the frequency of precession one characterizes various chemical states of the muon; from the decay of the signal one evaluates the rate of reaction; and from the initial amplitude of the signal one calculates a yield - the probability that a muon will initially form that particular chemical state.

imentalist in the form of relatively high energy (up to 53 MeV) decay positrons which readily penetrate sample holders, cryostats or ovens and the detectors used to establish the time and direction of the muon spin at the instant of decay [133]. The emitted positrons are detected and collected in intensity versus time histograms. Typical histograms are shown in Figures 2.7 and 2.8 for transverse field geometry and Figures 2.9 and 2.10 for zero / longitudinal field geometry. The two experimental geometries are as shown in Figure 2.11. The zero-field measurements are performed with the longitudinal geometry.

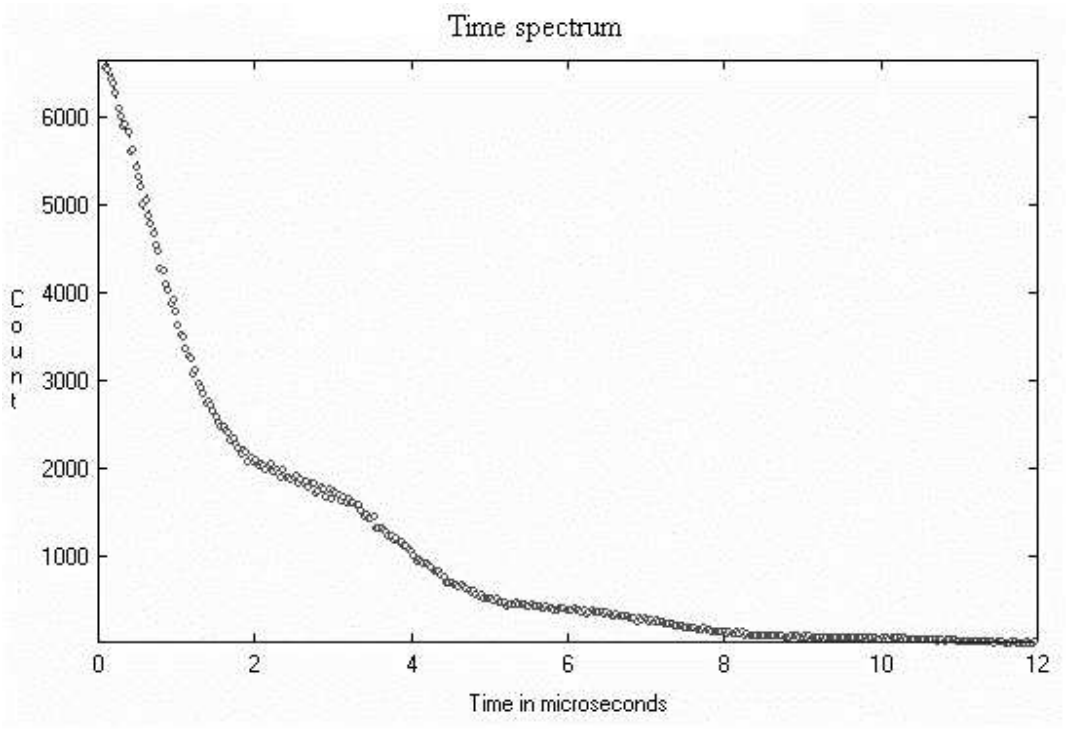

Figure 2.7: The histogram shows an exponential decay corresponding to the muon lifetime and periodic maxima and minima as the spins are aligned towards and away from the counter.

In the longitudinal geometry an external magnetic field $\mathbf{B}_{ext}$ is applied along the initial muon beam polarization direction ($\vec{\mathbf{P}}_{\mu}(0)$) and positron detectors are set parallel and antiparallel to ($\vec{\mathbf{P}}_{\mu}(0)$). These detectors are usually referred to as forward and backward, respectively. In this geometry any reduction of the initial asymmetry must be attributed

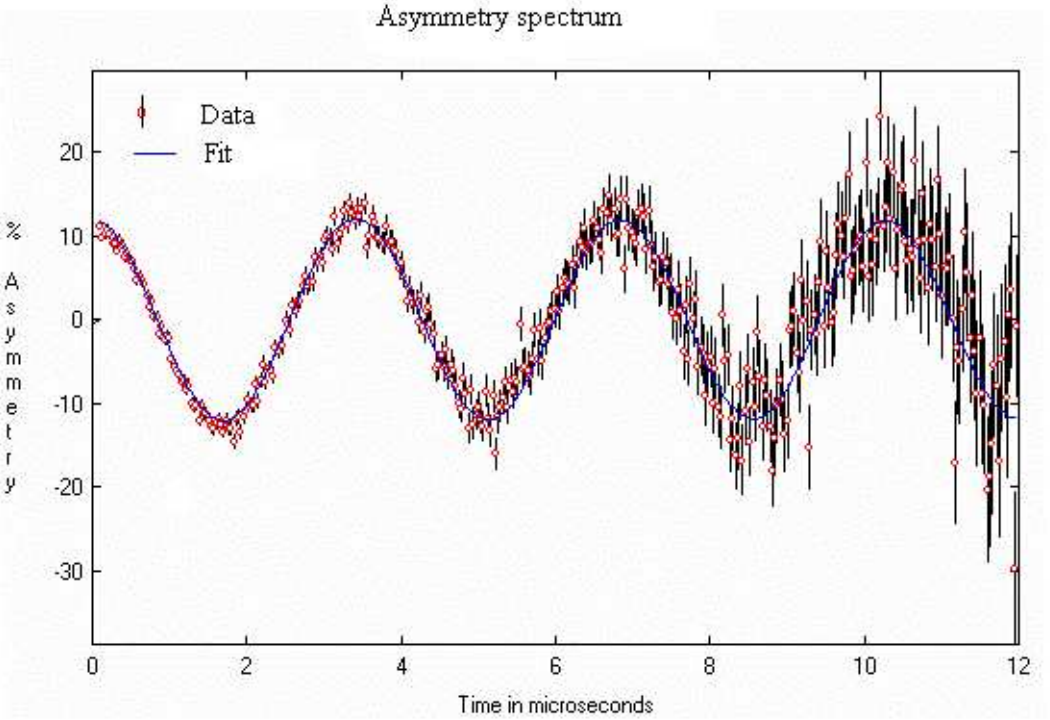

Figure 2.8: From the raw collected histograms the exponential decay due to the finite muon lifetime is divided out and the so-called asymmetry spectrum is obtained, which contains the information about the precessing and relaxing muon spins in the total local field.

to the so-called spin lattice relaxation[6] . The muon spin can be visualised as a two-level quantum system which may exchange energy with the system under study through magnetic interactions. The relaxation function $G_{zz}(t) = \exp(-t/T_1)$ appears in the difference between the count rates in the forward and backward detectors. In the transverse geometry $\mathbf{B}_{ext}$ is perpendicular to ($\vec{\mathbf{p}}_{\mu}(0)$) and the positrons are detected perpendicularly to $\mathbf{B}_{ext}$ and any dephasing in the observed oscillations is evidence of either an inhomogeneous internal field distribution or spin-spin (T_2) relaxation. The anisotropy lobe of the decay positron momentum probability follows the spin precession and the resulting positron count rate consists of a sinusoidal modulation superimposed on the muon decay curve.

[6] Muon spin flips due to creation or destruction of an excitation which couples to the muon spin vector.

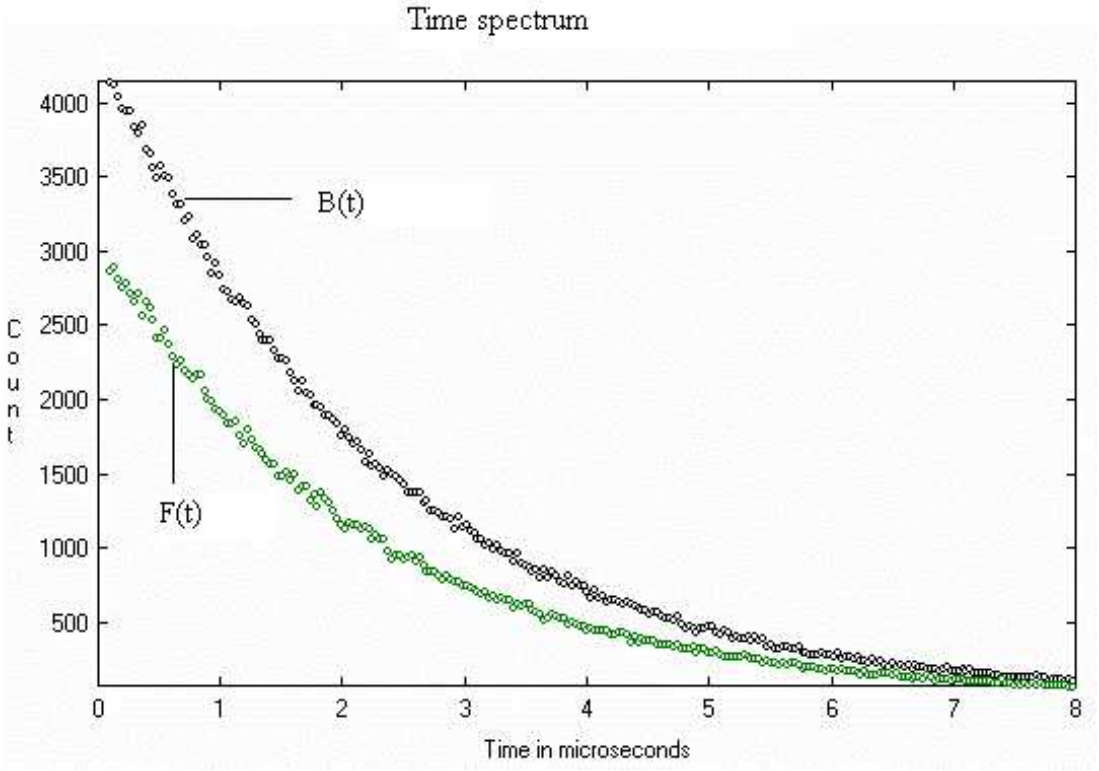

Figure 2.9: F-B polarization asymmetry measured in a longitudinal magnetic field.

In the absence of any external or internal magnetic fields, the ith positron counter with an average angle ϕ_i with respect to the muon polarization will register the following distribution of decay times

$$N_i(t) = N_i^o \{exp\,(t/\tau_\mu)[1 + A_i^o \cos\,(\phi_i)] + \mathcal{B}_i\} \tag{2.42}$$

where N_i^o is a normalization constant, A_i^o is the average positron asymmetry and $\mathcal{B}_i$ is the time-independent background fraction. In an applied magnetic field $\mathbf{B}_{ext}$, the muon spin starts precessing with the Larmor frequency $\omega_\mu = \gamma_\mu|\mathbf{B}_{ext}|$. If $\mathbf{B}_{ext}$ is perpendicular to the initial muon polarization ($\vec{\mathbf{p}}_\mu(0)$) then the positrons angular distribution rotates as a whole with the same angular frequency ω_μ which is reflected in $N_i(t)$ as

$$N_i = N_i^o \{exp\,(-t/\tau_\mu)[1 + A_i^o \cos\,(\omega_\mu t + \phi_i)] + \mathcal{B}_i\}. \tag{2.43}$$

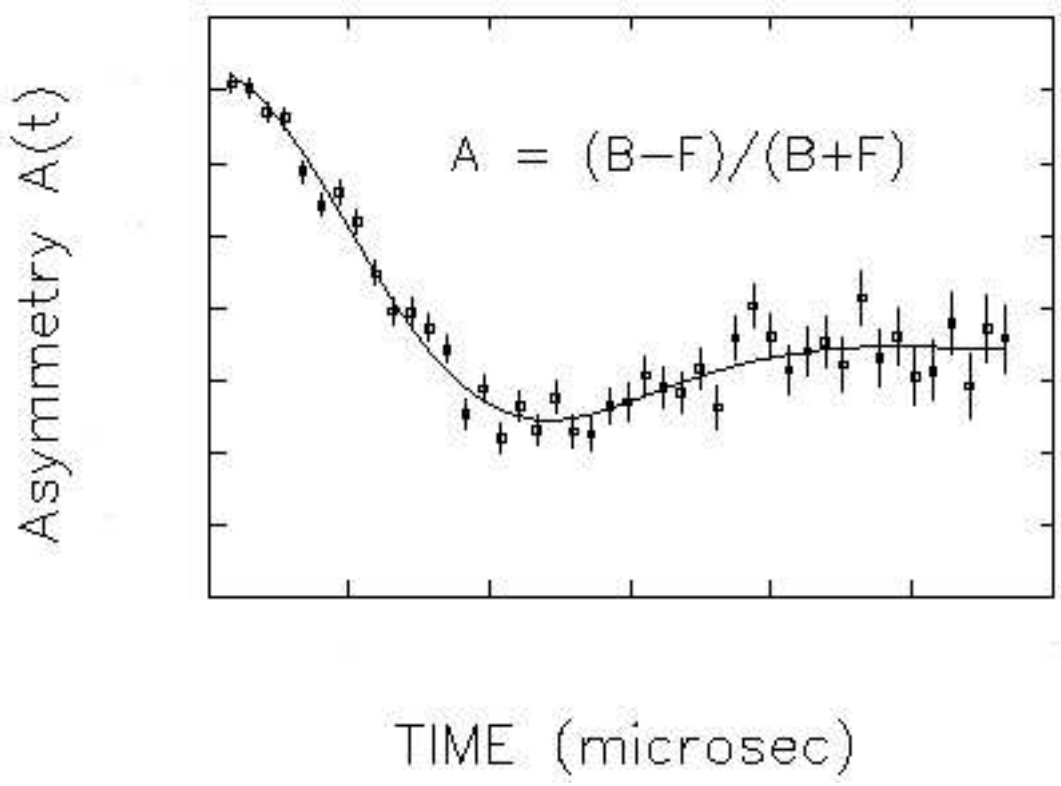

Figure 2.10: Muon spin polarization asymmetry measured in a longitudinal magnetic field.

In a real μSR experiment, the implanted muon experiences the magnetic environment $\mathbf{B}_{int}$ of a sample which originates from dipolar interaction with surrounding nuclear and electronic spins, the externally applied magnetic field $\mathbf{B}_{ext}$, as well as contact with hyperfine fields from the spin density at the muon site. The internal field is often random in direction, magnitude or time, and usually fluctuates and depolarizes the muon spin. To account for this effect equation 2.43 should be modified by replacing the $\cos(\omega_\mu + \phi)$ term with a spectra of frequencies, i.e. $G_{xx}(t)\cos\ (\langle\omega_\mu\rangle t + \phi_i)$. The envelope of these oscillations is called the transverse relaxation function $G_{xx}(t)$. If the average precession frequency is given by [107]

$$\langle\omega_\mu\rangle = \gamma_\mu\langle B_{int}^{\perp}\rangle \tag{2.44}$$

then the number of positron counts $N_i(t)$ is

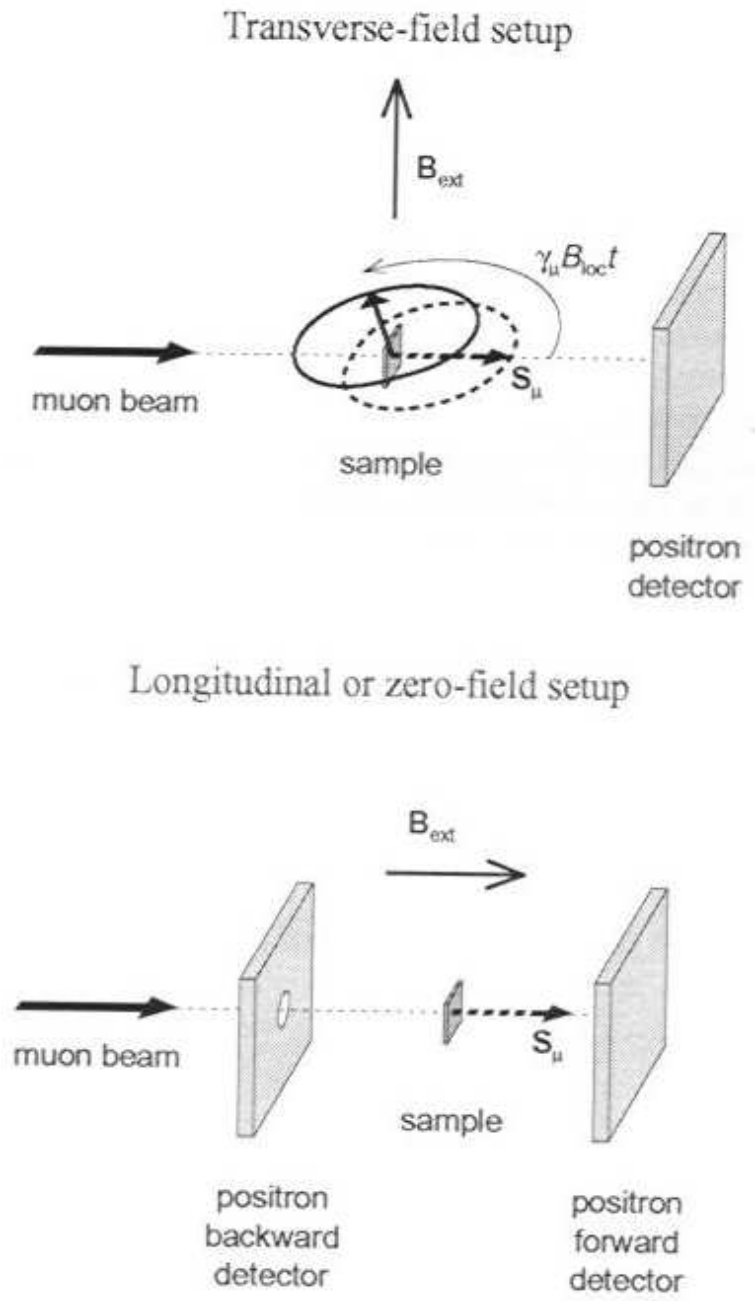

Figure 2.11: The two types of experimental geometry: the transverse and longitudinal setups are illustrated in the upper and lower panel, respectively. The muon beam momentum and the initial muon beam polarization have been taken as parallel but in reality, these two vectors are antiparallel. The arrows originating from the sample sketch the muon spin direction: the dashed one at $t = 0$ and the solid one at t. This figure is taken from Ref. [137].

$$N_i(\phi, t) = N_i^o \{exp\,(-t/\tau_\mu)[1 + A_i^o G_{xx}(t)\cos(\langle\omega_\mu\rangle t + \phi_i)] + \mathcal{B}_i\}. \qquad (2.45)$$

Equation 2.45 is a common approximation of μSR data analysis. By fitting the $N_i(t)$ histograms in the time domain one can obtain the two fundamental quantities of interest, namely the average frequency $\langle\omega_\mu\rangle$ and the relaxation function $G_{xx}(t)$. Field fluctuations due to, for example, fluctuating surrounding electronic magnetic moments or muon hopping lead to gradual and irreversible loss of muon polarization and this is observed as a decrease in the amplitude of the asymmetry function [119]. In this case, $G_{xx}(t)$, which can be expressed as the muon autocorrelation function [35] gives information about the nature of the internal magnetic fields, which can be of static or dynamic origin. The effect of static and dynamic fields can be decoupled by applying a longitudinal field.

For conventional longitudinal field (LF) measurements, the positron detectors are arranged in front of and behind the sample (as 'seen' by the muon beam) and are usually labeled as forward (F) and backward (B) (see Fig. 2.11). The number of registered positrons is described by equation 2.45 with $\phi_B = 0°$, $\phi_F = 180°$ and $\omega_\mu = 0$. That is

$$N_{B,F}(\phi, t) = N_o^{B,F}\ \{exp\ (-t/\tau_\mu)[1 + A_o^{B,F} G_{zz}(t)\cos(\phi_{B,F})] + \mathcal{B}_{B,F}\ \}. \tag{2.46}$$

In the zero field case, the muon spin will precess around local axes in the jth site with angle δ_j and with frequency ω_j. The time evolution of the longitudinal components of the polarization vector $G_{zz}^{(j)}(t)$ in the jth site is given by

$$G_{zz}^{(j)}(t) = \cos^2(\delta_j) + \sin^2\delta_j \cos(\omega_j t). \tag{2.47}$$

Averaging over all possible directions of the local magnetic fields gives

$$\langle G_{zz}^{(j)}(t)\rangle = \frac{1}{3} + \frac{2}{3}\langle\cos(\omega_j t)\rangle. \tag{2.48}$$

2.4.1 Extraction of information from longitudinal field μSR spectra

The real value of the longitudinal-field technique is for muonium studies in the presence of static and dynamic random disturbances. A time-differential approach is required to follow the longitudinal spin relaxation of the muon. In a time-differential experiment, repeated measurements are made of the time interval between the entrance of the muon into the sample and the detection of decay positron in a particular direction. These intervals are compiled into a time histogram $N(t)$, which has the form

$$N(t) = \mathcal{B}N_0 + N_0 e^{(-t/\tau_\mu)} [1 + a_0 P(t)], \tag{2.49}$$

where $\mathcal{B}$ is a time-independent background, $\tau_\mu = 2.197\ \mu$s is the muon lifetime, N_0 and a_0 are the normalisation constant and the asymmetry constant, respectively.

We are interested in extracting the spectral parameters a_0 and P(t)[7] , as a function of temperature and magnetic field, since it is these signals that manifest the influence of the muon's environment on its spin. Extraction of asymmetry spectra from the time histogrammed decay positron spectra taken in a longitudinal geometry requires knowledge of N_0 and B, neither of which can be extracted numerically from the data without some model of the time dependence of the longitudinal polarisation. One way of extracting the signal from the raw data is to make use of the symmetry of the detectors on opposite sides of the sample. With this geometry the two detectors view the same positron angular distribution, but from diametrically opposed directions, so that the counts in the two histograms (for the Back-Front pair) becomes [133]

$$N_{B,F}(t) = B_{B,F} + N_0\, \epsilon_{B,F} \left[1 \pm A_{B,F} P_z(t)\right], \tag{2.50}$$

[7] The polarisation function $P(t)$ is, in general, a superposition of several contributions, depending on how many different muon species are formed or how many different magnetic environments exit [138].

where

$\epsilon_{B,F}$ = efficiency of B or F positron detector

$B_{B,F}$ = beam-borne background in positron detector

$A_{B,F}$ = intrinsic asymmetry of the positron detector

P_z (t) = time dependent muon polarisation along the z-axis

The experimental asymmetry a_0(t) is then obtained from

$$a_0(t) = \frac{(1-\alpha) + (1+\alpha\beta)A_B P_{B,F}(t)}{(1+\alpha) + (1-\alpha\beta)A_B P_{B,F}(t)} \tag{2.51}$$

where $\alpha = (\epsilon_F / \epsilon_B)$ and $\beta = (A_F / A_B)$ and (1 - α) / (1 + α) is the "baseline" asymmetry for totally unpolarised muons. There is a distortion in a_0(t) due to baseline-shift and when $\alpha\beta \neq 1$. To remove these distortions α and β must be determined independently, usually through fitting spectra taken in a weak transverse field. The corrected asymmetry is then given by

$$A_B P_z(t) = \frac{(\alpha-1) + (\alpha+1)a_0(t)}{(\alpha\beta+1) + (\alpha\beta-1)a_0(t)} \tag{2.52}$$

It is not unusual to assume that $\beta = 1$. The beam-borne background is negligible on a pulsed muon source [133], and therefore the experimental asymmetry simplifies to

$$a_0(t) = \frac{N_B(t) - \alpha N_F(t)}{N_B(t) + \alpha N_F(t)} \tag{2.53}$$

2.4.2 Extraction of information from transverse field μSR spectra

There are two perspectives for the interpretation of transverse field μSR spectra [139]:

(1) The muon spins precess at a unique frequency ω_L, but their polarisation decays with time due to the muons' interaction with static fields or dynamic fluctuations in its

environment.

(2) The muons at different sites see a different internal fields, and therefore precess at different rates.

If the muons precess at a common frequency ω_L, but their polarisation decays with time, the counts in the nth time channel of the jth detector can be expressed as

$$C_j(t_n) = N_j^0 \Delta t \exp(-t_n/\tau_\mu)\left[1 + A_j P_f(t_n)\cos(\omega_L t_n - \phi_j)\right], \tag{2.54}$$

where A_j is the asymmetry parameter, ϕ_j is the phase, Δt is the channel width, N_j^0 is the initial count rate, $\omega_L = \gamma B$ is the muon Larmor precession frequency for an applied field B and the gyromagnetic ratio $\gamma/2\pi = 135.54$ MHz/tesla. $P_f(t)$ describes the decay of the ”forward” component of the muon polarisation. The form of this decay depends on the physics of the muon’s interaction with its environment. In the limit of fast temporal fluctuations of the local field or of rapid hopping of the muon from site to site it can be shown that $P_f(t) = \exp(-\lambda t)$ (Lorentzian damping). In the limit of slow temporal fluctuations, but where there is a Gaussian distribution of local fields, it is readily shown that $P_f(t) = \exp(-\sigma^2 t^2)$. The shape of the envelope of the decaying polarisation gives information about the physics of the interaction at the muon site, which can be described by an analytical fuction with a few parameters (e.g. λ or σ in the above expressions) or in-between Lorentzian and Gaussian (Abragam relaxation).

Let us consider the behaviour of an unperturbed isotropic muonium state in a transverse field. An expression for the forward component of the time-dependent muon polarisation is given by [127]

$$P_f(t) = \sum a_{nm}\cos(\omega_{nm} t), \tag{2.55}$$

where

$$\omega_{12} = +\frac{\omega_0}{2} + \omega_- - \frac{\omega_0}{2}\sqrt{1+x^2}, \qquad a_{12} = \frac{1}{4}\left[1 + \frac{x}{\sqrt{1+x^2}}\right], \tag{2.56}$$

$$\omega_{23} = -\frac{\omega_0}{2} + \omega_- + \frac{\omega_0}{2}\sqrt{1+x^2}, \qquad a_{23} = \frac{1}{4}\left[1 - \frac{x}{\sqrt{1+x^2}}\right], \tag{2.57}$$

$$\omega_{34} = +\frac{\omega_0}{2} + \omega_- + \frac{\omega_0}{2}\sqrt{1+x^2}, \qquad a_{34} = \frac{1}{4}\left[1 + \frac{x}{\sqrt{1+x^2}}\right], \tag{2.58}$$

$$\omega_{14} = +\frac{\omega_0}{2} + \omega_- + \frac{\omega_0}{2}\sqrt{1+x^2}, \qquad a_{14} = \frac{1}{4}\left[1 - \frac{x}{\sqrt{1+x^2}}\right]. \tag{2.59}$$

with

$$x = \frac{2\omega_+}{\omega_0} = \frac{B}{B_0}, \tag{2.60}$$

where

$$B_0 = \hbar\omega_0/(g_\mu\mu_\mu - g_e\mu_B) \tag{2.61}$$

For muonium in vacuum $B_0 = 1585$ G. The frequencies $\omega_\pm$ are given by

$$\omega_\pm = (\omega_e \pm \omega_\mu)/2. \tag{2.62}$$

The x^2 terms are neglected at low fields and this causes the two observable low-frequency lines ω_{12} and ω_{23} to concide, and hence we obtain

$$P_f(t) \simeq \frac{1}{2}\cos(\omega_- t) \tag{2.63}$$

The observation of this strong line at 13.94 MHz/mT serves as a quick manifestation of the presence of muonium in the sample.

The analysis of a transverse-field μSR experiment involves a determination of the precession frequencies contained in the frequency spectrum, their amplitudes, their linewidths, the shapes of the lines (relaxation functions), and their initial phases. This determination can be made by least-squares fitting of the time histogram to a function analogous to equation 2.64

$$N_f(t_i) = \beta N_0 + N_0 \exp(-t_i/\tau_\mu)[1 + A_e P_f(t_i)], \qquad t_i = i\Delta t \;\; (i = 1, N), \tag{2.64}$$

(A_e is the experimentally determined asymmetry constant) with P_f given by a sum of damped oscillations [127]:

$$P_f(t) = \sum_i A_i \exp(-\lambda_i\, t) \cos(\omega_i\, t + \phi_i). \tag{2.65}$$

If the muons at a given site (or in a given subset of the ensemble) see a distribution of internal fields, the counts in each detector will be [139]:

$$C_j(t_n) = N_j^0 \Delta t \exp(-t_n/\tau_\mu) \left[1 + A_j F_j(t_n)\right], \tag{2.66}$$

where

$$F_j(t_n) = \int_0^\infty F_j(\omega) \cos(\omega t_n - \phi_j) d\omega. \tag{2.67}$$

The function $F_j(\omega)$ gives the distribution of precession frequencies, which maps directly onto the distribution of internal fields through the gyromagnetic ratio: $\omega = \gamma B$.

A more detailed discussion of the μSR techniques and their applications can be found in many books dedicated to this subject (see for example [107, 140, 141]).

2.5 Muonium Formation in Diamond

The positive muon is a prototypical atomic probe [8] best thought of as a ”hydrogen-like centre”, that can often extract a characterisation of the microscopic magnetic or electronic environment that is very difficult (or indeed impossible) to obtain by other means. The electronic properties of the positive muon mimic that of the proton, see Table 2.2. The mass, magnetic moment and gyromagnetic ratio of the muon are inter-

Table 2.2: Properties of the positive muon [126]. m_e is the mass of the electron and m_p is the mass of the proton; μ_N is the nuclear magneton.

Mass m_μ	$206.76826(11)m_e = 0.112609513(17)\ m_p$
Charge	+e
Spin	$\frac{1}{2}$
Magnetic moment μ_μ	$3.18334547(47)\ \mu_p = 8.8905981(13)\mu_N$
Gyromagnetic ratio γ_μ	$\frac{\gamma_\mu}{2\pi} = 13.553879(\pm 0.7\ \text{ppm})\text{kHz/G}$
Average lifetime τ_μ	$2.197034 \pm 0.00004\mu$s

mediate between that of the electron and the proton.

In a crystalline solid the μ^+ is repelled[9] by the charge of the host nuclei, but in a molecular gas or liquid it is attracted to the electron cloud around the host molecules. In a solid μ^+ generally comes to rest at an interstitial site of high symmetry between the lattice ions, where it exists in a diamagnetic state as a “quasi-free” probe. However, in oxides the μ^+ may localize near an oxygen atom, forming a μ-O bond similar to an OH bond. In semiconductors the positive muon can thermalise and capture an electron to form a neutral paramagnetic defect state called muonium[10] (Mu = μ^+e^-)

[8] The muon carries a relatively large magnetic moment which even exceeds the largest nuclear moment $\mu_\mu = 3.2\mu_p$, see Table 2.2. It therefore acts as a very sensitive local magnetic probe. However, due to the absence of a quadrupolar electric moment ($S_\mu = \frac{1}{2}$) the muon does not couple to electric field gradients.

[9] While μ^+ avoids the positively charged nuclei in the host material, μ^- behaves as a heavy electron and is easily captured into the atomic orbitals, where it quickly cascades to the atomic 1s ground state in close proximity to host nuclei.

[10] Muonium differs from protium, ^{1}H, only by virtue of having the light, short-lived positive muon as its nucleus rather than a proton.

[142, 32, 33, 127, 143, 35] which is an analogue of atomic hydrogen, see Table 2.3. In such instances, the electron is the extremely sensitive probe that passes on what it senses to the μ^+ by way of its hyperfine coupling. The dynamic behaviour of Mu may differ from that of hydrogen due to the different masses of the proton and the muon. The slowing down of a μ^+ in matter involves several stages of energy loss mechanisms

Table 2.3: Comparison of hydrogen and muonium [33]

Properties	Mu	H
Mass (m_e)	1837.15	207.769
Reduced electron mass (m_e)	0.999 456	0.995 187
Ground-state radius a(Å)	0.529 465	0.531 736
Ground-state energy (eV)	-13.5984	-13.5403
Nuclear gyromagnetic ratio $\gamma(s^{-1}T^{-1})$	2.67520 x 10^8	8.51607 x 10^8
Hyperfine frequency ν_0(GHz)	1.42041	4.46330

[35](see Figure 2.12).

The various processes by which muons lose their initial kinetic energy are fast and also the primary processes bring into play only electrostatic interactions, which are not spin-dependent. So there is rarely any loss of polarisation during thermalisation [144]. A high energy μ^+ interacting with matter will first lose energy by scattering with electrons. When the μ^+ velocity approaches that of the valence electrons of the target atoms (corresponding to a μ^+ kinetic energy of 2-3 KeV), the energy loss per unit time occurs primarily through ionization, in accordance with the Bethe equation [145, 146]. Below about 2 KeV, energy loss still occurs through collisions with electrons, except that in this case the Bethe equation does not hold since the electrons now behave as a degenerate gas. In this energy region, a muon can also capture and lose electrons in its interactions with the target medium, forming short-lived muonium atoms. In many cases, the neutral muonium atom is the favoured charge state as the μ^+ velocity drops below the threshold for this capture/loss cycle. The final muonium atom then slows

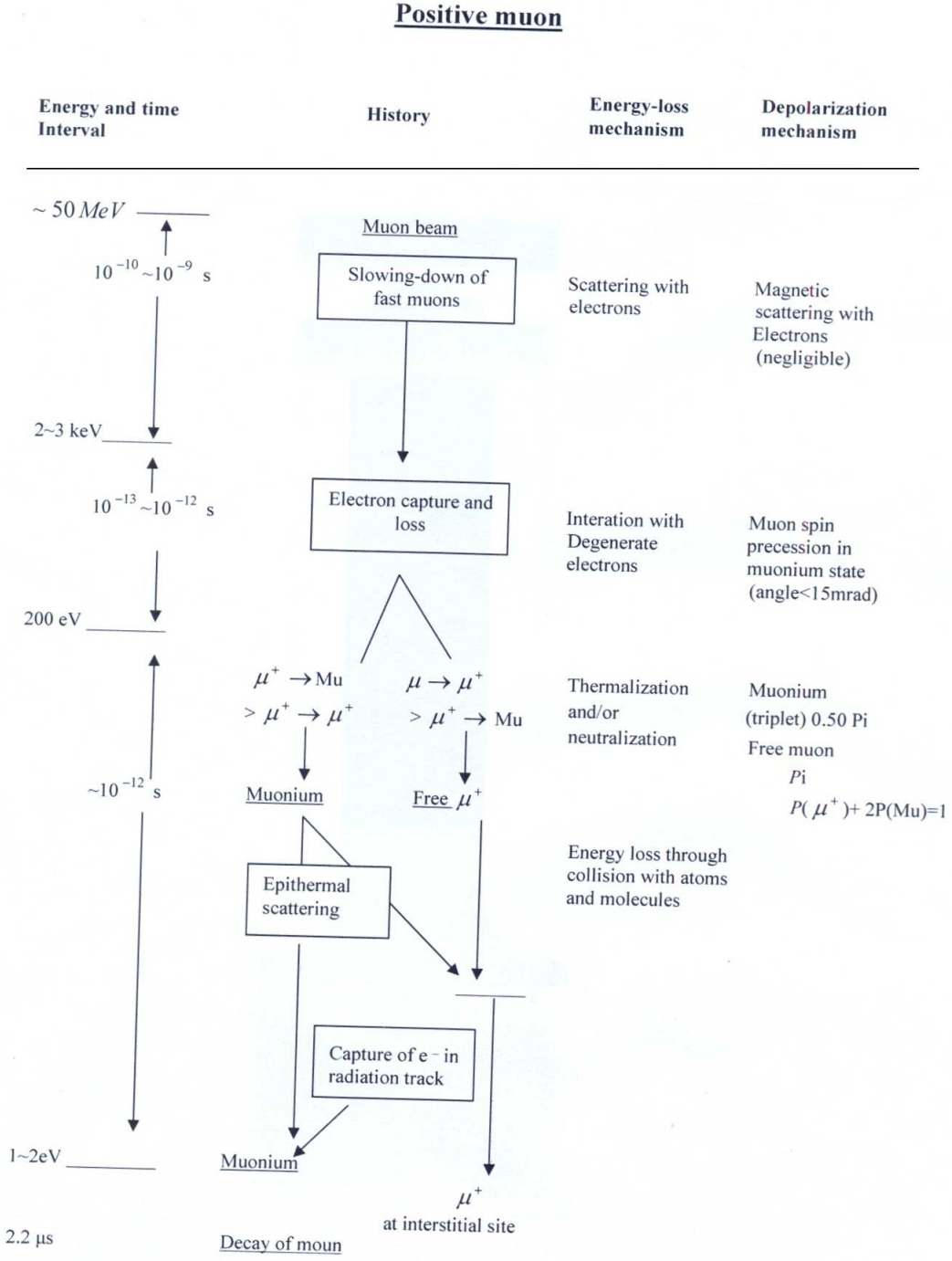

Figure 2.12: Schematic diagram of the history of energetically introduced positive muon in condensed matter; energy loss and depolarization mechanisms. This diagram is taken from Ref. [141].

down through subsequent non-ionising collisions with atoms and/or molecules.

Another important issue is the radiation damage produced by the muon in a sample. During the thermalisation process, the muon collides with atoms and produces interstitial Frenkel pairs [147]. Therefore, there is a probability that the positive muon might interact with these lattice defects, which may subsequently complicate the interpretation of experimental data. However, the process of vacancy creation has a significant energy threshold and the vacancy pairs are produced only during the initial 'hot' stage of the thermalisation process when the muon kinetic energy is high enough to produce such defects. Beyond that point, the muon will still penetrate deeper into the sample without creating any more vacancies.

Two different neutral paramagnetic muonium centres are observed in diamond [33], Si [142, 32] and Ge [148] when positive muons are implanted at low temperatures into these materials. These centres have been coined normal muonium (Mu or Mu_T^0) with isotropic hyperfine interaction which is a substantial fraction of that of free muonium, and anomalous muonium (Mu* or Mu_{BC}^0) with a weak and highly anisotropic hyperfine interaction [149, 29, 150, 151]. Besides Mu_T^0 and Mu_{BC}^0 it has been observed that a fraction of the muons are in a diamagnetic state (μ^+) [152] with the muon precessing in the external field with the Larmor frequency.

2.5.1 Tetrahedral Muonium (Mu_T^0) in diamond

Normal muonium is quasi-atomic, since it most likely resembles atomic muonium, and corresponds to neutral interstitial muonium at the tetrahedral (T) site or diffusing rapidly among sites of lower symmetry in such a way that its hyperfine (hf) interaction is isotropic, even at low temperatures [21]. In Si and Ge, measurements of the depolarization rate show that Mu_T^0 is very mobile at all temperatures [127]. It is less

mobile in GaP and GaAs [153], and it is localized around a single T site in diamond [154, 127, 155]. The Fermi contact density of Mu_T^0 is a substantial fraction of the free atom value, indicating that the unpaired electron resides primarily in a 1*s*-type orbital.

The time evolution of the muon spin polarization in normal muonium is governed by the spin Hamiltonian, consisting of the isotropic hf interaction and the electron and muon Zeeman interactions:

$$\mathcal{H}_{Mu_T^0} = A\vec{I}_\mu \cdot \vec{\mathbf{S}}_e - g_e\mu_B^e \vec{\mathbf{S}}_e \cdot \vec{\mathbf{B}} - g_\mu \mu_B^\mu \vec{I}_\mu \cdot \vec{\mathbf{B}}, \tag{2.68}$$

where $\vec{I}_\mu$ and $\vec{\mathbf{S}}_e$ are the spin operators of the muon and electron, respectively. The value of *A* ranges from 0.83 of the free-muonium value in diamond down to 0.45 of same in Si [33, 21].

2.5.2 Bond-centred Muonium (Mu_{BC}^0) in diamond

Bond-centred muonium corresponds to a muon bridging a substantially relaxed host atom bond. It may be regarded as muonium which has reacted chemically with the host lattice, moving from an interstitial cage to the centre of a stretched bond [109]. The hf tensor has axial ($\langle 111 \rangle$) symmetry, and the contact density at the muon is very small. The unpaired electron spin density is located on the two adjacent host atoms of the stretched bond [109]. This makes the hf interaction highly anisotropic and predominantly dipolar in character [156]. For Mu_{BC}^0 in Si, Ge and diamond, the unpaired electron borrows a host antibonding orbital, giving it donor character. The wavefunction is completely antisymmetric about the muon site, so that there can be no admixture of 1*s*(Mu), in other words, no atomic character at all [109]. Since the odd electron never participates in the bonding, Mu_{BC}^0 is easily thermally ionized, except in the case of diamond where it is stable up to at least 1000 K [33]. The spin Hamiltonian operator

for the anisotropic muonium state is given by

$$\mathcal{H}_{Mu^0_{BC}} = A_\perp(I_x S_x + I_y S_y) + A_\parallel I_z S_z - g_e \mu_B^e \vec{\mathbf{S}} \cdot \vec{\mathbf{B}} - g_\mu \mu_B^\mu \vec{\mathbf{I}} \cdot \vec{\mathbf{B}}. \tag{2.69}$$

It is convenient to express the Mu^0_{BC} hyperfine constants $A_\parallel$ and $A_\perp$ in terms of the isotropic or contact interaction A_s and the axial dipolar (anisotropic) interaction A_p [157]

$$A_s = \frac{1}{3}(A_\parallel + 2A_\perp), \qquad A_p = \frac{1}{3}(A_\parallel - A_\perp). \tag{2.70}$$

For Mu^0_{BC} in diamond, μSR measurements extrapolated to 0 K yield $A_s = 205.7$ MHz and $A_p = -186.6$ MHz [158]. The hyperfine constants $A_\parallel$ and $A_\perp$ are temperature dependent and the temperature dependence is ascribed to the spin-phonon interaction. The Debye model [33, 157]

$$A(T) = A(0)\left[1 - C\left[\frac{T}{\theta_D}\right]^4 \int_0^{\theta_D/T} \frac{x^3}{e^x - 1} dx\right], \tag{2.71}$$

where θ_D is the Debye temperature and C is a constant, gives a better fit to $A_\parallel$ and $A_\perp$ in diamond.

The Mu^0_{BC} hyperfine parameters are much smaller than the vacuum Mu value. Table 2.4 lists the hyperfine coupling constants of Mu^0_T and Mu^0_{BC} in diamond together with the corresponding values for Si and Ge (for comparison).

Diamond has the largest, and hence most vacuum-like, hyperfine coupling constants of the three materials. Furthermore, $A_\parallel$ and $A_\perp$ have opposite signs, in contrast to the case of Si and Ge [158]. But like Si and Ge, $A_\parallel$ and $A_\perp$ are temperature dependent [148, 33].

Table 2.4: Comparison of the hyperfine coupling constants of Mu^0_T and Mu^0_{BC} at 0 K [33]

Material	Mu^0_T A/h (MHz)	f = A/Avac	Mu^0_{BC} $A_{\parallel}/h$(MHz)	$A_{\perp}/h$ (MHz)
Diamond	3711	0.831	-167.9	392.5
Silicon	2012	0.450	16.8	92.6
Germanium	2361	0.529	26.8	130.7
Vacuum	4463	1.000		

.

Mu^0_{BC} is a bond-centred (BC) interstitial in semiconductors [159, 156, 160, 161]. Estle et al. [29] have used theoretical calculations to show that the bond-centred interstitial muonium (or hydrogen) in diamond is more stable than the tetrahedral interstitial site.

2.5.3 Muonium charge-state and site transitions in diamond

The fraction of incoming muons forming Mu^0_T, Mu^0_{BC}, and μ^+ varies with the host, the doping (donor and acceptor) concentrations, the temperature [162, 163] and other factors related to the impurity content [21]. Mu^0_{BC} and Mu^0_T are observed at low temperature in pure or lightly doped material [164] with Mu^0_T accounting for 60 %, Mu^0_{BC} for 30 % and μ^+ for at most 10 %, of the incoming muons [165]. Furthermore, the muonium spin states are sufficiently long-lived to permit the local distribution of (electron) spin density to be mapped fully [166]. This demonstrates the metastability of the paramagnetic species [29, 166]. The tetrahedral (T) interstitial is metastable because of the unusually large lattice relaxation of the bond-centred (BC) interstitial which makes tunnelling improbable[29].

Temperature-dependent measurements yield the limits of stability of the states, where transitions from one state to another are often observed. On heating, Mu^0_{BC} and Mu^0_T convert to diamagnetic Mu^+_{BC} by ionization, i.e., by loss of the unpaired electron to the conduction band. In Si, the one-way reaction

$$Mu^0_{BC} \longrightarrow Mu^+_{BC} + e^- \tag{2.72}$$

sets in just above 100 K [11] and the one-way reaction

$$Mu^0_T \longrightarrow Mu^+_{BC} + e^- \tag{2.73}$$

around room temperature [12] [164]. Equation 2.73 involves the sequence $Mu^0_T \rightarrow Mu^0_{BC}$ followed by the immediate ionization of the BC species [21] (i.e., a change of both site and charge state, presumably in that order). The increase of the diamagnetic fraction due to the process in equation 2.72 is expected to be observable if

$$\omega_\mu \tau_{BC} \ll 1, \tag{2.74}$$

where $\omega_\mu = 2\pi H \gamma_\mu$ is the Larmor frequency of diamagnetic precession signal; γ_μ = 13.55 KHz/G is the muon magnetogyric ratio; and τ_{BC} is the Mu^0_{BC} lifetime [167]. Unless the criterion in equation 2.74 is satisfied, coherence among diamagnetic species formed at different times will be lost and the amplitude of the diamagnetic precession signal must be drastically reduced. For a more comprehensive treatment of muonium dynamics see [168].

On further heating, a remarkable depolarization or relaxation sets in. This high-temperature relaxation is due to the trapping and detrapping of the thermally generated conduction electrons by the muon, i.e., repeated formation and ionization of muonium. The variation of this relaxation rate with applied magnetic field determines the muon-electron hyperfine interaction and thereby identifies the active muonium state.

[11] Mu^0_{BC} is observable in diamond up to at least 1100 K [33] while in Si and Ge it disappears above 165 and 85 K respectively [158].

[12] Although Mu^0_{BC} is the more stable of the two neutral states in Si, its one-electron energy level lies closer to the conduction band so that it ionises with the lower onset temperature [167].

The paramagnetic muonium centres correspond to singly-occupied energy levels within the forbidden gap between the valence and conduction band [166]. At room temperature in near-intrinsic and p-type samples the Fermi level is at or below midgap, most likely below either muonium-related level, implying that Mu_T^0 and Mu_{BC}^+ are the expected states [168]. After a sufficiently long time Mu_{BC}^+ should be dominant in p-type materials since Mu_T^0 is metastable, and therefore the expected transitions are :
(1) site change to the stable configuration,

$$Mu_T^0 \longrightarrow Mu_{BC}^0; \tag{2.75}$$

and, (2) the hole capture process,

$$Mu_{BC}^0 + h^+ \longrightarrow Mu_{BC}^+. \tag{2.76}$$

In contrast, for strongly n-type materials at room temperature, the Fermi level lies above both muonium levels leading to Mu_T^- and Mu_{BC}^0 at the two sites. In this case, the excess electron concentration increases the electron-capture rate by the neutral state, i.e., $Mu_{BC}^0 + e^- \rightarrow Mu_T^-$, and hence pushes the system to eventual Mu_T^- occupancy. Figure 2.13 summarises the site and stability information for both the neutral and charged centres in silicon.

The configuration co-ordinate diagram emphasises the metastability for the neutral and the bistability for the charged centres; it shows the energy-level separations used to construct donor and acceptor levels within the semiconductor gap. The donor and acceptor levels are denoted by 0/+ and -/0 [13] , respectively.

Several researchers [33, 169, 158, 170, 3, 2] have investigated the electronic structure

[13] The donor state is defined to be neutral when occupied, positive when empty. The acceptor level is defined to be negative when doubly occupied, neutral when singly occupied.

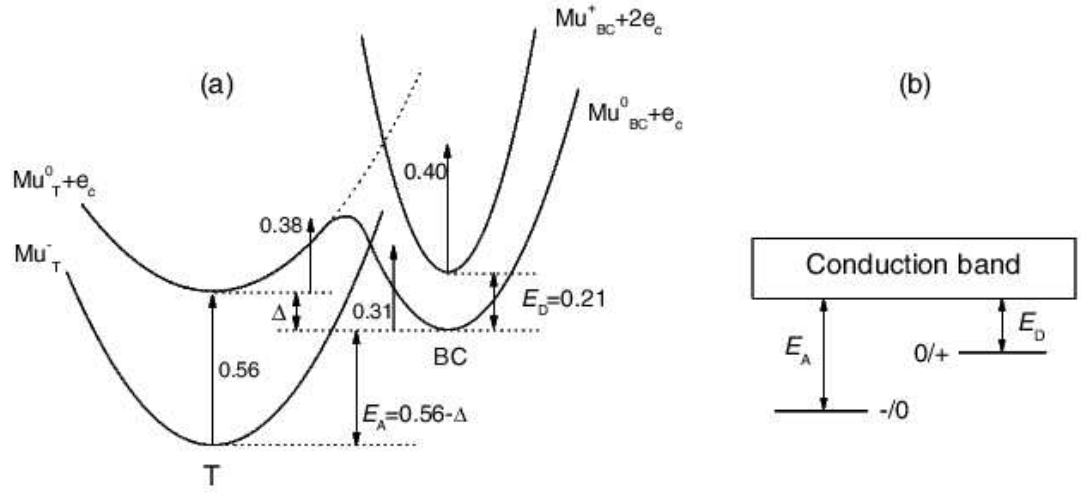

Figure 2.13: The configuration diagram for three charge states of muonium and hydrogen in silicon showing (a) the experimental energy parameters for muonium, and (b) the correspondence with the deep donor and acceptor levels. This figure is taken from Ref. [82].

and dynamics of μ^+, Mu^0_T and Mu^0_{BC} in diamond and discovered that some part of the muon polarization could not be accounted for. This situation is more pronounced in nitrogen-rich diamond. Table 2.5 shows a comparison of the absolute fractions of Mu^0_T, Mu^0_{BC}, μ^+ and unknown states called missing fractions (MF)[14] in some published experiments.

Table 2.5: Comparison of the absolute fractions of tetrahedral interstitial Mu^0_T, bond-centred Mu^0_{BC}, diamagnetic μ^+, Mu_X, and MF in some published experiments

Sample	Mu^0_T(%)	Mu^0_{BC}(%)	μ^+(%)	Mu_X(%)	MF (%)
CVD polycrystalline diamond film [2] (crystalline size: 20-70μ m)	50.2	6.8	19.4		23.6
CVD polycrystalline diamond film [170] (crystalline size: 100μ m)	50	-	6		-
IIa diamond [127](crystal)	68.9	22.7	8.1		0.3
IIa diamond [171] (crystal)	65	25	10		0
Ia diamond [3] (composite type)	30	0	10	60	

[14] The missing fraction is generally thought to correspond to muonium which is depolarised by spin-flip encounters with other paramagnetic species generated radiolytically.

Chapter 3

Sample Preparations

”The observer is never entirely replaced by instruments; for if he were, he could obviously obtain no knowledge whatsoever ... They must be read! The observer’s senses have to step in eventuality. The most careful record, when not inspected, tells us nothing.”

Erwin Schrodinger

3.1 Preliminary Remarks

A suite of four natural type Ia single crystal diamond samples were selected for this investigation. In this chapter the techniques used to prepare the diamond samples are presented. The samples were characterised using fourier transform infrared (FTIR) and electron paramagnetic resonance (EPR) spectroscopies. The diamonds contained, among other defects, the A and B aggregates of nitrogen. The A centre consists of a pair of adjacent substitutional N atoms [55], and the B centre comprises four nitrogens plus a vacancy [55]. Both these defects give rise to distinctive, characteristic, one-phonon (~ 500-1500 cm^{-1}) [172] infrared (I.R.) absorption bands but there is no electron paramagnetic resonance (EPR) signal associated with the A and B centres because of the pairing of the spins of the extra electrons introduced by the nitrogen atoms. The diamonds also contained P1 and P2 centers which show electron spin paramagnetism. P1 centers are dispersed substituional nitrogens [173], and a P2 center consists of a vacancy and three

nitrogens in neighbouring positions in a {111} plane [174].

Section 3.2 presents the Diamond View images of the samples and Section 3.3 looks at FTIR spectroscopy which was used to characterise the A-and B-defects in the diamond samples. The paramagnetic nitrogen centres were characterised using EPR spectroscopy as described in Section 3.4.

3.2 Diamond View

The samples were first diamond-viewed at Element Six, Johannesburg, South Africa. The Diamond View^{TM} [175] was developed at De Beers Diamond Trading Company (DTC) Research Centre, Maidenhead, United Kingdom. The Diamond View^{TM} (see Figure 3.1) uses short wave ultraviolet (UV) light to produce a fluorescence image of the surface of a polished diamond [176] from which the growth structure maybe determined. The fluorescence pattern of natural diamonds are different in comparison to synthetic diamonds. The UV images of the four samples used in this study are as shown in Figure 3.2.



Figure 3.1: The DiamondView^{TM} fluorescent imager with associated PC.

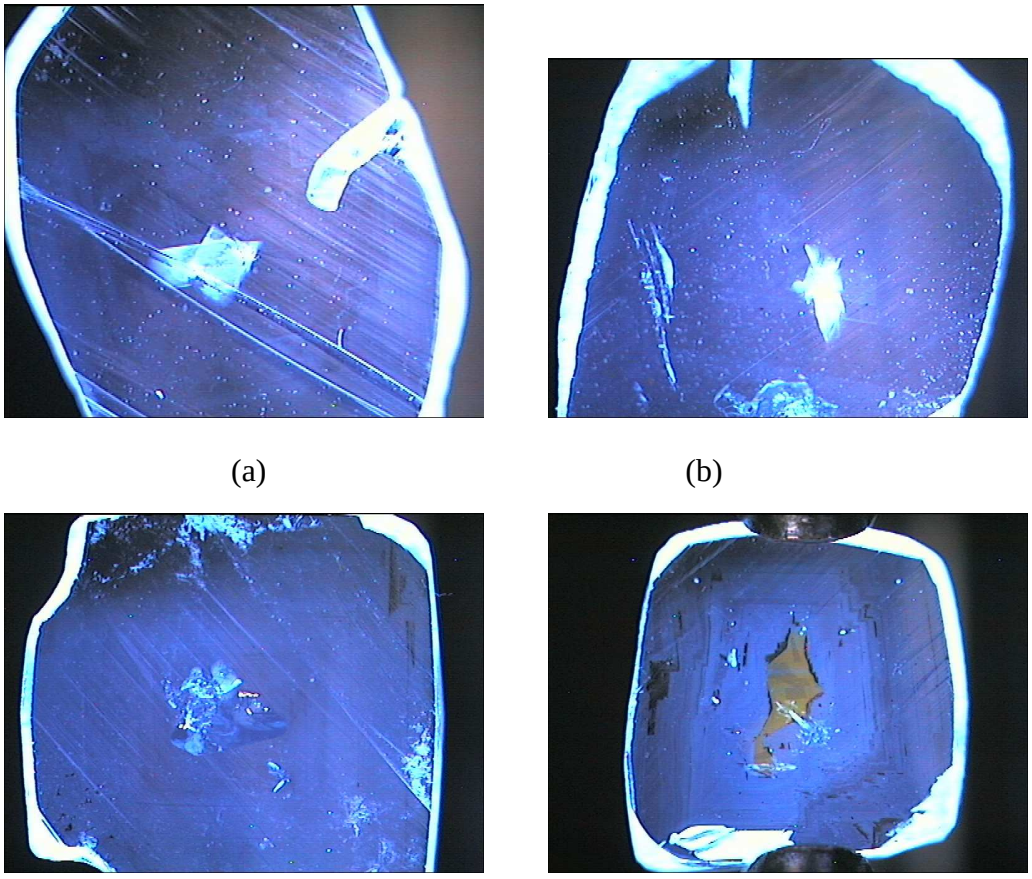

(a) (b)

(c) (d)

Figure 3.2: Diamond View images of the four natural type Ia diamond samples used in this study, showing some inclusions and growth zones.

3.3 Fourier Transform InfraRed (FTIR) Spectroscopy Measurements

Fourier transform infrared (FTIR) spectroscopy is a technique used to determine qualitative and quantitative features of IR-active molecules in organic or inorganic solid, liquid or gas samples. It is a rapid and relatively inexpensive method for the analysis of solids that are crystalline, microcrystalline, amorphous, or films. The fundamental measurement obtained in IR spectroscopy is an IR spectrum which is a plot of measured IR intensity (absorbance or transmittance) versus wavelength (or wavenumber) of light.

Here we present the characterisation of the natural type Ia diamond samples by means of fourier transform infrared spectroscopy. The FTIR characterisations were carried out at the Nationational Laser Centre (NLC) (Pretoria, South Africa). The main objective of these mesurements was to identify and quantify the aggregated nitrogen defects present in the natural type Ia diamond samples. The results indicate that the samples contained aggregated nitrogen in the form of A- centres, B- centres, and platelet-related nitrogen defects. The A aggregate was the predominant defect in all the four samples measured. This information was important in the muon spin rotation/relaxation measurements (see Chapter 5) since we needed to explore the possible thermal ionization of the N-H-N defect in natural type Ia diamond.

3.3.1 Principles of Infrared Spectroscopy

In the most basic terms, the infrared spectrum is formed as a consequence of the absorption of electromagnetic radiation at frequencies that correlate to the vibration of specific sets of chemical bonds from within a molecule. The distribution of energy possessed by a molecule at any given moment, defined as the sum of the contributing energy terms, is given by [177]

$$E_{total} = E_{electronic} + E_{vibrational} + E_{librational} + E_{translational}, \quad (3.1)$$

where $E_{translational}$ relates to the displacement of molecules in space as a function of the normal thermal motions of matter; $E_{librational}$ is observed as the periodic motion of a molecule as a result of the absorption of energy within the microwave region; $E_{vibrational}$ corresponds to the absorption of energy by a molecule as the component atoms vibrate about the mean centre of their chemical bonds; and $E_{electronic}$ is linked to the energy transitions of electrons, through the application of visible and ultraviolet radiation, as they are distributed throughout the molecule.

Vibrational motions within chemically bonded constituents of a material have frequencies in the infrared energy range. These motions or oscillations, which are induced by certain vibrational modes within the material, can interact with a beam of infrared radiation directed onto the material. Energy is exchanged between the beam and material when the frequencies are synchronous or ”in resonance”. Each molecule has its own distinct quantised vibrational energy level. This is often termed its ”fingerprint”. The absorption band can be characterised by two parameters: the wavelength at which maximum absorption occurs and the intensity of absorption at this wavelength. In an absorption spectrum, the y-axis measures the intensity of the band which is proportional to the number of molecules observed. This principle consequently leads to quantitative analysis. Figure 3.3 shows a schematic absorption spectrum.

In optics, the **Beer-Lambert law** is an empirical relationship that relates the absorption of light to the properties of the material through which the light is travelling. Applying this law to Figure 3.3:

$$T = \frac{I}{I_0} = \exp(-\alpha L c) \quad (3.2)$$

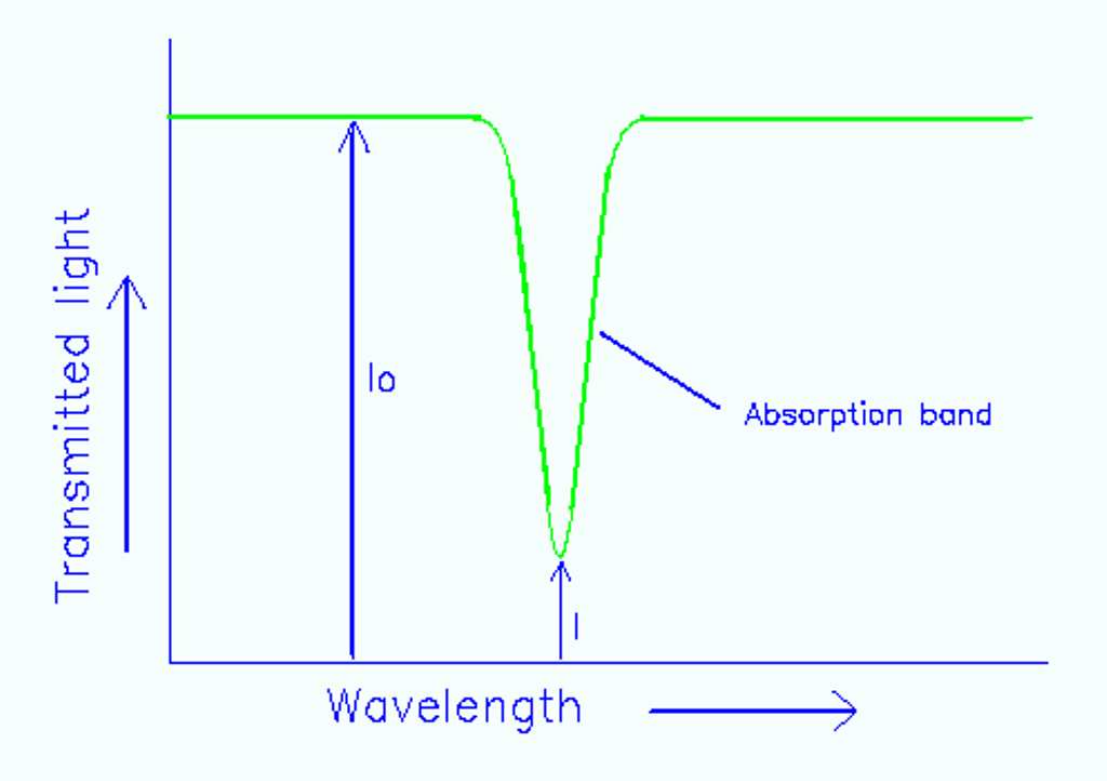

Figure 3.3: Schematic absorption spectrum.

$$A = -\log_{10}\left(\frac{I}{I_0}\right) = \epsilon L c \tag{3.3}$$

where

T is transmittance

A is absorbance

I_0 is the intensity of incident radiation

I is the intensity transmitted radiation

α is the absorption coefficient

L is the sample pathlength (cm)

c is the concentration of absorbing species in the material

ϵ is the molar extinction coefficient

3.3.2 Interferometry

The main component in the Fourier Transform Infrared (FTIR) spectrometer is an interferometer, shown schematically in Figure 3.4. This device splits and recombines a beam of light such that the recombined beam produces a wavelength-dependent interference pattern or an **interferogram**. The Michelson interferometer is most commonly used.

A Michelson interferometer consists of two mirrors and a beam splitter positioned at

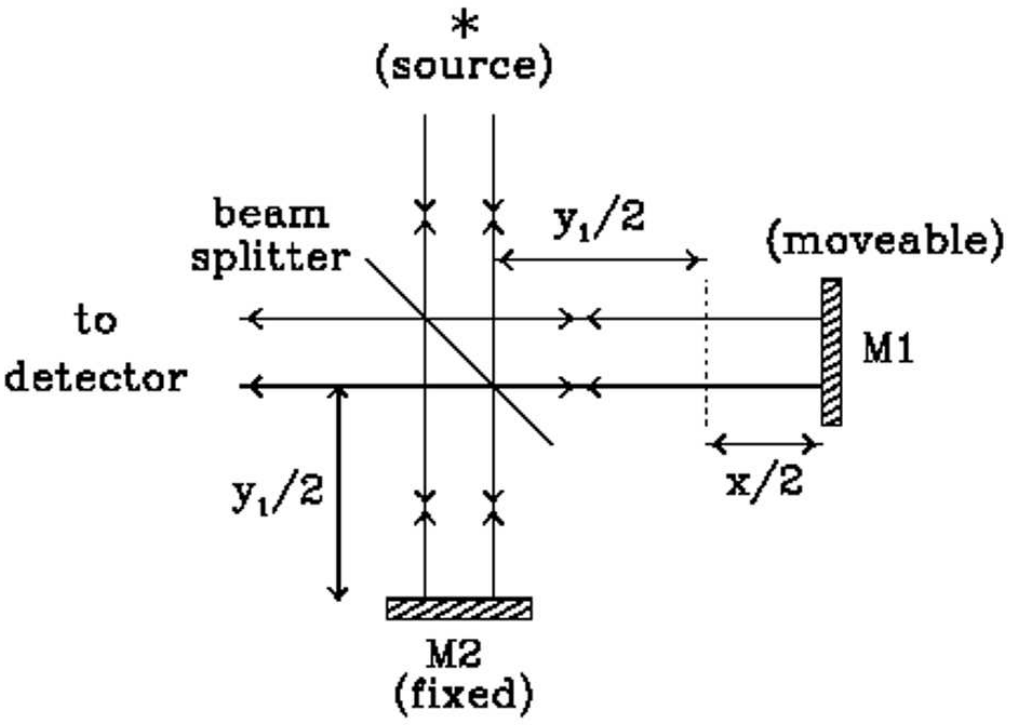

Figure 3.4: Optical schematic of a simple Michelson interferometer. The beam from the source is collimated and the wavefront is divided at the beam splitter. One arm of the interferometer consists of a fixed mirror, while the other arm contains a movable mirror. The beams are recombined at the beam splitter after having been reflected and transmitted once, and then proceed to the sample area and detector.

an angle of 45 ° to the mirrors. Incident light strikes the beam splitter so that half of the

light is transmitted through the beam splitter and half is reflected to the mirrors. The two components are then reflected back and recombined at the beam splitter with half of the light passing on towards the sampling areas and half travelling back towards the source.

Consider an incoming monochromatic plane wave with an average electric field amplitude E_m, frequency ω and wavenumber $\bar{\nu}$:

$$\bar{\nu} = \frac{1}{\lambda} = \frac{\omega}{2\pi c} \tag{3.4}$$

incident on the beam splitter (where c is the speed of light and λ is the wavelength in cm)

$$\vec{E} = \vec{E_m} \cos(\omega t - 2\pi \bar{\nu} y). \tag{3.5}$$

The beam from the mirror M2 after leaving the beam splitter in the direction of the condensing unit may be written as

$$\vec{E_2} = rtc\vec{E_m} \cos\left[\omega t - 2\pi \bar{\nu} y_1\right] \tag{3.6}$$

where r is the reflectance (amplitude) of the beam splitter, t is the transmittance, and c is a constant depending on the polarisation. Similarly, from the other mirror M1, at the same point, we have

$$\vec{E_1} = rtc\vec{E_m} \cos\left[\omega t - 2\pi \bar{\nu}(y_1 + x)\right] \tag{3.7}$$

where x is the path difference. By superposition, the resultant E is given by

$$\vec{E_R} = \vec{E_1} + \vec{E_2} = 2rtc\vec{E_m} \cos(\omega t - 2\pi y_1) \cos(\pi \bar{\nu} x). \tag{3.8}$$

The detected intensity (I) is the time average of E^2 and may be written as

$$I \propto 4r^2t^2c^2E_m^2 \cos^2(\omega t - 2\pi y_1 \bar{\nu}) \cos^2(\pi \bar{\nu} x) \tag{3.9}$$

where the time average of the first cosine term is just 1/2. Thus

$$I \propto 2I(\bar{\nu}) \cos^2(\pi \bar{\nu} x) \tag{3.10}$$

where $I(\bar{\nu})$ is a constant that depends only upon $\bar{\nu}$. This expression may be simplified to

$$I(x) = I(\bar{\nu}) [1 + \cos(2\pi \bar{\nu} x)] \tag{3.11}$$

where $I(x)$ is the *interferogram* from a monochromatic source.

A Fourier Transform Infrared (FTIR) spectrometer obtains infrared spectra by first collecting an interferogram of a sample signal with an interferometer, which measures all of infrared frequencies simultaneously. An FTIR spectrometer acquires and digitizes the interferogram, performs the FT function, and outputs the spectrum.

3.3.3 Analysis of FTIR spectra

The four natural type Ia diamond pieces had a total mass of 0.558 g and a total surface area of about 2.20 cm^2. The four pieces were 0.73, 0.78, 0.93, and 1.16 mm thick. The instrument was evacuated to eliminate atmospheric absorption.

The FTIR absorption spectra of these samples are shown in figure 3.5. The A aggregate appears near 1282 cm^{-1} and there is a correlation between the intensity of this band and nitrogen content in natural diamonds. The B aggregate is observed near 1175 cm^{-1}. The

band near 1370 cm^{-1} is thought to be related to platelets [178].

The FTIR spectra of the diamond samples used by Machi et al. [124] when they

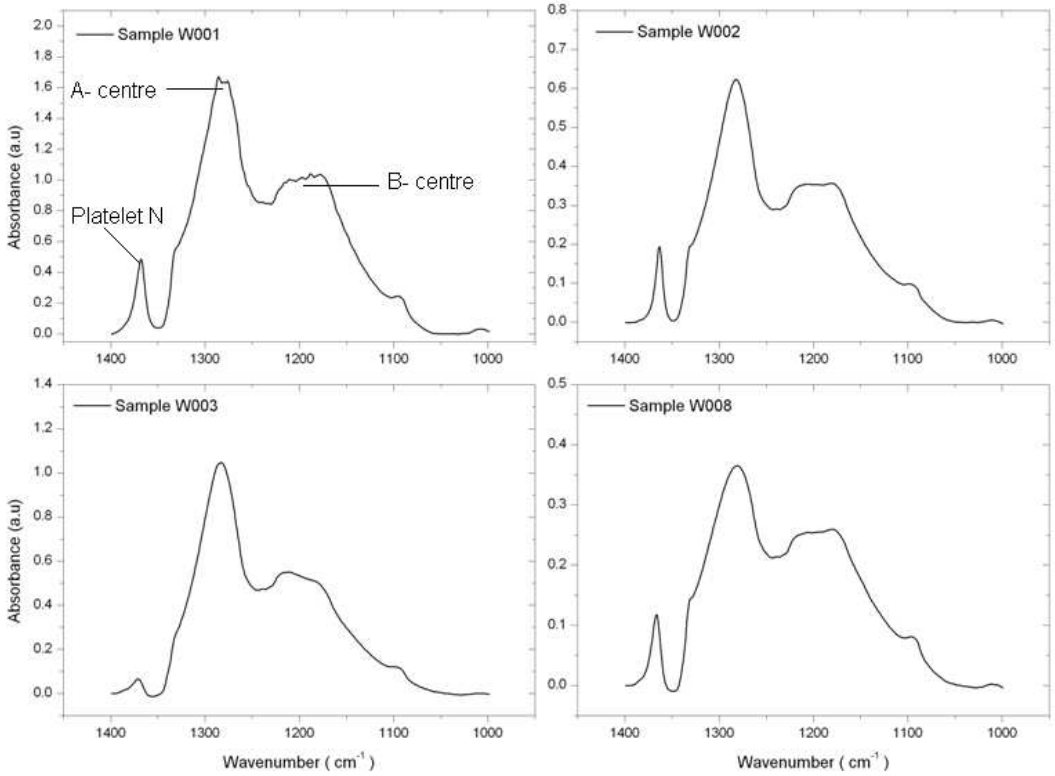

Figure 3.5: Infrared absorption spectra of the four natural type Ia diamond samples used in this study. The combined sample contained about 150 ppm of A-centres and 56.2 ppm of B-centres.

discovered the new muonium defect, Mu_X, associated with aggregated nitrogen defects are shown in figure 3.6. The samples contained about 650 ppm of A-centres and 400 ppm of B-centres.

The different forms of incorporated nitrogen give rise to characteristic spectra that can be used to estimate their respective concentrations. This was done by reconstructing the experimental spectra (Fig. 3.5) as an admixture of the well-known A, B, C and N^+ components. For the single substitutional nitrogen centre, the nitrogen concentration, N_C, is conventionally expressed in terms of the absorption coefficient, μ_S, at 1130 cm^{-1}.

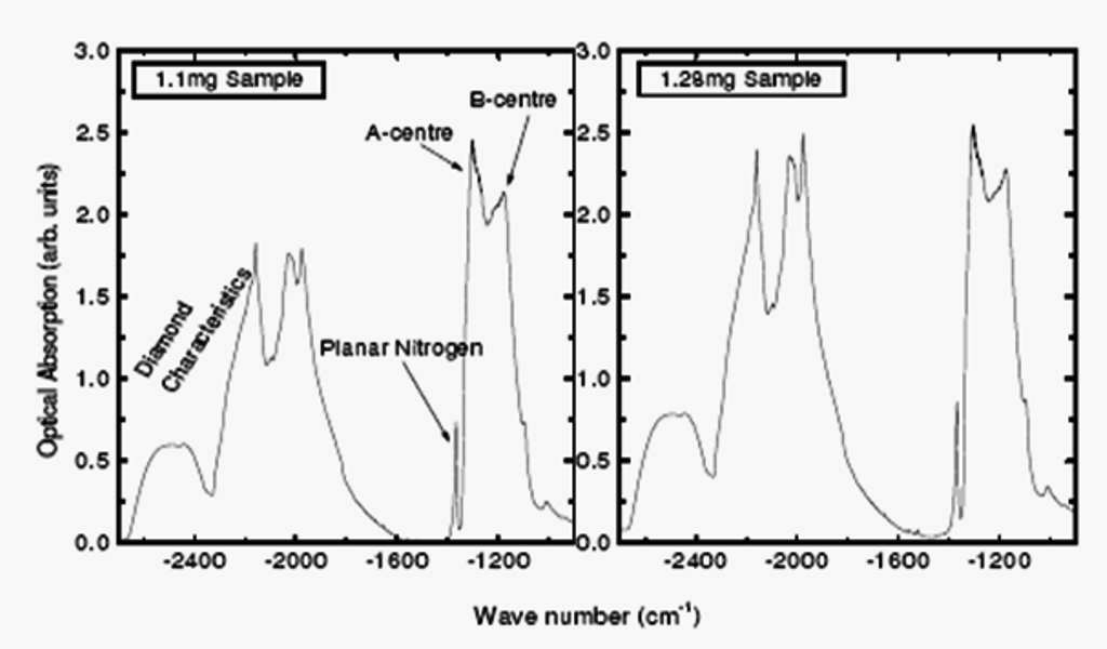

Figure 3.6: Infrared absorption spectra of the natural type Ia diamond samples used by Ref. [124]. These samples contained about 650 ppm of A-centres and 400 ppm of B-centres.

This is the wavenumber at which the maximum absorption produced by these centres occurs. One may write

$$[N_C] = k_C \mu_C \ (1130\ cm^{-1}). \tag{3.12}$$

Similar expressions can be written for the A and B[1] centres:

$$[N_A] = k_A \mu_{1282}. \tag{3.13}$$

and

$$[N_B] = k_B \mu_{1282}. \tag{3.14}$$

[1] In those diamond crystals that only show individual IR absorption bands related to A- and B-type defects, nitrogen concentrations are directly proportional to IR absorption coefficient values at 1282 cm^{-1} spectral peak [179]

Here $[N_A]$ and $[N_B]$ are the concentrations of nitrogen in the A and B centres, respectively, k_A and k_B are coefficients for the A and B centres, respectively, and μ_{1282} is the intensity of the absorption peak at the frequency 1282 cm^{-1}. The infrared absorption coefficients for the A, B, and C defects are given in Refs. [180, 181, 182, 172]. These absorption coefficients were built into the Diamond Trading Company (DTC) Excel program (IRspec-CAXBD97.XLS) [183] which was used to estimate the nitrogen concentrations in parts per million (ppm). The IRspec-CAXBD97 spreadsheet decomposes the single phonon region of a diamond infrared absorption spectrum in order to determine the concentrations of nitrogen present in various aggregation states. The decomposition is achieved using Excel's solver tool to carry out a least squares fit for the components and constraints. The combined sample contained about 150 ppm of A-centres and 56.2 ppm of B-cenres. The fits for the individual samples are as shown in Appendix A.

3.4 Electron Paramagnetic Resonance (EPR) Measurements

3.4.1 Preliminary remarks

The samples were also characterised using electron paramagnetic resonance (EPR). The EPR measuremets were carried out at the University of the Witwatersrand (Johannesburg, South Africa). For each diamond sample a continous wave (CW) spectrum was recorded at room temperature on an X-band Bruker ESP 380E pulsed/CW spectrometer. The EPR spectra of the four samples are shown in Figures 3.10 - 3.13. The main objective of these mesurements was to confirm and ensure that no other impurities were present in significant concentrations. The results indicate that the samples contained P1 and P2 nitrogen centres.

P1 centres (electron spin S = 1/2, nuclear spin I = 1) are dispersed substitutional nitrogens [173, 184, 185]. Nitrogen has five valence electrons, thus forming covalent bonds

with only three of the neighbouring carbon atoms in diamond, as shown in Figure 3.7. The fourth sp^3 hybrid of the nitrogen atom is then occupied by a lone pair, leaving one carbon atom with one unpaired electron. The internuclear vector between this carbon atom and the nitrogen atom coincides with one of the ⟨111⟩ directions. The EPR spectrum of a P1 center consists of a central transition ($m_I = 0$) and two hyperfine transitions ($m_I = \pm 1$), one on each side of the central transition [186].

A P2 centre consists of a vacancy and three nitrogens in neighbouring positions in a (111) plane [174] (Figure 3.7). Type Ia diamonds usually contain P1 and P2 centres, while type Ib diamonds contain mainly P1 centres. Type IIa diamonds contain relatively low concentrations of nitrogen [185].

Other paramagnetic impurity centres that have been observed in diamond are the N2 and N3 centres. The N3 centre[2] consists of substitutional nitrogen as well as substitutional oxygen [187]. The nitrogen is covalently bonded to three carbons with a lone pair in the remaining sp^3 orbital. The oxygen, with six valence electrons, forms bonds with two carbons, the remaining four electrons being accommodated in the remaining O-orbital, leaving an unpaired electron on a carbon atom, as shown in Figure 3.7.

The formation of the N2 centre is thought to be directly associated with the plastic deformation of the crystal [188]. This process is illustrated in Figure 3.8. The substitutional nitrogen pair N1N2 is transformed into a new impurity centre N1C1C2N2 on undergoing a translational slip by a distance equal to the vector $\vec{b}$. This centre may lose an electron and become paramagnetic if it is close to dislocations possessing acceptor properties [185]. Newton and Baker [189] have confirmed that nitrogen is a constituent of this centre.

[2] The N3 centre should not be confused with the optical centre also labelled N3 which has been shown to correlate with the P2 EPR centre [174]

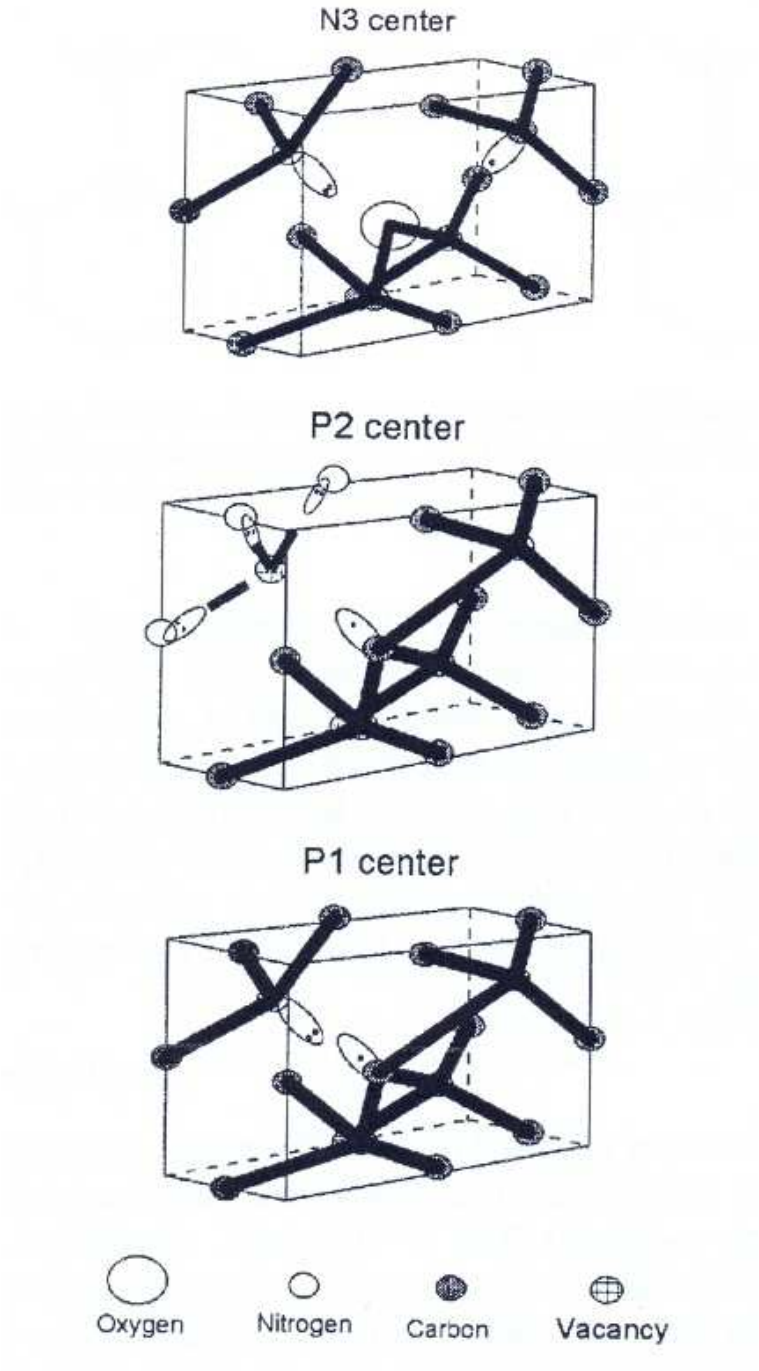

Figure 3.7: Illustrations of the geometries of the paramagnetic P1, P2, and N3 centres in diamond. The positions of the unpaired electrons are shown in the diagrams. These diagrams are taken from Ref. [185].

3.4.2 Principles of EPR Spectroscopy

Electron paramagnetic resonance (EPR) is a spectroscopic technique that detects the transitions induced by electromagnetic radiation between the energy levels of electron

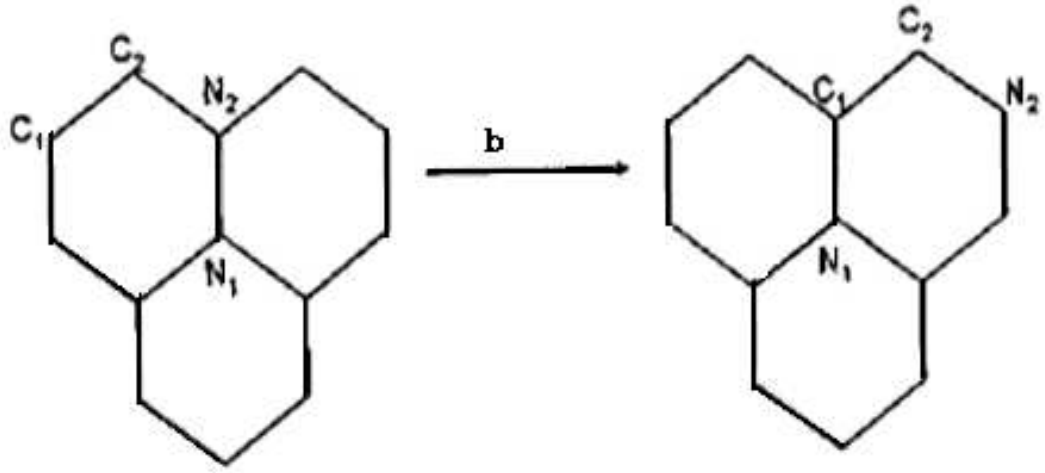

Figure 3.8: An illustration of the formation of the paramagnetic N2 centre by a translational slip in diamond. N1 and N2 are nitrogen atoms, while C1 and C2 are carbon atoms. This diagram is taken from Ref. [185]

spins in the presence of a static magnetic field. The method can be applied to the study of species containing one or more unpaired electron spins; examples include organic and inorganic radicals, triplet states, and complexes of paramagnetic ions. Spectral features, such as resonance frequencies, splittings, line shapes, and line widths, are sensitive to the electronic distribution, molecular orientations, nature of the environment, and molecular motions. Theoretical and experimental aspects of EPR have been covered in a number of books [190, 191].

The phenomenon of EPR can be explained by considering the behaviour of a free electron. According to quantum theory the electron has a spin which can be understood as an angular momentum leading to a magnetic moment. The spins can interact with external magnetic fields (Zeeman interaction) and with each other (couplings). The negative charge that the electron carries is also spinning and constitutes a circulating electric current. The "circulating current" induces a magnetic moment $\vec{\mu}_s$ which, if the electron is subjected to a steady magnetic field $\mathbf{H}_0 \parallel \mathbf{z}$, causes the electron to experience a torque tending to align the magnetic moment with the field. The relation between the

magnetic moment and the spin vector is

$$\vec{\mu}_s = -\frac{g\mu_B}{\hbar}\mathbf{S} \tag{3.15}$$

where μ_B is the Bohr magneton and g is the Lande factor. The energy of the system depends upon the projection of the spin vector along $\mathbf{H}_0$. Quantum theory stipulates that only two values are permitted for an electron $S_z = \pm\hbar/2$, which means that the electron magnetic moment can only assume two projections onto the applied field as shown in Figure 3.9.

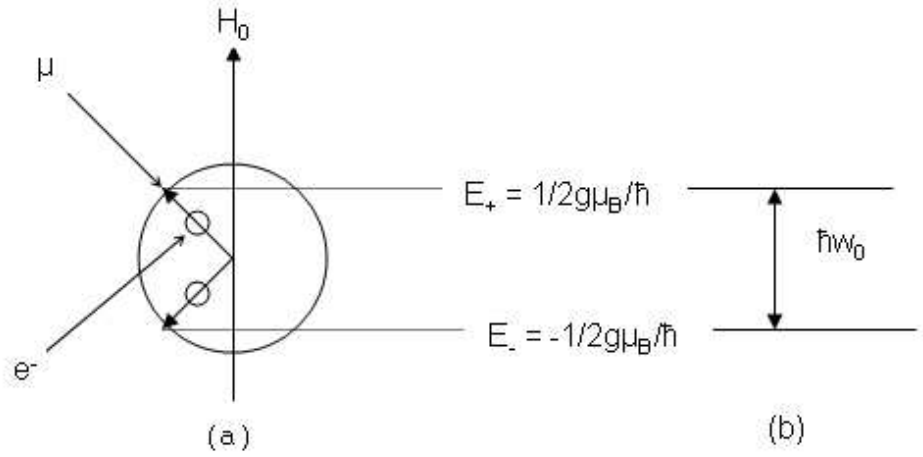

Figure 3.9: (a) Schematic representation of a single electron spin in a steady magnetic field $\mathbf{H}_0$ (b) Corresponding energy-level scheme

Consequently,

$$\mu_z = \pm\frac{1}{2}g\mu_B \tag{3.16}$$

and the ensemble of energy levels therefore reduce to the two values

$$E_\pm = \pm\frac{1}{2}g\mu_B H_0 \tag{3.17}$$

If electromagnetic radiation is applied at a frequency that corresponds to the separation between the permitted energies equal to $\Delta E = E_+ - E_- = g\mu_B H_0 = \hbar\omega$, energy is absorbed from the electromagnetic field. This is the phenomenon of EPR. The populations of the energy levels are determined by Boltzmann statistics. The population ratio between an upper and a lower level, N_+ and N_-, is given by

$$\frac{N_+}{N_-} = \exp\left(\frac{\Delta E}{k_B T}\right) \tag{3.18}$$

where $\Delta E = E_+ - E_-$, k_B is Boltzmann's constant, and T is the absolute temperature. The population difference caused by the energy separation can be detected as an absorption. An EPR spectrometer accomplishes resonance by using a fixed frequency, ν, while sweeping the magnetic field. A typical experiment utilises microwave frequencies of roughly 9 GHz which for organic radicals give resonances at magnetic fields of about 300mT or 3 kG.

3.4.3 EPR spectra

The EPR spectra of all the four natural type Ia single crystal diamond samples used in this study are shown in Figures 3.10 - 3.13. The EPR spectra show that all the four diamonds contained paramagnetic P2 and P1 centers.

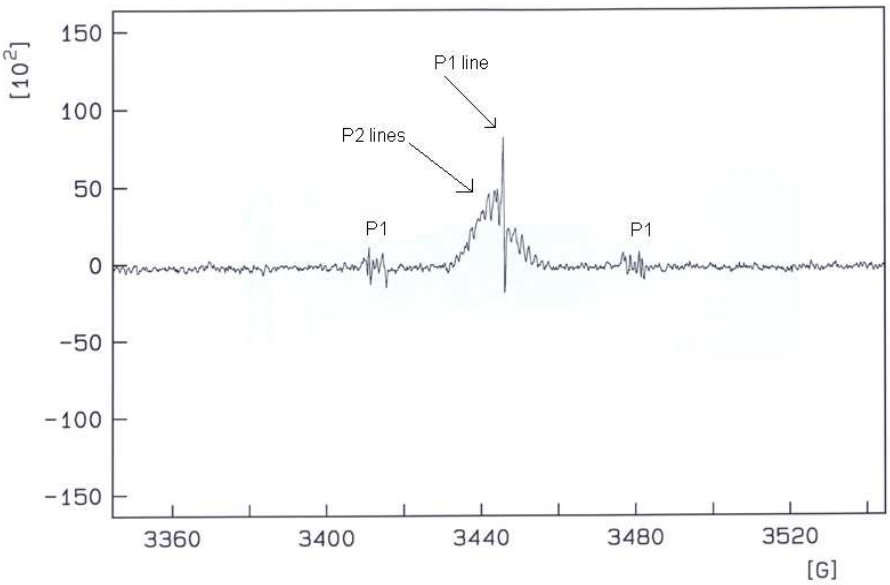

Figure 3.10: Room-temperature EPR spectrum of sample w001. The resonance lines of P1 and P2 centres are indicated.

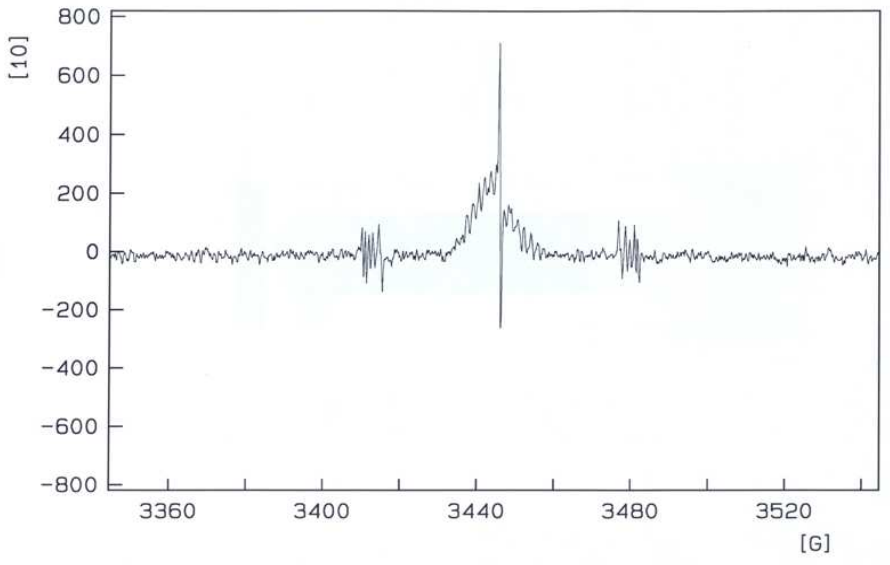

Figure 3.11: Room-temperature EPR spectrum of sample w002. The resonance lines of P1 and P2 centers are identical to Figure 3.10.

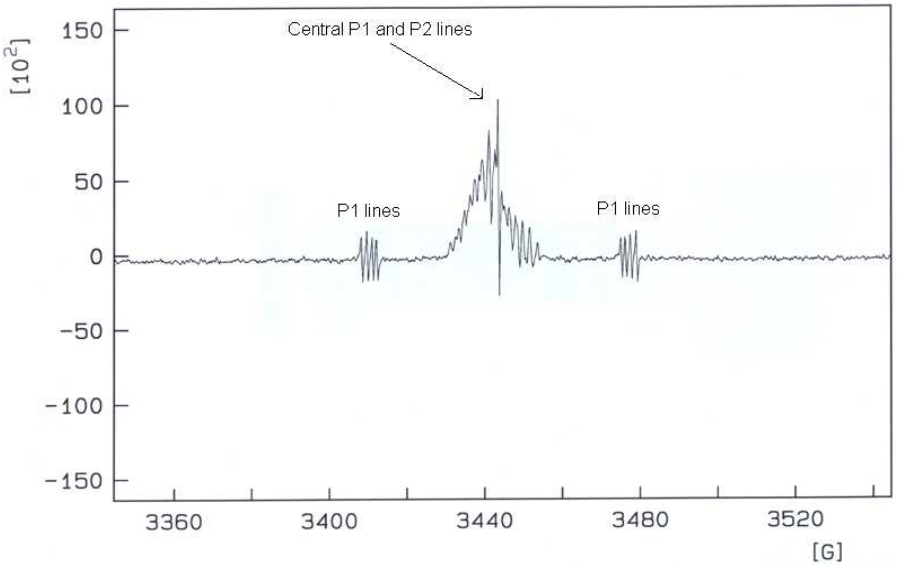

Figure 3.12: Room-temperature EPR spectrum of sample w003. The resonance lines of P1 and P2 centers are indicated.

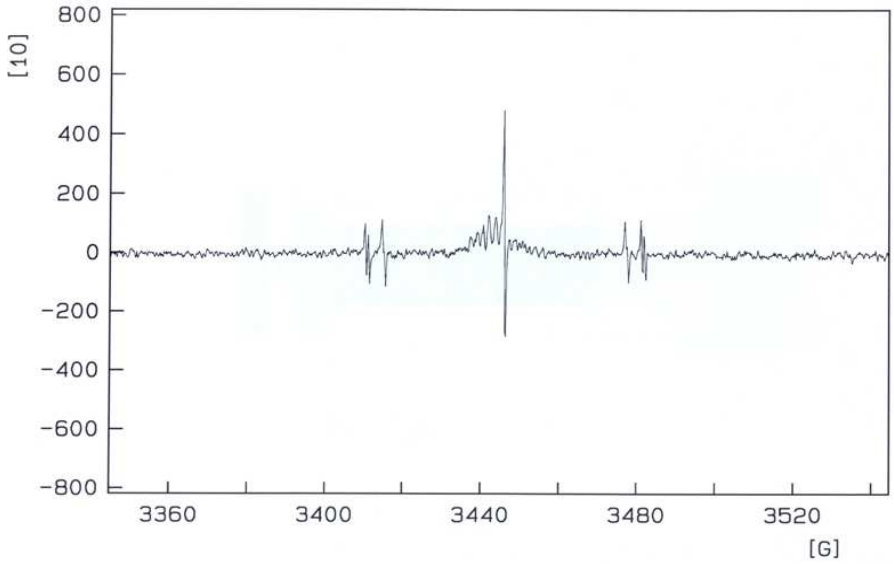

Figure 3.13: Room-temperature EPR spectrum of sample w008. The resonance lines of P1 and P2 centers are identical to Figure 3.12.

Chapter 4

Experimental Arrangements for Muon(ium) Studies in Natural Type Ia And Synthetic Type HPHT-IIa Diamond

"Since the measuring device has been constructed by the observer ... we have to remember that what we observe is not nature itself but nature exposed to our method of questioning."

Werner Heisenberg

4.1 Preliminary Remarks

In this Chapter the experimental arrangement for muonium studies in natural type Ia and high-purity type IIa HPHT single crystal diamond are presented. These measurements were conducted at the ISIS facility at the Rutherford Appleton Laboratory, in the United Kingdom. The main experimental technique was the longitudinal field muon spin relaxation (LF-μSR). This experimental configuration allows the various muonic species to be studied beyond the promptly formed components, so that their relative populations can be followed through several interactions. Small transverse fields of 2 and 20 G were employed to observe promptly formed tetrahedral (Mu_T) and diamagnetic (μ_d) muonium. The 20 G (T20) transverse field was also used to estimate the value of α (this parameter accomodates systematic effects in detectors and geometry) for a particular temperature point. The T20 run allows α and the baseline to be found for the subsequent longitudinal field runs.

Section 4.2 describes the experimental arrangements at the ISIS Muon Facility located at the Rutherford Appleton Laboratory (ISIS-RAL) and how the samples were prepared for mounting. Section 4.3 focuses on some alpha correction mechanisms that can be employed in fly-past mode and Section 4.4 describes how the data was analysed.

4.2 Experimental Details

The μSR measurements were conducted at the ISIS Facility located at Rutherford Appleton Laboratory (ISIS-RAL), in the United Kingdom, using the European Muon Spectrometer (EMU) in fly-past mode. Figure 4.1 shows the general arrangement of the European muon facility at ISIS.

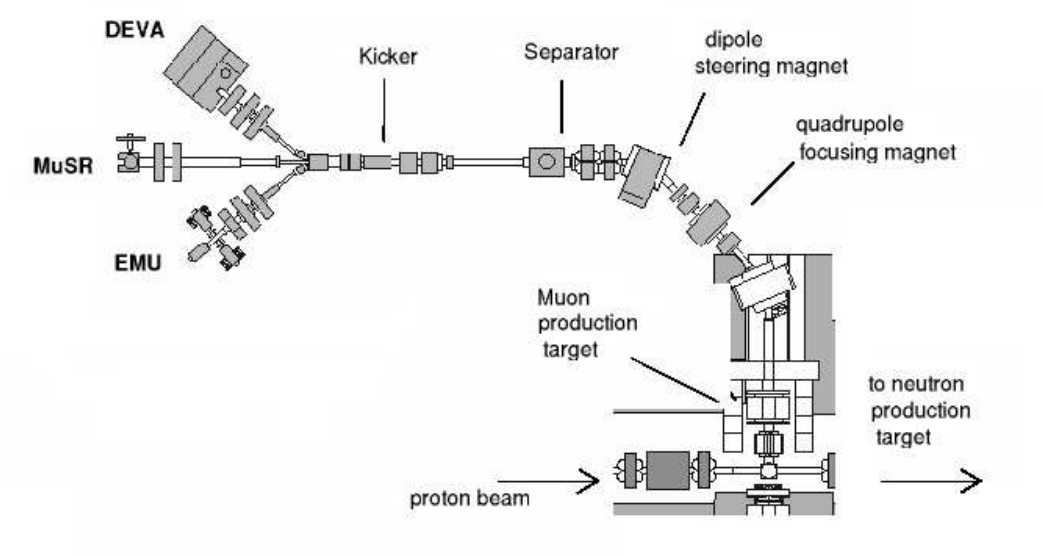

Figure 4.1: General layout of the European Muon Facility at ISIS. The data presented in this study were collected using the EMU spectrometer. This diagram is taken from Ref. [192]

The ISIS synchrotron produces a beam of protons pulsed with a repetition rate of 50 Hz. Each pulse is made up of two proton bunches each with a width of about 80 ns and a separation of 300 ns. The 800 MeV protons from the synchrotron pass through a

graphite intermediate target before reaching the main neutron production area. A small fraction of the protons collide with a proton or neutron of a carbon atom to produce pions. The muons produced at the graphite target very closely follow the proton time profile, slightly smeared out due to the 26 ns pion half-life. As a consequence muons are implanted in bunches and their time of arrival starts a separate clock for each spectrometer.

Muons are transported from the production target to the sample areas via a series of dipole (steering) and quadrupole (focusing) magnets (Figure 4.1) tuned to accept muons with a momentum of 26.5 MeV/c. Contaminant particles, particularly positrons produced during pion creation and from muon decays in flight, are eliminated using a crossed field electrostatic separator. The separator performs velocity selection of particles by means of mutually perpendicular **E** and **B** fields; the muons, travelling at about 0.24c, pass through undeflected whilst positrons, travelling at nearly the speed of light, are deflected from the beamline. The separator introduces a small rotation of the muon polarisation, of the order of 6°, so that the muon spins point slightly upwards from the momentum direction.

The three instruments of the EC muon facility are fed from the double pulse structure of the ISIS beam by means of an electrostatic kicker (Figure 4.1). This consists of a central electrode and two outer electrodes. Immediately before the arrival of the first muon pulse, a high voltage is applied to the central electrode, causing the first-pulse muons to be deflected. Half are fed to the EMU beamline and half to DEVA. Before the arrival of the second pulse, the voltage on the central electrode is reduced to zero, allowing the second-pulse muons to pass undeflected to the MuSR instrument. This whole process happens 50 times every second.

4.2.1 The EMU Spectrometer in Fly-past Mode

The experiments were conducted on the EMU spectrometer in fly-past mode. EMU is a 32-detector spectrometer which is optimised for zero field and longitudinal field measurements. Fields of up to 4500 G can be applied, and sample temperatures in the range of 350 mK to 1500 °C can be produced using a variety of sample environment equipment. Figure 4.2 shows the schematic layout of the EMU spectrometer.

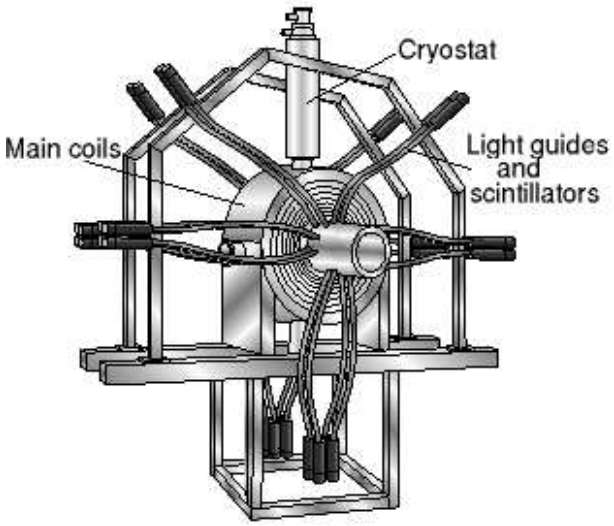

Figure 4.2: A schematic view of the EMU spectrometer. This diagram is taken from Ref. [192]

The detectors consist of plastic scintillators (high time resolution) which are connected via light pipes to a photomultiplier tube. Light pipes are used in order to reduce the magnetic field at the photomultiplier tube.

In traditional experiments at the ISIS muon facility samples are mounted onto a holder and the surrounding material is masked with silver. This creates unwanted signals from muons stopping in the surrounding mask which cannot be removed by collimation of the muon beam, making it extremely difficult to do experiments with samples with an

area smaller than the muon beam spot size. A technique of suspending samples in the beam as a method of overcoming these inherent difficulties has been developed [193]. Instead of using a normal masked sample, a holder the same size or smaller than the sample itself, presenting a minimal cross-section of material to the beam, is suspended in the muon beam and attached to the cryostat by a thin strip of metal. The cryostat vacuum vessel and intermediate heat shield are both equipped with thin exit windows to allow the muons that miss the sample to escape (fly-past) from the cryostat and stop some distance downstream. The detectors are arranged in such a way that the counting efficiency for these muon decays will be negligible compared to that for the decays in the sample itself.

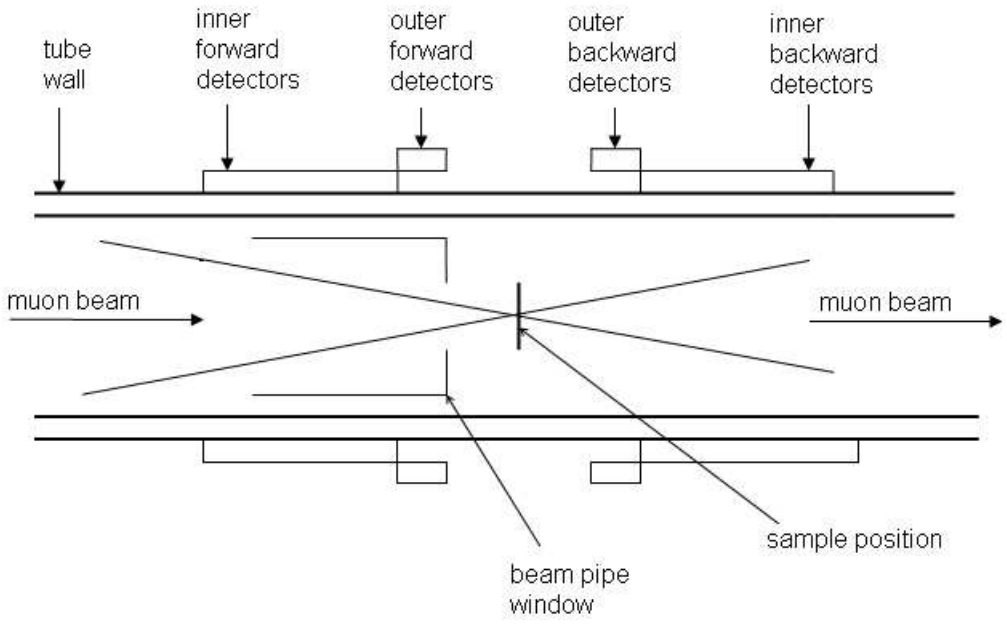

Figure 4.3: Schematic of the EMU spectrometer in fly-past mode showing the detector rings, muon beam, beam pipe window and sample position.

This fly-past technique has been set up on the EMU instrument at ISIS by addition of an

evacuated tube downstream of the sample position, providing a region for the muons to pass into, behind the sample. This arrangement is clearly shown in Figure 4.3 together with the locations of the four detector rings - inner and outer forward, and inner and outer backwards.

In order to investigate the behaviour of the muonium species in the natural type Ia diamond samples, longitudinal magnetic field measurements were performed from 300 to 1200 K, and the magnetic field was varied from 2 - 4500 G at each temperature point. The temperature range for the high-purity type IIa HPHT diamond samples was 5 - 290 K. The vacuum was maintained in the order of 10^{-5} torr using four pumps that were placed at the top, front (at the end of the fly-past tube), and at both sides of the sample area, as shown in Figure 4.4.

4.2.2 Sample Mounting

The two pieces of high-purity type IIa HPHT diamond were placed on a small silver plate of dimensions 4.0 x 9.0 mm. The Closed-cycle refrigerator (CCR) cryostat and Reflector furnace were used for the low temperature and high temperature measurements, respectively. For the latter, the four pieces of natural type Ia diamond samples were placed in a small sealed pouch made of titanium and then mounted on a thermocouple sitting in an optical furnace, as shown in Figure 4.5. The furnace was made up of two high power halogen bulbs placed opposite each other around the sample space. The heat generated was concentrated upon the sample by gold reflectors. The sample temperature was controlled by a Eurotherm crate. The furnace was cooled by chilled water, and the sample space was covered by titanium shields as shown in figure 4.6. Figure 4.7 shows the interlock wiring diagram for the furnace.

The control line from the Eurotherm crate was connected, via a junction box, to the

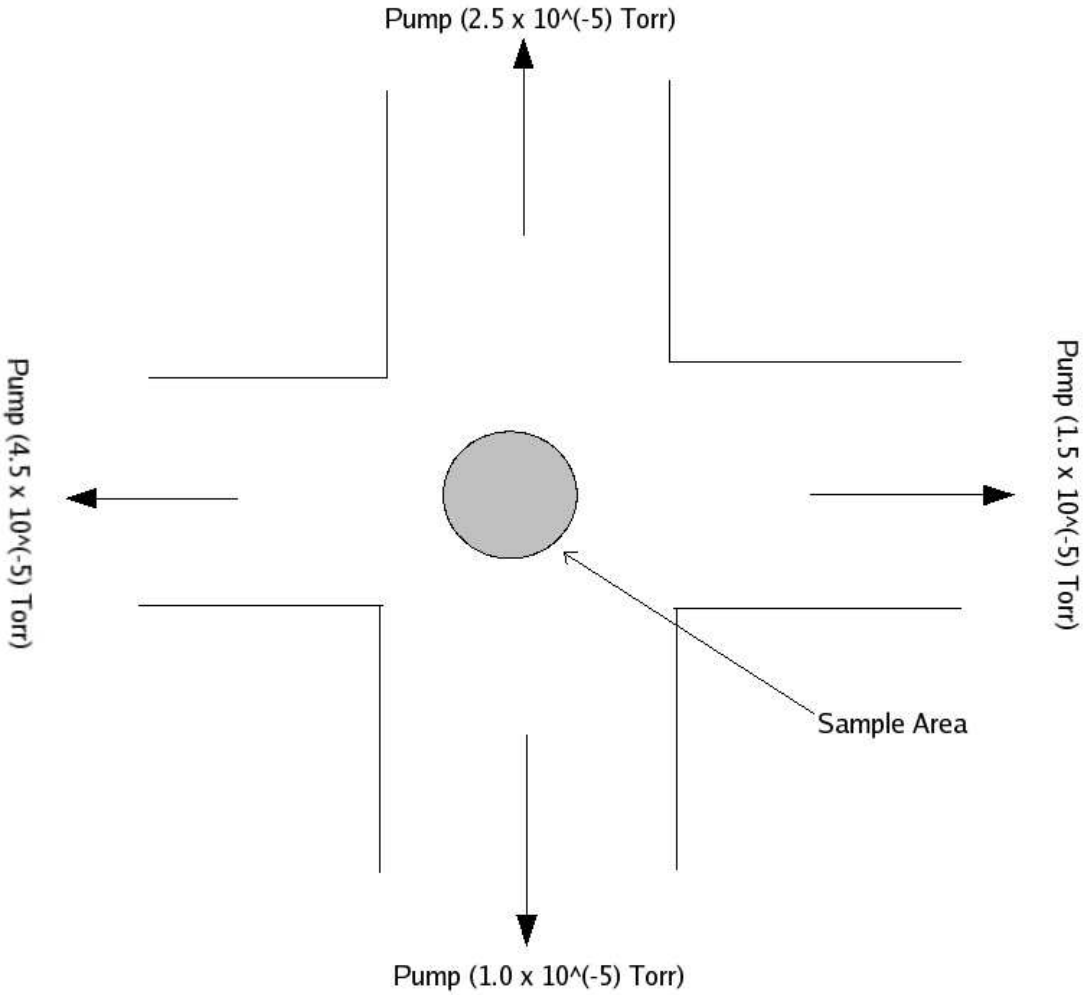

Figure 4.4: Schematic diagram of how the vacuum pumps were connected to the sample area. The vacuum was maintained in the order of 10^{-5} torr using this arrangement.

thermocouple trip box. The trip thermocouples were connected to the cruciform and the beam snout and the trip was set at 85 °C. The 0-5V line was then fed into the power unit which was connected to the furnace. Figure 4.8 shows the electrical and mechanical connections on the furnace body itself. After wiring and mounting the sample the furnace was placed into the space vacated by the CCR cryostat.

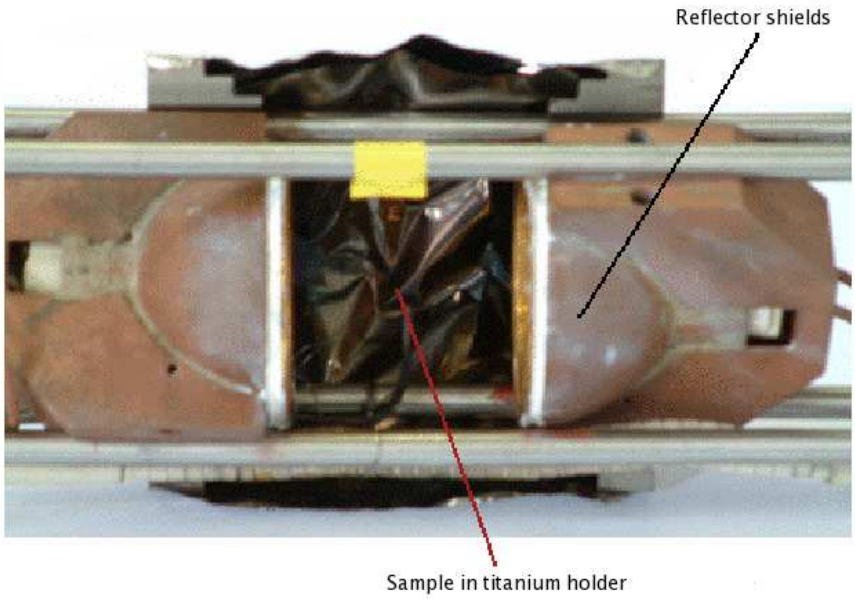

Figure 4.5: Picture of the reflector furnace showing two halogen bulbs mounted opposite each other around a sample space.

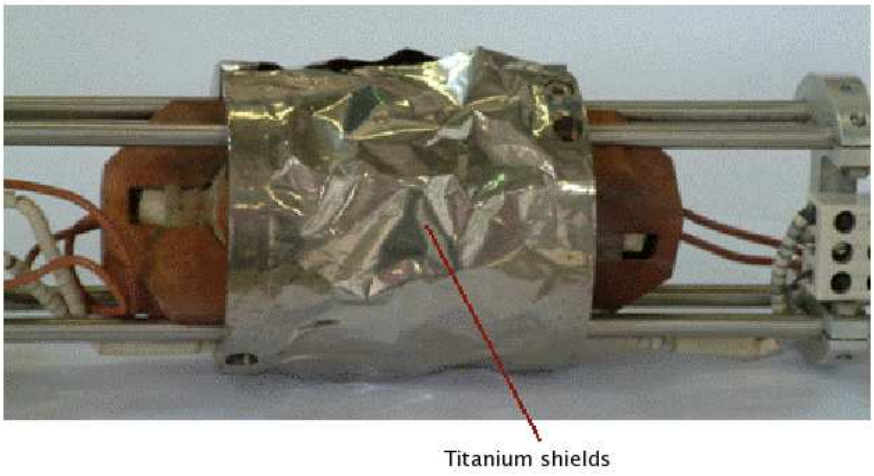

Figure 4.6: Picture of the reflector furnace showing the sample space enclosed by titanium shields.

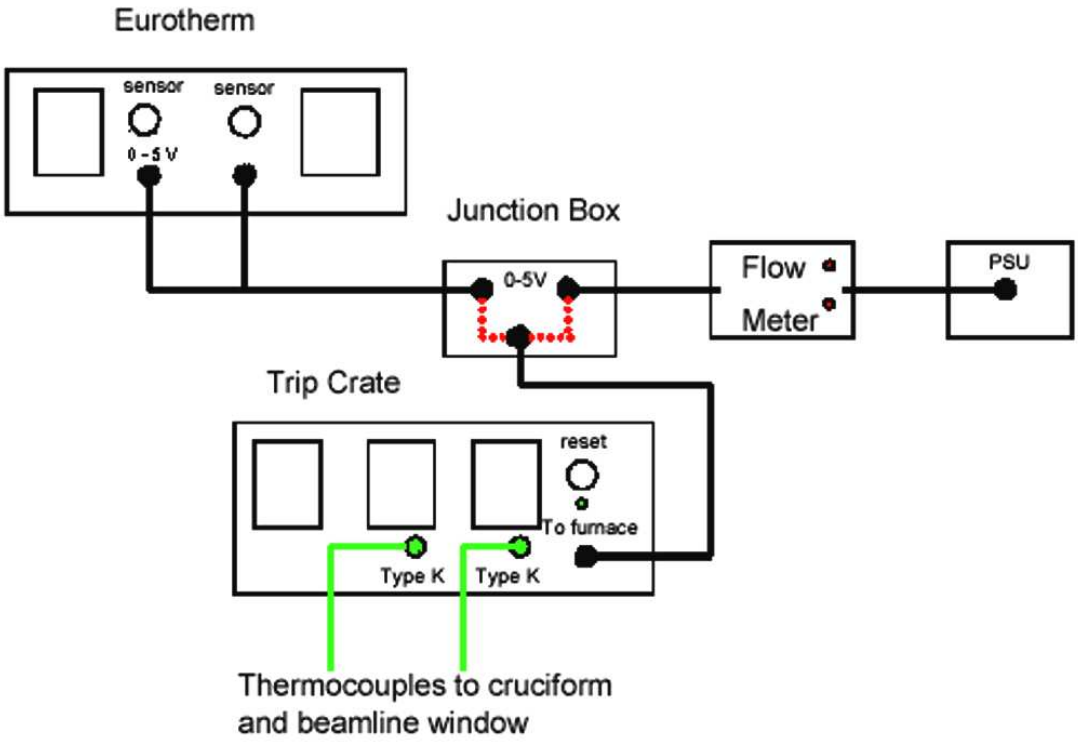

Figure 4.7: Wiring diagram for the furnace, showing the 0-5V trip line and the type K trip thermocouples which are attached to the cruciform and beam snout. This diagram is taken from Ref. [194].

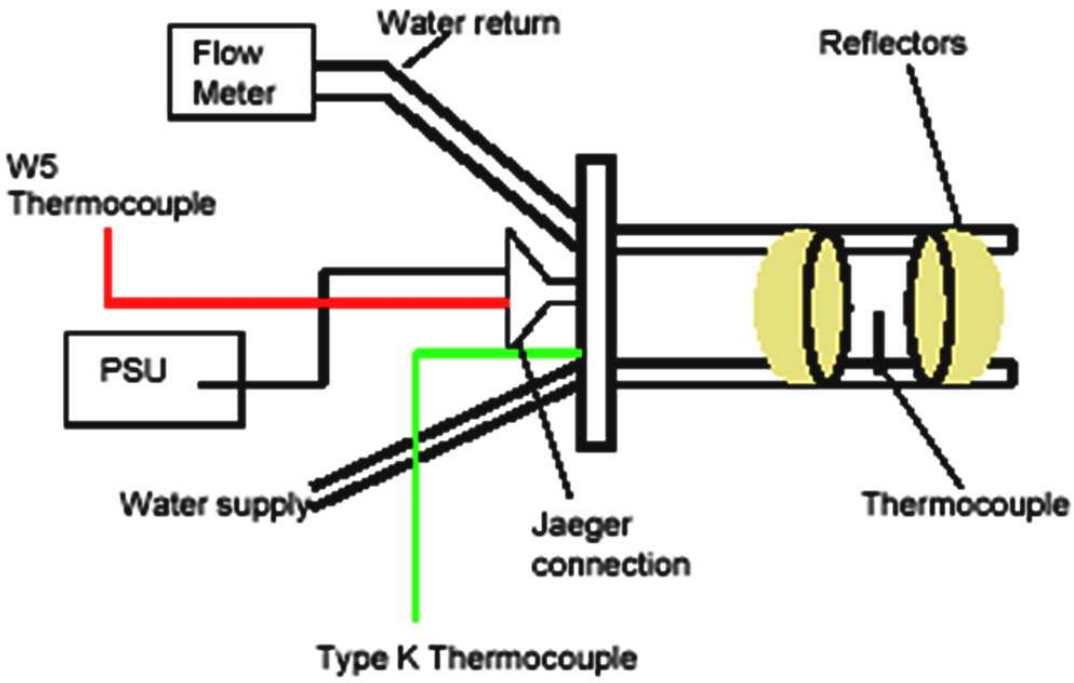

Figure 4.8: A schematic of the electrical and mechanical connections on the furnace. This diagram is taken from Ref. [194].

4.3 Geant4 Simulation of the Fly-Past and Alpha Correction

4.3.1 Field-dependent alpha value in fly-past mode

Higher magnetic fields steers the muons onto the sample, and hence reducing the amount of fly-past muons at higher fields. The positrons originating from the flypast muons which have decayed downstream of the sample position have a bigger solid angle subtended by the Backward as compared to the Forward detectors, therefore, more flypast (at lower fields) decreases the observed asymmetry. There must be an additional effect whereby the higher fields also affect the positron trajectories, such that they are detected in the Forward detector with higher probability or the backward detector with lower probability. Since the sample is symmetrical within the field, and this effect only happens with small samples, this statement must apply to flypast muons. The magnetic rigidity of 4 MeV muons is similar to 20-40 MeV positrons.

Figure 4.9 shows the field dependent asymmetry in a small silver sample, the size of the diamond sample. This should ideally be constant. One may imagine that the value of alpha changes with field, and find that value of alpha that keeps the silver asymmetry constant. This field dependent value of alpha is found and shown in Figure 4.10. This was done by varying alpha in the analysis code UDA until a constant asymmetry was found.

Also, using

$$A = \frac{F - \alpha B}{F + \alpha B}, \tag{4.1}$$

where F and B are the positron counts in the Forward and Backward detectors, respectively, and α is the correction factor, one can write for the silver calibration data

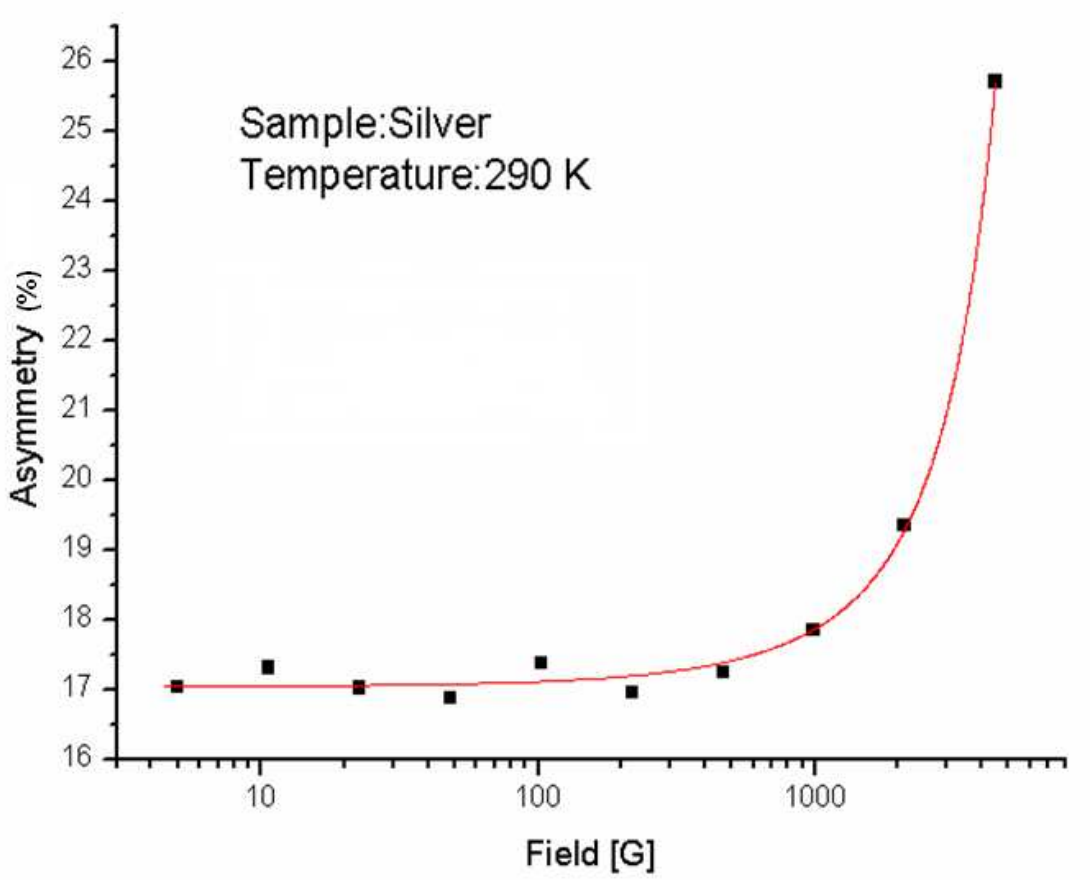

Figure 4.9: Field dependent asymmetry in a small silver sample.

$$\frac{F}{B}(B) = \alpha\left(\frac{1+A}{1-A}\right). \tag{4.2}$$

If we set A = A' = constant at the low field value, we obtain

$$\alpha(B) = \frac{F}{B}(B)\left(\frac{1-A'}{1+A'}\right). \tag{4.3}$$

It can be observed that this new corrected alpha can be used in the re-calculation of *A* for the silver calibration sample and it will be constant.

Now, for the diamond data

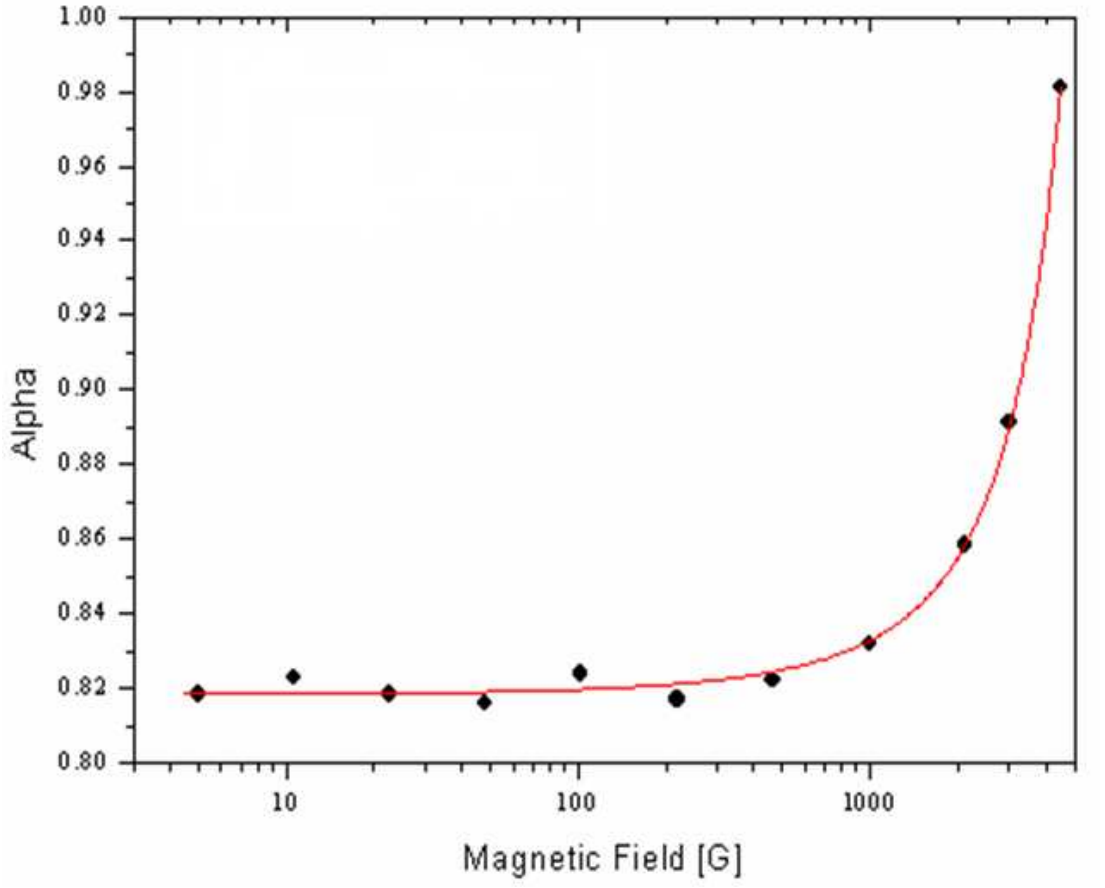

Figure 4.10: Field dependent value of alpha in a small silver sample. This was done by varying alpha in the analysis code UDA until a constant asymmetry was found.

$$\frac{F}{B}(B) = \alpha * \left(\frac{1 + A*}{1 - A*}\right). \tag{4.4}$$

where A* are the uncorrected asymmetries found by making alpha constant at its low field value of $\alpha*$. If we now take the α(B) that keeps the asymmetry of the silver data constant, fit it with an exponential to interpolate between points and make a correction, we obtain

$$A\text{”} = \left(\frac{F/B(B) - \alpha(B)}{F/B(B) + \alpha(B)}\right), \tag{4.5}$$

where α(B) is the corrected alpha described above, and A” is now corrected by using a corrected alpha. This is shown in Figure 4.11.

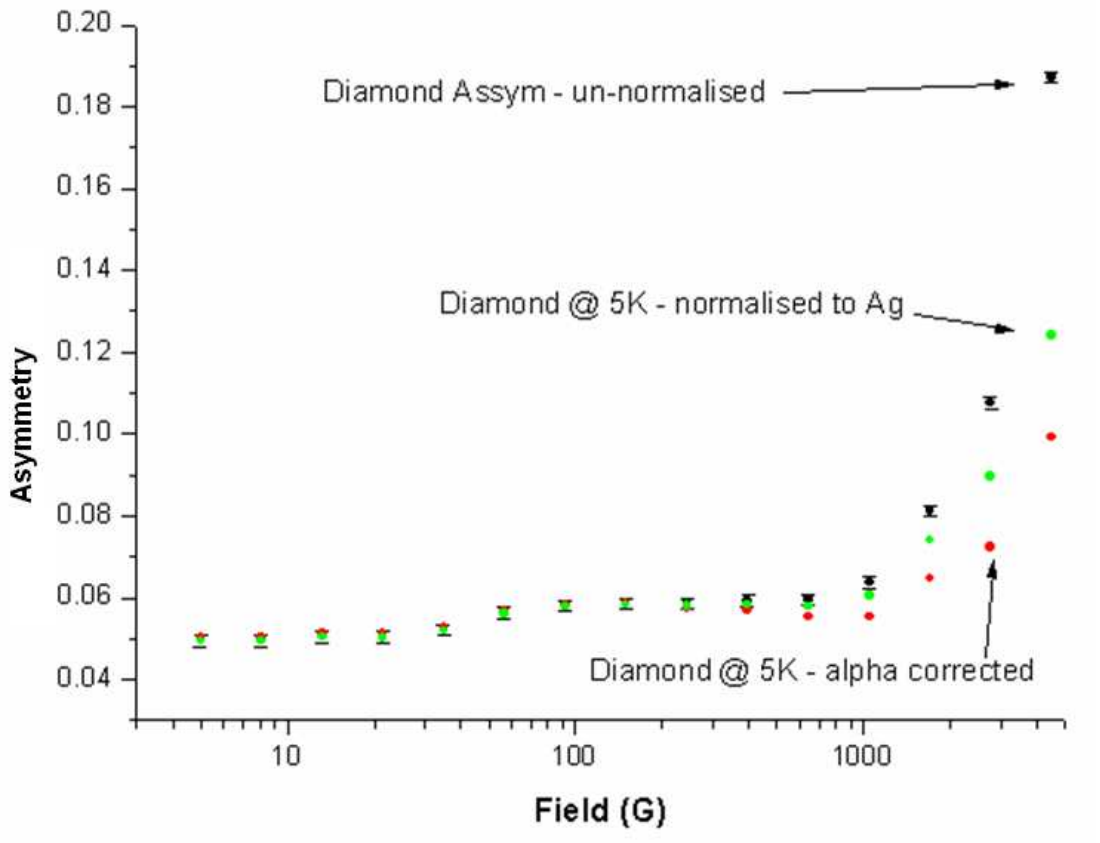

Figure 4.11: Diamond data corrected using a field-dependent alpha value plotted together with normalised (to Ag) and un-normalised diamond data.

4.3.2 Geant4 simulation

Geant4 (for GEometry ANd Tracking) is a C++ toolkit for Monte-Carlo simulation of the passage of particles through matter [195]. It contains information on many physics processes and particles. The physics processes offered cover a comprehensive range, including electromagnetic, hadronic and optical processes, a large set of long-lived particles, materials and elements, over a wide energy range starting from 250 eV to the TeV energy range [195]. For a simple simulation, one just has to define a geometry and the interactions one wants to consider. It has been used in applications in particle physics, nuclear physics, accelerator design, space engineering and medical physics.

The detector geometry : After going through the trigger detector, muons enter an electrostatic lens which accelerates them. A conical lens focuses the beam onto the sample which is mounted either on a cryostat or on another holder. All information about the detector are in the files DetectorConstruction.cc and DetectorConstruction.hh. There are different kinds of volumes which form a hierarchy in the Geant4 detector construction process. They are organised as the creation process of a detector component.

- First, we created an ”experimental hall”: a box of dimensions 150 x 150 x 300 cm with its logical and physical volumes.
- Next, a muon beam tube of inner radius 140 mm, outer radius 170 mm, and height 100 mm was created.
- A ”beam stop” was placed at one end of the muon beam tube so that muons that miss the target (fly-past muons) will stop and decay downstream.
- Rings of Forward and Backward detectors were placed around the muon beam tube and the resultant detector set-up is as shown in Figure 4.12.

The code for the construction of the detector geometry in Figure 4.12 is as shown in Appendix B.

After the decay of muons, positrons are collected in scintillators for data analysis. This is made possible by the *sensitive detector* facility. A sensitive detector is able to store all data about each particle that enters it in a object called *hit*. Sensitive detectors were created for the Forward (Inner, Outer) and Backward (Inner, Outer) detectors.

Generating primary particles : The primary generator action is the class where the user sets up the initial conditions of a new event. In the GeneratePrimaries() method, the new event receives objects called primary particles, which define particle types and

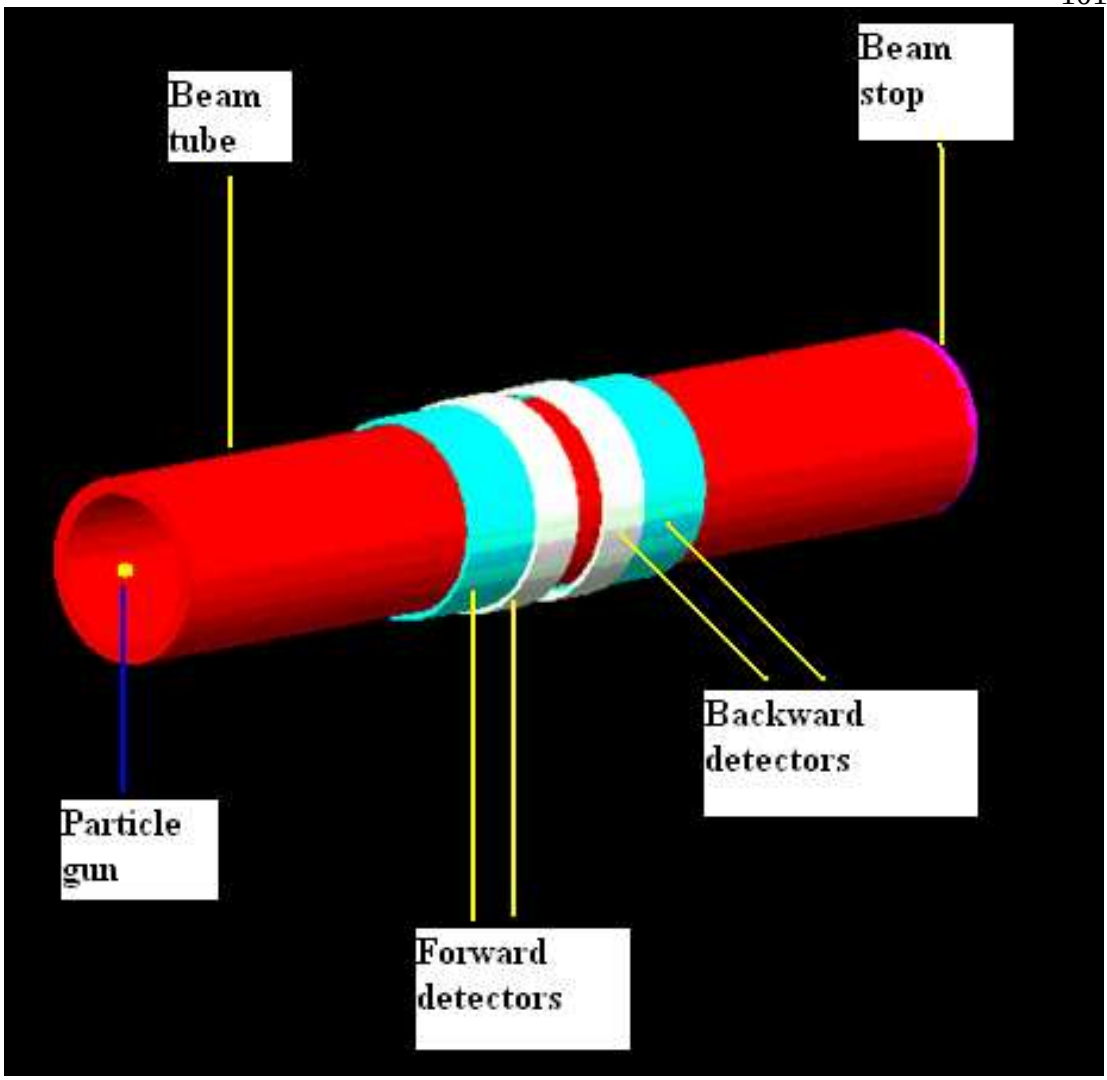

Figure 4.12: A Geant4 generated detector geometry showing the detector rings, muon beam pipe, particle gun, and beam stop.

all the parameters like their positions, momenta, mass, etc. The primary particles can be generated using an object called a particle gun. When one uses a particle gun to generate primary particles, one has to specify the gun position, the number of particles to generate per event, and all the particle parameters.

In this simulation a positive muon of energy 4.0 MeV was generated per event. The muons were implanted into a small diamond sample of area 16 mm^2 and, after the de-

cay of the muons, the positron asymmetry (A) was obtained from the front/back counts difference. The simulation was carried out in zero magnetic field, and therefore the asymmetry could be measured precisely since there would be no precession. In this case,

$$A = \frac{F - B}{F + B} \tag{4.6}$$

where F and B are the total counts in the forward and backward detectors, respectively, according to the muon spin.

Results of the Geant4 simulation : The beam radius was varied from 0.1 - 2.0 cm. When the beam radius is less than or equal to the sample radius, no fly-past muons are expected. In the case of a beam radius larger than the sample radius, the amount of fly-past muons is proportional to the difference between the beam area and the sample area. Figure 4.13 shows how the positron asymmetry varies with the amount of fly-past for one, two and three million muons simulation.

Figure 4.13 shows that there is a decrease in the positron asymmetry as the amount of fly-past muons increases. From equation 4.6, there are two possibilities that can give rise to a reduced asymmetry: a decrease in the forward counts (F) or an increase in the backward counts (B). The simulation was carried out in zero magnetic field and therefore a decrease in F is not expected.

The change in the asymmetries of the individual detector rings with the amount of fly-past muons were compared. The results, summarised in Figure 4.14, show clearly that those detectors measuring a signficant amount of stray counts show a marked reduction in signal asymmetry. Lynch et al. [193] have also made the same observation. This explains why one set of detectors was omitted from the backward group in the data

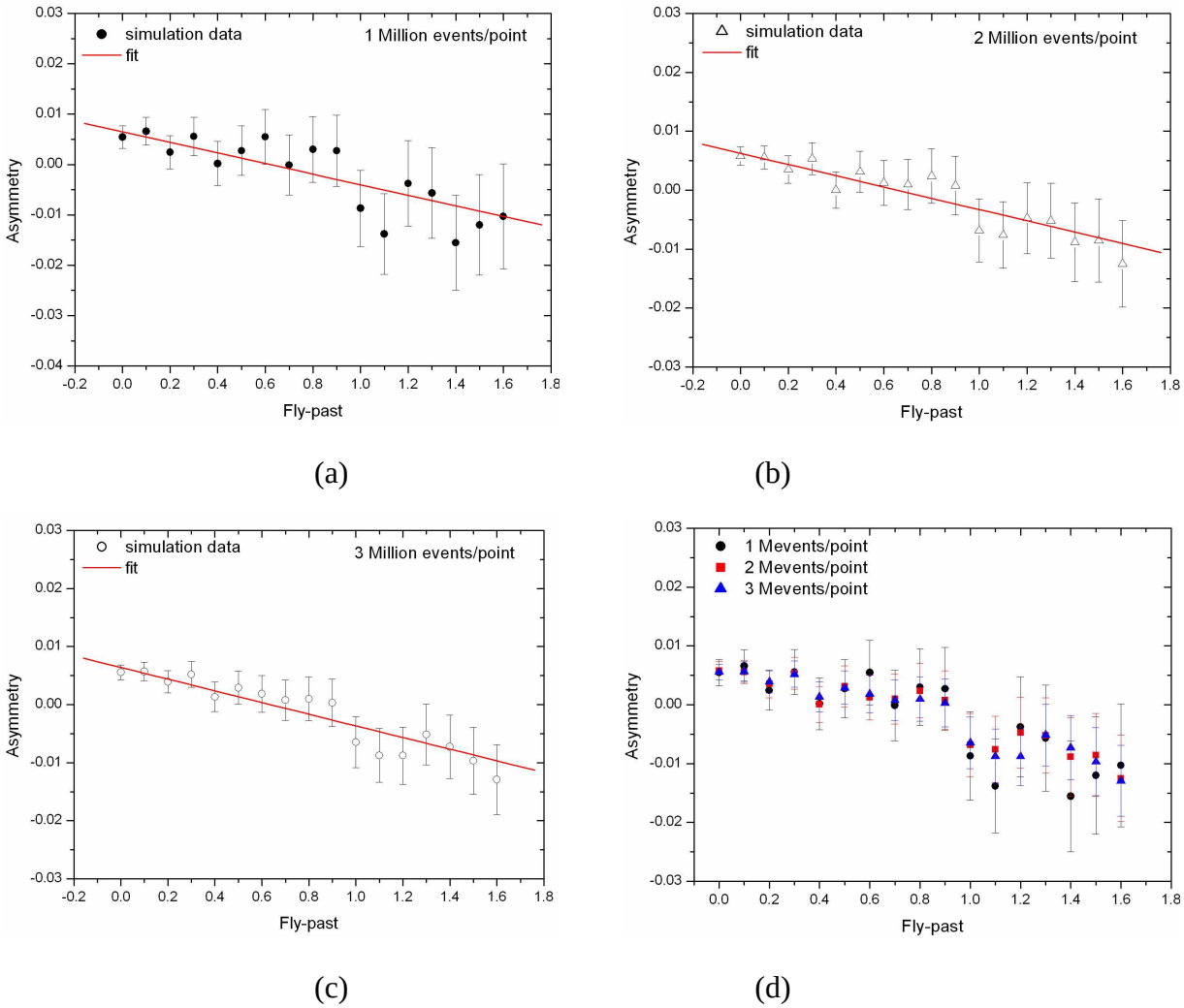

Figure 4.13: Variation of positron asymmetry with fly-past for (a) 1 million, (b) 2 million, and (c) 3 million events per data point. The three graphs are plotted together in (d) for comparison.

analysis (see section 4.4).

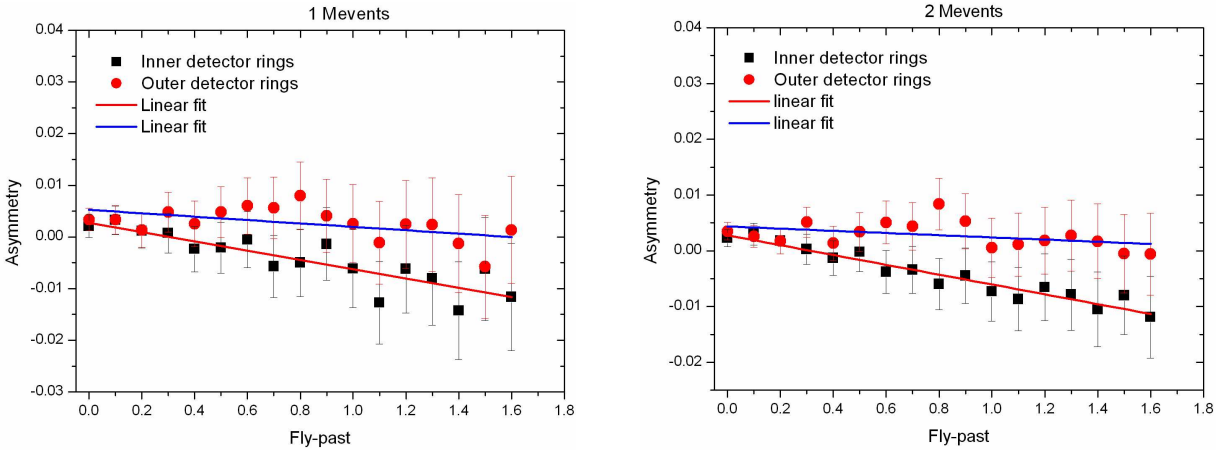

(a) (b)

Figure 4.14: Variation of signal asymmetry with fly-past for the individual detector rings for (a) 1 million events, (b) 2 million events. Note the marked reduction in asymmetry for the inner detector rings.

4.4 Data Analysis Approach

The data was analysed using WiMDA (**Wi**ndows **M**uon **D**ata **A**nalysis) [196], a package for analysing μSR data developed for Microsoft Windows operating systems. The counts measured in each detector are histogrammed as a function of time using a time to digital converter (TDC) and stored in a raw data file; these histograms are later combined in software to form the signal used during data analysis. All μSR histograms are accumulated from one-at-a-time events (except in pulsed mode), so that a large number of isolated events are summed together and it is assumed that this is equivalent to the time distribution that a large instantaneous ensemble would have. To minimise background counts in the data the detectors 18,20,22,...,32 were omitted from the backward group as they appear to be picking up more background counts. In flypast mode one ”ring” of backward detectors picks up more background counts and there is an increase

in total counts in these histograms [193]. This observation has also been confirmed by a Geant4 simulation, as explained in Section 4.3.2.

The data analysis for the longitudinal field measurements was divided into two time zones[1] : 0-2 μs for young muons, and 4-15 μs for old muons, shown in Figure 4.15. First, the value of the correction factor, α, for a particular temperature point was obtained from a fit to a 20 G transverse field (T20) run for the same temperature point. The T20 run allows α and the baseline to be found for the subsequent longitudinal field runs. Alpha (α) and the baseline values were then fixed and the asymmetry for each field point, from 2 - 4500 G, was then obtained from a fit to a longitudinal field spectrum. This procedure was repeated for all the temperature points (300 to 1200 K). Calibration measurements were performed on a silver plate of similar shape to the diamond specimens. The silver plate yields the muon beam asymmetry a_{beam} corresponding to 100 % polarisation. Full asymmetry on a large silver sample in EMU is around 23 %.

To correct for variable α, the true silver asymmetry $a(Ag, 0)$, was first obtained from the zero field silver run, and then the true asymmetry for each measured asymmetry on the sample was obtained from [198]

$$Asymmetry = a(sample, B) - a(Ag, B) + a(Ag, 0) \tag{4.7}$$

where $a(sample, B)$ and $a(Ag, B)$ are the sample and silver asymmetries, respectively, at the same magnetic field B.

To correct for variable asymmetry, the asymmetry from equation 4.7 was divided by

[1] This separation is designed to observe the effect of changing the positron observation period with respect to the muon arrival time [197].

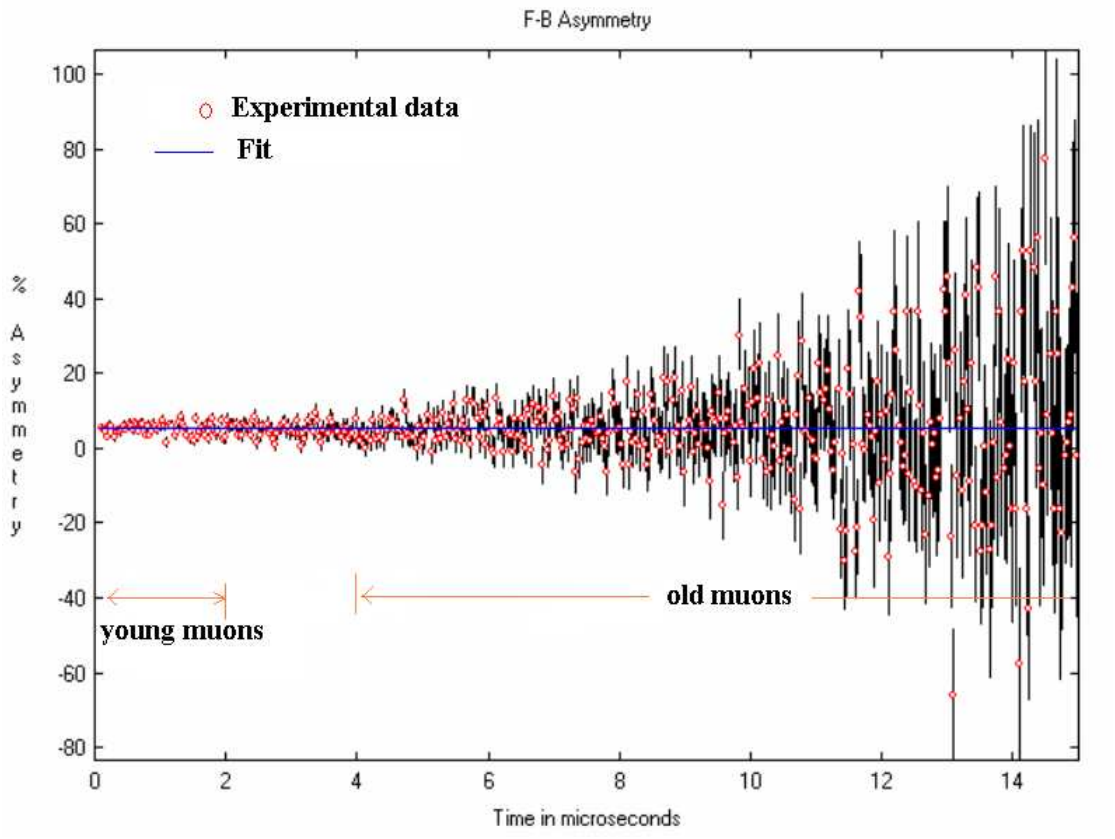

Figure 4.15: An LF histogram collected using the ISIS EMU spectrometer. The time zones for the young and old muons used in this analysis are indicated.

the asymmetry from the silver at the same field, and then multiplied by 23 %. That is,

$$corrected\ asymmetry = \frac{(Asymmetry, B)}{a(Ag, B)} \times 0.23. \qquad (4.8)$$

Chapter 5

Experimental Results of Muon(ium) Studies in Natural Type Ia and Synthetic Type HPHT-IIa Diamond

"There are two possible outcomes: if the result confirms the hypothesis, then you've made a measurement. If the result is contrary to the hypothesis, then you've made a discovery."

Enrico Fermi

5.1 Preliminary Remarks

Here we present the experimental results of muonium studies in natural type Ia and synthetic type HPHT IIa diamond by means of the longitudinal field muon spin relaxation (LF-μSR) and transverse field muon spin rotation (TF-μSR) techniques. The studies in natural type Ia diamond originated from the discovery of Mu_X, a new muonium centre peculiar to nitrogen-rich diamonds with aggregated nitrogen defects [3] and some theoretical calculations that indicated the possibility that Mu_X could be a shallow n-type dopant [4]. This scenario needed to be tested and confirmed experimentally. The experimental results showed that bond-centred muonium (Mu_{BC}) in diamond "ionises" around 1000 K. Different model fits give activation energies between 0.60 and 1.80 eV. This is the first time in this research that the ionization energy of Mu_{BC} in diamond has been determined.

The muonium studies on the low strain pure diamond material grown by the high pressure high temperature (HPHT) synthesis were aimed at illuminating the configuration of unknown states, generally called missing fraction (MF) observed in many previous studies. The experimental results showed the existence of a diamagnetic muon state (μ^+), two paramagnetic muonium states [tetrahedral interstitial (Mu_T) and bond-centred (Mu_{BC})], and MF formed by positive muons implanted into the sample. The absolute fractions of μ^+,Mu_T, Mu_{BC} and MF in the sample were 4, 54, 30 and 12 %, respectively.

Section 5.2 looks at the data reduction and analysis methods in LF-μSR, which was the main experimental technique used in this study. Section 5.3 and Section 5.4 presents the results of the muonium studies on natural type Ia and high-purity synthetic type IIa diamond, respectively.

5.2 The Longitudinal Field Technique - Data Reduction and Analysis

The main experimental technique was the LF-μSR technique. The real value of the longitudinal-field technique is for muonium studies in the presence of static and dynamic random disturbances. A time-differential approach is required to follow the longitudinal spin relaxation of the muon. In a time-differential experiment, repeated measurements are made of the time interval between the entrance of the muon into the sample and the detection of a decay positron in a particular direction. Counts from the detectors are collected in individual 16 ns time channels over periods lasting many muon lifetimes. These data are then grouped together into forward F(t) and backward B(t) counts, and are displayed as a histogram of the forward-backward asymmetry, $a(t)$, given by

$$a(t) = \mathbf{a}P(t) = \left[\frac{F(t) - \alpha B(t)}{F(t) + \alpha B(t)}\right], \tag{5.1}$$

where **a** is the absolute positron asymmetry at the beam energy used [144], P(t) is the polarisation function, and α is an experimental correction factor which compensates for the difference in efficiency between the forward and backward detectors. The correction factor, α, is obtained from a least-χ^2 fit to transverse field data measured in a field of 20 G.

Repolarisation measurements must be made on a timescale that is long compared with the coherent oscillatory evolution. This condition is fulfilled in experiments at a pulsed muon source such as ISIS, where the hyperfine oscillations cannot be resolved. The repolarisation curve for the isotropic Mu_T^0 state, with hyperfine interaction $A\mathbf{I}\cdot\mathbf{S}$ is monotonic and has the analytical form

$$P(x) = \frac{1}{2} + \frac{1}{2}\left[\frac{x^2}{(1+x^2)}\right] \tag{5.2}$$

The repolarisation function arises from equal probabilities that the muon is associated with electron spins parallel and anti-parallel to its own spin. The former gives the field-independent fraction $\frac{1}{2}$ and the latter evolves as a high frequency oscillation between eigenstates. Only the time average of this oscillatory component is detected and this reflects the decoupling of the hyperfine interaction by the applied field. The theoretical repolarisation curve for Mu_T^0 in diamond is plotted in figure 5.1. When the applied field is comparable to the hyperfine field, the electron and muon become decoupled and the polarisation rises to unity.

For the anisotropic, but axially symmetric, Mu_{BC}^0 state, the hyperfine interaction takes the form $A_{\|}I_zS_z + A_{\perp}(I_xS_x + I_yS_y)$, where z defines the axis of symmetry. The repolarisation curve for Mu_{BC}^0 depends on the angle θ between this axis and the applied field. The theoretical repolarisation curves for Mu_{BC}^0 in diamond are plotted in figure 5.2.

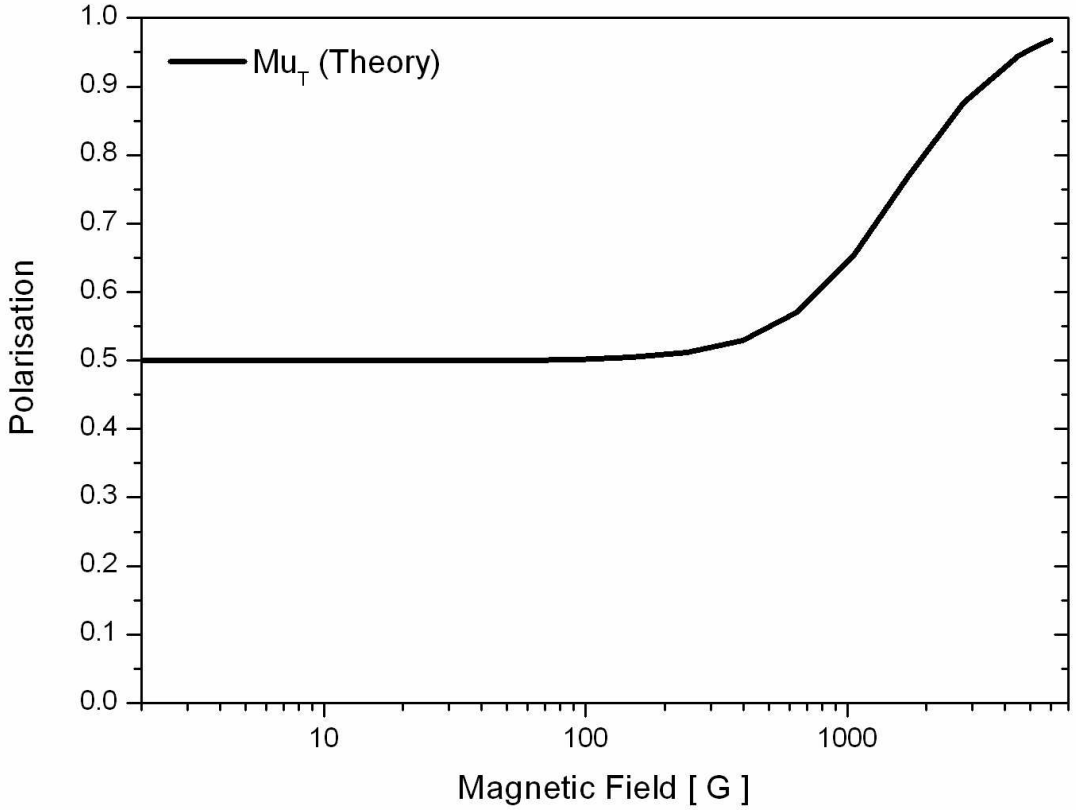

Figure 5.1: Theoretically simulated polarisation for the Mu_T state in diamond, in longitudinal field ranging from 0 to 6000 G. The hyperfine constant of Mu_T in diamond is given in Table 2.4.

The characteristic features of the Mu^0_{BC} theoretical curves are: the polarisation, $P(t) = 1/6$ at low fields (B $\leq$ 10 G) and it increases gradually at around $B = 50G$. There is a plateau around $B = 300 - 1500G$ and a dip at about 6 000 G, and then the polarisation eventually reaches 1.0 at very high fields.

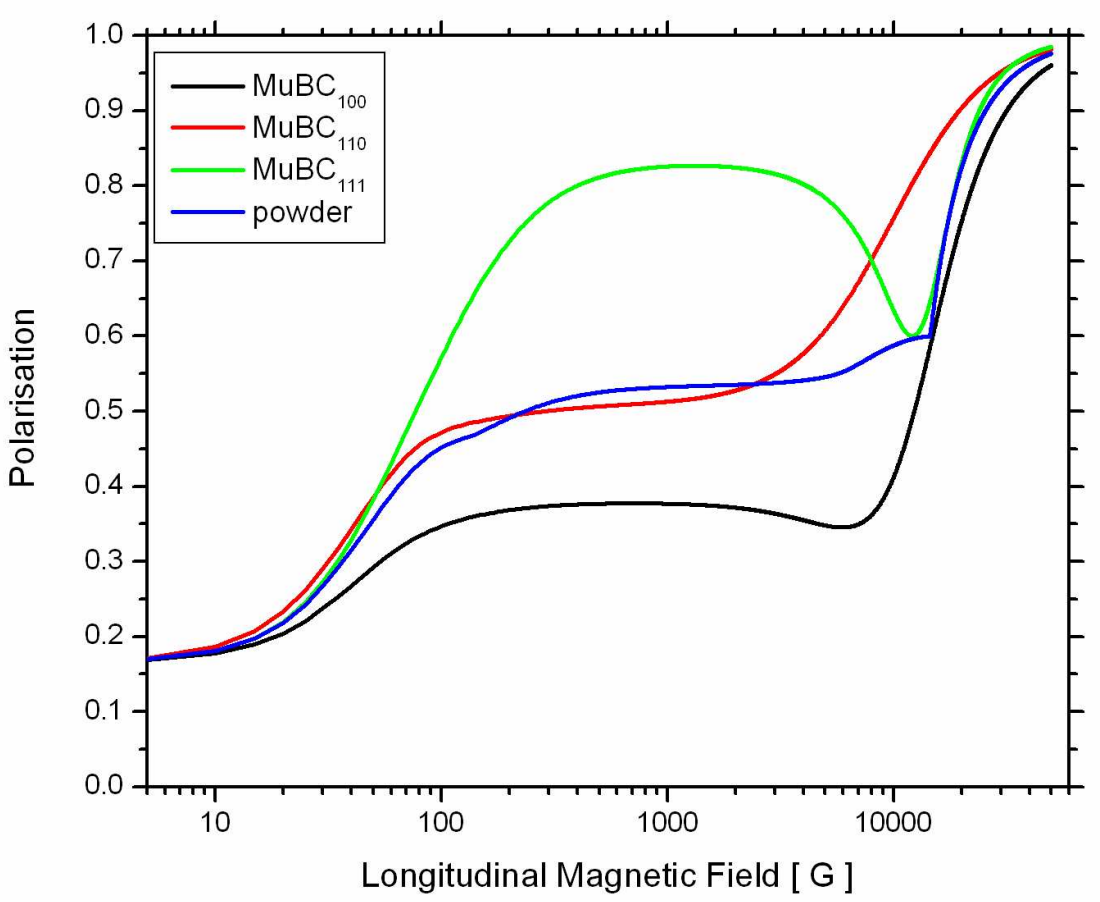

Figure 5.2: Theoretical polarisations for the Mu^0_{BC} state in a diamond (simulations due to James Lord [198]). The polarisation is orientation-dependent. The hyperfine constants of Mu^0_{BC} in diamond are given in Table 2.4.

5.3 Thermal Ionisation of Muonium in Natural Type Ia Diamond

5.3.1 Results From Longitudinal Field Measurements

Here we present the experimental results that were obtained in natural type Ia diamond using the longitudinal field muon spin relaxation (LF-μSR) method. These results were obtained by measuring the spin polarisation of the muon ensemble. Our main interest here was to investigate the thermal ionization of Mu^0_{BC}, and possibly Mu_X. The FTIR characterisations (see Chapter 3) have shown that the natural type Ia diamonds used in this study had few aggregated nitrogen defects and therefore we expected little Mu_X in the samples. Figures 5.3 - 5.4 show some of LF histograms collected using the ISIS EMU spectrometer.

Inorder to explore the thermal ionization of the muonium states we conducted temper-

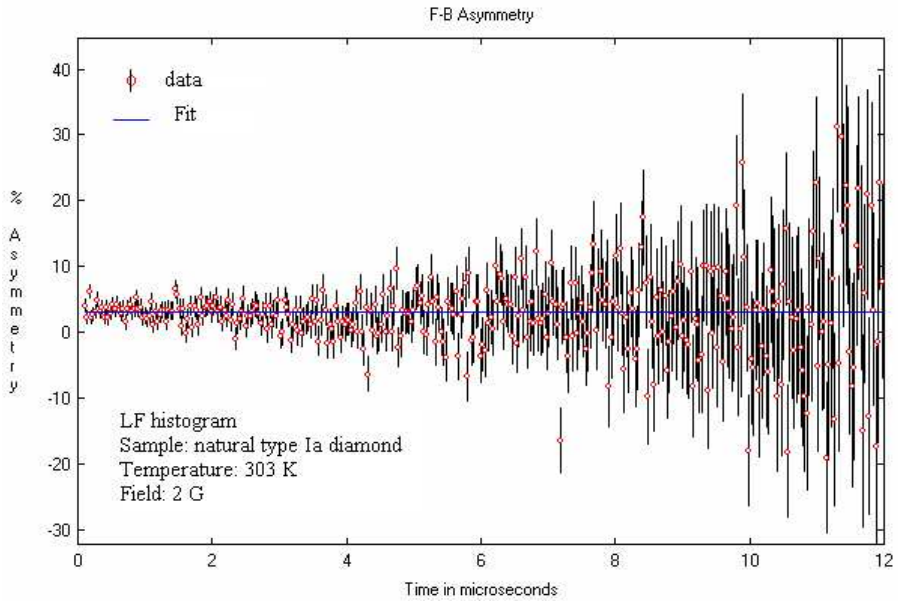

Figure 5.3: An LF histogram collected using the ISIS EMU spectrometer at an applied field of 2 G. The data are for natural type Ia diamond at 303 K.

ature dependent field scans from 300 to 1200 K. Figure 5.5 compares our repolarisation data at almost the same temperature with those of Machi et al. [124], shown in Fig-

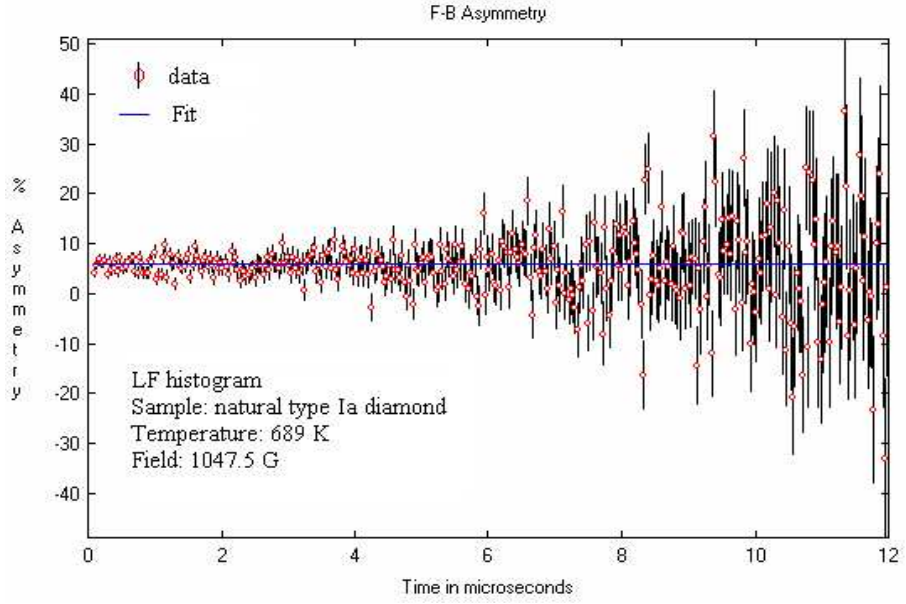

Figure 5.4: An LF histogram collected using the ISIS EMU spectrometer at an applied field of 1047.5 G. The data are for natural type Ia diamond at 689 K.

ure 5.6, in which the Mu_X was discovered in natural type Ia diamond.

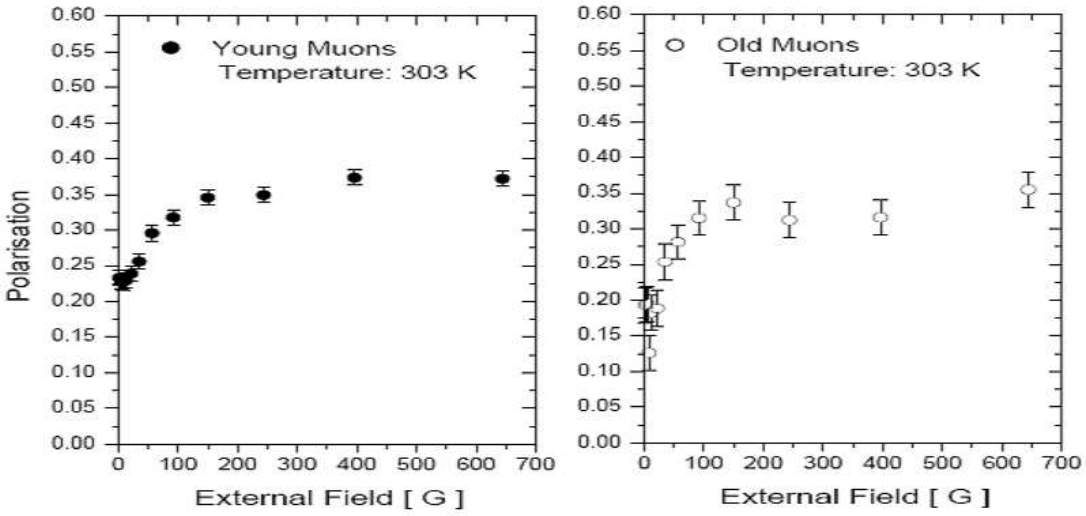

Figure 5.5: Longitudinal field repolarisation curves for young and old muons in the single crystal natural type Ia diamonds used in this study at 303 K. It was below these temperatures when Machi et al. [124] discovered Mu_X in natural type Ia single crystal diamonds with aggregated nitrogen defects, and their repolarisation curves are reproduced in Figure 5.6 for comparison.

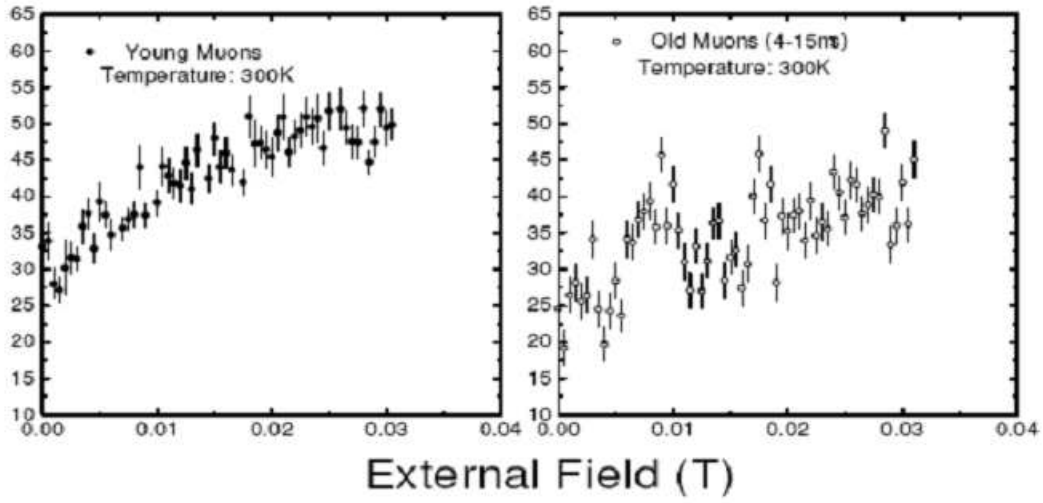

Figure 5.6: Longitudinal field repolarisation curves for young and old muons in single crystal natural type Ia diamond at 300 K. These data are from Mach et al. [124] who discovered Mu_X in single crystal natural type Ia diamonds with aggregated nitrogen defects.

The asymmetry parameters depend on several experimental variables including the polarisation of the muon beam; the size and solid angle subtended by the detectors; the amount of positron degrader used to enhance the effective positron anisotropy; plus geometrical factors associated with the shape, thickness, density and positioning of the sample. In order to eliminate these individual variations, an internal calibration with metallic silver was done so that fractional, or normalised, yields could be quoted rather than measured asymmetries. Metallic silver always seems to show all incident muons as diamagnetic states and it has become common practice to use it as reference material and to equate the value of A_D measured with silver with A_{max} for the particular experimental set-up used. Thus, the asymmetry spectra were normalised with the full asymmetry of the μSR system (0.23 for the EMU spectrometer), as measured with a silver sample and the repolarisation curves in Figures 5.7 - 5.8 were obtained. There were no significant differences observed between young and old muons up to about 1000 K.

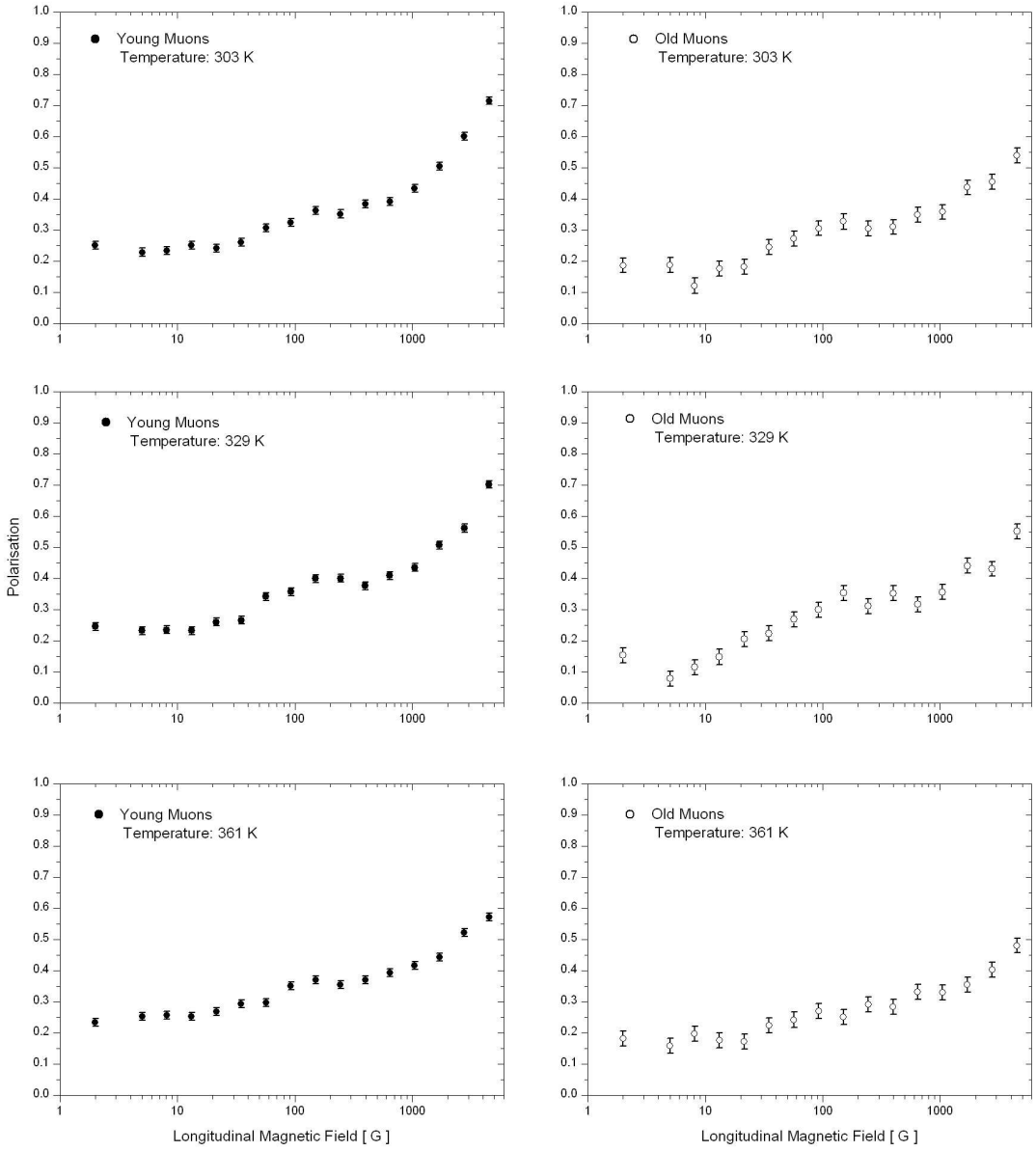

Figure 5.7: Longitudinal field repolarisation curves for young and old muons in the single crystal natural type Ia diamonds used in this study, in the temperature range 303-361 K and in the magnetic field range 2-4500 G. There were no significant differences observed between young and old muons in this temperature regime. The same trend was observed up to about 1000 K.

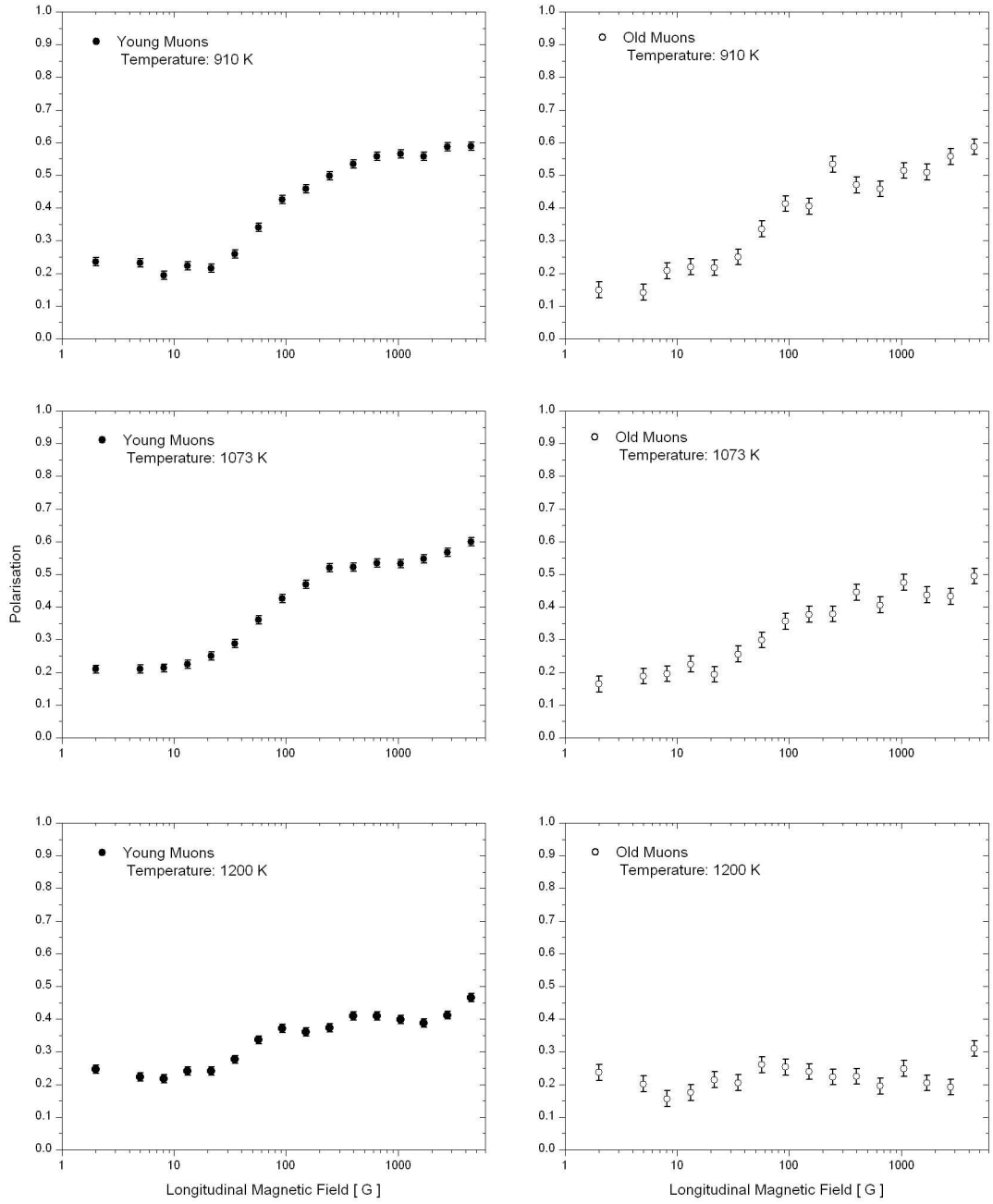

Figure 5.8: Longitudinal field repolarisation curves for young and old muons in the temperature range 910-1200 K. Note the differences between young and old muons above 1000 K. This difference between young and old muons beyond 1000 K is due to the spin relaxation.

Assuming that the total polarisation is a sum over all possible muonium states, we have

$$P_T(B) = [F_d + F_{MuT}P_{MuT}(B) + F_{MuBC}P_{MuBC}(B) + F_{MuX}P_{MuX}(B)]\,, \qquad (5.3)$$

where F_d, F_{MuT}, F_{MuBC} and F_{MuX} are the fractional yields for μ^+, Mu_T^0, Mu_{BC}^0, Mu_X, respectively. Equation 5.3 is determined by eight parameters, which are the four muonium fractions F_d, F_{MuT}, F_{MuBC}, and F_{MuX} and the four hyperfine (hf) constants of the three paramagnetic centres. The hf constants can be understood by considering the spin Hamiltonian of the axially symmetric centre. This is given by[32]

$$\mathbf{H} = A_\perp(I_x S_x + I_y S_y) + A_\parallel I_z S_z - H_{zeeman}, \qquad (5.4)$$

where $A_\perp$ and $A_\parallel$ are the non-zero elements of the hyperfine tensor

$$\mathbf{A} = \begin{bmatrix} A_{\perp MuT} & & & 0 \\ & A_{\perp MuBC} & & \\ & & A_{\parallel MuBC} & \\ 0 & & & A_{rho\ MuX} \end{bmatrix}. \qquad (5.5)$$

where $A_{rho\ MuX}$ is the hyperfine constant of Mu_X at a rhombohedral site [124].

Instead of $A_\perp$ and $A_\parallel$ the alternative quantities A_{iso} and $B_{dipolar}$ can be used to define the anisotropic hyperfine tensor. These are related to $A_\perp$ and $A_\parallel$ by

$$A_{iso} = \frac{1}{3}(A_\parallel + 2A_\perp) \qquad (5.6)$$

$$B_{dipolar} = \frac{1}{3}(A_\parallel - A_\perp) \qquad (5.7)$$

For Mu_T, $A_{\parallel}$ is equal to $A_{\perp}$ and therefore from Equation 5.6 $A_{iso} = A_{\parallel} = A_{\perp}$ (with $B_{dipolar}$ = 0). Thus there is a total of four hf constants describing the three paramagnetic centres in equation 5.3. Thus, knowing the four hf constants describing the three paramagnetic centres, equation 5.3 can be used to determine the muonium fractions by a numerical fitting technique[199].

For the sample investigated, no Mu_T was observed in 2 G transverse field (T2) above 300 K (see Figure 5.9). We suspect that the Mu_T was converting rapidly to the Mu_{BC} state. This would not appear in the T2 measurement but could still contribute to the rapid rise in asymmetry at the high field end of the repolarisation curves. The prompt diamagnetic muon state was extracted by a low transverse field (20 G) measurement (see section 5.3.2). Furthermore, there was no evidence of the trapping of the mobile Mu_T species to form Mu_X presumably because the transition to Mu_{BC} competes effectively with trapping at nitrogen aggregates above room temperature, and this allowed the analysis to concentrate on F_{MuBC}.

The natural type Ia diamond samples were cut along [111] direction so that one Mu_{BC} axis was parallel to the field and the other three were at an angle of 70.5 ° to the field. Hence, the axis parallel to the field has the analytic form

$$P_0(t) = \frac{1}{2} + \frac{1}{2}\left[\frac{x^2}{1+x^2}\right] \tag{5.8}$$

where $x = \frac{(\gamma_e+\gamma_\mu)H}{A_{eff}}$ with effective hyperfine constant $A_{eff} = |A - \frac{D}{2}|$. γ_e and γ_μ are the electron and muon gyromagnetic ratios. For diamond, A = -206 MHz and D = +374 MHz. For the three Mu_{BC} axes at angle 70.5 ° to the field, the empirical function can be described well by the sum of three Lorentzians [198] (see Figure 5.10):

$$P_{70.5}(t) = \frac{a_1 w_1}{w_1^2 + (x-b_1)^2} + \frac{a_1 w_1}{w_1^2 + (x+b_1)^2} + \frac{a_0 w_0}{w_0^2 + x^2} + 1 \tag{5.9}$$

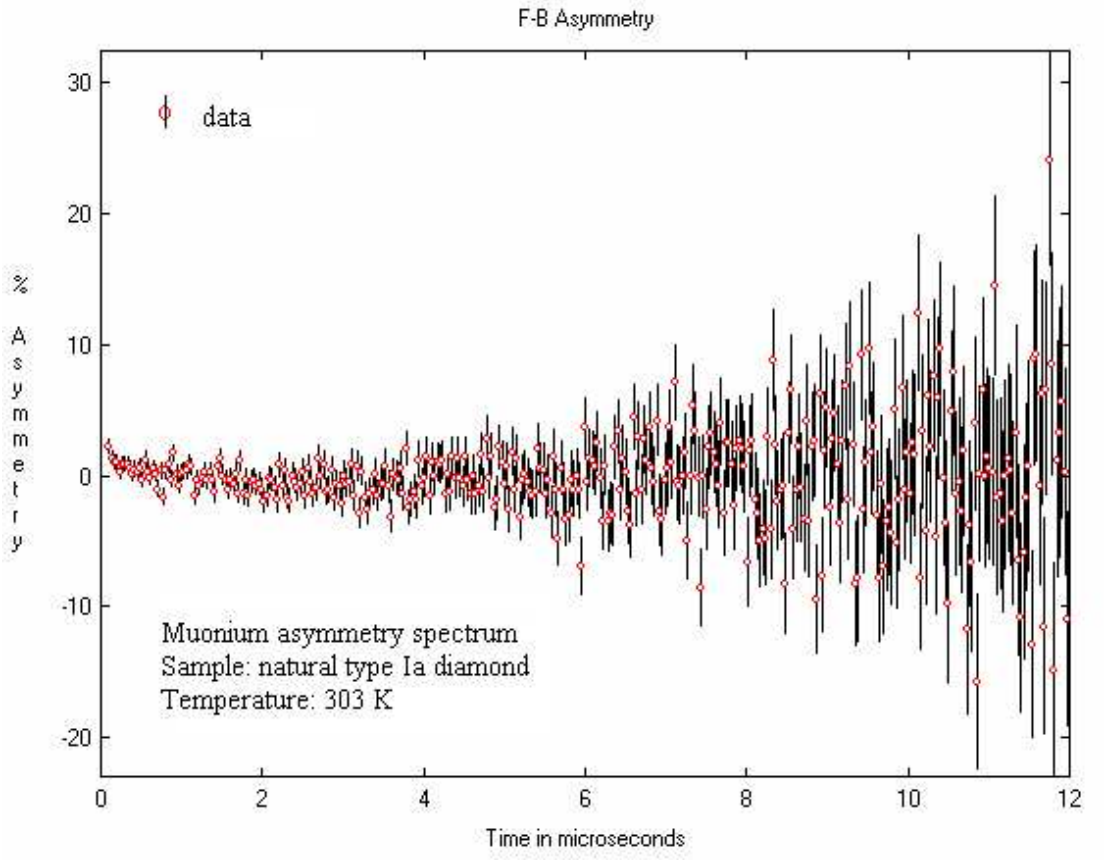

Figure 5.9: A TF histogram collected using the ISIS EMU spectrometer at an applied field of 2 G. There are no oscillations in the histogram. The data, which are for natural type Ia diamond at 303 K show that tetrahedral interstitial muonium (Mu_T) was relaxing rapidly in the sample at this temperature.

where x = field in Gauss and a_0, a_1, b_1, w_0, w_1 are the theoretical fit parameters, related to A and D. The total Mu_{BC} polarisation is then a weighted sum of the two expressions in equations 5.8 and 5.9. That is

$$P_{MuBC}(t) = 1/4\ P_0(t) + 3/4\ P_{70.5}(t), \tag{5.10}$$

so that

$$P(t) = P_{MuBC}(t) + Background. \tag{5.11}$$

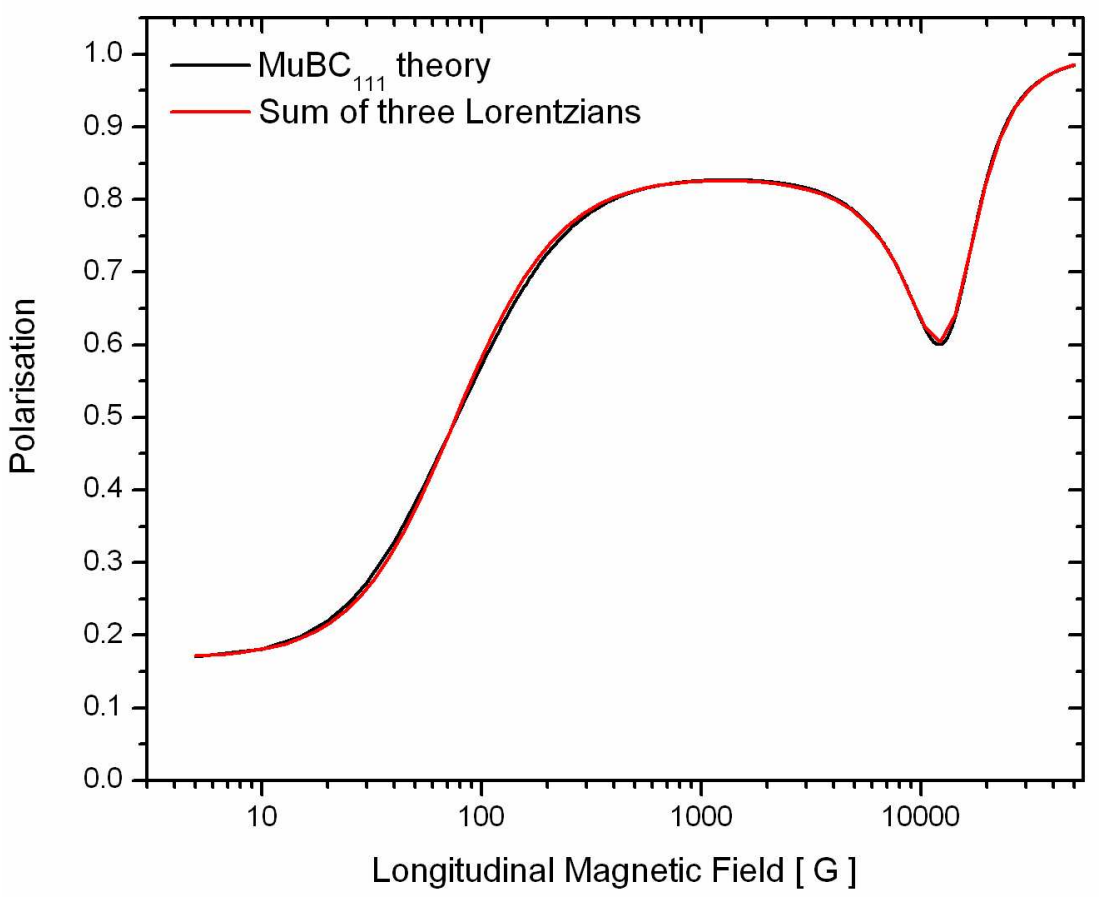

Figure 5.10: Mu_{BC} [111] theory fitted with the sum of three Lorentzians to show how good a job it does replicating the full simulation.

The polarisation data in Figures 5.7 - 5.8 were fitted from 2 - 1000 G with equation 5.11 to extract F_{MuBC} and the background, F_d. The rationale for fitting from 2 - 1000 G was that there are changes in asymmetry/alpha observed in fly-past mode at high fields. Furthermore, the main repolarisation information is, in any case, in this 10 - 1000 G range, as shown in Figure 5.2, for the orientation chosen. The fitted curves are shown in Figures 5.11 - 5.15. The extracted F_{MuBC} values are tabulated in Table 5.1 and plotted in Figure 5.16.

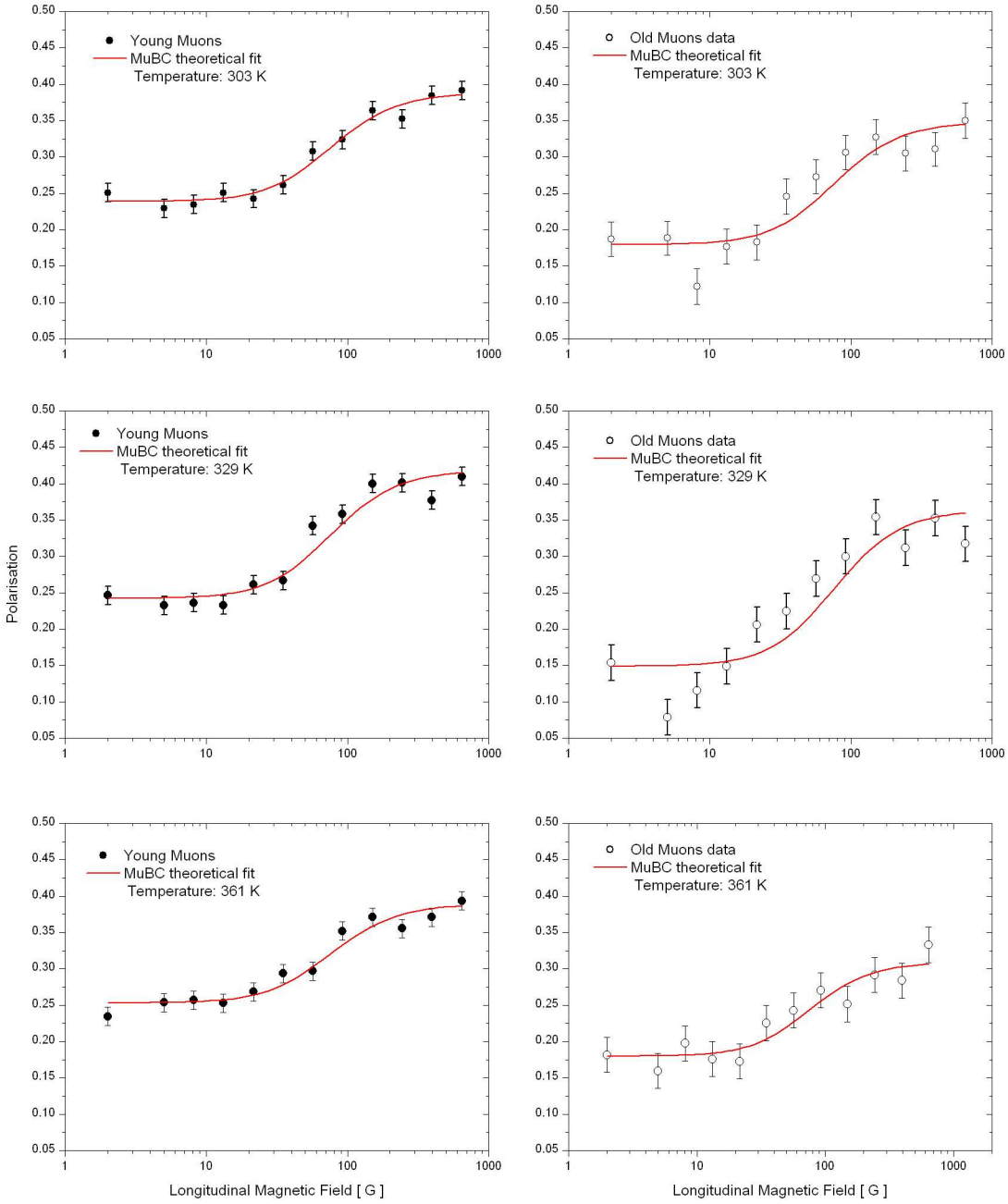

Figure 5.11: Mu_{BC} theoretical fitting to the data in the magnetic field range 2 - 1000 G. These data are for single crystal natural type Ia diamond from 303 - 361 K.

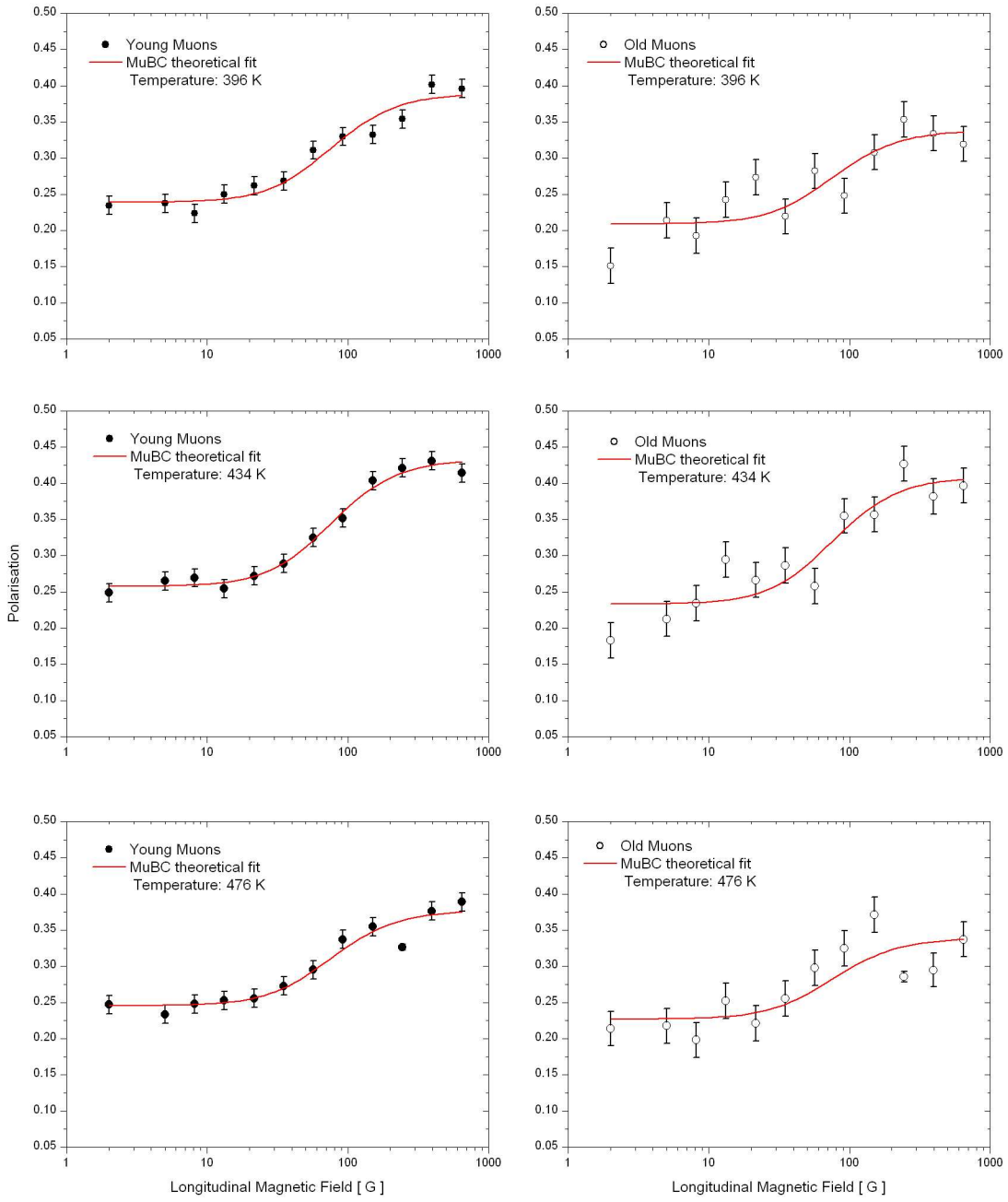

Figure 5.12: Mu_{BC} theoretical fitting to the data in the magnetic field range 2 - 1000 G. These data are for single crystal natural type Ia diamond from 396 - 476 K.

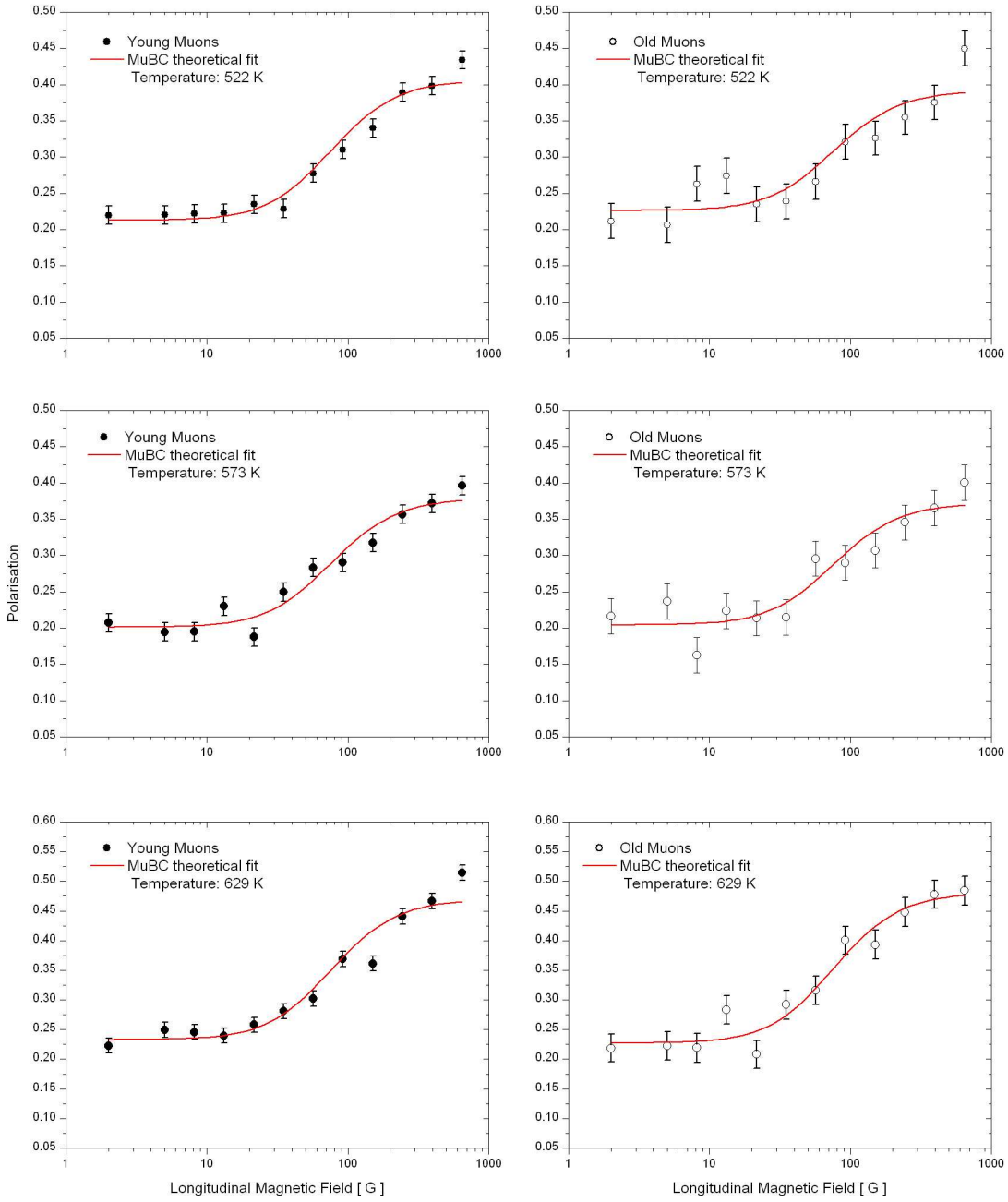

Figure 5.13: Mu_{BC} theoretical fitting to the data in the magnetic field range 2 - 1000 G. These data are for single crystal natural type Ia diamond from 522 - 629 K.

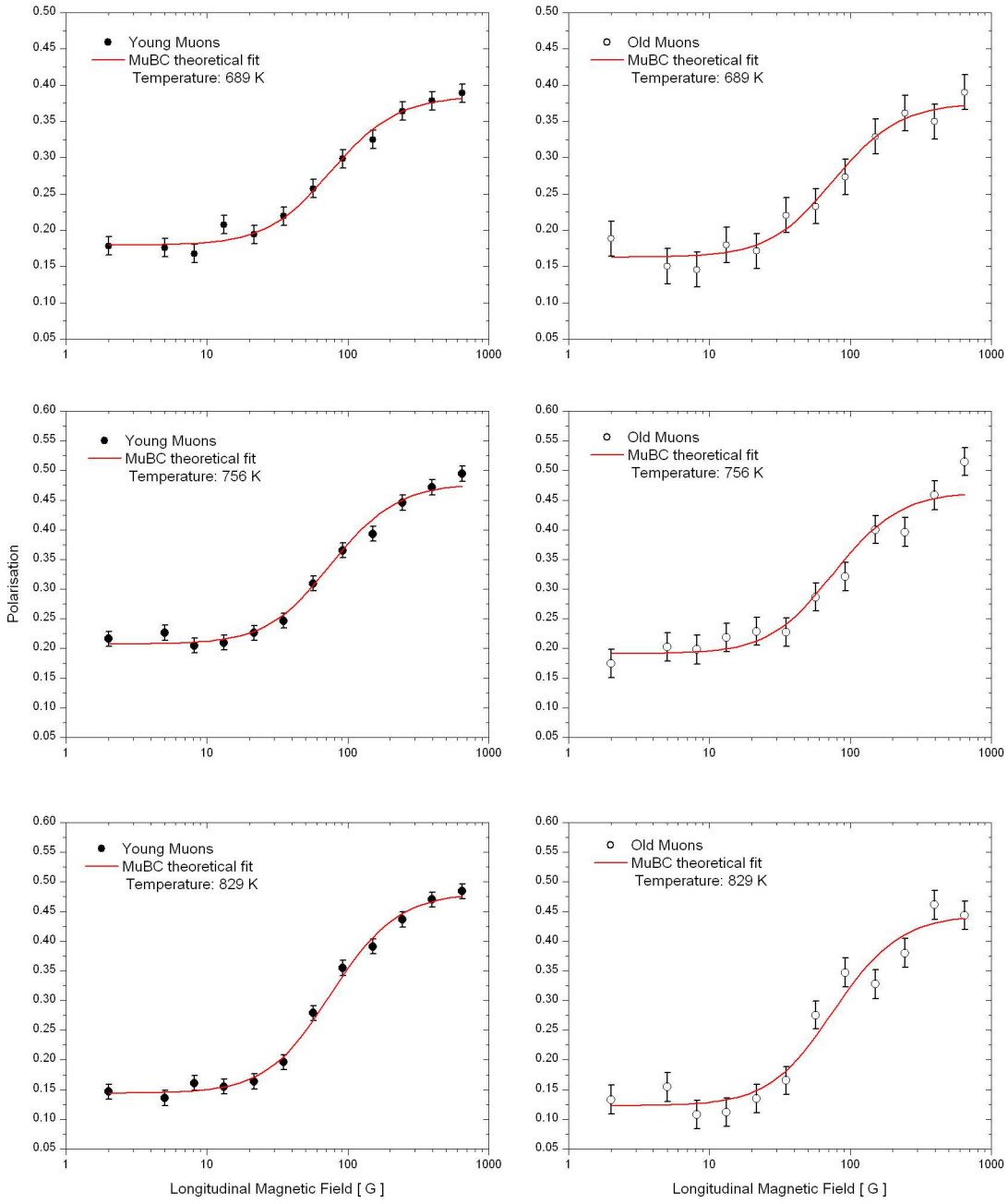

Figure 5.14: Mu_{BC} theoretical fitting to the data in the magnetic field range 2 - 1000 G. These data are for single crystal natural type Ia diamond from 689 - 829 K.

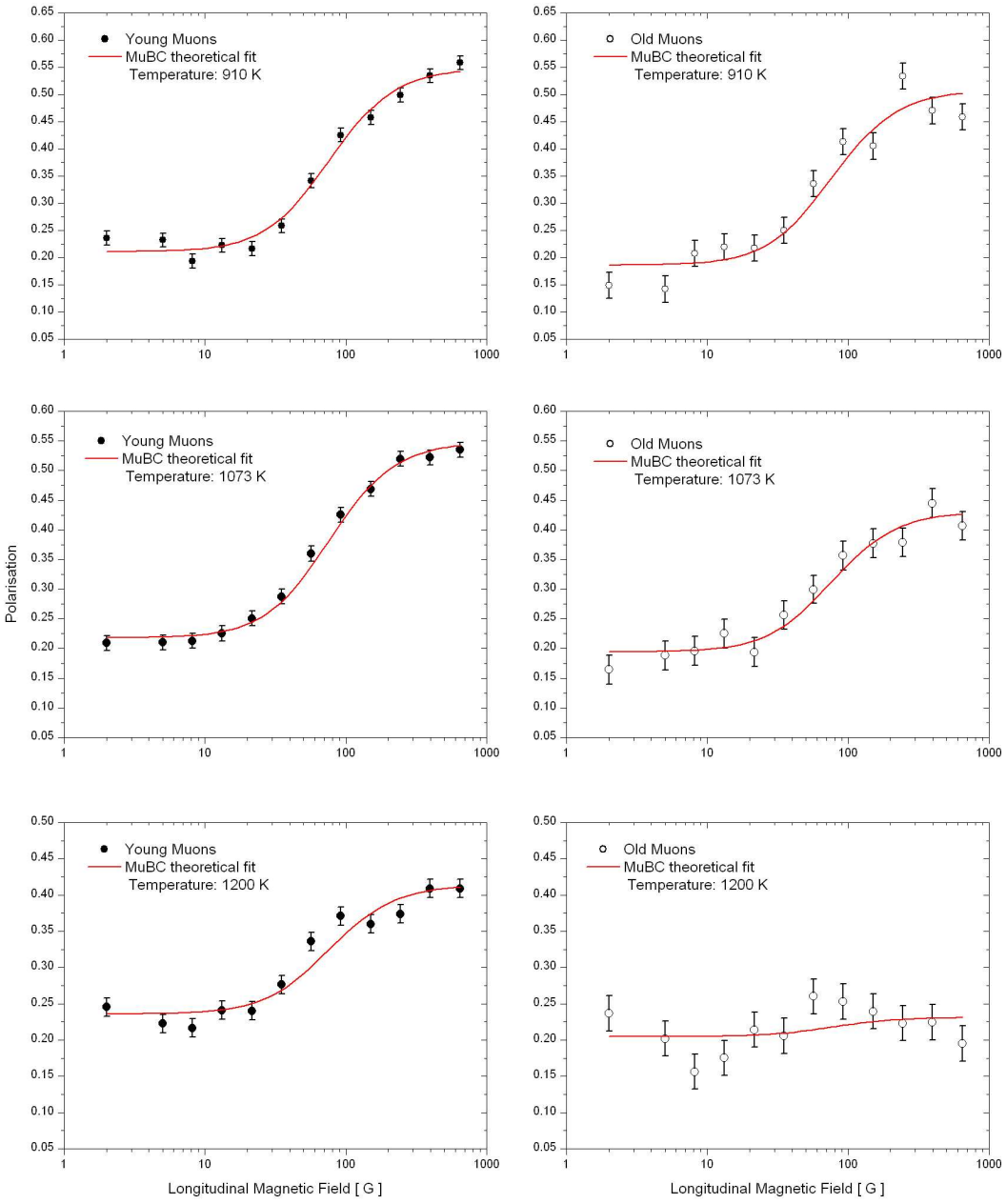

Figure 5.15: Mu_{BC} theoretical fitting to the data in the magnetic field range 2 - 1000 G. These data are for single crystal natural type Ia diamond from 910 - 1200 K.

Table 5.1: F_{MuBC} and F_d fractions in natural type Ia diamond samples determined by fitting to equation 5.11.

Temperature	Young Muons		Old Muons	
(K)	F_{MuBC}	F_d	F_{MuBC}	F_d
303.15	0.23	0.20	0.24	0.14
329.20	0.27	0.20	0.31	0.10
361.06	0.21	0.22	0.18	0.15
396.00	0.23	0.20	0.18	0.18
434.33	0.26	0.21	0.25	0.19
476.37	0.20	0.21	0.15	0.20
522.48	0.29	0.16	0.23	0.19
573.05	0.27	0.16	0.24	0.17
628.53	0.36	0.17	0.37	0.17
689.37	0.31	0.13	0.31	0.11
756.10	0.41	0.14	0.40	0.13
829.30	0.51	0.06	0.47	0.04
909.58	0.51	0.13	0.47	0.11
1073.15	0.50	0.13	0.34	0.14
1200.15	0.27	0.19	0.03	0.20

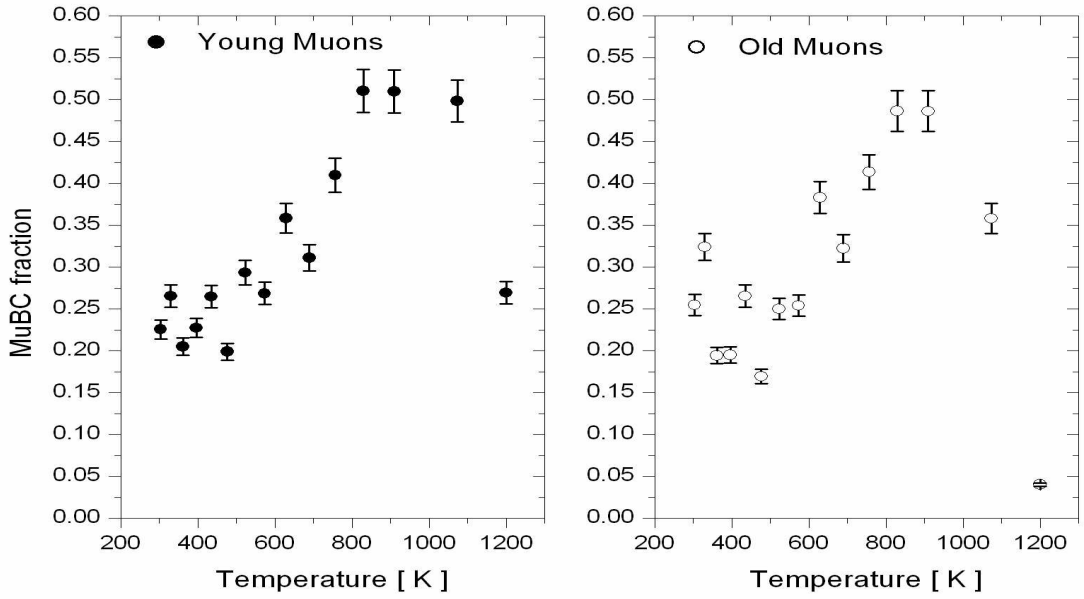

Figure 5.16: Temperature dependence of the Mu_{BC} fractions in (a) young and (b) old muons obtained by theoretical fitting to equation 5.11. There is a decrease in the Mu_{BC} populations above 1 000 K. These data are for natural type Ia single crystal diamond.

5.3.2 Results From Transverse Field Measurements

Promptly formed Mu_T and Mu_D are easily observable in transverse fields of 2 and 20 G, respectively. Prompt Mu_T was observed to relax rapidly (see Figure 5.9) forming Mu_{BC}. Figures 5.17 - 5.20 show the Mu_D spectra at various temperatures in the natural type Ia diamond samples used in this study.

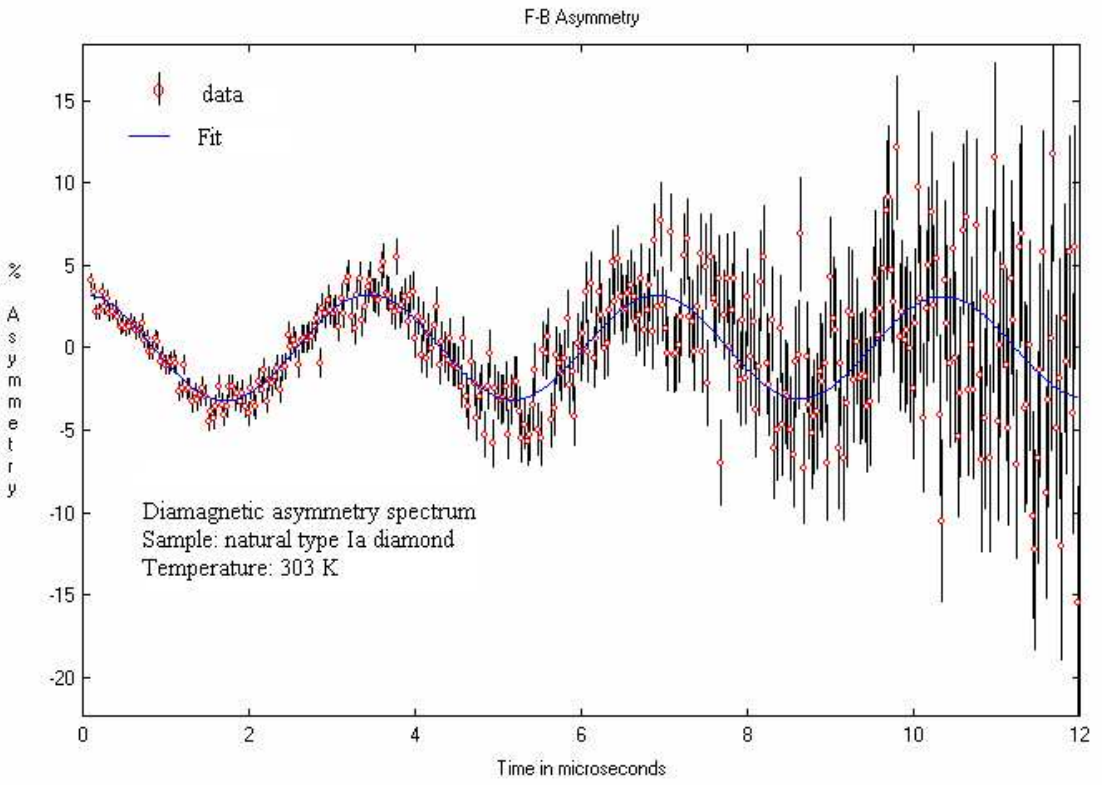

Figure 5.17: A TF histogram collected using the ISIS EMU spectrometer at an applied field of 20 G. The oscillations in the signal are due to the precession of the muon spin in the transverse field. The data, which are for natural type Ia diamond at 303 K, were used to determine both the alpha value as well as the promptly formed diamagnetic fraction for the sample.

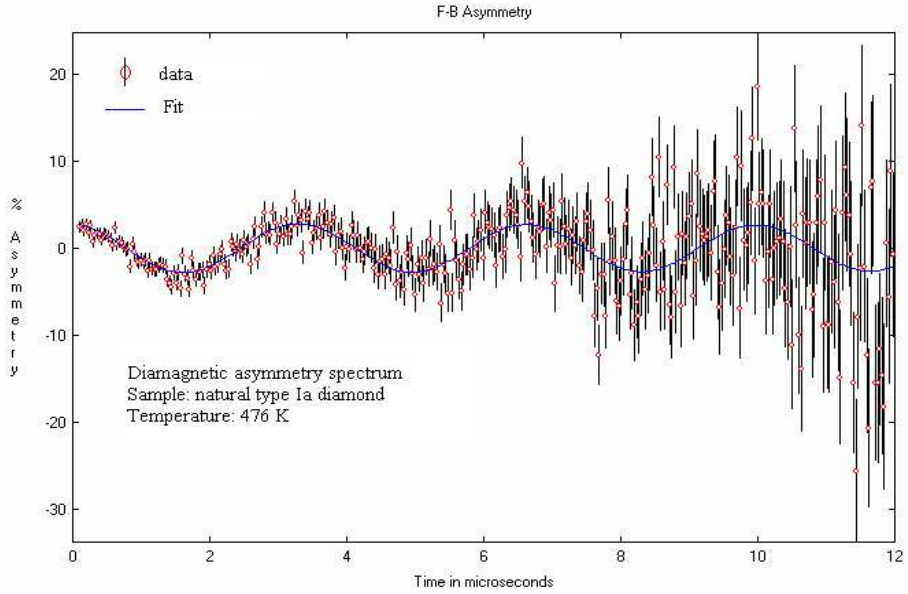

Figure 5.18: A TF histogram collected using the ISIS EMU spectrometer at an applied field of 20 G. The oscillations in the signal are due to the precession of the muon spin in the transverse field. The data, which are for natural type Ia diamond at 476 K, were used to determine both the alpha value as well as the promptly formed diamagnetic fraction for the sample.

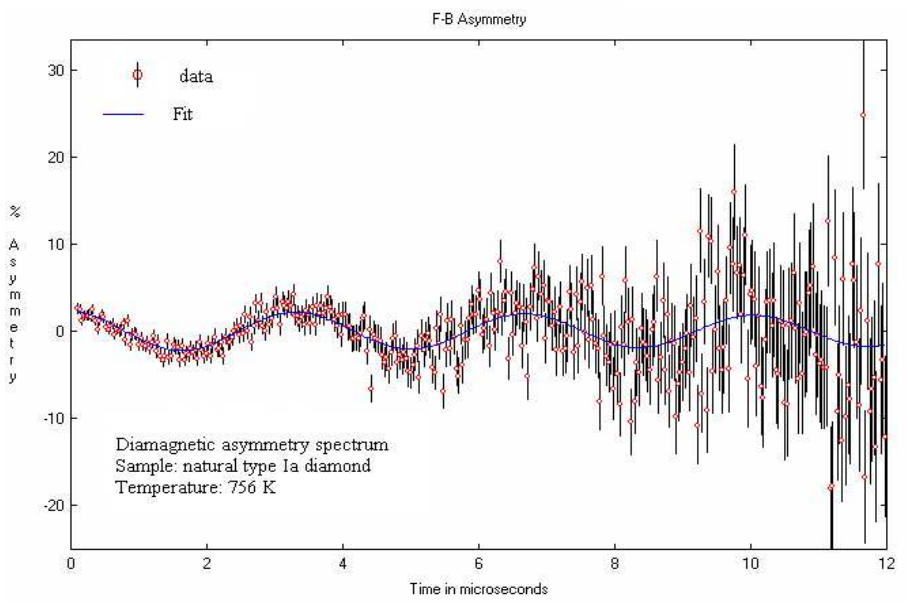

Figure 5.19: A TF histogram collected using the ISIS EMU spectrometer at an applied field of 20 G. The oscillations in the signal are due to the precession of the muon spin in the transverse field. The data, which are for natural type Ia diamond at 756 K, were used to determine both the alpha value as well as the promptly formed diamagnetic fraction for the sample.

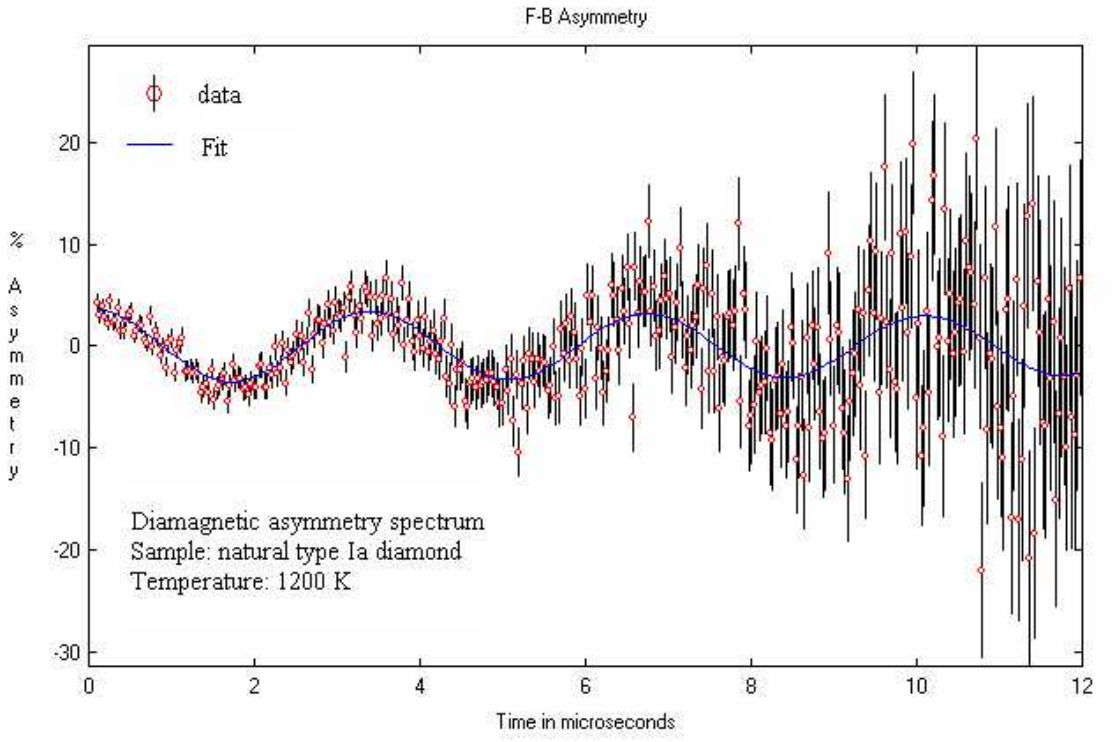

Figure 5.20: A TF histogram collected using the ISIS EMU spectrometer at an applied field of 20 G. The oscillations in the signal are due to the precession of the muon spin in the transverse field. The data, which are for natural type Ia diamond at 1200 K, were used to determine both the alpha value as well as the promptly formed diamagnetic fraction for the sample.

In order to estimate the diamagnetic fraction in the sample the asymmetries from the TF histograms were normalised, after correcting for variable background and variable asymmetry, to the full asymmetry of the MuSR system as measured with a silver sample, and the results obtained are as indicated in Table 5.2 and plotted in Figure 5.21 together with the corresponding spin relaxation rate.

Table 5.2: Prompt diamagnetic fractions in natural type Ia diamond samples determined by fitting to T20 histograms

Temperature (K)	Prompt Mu_D
303.15	0.20
329.15	0.22
361.06	0.20
396.00	0.20
434.33	0.21
476.37	0.21
522.48	0.21
573.05	0.19
628.53	0.19
689.37	0.21
756.10	0.18
829.30	0.24
909.58	0.18
1073.15	0.22
1200.15	0.28

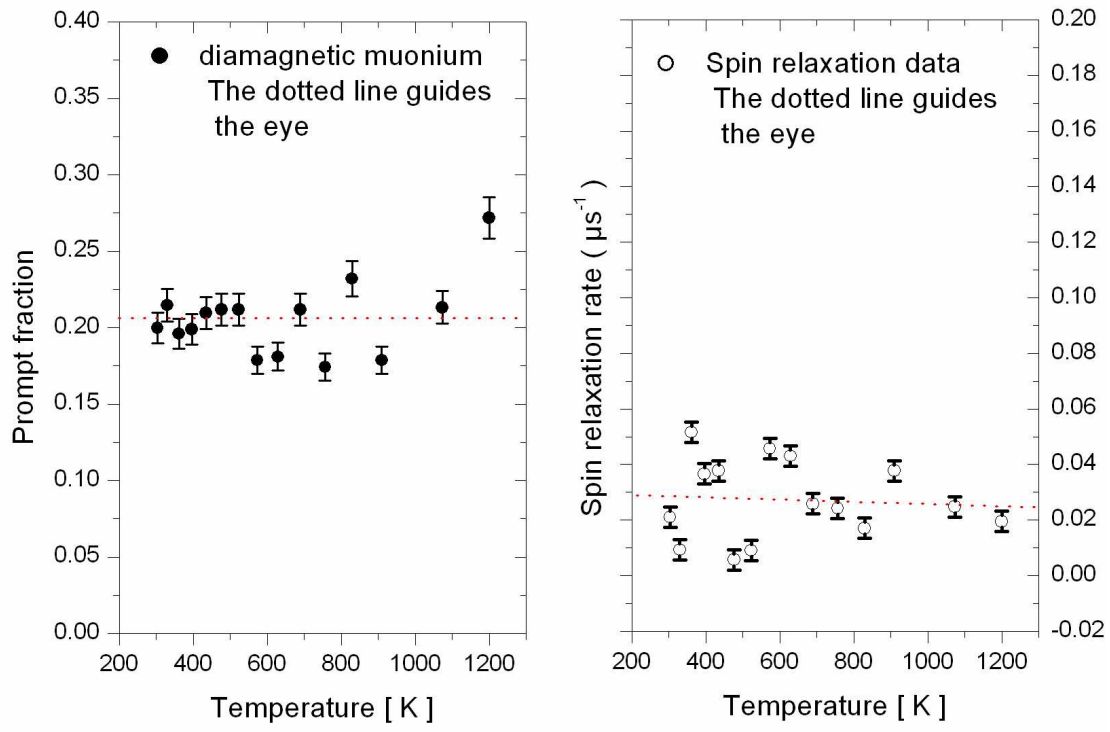

Figure 5.21: Variation of (a) prompt diamagnetic fraction and (b) spin relaxation rate with temperature in the natural type Ia diamond sample used in this study. There is an increase in the population of the diamagnetic fraction above 1 000 K.

5.4 Muonium Studies in High-purity Type IIa Diamond grown by HPHT Synthesis

5.4.1 Results From Longitudinal Field Measurements

Here we present the experimental results that were obtained in high-purity type IIa HPHT diamond using the longitudinal field Muon spin relaxation (LF-μSR) method. It is generally accepted that the population of different isolated muonium states formed in diamond is affected by the sample quality. However, the situation regarding sample quality has improved recently with the advent of HPHT and CVD syntheses of diamond. It was therefore very important to study the latest very recently available pure material to establish whether the missing fraction is related to defect or intrinsic processes. Understanding the origin of the missing fraction would lead to some clarification of the hydogen-related properties of diamond.

The measurements consisted mainly of studying the longitudinal field repolarisation curves at 5 and 290 K. The absolute fractions of the muonium states were estimated by measuring the full asymmetry of the MuSR system and extracting the absolute fractions of the muonium states by theoretical fitting to the repolarisation curves.

Figure 5.22 shows a typical LF histogram collected using the ISIS EMU spectrometer for synthetic type IIa diamond at 290 K. From these histograms, the polarisation spectra shown in Figures 5.23 and 5.24 were obtained, after correcting for background and variable asymmetry and normalising to the full asymmetry of the MuSR system as measured with a silver sample.

The type IIa HPHT diamond samples were cut along [100], so all the Mu_{BC} axes were along the (111) C-C bond directions and therefore at equivalent angles of 54.7 ° to the field. A theoretically simulated repolarisation curve for Mu_{BC} in this sample is shown

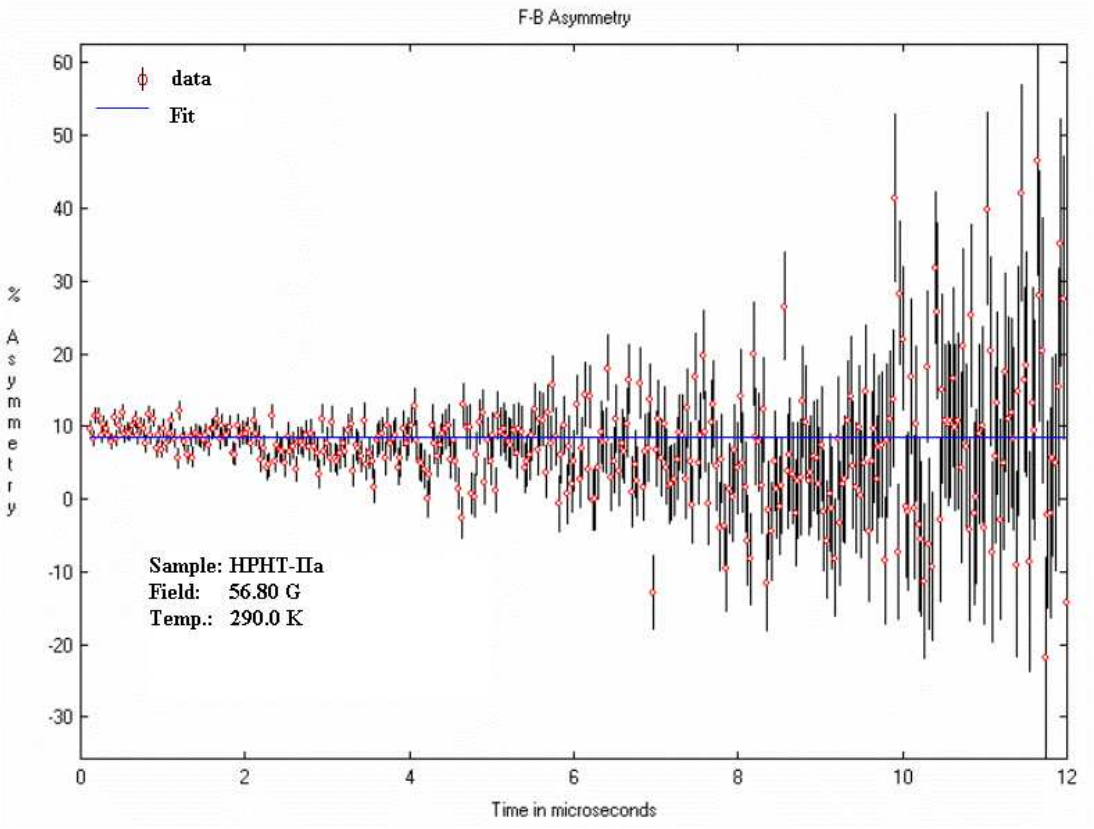

Figure 5.22: A typical LF histogram collected at the ISIS EMU spectrometer. The data are for synthetic type HPHT IIa diamond taken at 290 K for an applied field of 56.80 G.

in Figure 5.2. This curve can be described well by the sum of three Lorentzians (see equation 5.9), one at zero field and the other two at the high field dip for both signs of field [198].

Assuming that the total polarisation is a sum over all possible muonium states, we have

$$P_T(B) = [F_d + F_{MuT}P_{MuT}(B) + F_{MuBC}P_{MuBC}(B)]\,, \tag{5.12}$$

where F_d, F_{MuT} and F_{MuBC} are the fractional yields for μ^+, Mu_T^0, Mu_{BC}^0, respectively, with

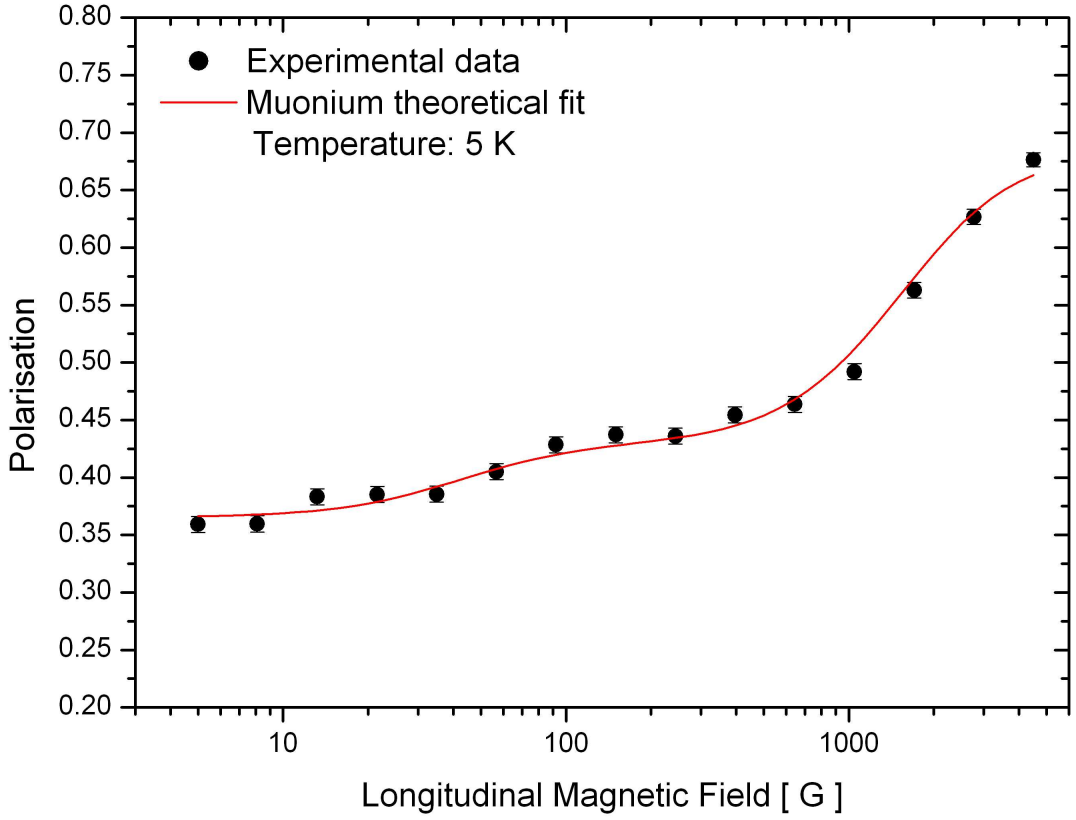

Figure 5.23: Longitudinal field repolarisation curve for high-purity type IIa HPHT diamond at a temperature of 5 K. A missing fraction of about 12 % was observed.

$$F_d + F_{MuT} + F_{MuBC} = 1. \tag{5.13}$$

The function for the isotropic paramagnetic muonium is given by

$$P_{MuT} = \frac{(\frac{1}{2} + X^2)}{(1 + X^2)} \tag{5.14}$$

with

$$X = B/B_0 \tag{5.15}$$

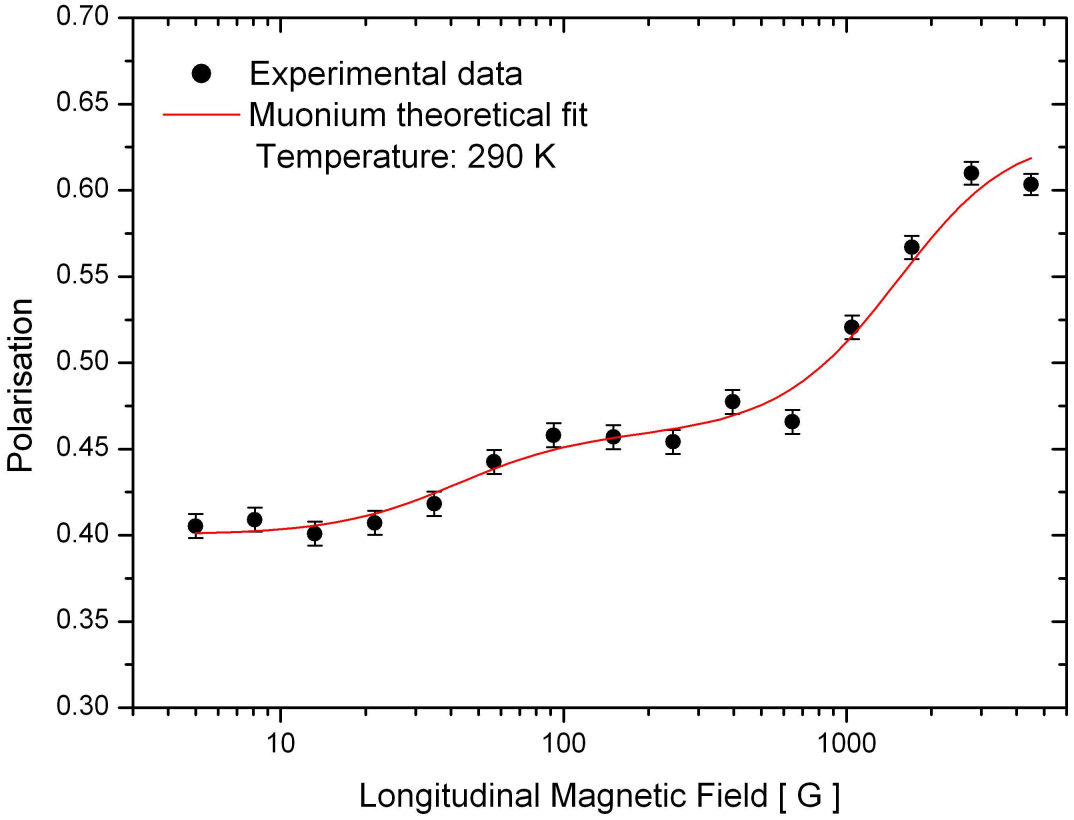

Figure 5.24: Longitudinal field repolarisation curve for high-purity type IIa HPHT diamond at a temperature of 290 K. No thermal ionization of Mu_{BC} was observed from 5 - 290 K.

$$B_0 = \frac{A_{iso}}{(\gamma_\mu - \gamma_e)} \tag{5.16}$$

where A_{iso} is the isotropic, or contact, hyperfine (hf) constant, and γ_μ, γ_e are the muon and electron gyromagnetic ratios, respectively. The function for the anisotropic paramagnetic muonium is given by (see equation 5.9)

$$P_{MuBC} = \frac{a_1 w_1}{w_1^2 + (x - b_1)^2} + \frac{a_1 w_1}{w_1^2 + (x + b_1)^2} + \frac{a_0 w_0}{w_0^2 + x^2} + 1 \tag{5.17}$$

Hence, equation 5.12 becomes

$$P_T(B) = \left[F_d + F_{MuT}\left(\frac{\frac{1}{2}+X^2}{1+X^2}\right) + F_{MuBC}\left(\frac{a_1 w_1}{w_1^2+(x-b_1)^2} + \frac{a_1 w_1}{w_1^2+(x+b_1)^2} + \frac{a_0 w_0}{w_0^2+x^2} + 1\right)\right]. \tag{5.18}$$

The data in Figures 5.23 and 5.24 were fitted to equation 5.18 to estimate the muonium fractions F_d, F_{MuT} and F_{MuBC}. Table 5.3 shows the muonium fractions F_{MuT}, F_{MuBC}, F_d, and MF determined in this study.

Table 5.3: Muonium fractions F_{MuT}, F_{MuBC}, F_d, and MF at a temperature of 5 K in this study determined by theoretical fitting to equation 5.18.

Sample	F_{MuT}(%)	F_{MuBC}(%)	F_d(%)	MF(%)
HPHT IIa SC diamond	54 ± 2	30 ± 1	4 ± 1	12 ± 4

5.4.2 Results From Transverse Field Measurements

Here we present the experimental measurements of the transverse field muon spin rotation (TF-μSR). The objectives of these measurements were to explore the promptly formed isotropic muonium (Mu_T) and diamagnetic muonium (Mu_D) since these muonium species are easily observable, from the characteristic precession signal, in muon spin rotation rather than in muon spin relaxation. The measurements were conducted in transverse fields of 2 and 20 G to explore Mu_T and Mu_D, respectively, on the high-purity type IIa HPHT diamond samples. The transverse-field technique has two important advantages over the longitudinal-field technique:

- It generally provides a more accurate determination of the muonium hyperfine parameters, since the systematic errors involved in a frequency measurement are smaller than those in an amplitude measurement,
- The μSR frequency spectrum allows the individual identification and investigation of simultaneously occurring muonium states.

The TF measurements were taken from 5 - 290 K in 20 and 2 G inorder to estimate the promptly formed fractions of the diamagnetic and Mu_T state, respectively. Figures 5.25 - 5.27 show some of the TF histograms collected using the ISIS EMU spectrometer in an applied field of 20 G, and Figures 5.28 - 5.30 show some of the TF histograms collected using the ISIS EMU spectrometer in an applied field of 2 G.

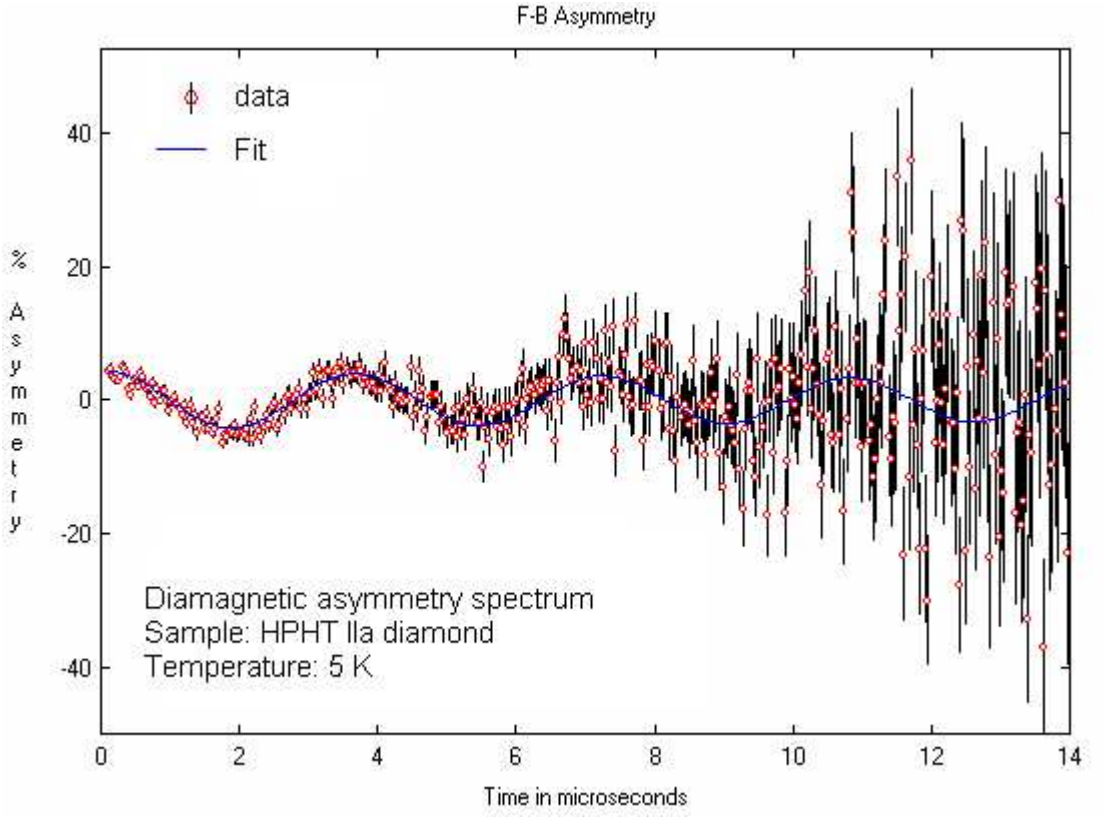

Figure 5.25: A TF histogram collected using the ISIS EMU spectrometer at an applied field of 20 G. The data, which are for high-purity type IIa HPHT diamond at 5 K, were used to determine both the alpha value as well as the prompt diamagnetic fraction for the sample.

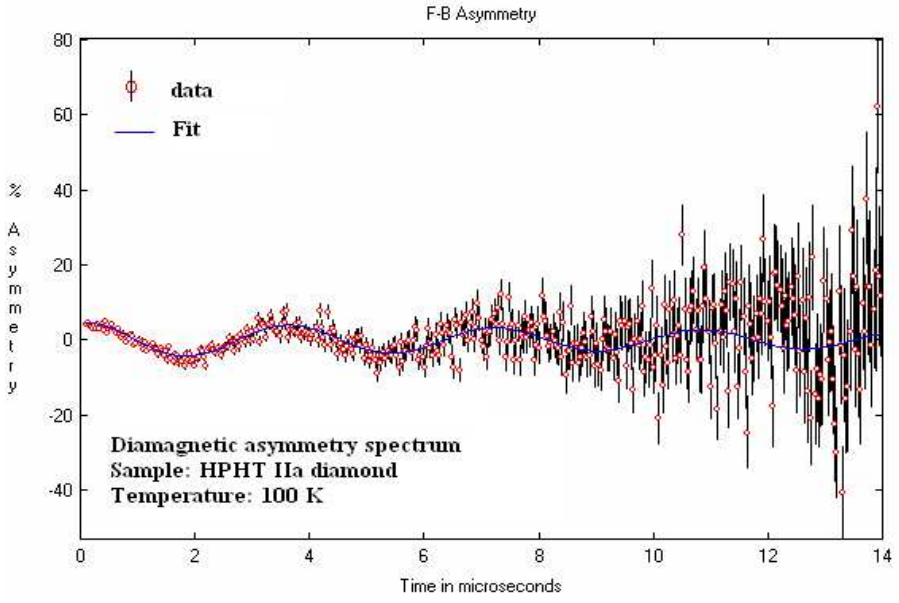

Figure 5.26: A TF histogram collected using the ISIS EMU spectrometer at an applied field of 20 G. The data, which are for high-purity type IIa HPHT diamond at 100 K, were used to determine both the alpha value as well as the prompt diamagnetic fraction for the sample.

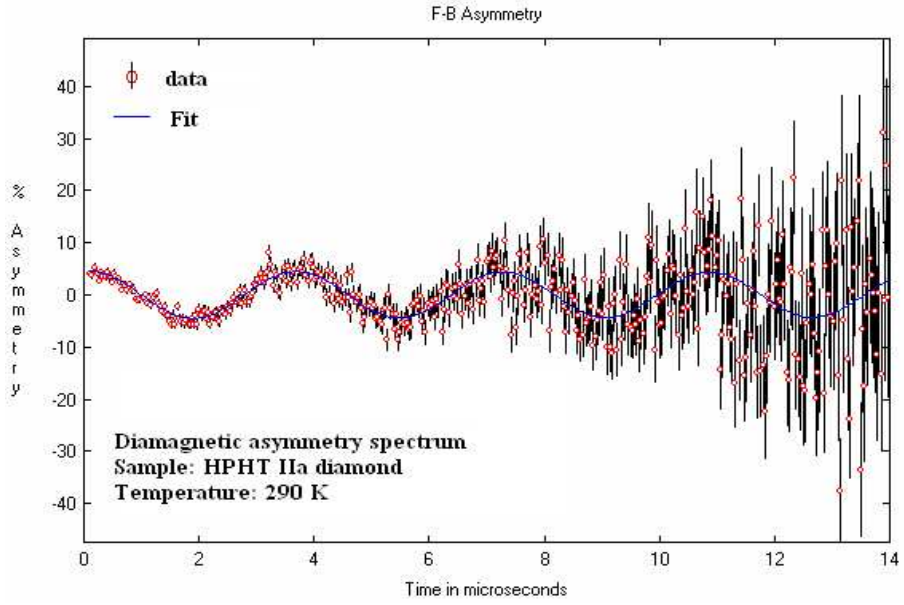

Figure 5.27: A TF histogram collected using the ISIS EMU spectrometer at an applied field of 20 G. The data, which are for high-purity type IIa HPHT diamond at 290 K, were used to determine both the alpha value as well as the prompt diamagnetic fraction for the sample.

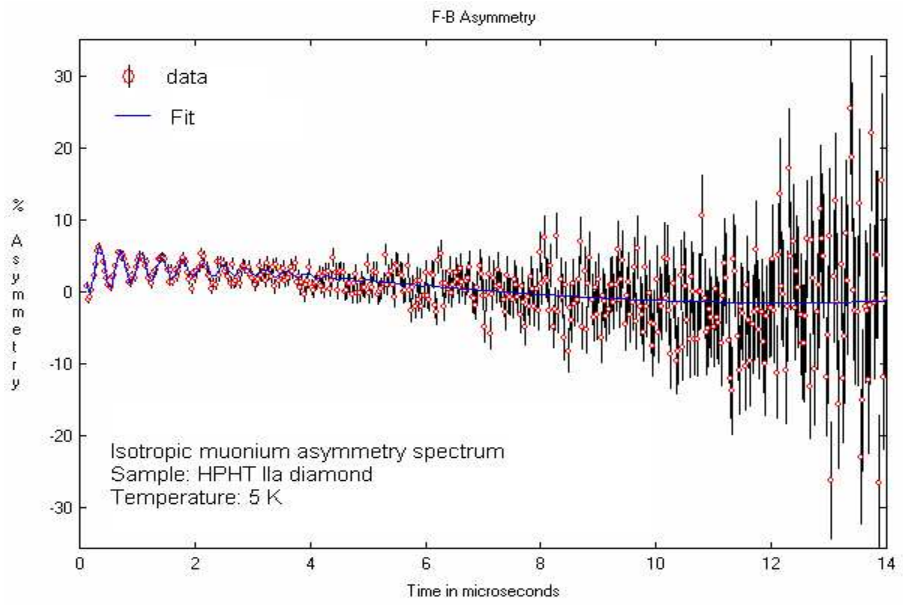

Figure 5.28: A TF histogram collected using the ISIS EMU spectrometer at an applied field of 2 G, showing the presence of the isotropic muonium state in the sample. The data, which are for high-purity type IIa HPHT diamond at 5 K, were used to determine the promptly formed isotropic muonium fraction for the sample.

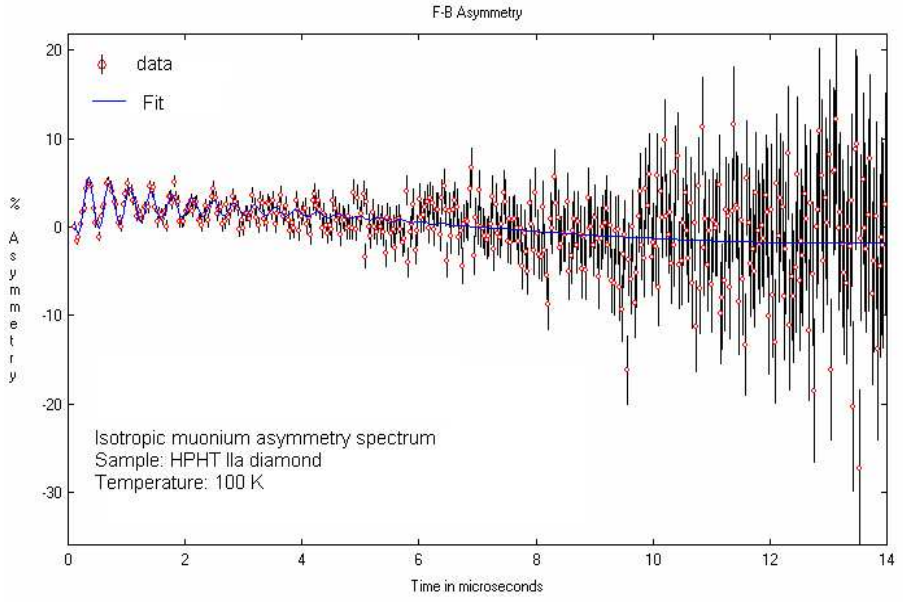

Figure 5.29: A TF histogram collected using the ISIS EMU spectrometer at an applied field of 2 G, showing the presence of the isotropic muonium state in the sample. The data, which are for high-purity type IIa HPHT diamond at 100 K, were used to determine the promptly formed isotropic muonium fraction for the sample.

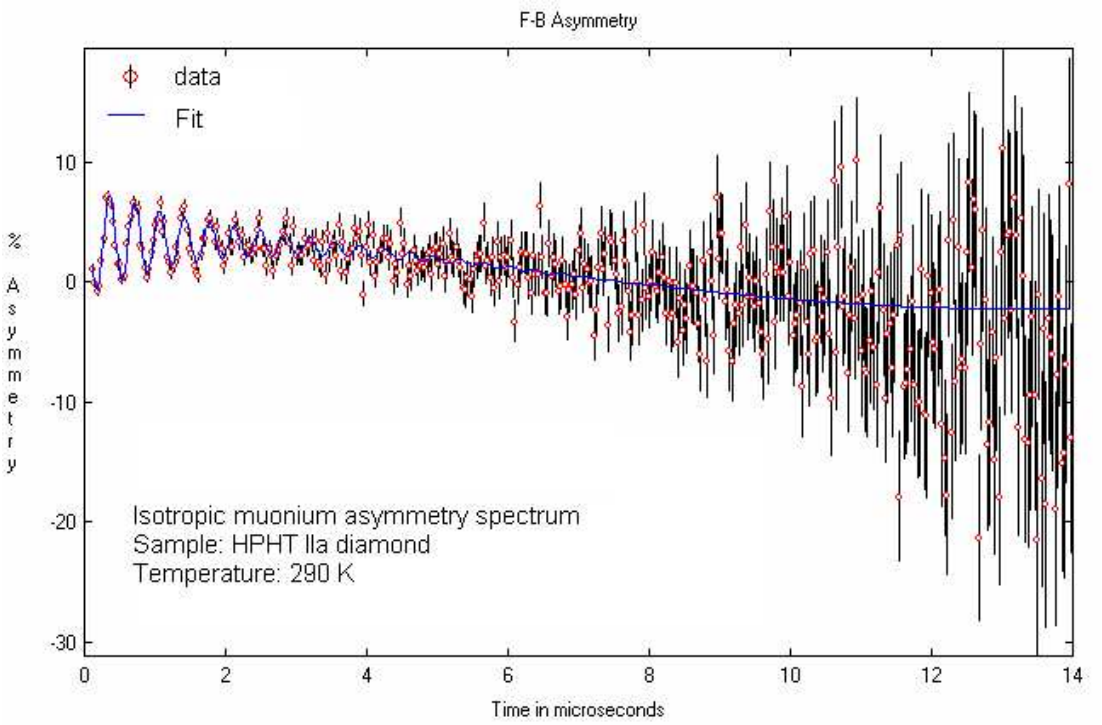

Figure 5.30: A TF histogram collected using the ISIS EMU spectrometer at an applied field of 2 G, showing the presence of the isotropic muonium state in the sample. The data, which are for high-purity type IIa HPHT diamond at 290 K, were used to determine the promptly formed isotropic muonium fraction for the sample.

In order to estimate the promptly formed muonium fractions in the sample the asymmetries from the TF histograms were normalised, after correcting for variable background and variable asymmetry, to the full asymmetry of the MuSR system as measured with a silver sample, and the results obtained are as indicated in Table 5.4 and plotted in Figures 5.31 and 5.32 together with the corresponding spin relaxation rates.

Table 5.4: Prompt muonium fractions in high-purity type IIa HPHT diamond samples determined by fitting to T20 and T2 histograms.

Temperature (K)	Prompt Mu_D	Prompt Mu_T
5	0.237	0.197
7.25	0.225	0.193
10.53	0.233	0.189
15.27	0.227	0.205
22.16	0.224	0.235
32.15	0.223	0.222
46.65	0.241	0.197
67.69	0.242	0.191
100	0.250	0.186
142.5	0.229	0.190
206.76	0.246	0.232
250	0.236	0.243
290	0.246	0.237

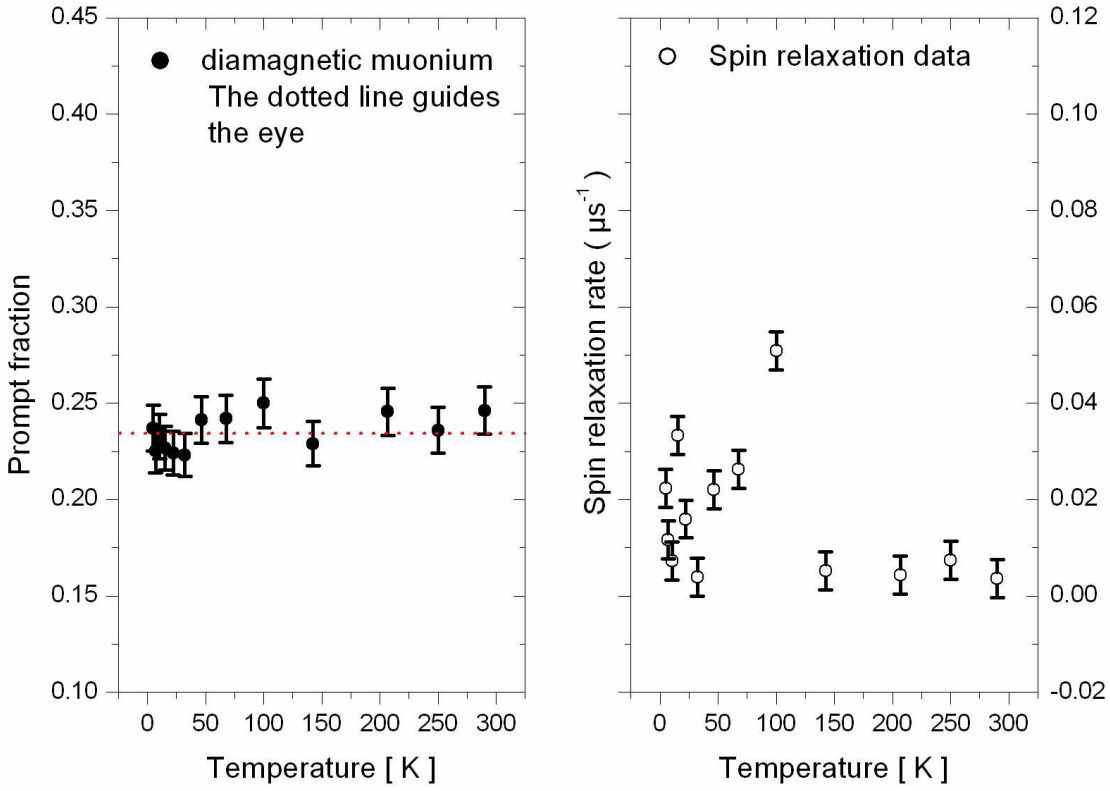

Figure 5.31: Variation of (a) prompt diamagnetic fraction and (b) spin relaxation rate with temperature in the high-purity type IIa HPHT diamond samples used in this study.

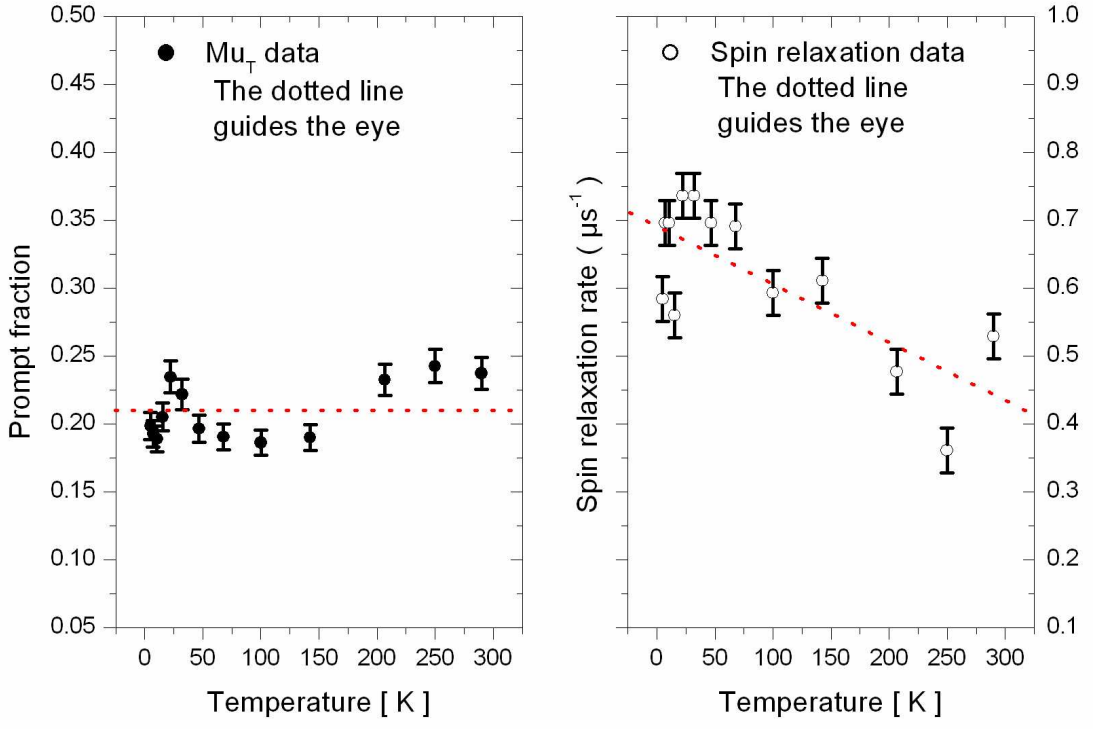

Figure 5.32: Variation of (a) prompt isotropic muonium fraction and (b) spin relaxation rate with temperature in the high-purity type IIa HPHT diamond samples used in this study.

Chapter 6

Discussion: Ionization of Mu_{BC} in Natural Type Ia and Muonium States in Synthetic Type IIa Diamond

"A new scientific truth does not triumph by convincing its opponents and making them see light, but rather because its opponents eventually die, and a new generation grows up that is familiar to it."

Max Planck

6.1 Muonium dynamics in natural type Ia diamond above 300 K

Bond-centred muonium (Mu_{BC}) is the most stable muonium state in diamond. Its experimental spectroscopy and theoretical description is well established [34, 28]. The analogous bond-centred hydrogen (H_{BC}) state has not yet been observed experimentally. It is expected to be a donor, where the donor level varies according to the models used [28]. In a typical muon spin rotation experiment in diamond, there is a certain fraction of Mu_{BC} which is formed promptly upon thermalisation after implantation. In measurements conducted above room temperature, this fraction is enhanced by the delayed formation of Mu_{BC} which is due to a thermally activated transition from Mu_T to Mu_{BC}. This transition begins to be significant at a temperature of about 400 K [158, 127]. The total population of Mu_{BC} is best observed in a longitudinal field experiment.

Figure 5.16 shows a gradual increase in the Mu_{BC} fractions from 303 to about 1 000 K and a decrease thereafter. This implies that the ionization temperature of Mu_{BC} in natural type Ia single crystal diamond is around 1 000 K. This is further confirmed by an increase in the population of the diamagnetic species from around 1 000 K (see Figure 5.21(a)) since the ionization of Mu_{BC} results in a higher diamagnetic fraction, which serves to raise the overall level of polarisation, as observed. The two figures are plotted together in Figure 6.1. The data shown are from two independent methods (LF-μSR and TF-μSR) confirming the same observation, namely, the ionization of bond-centred muonium above 1 000 K.

Observation of the Mu_{BC} theory fits in Figures 5.11 - 5.15 shows that there is only

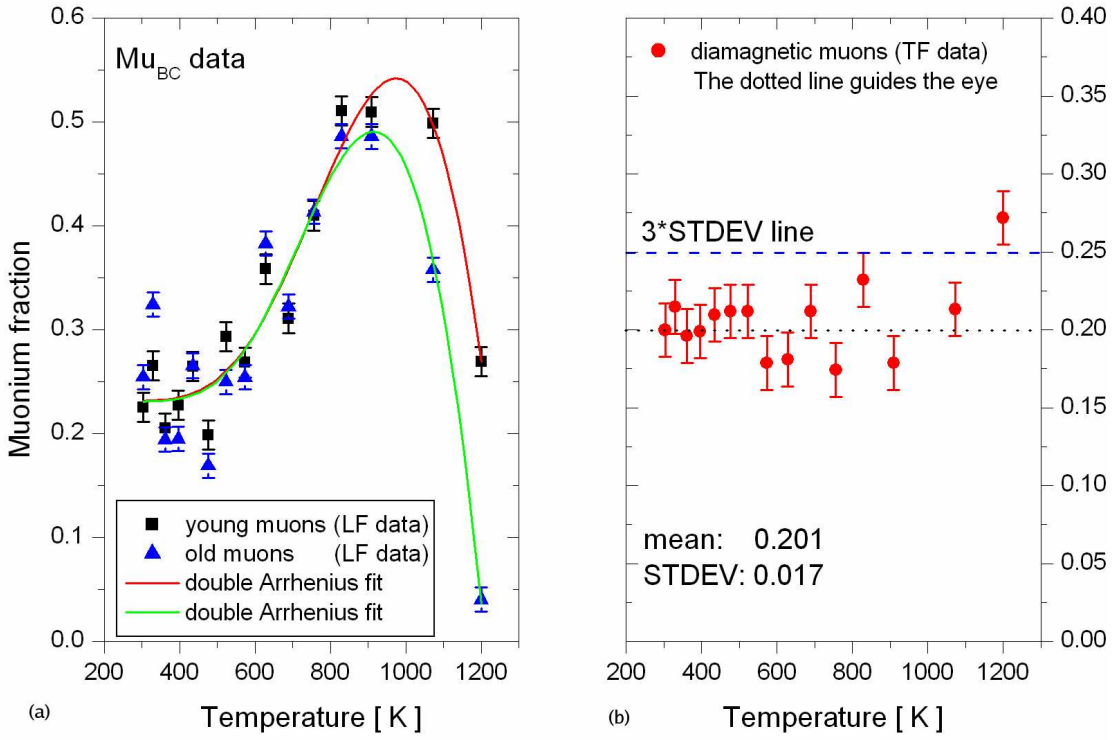

Figure 6.1: Variation of (a) bond-centred muonium (LF data) and (b) diamagnetic muonium (TF data) with temperature. The decrease in the Mu_{BC} fraction and the corresponding increase in the diamagnetic fraction above 1 000 K are interpreted as due to the thermal ionization of Mu_{BC}.

Mu_{BC} (plus diamagnetic muons) in the sample. Previous MuSR measurements in natural type Ia single crystal diamonds have shown the existence of a new muonium state, coded Mu_X, which is thought to be formed when mobile muonium, Mu_T, traps at nitrogen impurities in the form of A-and B-centres. The open question is therefore: why is there no Mu_X and only Mu_{BC} formed in the current study?

One possible explanation for such a weak influence of impurities on Mu_T might be a **local** character of the particle tunneling or phonon scattering towards higher temperatures. It is now established that the diffusion of interstitial muonium at lower temperatures is described by the tunneling of the muonium-polaron state associated with two-phonon exchange processes [200]. One of the possible mechanisms for localisation of a particle is its interaction with the lattice excitations resulting in a spatial localisation of its wave function [201]. At very low temperatures in a perfect crystalline insulator, Mu_T is thought to display a temperature-independent diffusion constant [26, 202] and it tunnels coherently in the crystal. As the temperature increases, lattice vibrations scatter the muonium waves, destroying the coherence and the diffusion constant decreases according to a strong power law [26]. Therefore, the mobile Mu_T does not diffuse far enough to reach the aggregated nitrogen defects to form Mu_X due to the interaction with the phonon bath. The result is a localisation of the wave function of the Mu_T at bond-centred (BC) sites forming Mu_{BC}.

To understand the behaviour of the Mu_{BC} population with temperature, it is important to briefly look at the effect of temperature on the positive muons as they enter the sample. We will divide the temperature regime into three zones, namely, low temperatures (< 300 K), high temperatures (300-1000 K), and very high temperatures (> 1000 K).

Low Temperatures (< 300 K): At temperatures below 300 K, the muons are moving fast by quantum diffusion and their wave functions are delocalised. Hence the dominant

Mu_T fraction undergoes rapid quantum diffusion followed by trapping at the aggregated nitrogen defects to form Mu_X, where the $Mu_T \rightarrow Mu_{BC}$ transition does not yet occur [203]. Few muons get to the bond-centred (BC) site to form Mu_{BC}.

High Temperatures (300-1000 K): The muons move slowly - phonons destroy the coherence. This results in a localisation of the muons at BC sites to form Mu_{BC}. There is no significant trapping of the mobile Mu_T species at nitrogen defects because the conversion to Mu_{BC} competes effectively with this process above room temperature. The result is an increase in the Mu_{BC} fraction as temperature increases.

Very High Temperatures (> 1000 K): As much as the positive muons move faster to reach the BC sites there is lower probability for the formation of Mu_{BC}. This is due to the start of ionization, and the μ^+ formed from Mu_{BC} ionization is indistinguishable from the diamagnetic μ^+ that has found a BC site. The result is a decrease in the Mu_{BC} fraction, as shown in Figure 5.16, until it eventually disappears above 1200 K.

6.2 The gap-level of Mu_{BC} in diamond: Mathematical model

At temperatures above 1000 K in Figure 5.16, the Mu_{BC} fraction decreases with increasing temperature. This disappearance of Mu_{BC} is correlated with the increase in the population of the diamagnetic species as shown in Figure 6.1. We relate this conversion to ionization (i.e., dissociation). For an understanding of this behaviour, we will consider the last steps in the muon implantation. There are two stages in the muon stopping process, an intermediate epithermal and a final thermal stage. In the epithermal stage there is loss and gain of electrons by the muon, i.e., an exchange of electrons with the matrix. At the transition from the epithermal to the thermal stage, the muon ends up either with or without an electron, and this situation determines whether the paramagnetic or diamagnetic fraction is formed at low temperatures. The partition into

these fractions can depend on temperature and doping level. The rapid change of the fractions (Figure 5.16) at temperatures above 1000 K and the complete conversion to the diamagnetic fraction is due to a different process. We associate it with the ionization of the muonium centre in the final thermal stage.

This observation is consistent with previous MuSR studies where Mu_{BC} in diamond was observed up to at least 1100 K [33, 144, 158], although these studies do not say what happens to it beyond this temperature. The high stability of the Mu_{BC} state is probably related to the large band gap of diamond which inhibits the conduction electron concentration [204].

Different model fits give Mu_{BC} ionization energies of between 0.60 and 1.80 eV. A double Arrhenius fit [1] (see Figure 6.1 (a)), assuming the $Mu_{BC} \rightarrow Mu_{BC}^{+}$ conversion occured within the muon life-time, gives an ionization energy of 0.57 ± 0.13 eV. Introducing the muon decay constant and solving the rate equations, as explained below, gives a value of 1.79 ± 0.04 eV.

In discussing the formation and depletion of Mu_{BC} we will assume that we have a large amount of Mu_T, which diffuses at rate k_1 to form Mu_{BC}, which in turn converts into Mu_{BC}^{+} at rate k_2 as indicated in the illustration below.

$$Mu_T \quad \overrightarrow{k_1} \quad Mu_{BC} \quad \overrightarrow{k_2} \quad Mu_{BC}^{+}$$

[1] A double Arrhenius equation [205] describes the effect of temperature on two opposing processes. The first of the two Arrhenius equations predicts the increase in the rate of formation of Mu_{BC} due to a reduced energy barrier for the $Mu_T \rightarrow Mu_{BC}$ conversion at higher temperatures, while the second predicts the decrease in the rate of formation of Mu_{BC} due to thermal ionization and other destructive processes that occur at higher temperatures. This equation allows simultaneous estimation of activation energies for both processes.

Let the original amount of Mu_T be N_0, and the original amount of Mu_{BC} and Mu^+_{BC} be zero. The problem is to find the amount of Mu_{BC} as a function of time. As time progresses the amount of Mu_{BC} increases from the conversion of Mu_T, and decreases from muon decay and from thermal ionization. The rate equations for the concentrations of Mu_T and Mu_{BC} are:

$$\frac{d[N_T]}{dt} = -k_1[N_T] - \lambda[N_T] \tag{6.1}$$

$$\frac{d[N_B]}{dt} = k_1[N_T] - k_2[N_B] - \lambda[N_B] \tag{6.2}$$

where $[N_B]$ is the amount of Mu_{BC}, $[N_T]$ is the amount of Mu_T and λ is the muon decay constant. Integrating equation 6.1 gives

$$N_T = N_0 e^{-(k_1+\lambda)t}. \tag{6.3}$$

Substituting equation 6.3 into equation 6.2 gives

$$\frac{d[N_B]}{dt} + (k_2 + \lambda)[N_B] = k_1 N_0 e^{-(k_1+\lambda)t} = f(t), \tag{6.4}$$

a differential equation with a solution comprised of two parts, a complementary function (CF) and a particular integral (PI). The CF is the solution of the equation

$$\frac{d[N_B]}{dt} + (k_2 + \lambda)[N_B] = 0. \tag{6.5}$$

That is, $CF = Ae^{-(k_2+\lambda)t}$, where A is a constant to be found from the initial conditions. The PI is any solution for $[N_B](t)$ which satisfies equation 6.4. To find the PI, note that

$f(t)$ varies as $e^{-(k_1+\lambda)t}$, and so we will assume that the particular integral will do so also. We will therefore assume a PI of the form $[N_B] = Ce^{-(k_1+\lambda)t}$, where C is a constant. Substituting into equation 6.2 and re-arranging gives

$$C = \frac{k_1 N_0}{(k_2 - k_1)} \tag{6.6}$$

The solution to equation 6.4 can therefore be written as the sum of the CF and the PI. That is,

$$[N_B] = Ae^{-(k_2+\lambda)t} + \frac{k_1 N_0}{(k_2 - k_1)} e^{-(k_1+\lambda)t}. \tag{6.7}$$

If we now add the condition that $[N_B] = 0$ when t = 0, we can solve for A, and then write the final result as

$$[N_B] = \frac{k_1 N_0}{(k_2 - k_1)} \left[e^{-(k_1+\lambda)t} - e^{-(k_2+\lambda)t} \right], \tag{6.8}$$

which can also be expressed as

$$[N_B] = \frac{k_1 N_0}{(k_2 - k_1)} \left[e^{(-k_1 t)} - e^{(-k_2 t)} \right] e^{(-\lambda t)} \tag{6.9}$$

The reaction rates coefficients k_1 and k_2 have a temperature dependence, which is usually given by the Arrhenius equations:

$$k_1 = \Psi_1 e^{(-E_1/kT)} \tag{6.10}$$

and

$$k_2 = \Psi_2 e^{(-E_2/kT)}, \tag{6.11}$$

where Ψ_1, Ψ_2 are the frequency factors; E_1, E_2 are the activation energies; k is the Boltzmann constant; and T is the temperature in Kelvin. The fractional accumulated $[N_B]$ signal as a function of the initial signal (if decay were the only removal mechanism) is given by

$$\langle [N_B] \rangle = \frac{\int_0^\infty [N_B]\, dt}{\int_0^\infty N_0 e^{(-\lambda t)}\, dt} = \frac{k_1 N_0}{(k_2 - k_1)} \int_0^\infty \left[e^{-(k_1+\lambda)t} - e^{-(k_2+\lambda)t} \right] dt \; / \int_0^\infty N_0 e^{(-\lambda t)}\, dt \tag{6.12}$$

That is,

$$\langle [N_B] \rangle = \frac{k_1 N_0}{(k_2 - k_1)} \left[\left(\frac{-1}{(k_1+\lambda)} e^{-(k_1+\lambda)t} + \frac{1}{(k_2+\lambda)} e^{-(k_2+\lambda)t} \right) / \left(\frac{-N_0}{\lambda} \right) e^{-(\lambda t)} \right]_0^\infty, \tag{6.13}$$

which becomes

$$\langle [N_B] \rangle = \frac{\lambda k_1}{(k_2 - k_1)} \left(\frac{1}{(k_1+\lambda)} - \frac{1}{(k_2+\lambda)} \right). \tag{6.14}$$

Equation 6.14 simplifies to

$$\langle [N_B] \rangle = \frac{\lambda k_1}{(k_1+\lambda)(k_2+\lambda)} \tag{6.15}$$

Substituting for k_1 and k_2 from equations 6.10 and 6.11, respectively, into equation 6.15 gives

$$\langle [N_B] \rangle = \frac{\lambda \Psi_1 e^{(-E_1/kT)}}{\left(\Psi_1 e^{(-E_1/kT)} + \lambda\right)\left(\Psi_2 e^{(-E_2/kT)} + \lambda\right)}. \tag{6.16}$$

So, in order to estimate the activation energies of the muonium states the Mu_{BC} data in Figure 5.16 was fitted to an equation of the form

$$[F_{MuBC}] = A_0 + \frac{\lambda \Psi_1 e^{(-E_1/kT)}}{\left(\Psi_1 e^{(-E_1/kT)} + \lambda\right)\left(\Psi_2 e^{(-E_2/kT)} + \lambda\right)}, \tag{6.17}$$

where A_0 is the promptly formed Mu_{BC}, E_1 and E_2 are the activation energies for the $Mu_T \rightarrow Mu_{BC}$ and $Mu_{BC} \rightarrow Mu_{BC}^+$ conversions, respectively.

Now, the $Mu_T \rightarrow Mu_{BC}$ activation energy (E_1) was fixed at 0.476 eV as obtained by Odermatt et al. [204, 158]. Using this model the $Mu_{BC} \rightarrow Mu^+_{BC}$ activation energy (E_2) was found to be 1.789 ± 0.044 eV and the fit is as shown in Figure 6.2. The frequency factors, Ψ_1 and Ψ_2, were found to be about 7.87 x 10^8 s^{-1} and 1.0 x 10^{14} s^{-1}, respectively.

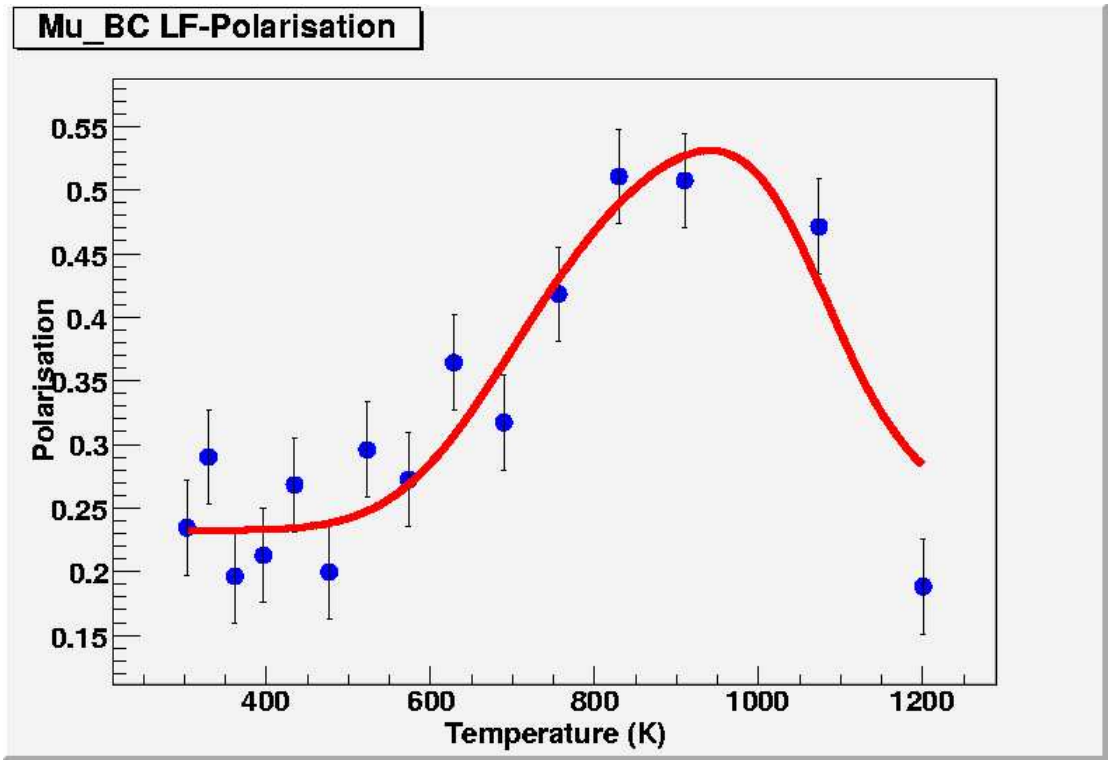

Figure 6.2: F_{MuBC} variation with temperature fitted with equation 6.17 in order to estimate the ionization energy of the Mu_{BC} state. This model gives an ionization energy of about 1.80 eV while a double Arrhenius fit gives a value of about 0.60 eV.

There seems to be a big spread in theoretical expectations (see section 3.2 in Ref. [28]) on the ionization energy or donor level of Mu_{BC} in diamond. Some of the calculated donor levels are even band resonant, that is, they are not even in the band gap! Our values of between 0.60 and 1.80 eV below the conduction band are certainly not band-resonant, as some authors claim, otherwise Mu_{BC} would never be seen as a neutral

state.

6.3 Muonium states in high-purity type IIa HPHT diamond

Table 6.1 shows a comparison of the absolute fractions of Mu_T, Mu_{BC}, μ_D and MF in this study and other published experimemts. This is the first time in this research that absolute fractions of Mu_T, Mu_{BC}, μ_D and MF in high-purity type IIa HPHT single crystal diamond have been determined.

The absolute fraction of Mu_T determined in this study is lower than those found by

Table 6.1: Comparison of F_{MuT}, F_{MuBC}, F_d, and MF in the present study and other published experiments (see Table 2.5)

.

Sample	F_{MuT}(%)	F_{MuBC}(%)	F_d(%)	F_{MuX}(%)	MF(%)	Reference
HPHT IIa SC diamond	54	30	4		12	Present study
CVD PC diamond	50.2	6.8	19.4		23.6	[2]
CVD PC diamond	50	-	6		-	[170]
IIa diamond SC	68.9	22.7	8.1		0.3	[127]
IIa diamond SC	65	25	10		0	[171]
Ia diamond	30	0	10	60		[3]

Refs. [127, 171] in type IIa single crystal diamond, but is comparable to the values reported by Refs. [170, 2] in CVD polycrystalline diamond. The estimated MF in this study is lower than that reported by Ref. [2] in CVD polycrystalline diamond but higher than that of natural type IIa single crystal diamond.

To determine why the fraction of MF in this study was higher than that of natural type IIa single crystal diamond, we considered the dynamic environment of the muonium states. The evolution of the muon spin polarisation is influenced by random pertubations from fluctuating local magnetic fields arising from the relative motion of muonium and paramagnetic species such as free electrons/holes, bound donors/acceptors or de-

fects [127]. The Mu_T and Mu_D signals are much more sensitive to the presence of defects than the Mu_{BC} signals [63]. The temperature dependence of the spin relaxation rates of Mu_D and Mu_T are shown in Figure 5.31 and Figure 5.32, respectively. The synthetic type IIa HPHT single crystal diamonds used in this study contain virtually no substitutional nitrogen atoms, and hence their influence as the origin of the MF are disregarded.

Molten metal solvents can be sources of contamination of metallic impurities for diamond crystals grown by HPHT synthesis. Kaneko et al. [206] have used neutron activation analysis to determine the metallic impurities in the high-purity type IIa diamond crystals as part of the investigation into trapping levels in the diamond crystals. Metallic impurities of iron (Fe), cobalt (Co), chromium (Cr) and other minor elements were detected at concentrations of a few ppb in the high-purity type IIa diamond crystals. So, since the amounts of metallic inclusions are extremely small, these could also be disregarded as the origin of MF.

Although synthetic type IIa diamonds were found to have high crystalline quality with fewer crystal defects, less internal strain and less variation in defects among crystals than those of natural diamonds, some line and plane defects were observed [207]. We presume that the small MF observed in this study could be due to the trapping of the mobile muonium at these defects.

Chapter 7

Concluding Remarks on Major Findings

"In physics, your solution should convince a reasonable person. In math, you have to convince a person who's trying to make trouble. Ultimately, in physics, you're hoping to convince Nature. And I've found Nature to be pretty reasonable."

Frank Wilczek

American physicist (1951 -)

This thesis has presented experimental results on two separate topics within the field of muon spin rotation/relaxation/resonance (μSR) spectroscopy: The gap-level of bond-centred hydrogen in diamond and the muonium states in high-purity synthetic type IIa diamond grown by high-pressure and high-temperature (HPHT) synthesis. These are summarised separately below.

7.1 Natural type Ia single crystal diamond

The first part of this work presented results from μSR experiments in which the thermal ionization of muonium in natural type Ia single crystal diamond was studied using the longitudinal magnetic field muon spin relaxation (LF-μSR) and the transverse magnetic field muon spin rotation (TF-μSR) techniques. The diamond samples were characterised using fourier transform infrared (FTIR) spectroscopy and electron paramagnetic resonance (EPR) spectroscopy. The samples contained nitrogen defects in the

form of A-centres, B-centres, P1 and P2 centres.

These experiments have found that the immobile Mu_{BC} forms sufficiently fast at higher temperatures so that there is no trapping of the Mu_T leading to Mu_X above 300 K. This makes an interesting contrast with measurements conducted below room temperature, where Mu_{BC} is not observed due to the prompt trapping of Mu_T at nitrogen-related defects forming Mu_X. These results imply that temperature influences the probability of formation of Mu_X in nitrogen-rich diamonds as the conversion to Mu_{BC} competes effectively with this process at higher temperatures. The experiments have also found that bond-centred muonium (Mu_{BC}) in diamond ionises around 1000 K. Different model fits give activation energies between 0.60 and 1.80 eV, and hence the ionization energies obtained are inconsistent. There is an indication that the decrease in the fractional population of the Mu_{BC} is correlated with the increase in the population of the diamagnetic species. This is the first time in this research that the ionization energy of bond-centred muonium in diamond has been determined.

It can be concluded that Mu_{BC} (and hence bond-centred hydrogen) is a deep donor in diamond. This is the first time that the $Mu_T \rightarrow Mu_{BC}$ transition has been observed in longitudinal field. There are wide ranging theoretical estimates of the electronic level of bond-centred hydrogen in diamond. Some of the calculated donor levels are even band resonant, that is, they are not even in the band gap! Our values of between 0.60 and 1.80 eV below the conduction band are certainly not band-resonant.

7.2 Synthetic type IIa diamond

The muonium states in high-purity synthetic type IIa diamond grown by high-pressure and high-temperature (HPHT) synthesis were studied using the longitudinal magnetic field muon spin relaxation (LF-μSR) and the transverse magnetic field muon spin ro-

tation (TF-μSR) techniques. Many previous μSR studies in diamond have observed missing fractions (MF) which are thought to be caused by the trapping of the incoming muons at defects. The high-purity sample may resolve some of these open questions pertaining to whether the observed missing fraction is related to defect or intrinsic processes.

These experiments have found the existence of a diamagnetic muon state (μ_D), two paramagnetic muonium states (tetrahedral interstitial (Mu_T) and bond-centred (Mu_{BC})) and missing fraction (MF) in the synthetic type IIa diamond. The absolute fractions of μ_D, Mu_T, Mu_{BC} and MF in the synthetic type IIa diamond samples were 4, 54, 30 and 12 %, respectively, at 5K.

It can be concluded that even though the synthetic type IIa diamonds grown by high-pressure and high-temperature (HPHT) synthesis are of high crystal quality, they still contain defects that trap the incoming muons resulting in a small MF.

Appendix A

CAXBD97 decomposition spreadsheet fits

This appendix presents the fits obtained from the FTIR spectra using the Diamond Trading Company's CAXBD97 Excel program. Nitrogen concentrations were determined from absorption coefficient values for the various components. The spreadsheet uses the following figures from the literature.

Single nitrogen

$$[N_C] = 25\,\mu_C\ (1130\ cm^{-1}) \tag{A.1}$$

A-centres

$$[N_A] = 16.5\,\mu_A\ (1282\ cm^{-1}) \tag{A.2}$$

B-centres

$$[N_B] = 79.4\,\mu_B\ (1282\ cm^{-1}) \tag{A.3}$$

N^+

$$[N^+] = 5.5\,\mu_{N+}\ (1332\ cm^{-1}) \tag{A.4}$$

where [N] is the nitrogen concentration in parts per million (ppm) and μ is the absorption coefficient in cm^{-1} at the stated wavenumber value for the chosen component.

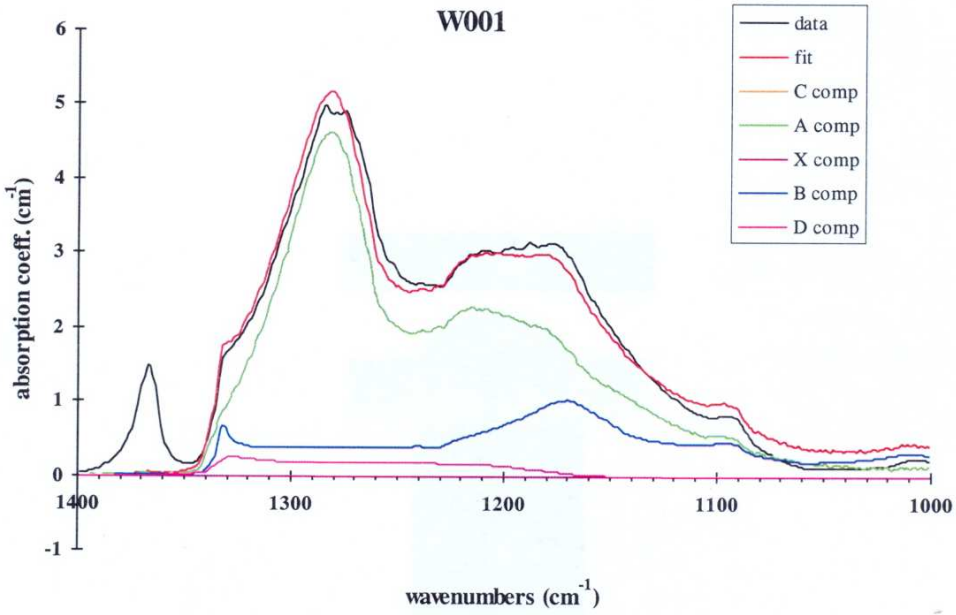

type Ib	$\mu(1130cm^{-1})$	0.00	cm^{-1}	$[N_C]$	0.0	ppm	
type IaA	$\mu(1282cm^{-1})$	4.62	cm^{-1}	$[N_A]$	76.2	ppm	
N^+	$\mu(1332cm^{-1})$	0.00	cm^{-1}	$[N^+]$	0.0	ppm	
type IaB	$\mu(1282cm^{-1})$	0.38	cm^{-1}	$[N_B]$	29.8	ppm	*fit range*
D	$\mu(1282cm^{-1})$	0.17	cm^{-1}	$[N_T]$	106.1	ppm	*1001 to 1399*

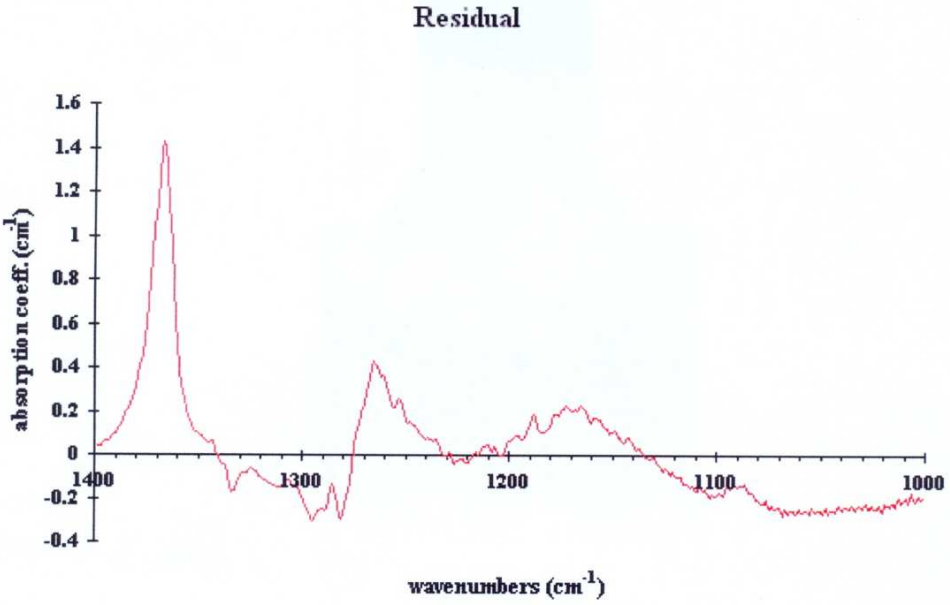

Figure A.1: CAXBD97 decomposition spreadsheet fits to the FTIR spectrum of sample W001 to determine the nitrogen concentrations in the sample. This sample contains 76.2 ppm of A-centres and 29.8 ppm of B-centres.

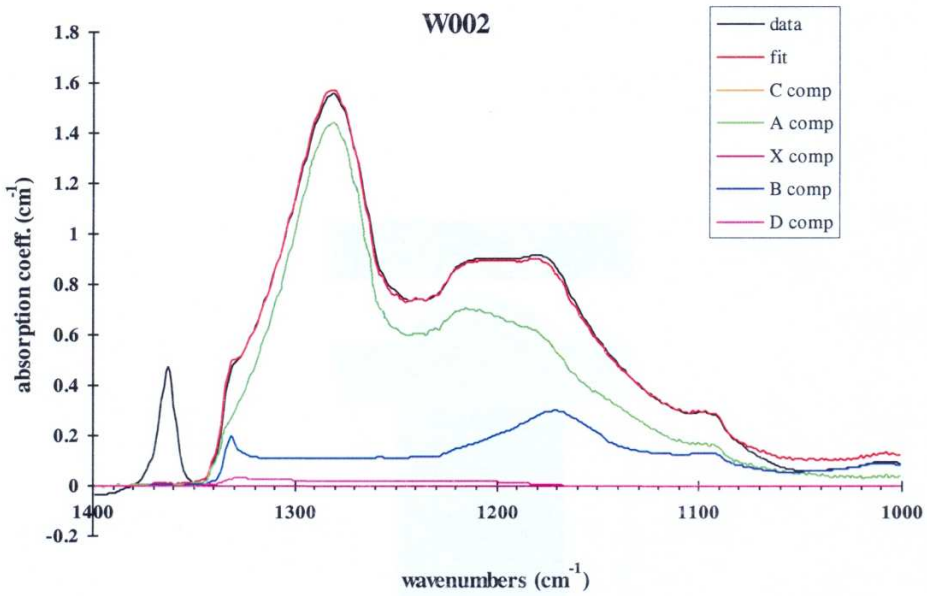

type Ib	$\mu(1130cm^{-1})$	0.00	cm^{-1}	$[N_C]$	0.0	ppm	
type IaA	$\mu(1282cm^{-1})$	1.44	cm^{-1}	$[N_A]$	23.8	ppm	
N^+	$\mu(1332cm^{-1})$	0.00	cm^{-1}	$[N^+]$	0.0	ppm	
type IaB	$\mu(1282cm^{-1})$	0.11	cm^{-1}	$[N_B]$	8.8	ppm	*fit range*
D	$\mu(1282cm^{-1})$	0.02	cm^{-1}	$[N_T]$	32.6	ppm	*1001 to 1399*

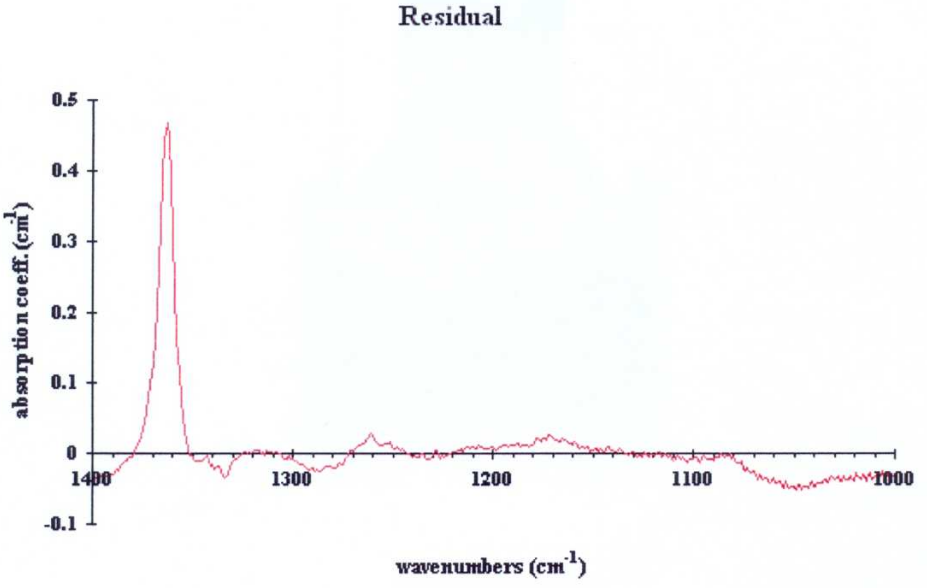

Figure A.2: CAXBD97 decomposition spreadsheet fits to the FTIR spectrum of sample W002 to determine the nitrogen concentrations in the sample. This sample contains 23.8 ppm of A-centres and 8.8 ppm of B-centres.

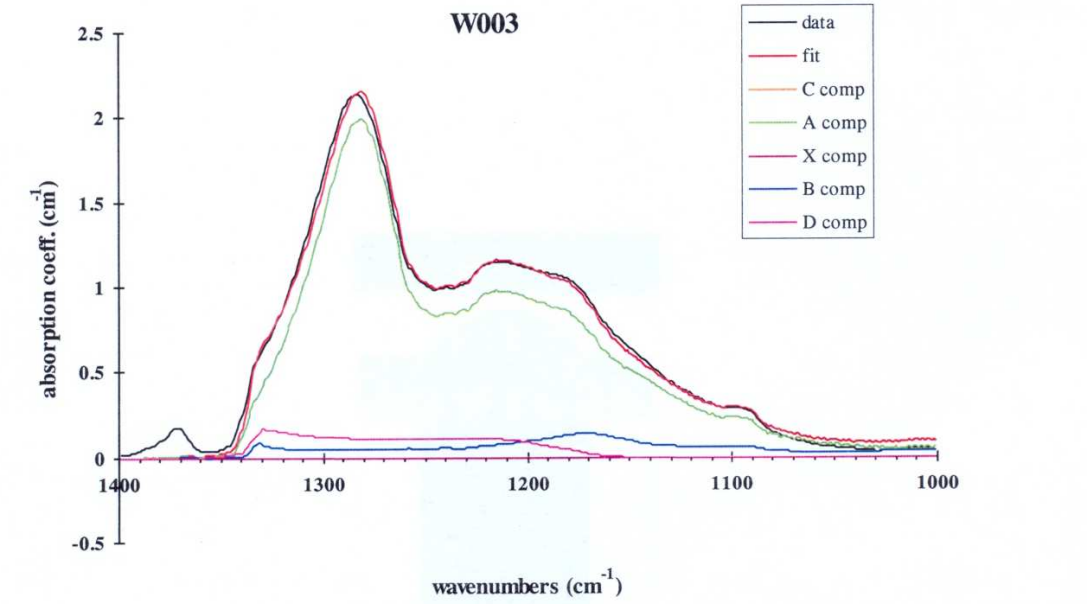

type Ib	$\mu(1130cm^{-1})$	0.00	cm^{-1}	$[N_C]$	0.0	ppm	
type IaA	$\mu(1282cm^{-1})$	1.99	cm^{-1}	$[N_A]$	32.8	ppm	
N^+	$\mu(1332cm^{-1})$	0.00	cm^{-1}	$[N^+]$	0.0	ppm	
type IaB	$\mu(1282cm^{-1})$	0.05	cm^{-1}	$[N_B]$	4.1	ppm	*fit range*
D	$\mu(1282cm^{-1})$	0.11	cm^{-1}	$[N_T]$	37.0	ppm	*1001 to 1399*

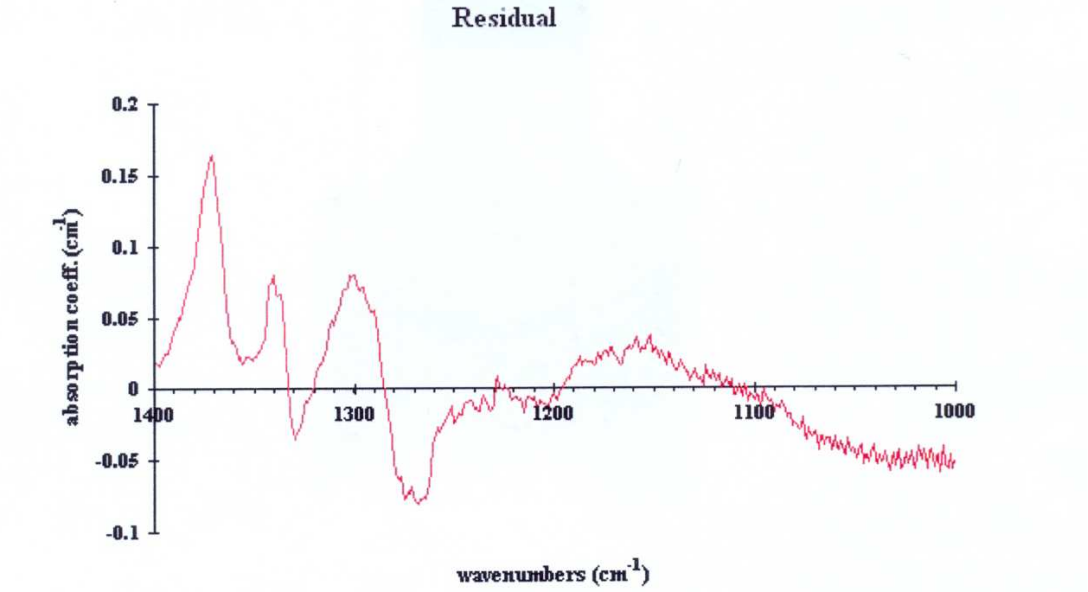

Figure A.3: CAXBD97 decomposition spreadsheet fits to the FTIR spectrum of sample W003 to determine the nitrogen concentrations in the sample. This sample contains 32.8 ppm of A-centres and 4.1 ppm of B-centres.

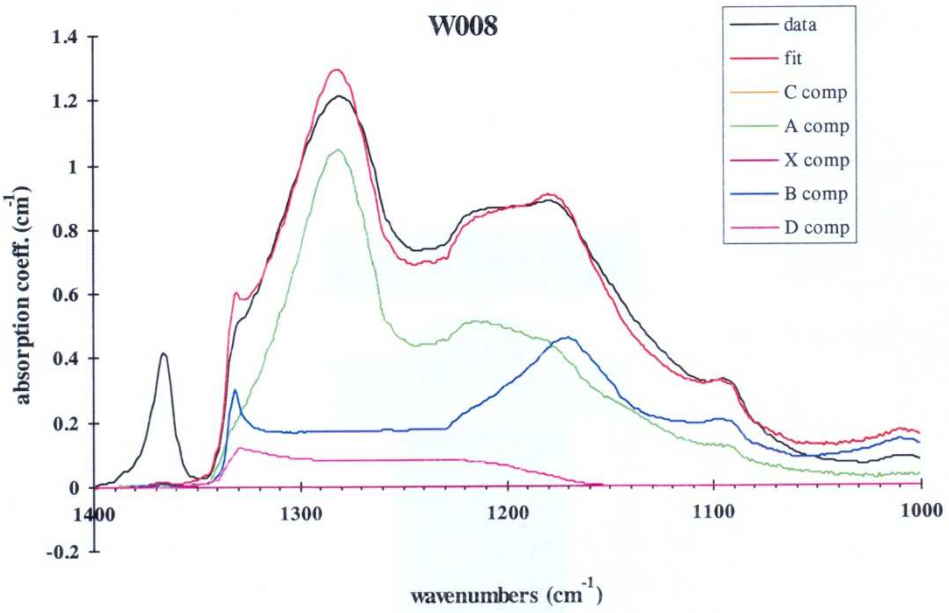

type Ib	$\mu(1130cm^{-1})$	0.00	cm^{-1}	$[N_C]$	0.0	ppm	
type IaA	$\mu(1282cm^{-1})$	1.05	cm^{-1}	$[N_A]$	17.2	ppm	
N^+	$\mu(1332cm^{-1})$	0.00	cm^{-1}	$[N^+]$	0.0	ppm	
type IaB	$\mu(1282cm^{-1})$	0.17	cm^{-1}	$[N_B]$	13.5	ppm	*fit range*
D	$\mu(1282cm^{-1})$	0.08	cm^{-1}	$[N_T]$	30.7	ppm	*1001 to 1399*

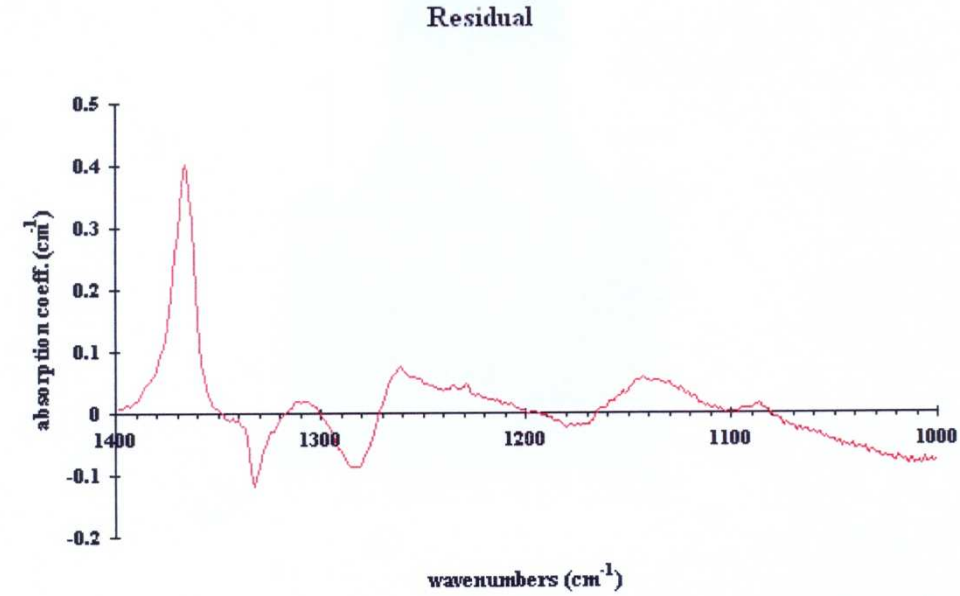

Figure A.4: CAXBD97 decomposition spreadsheet fits to the FTIR spectrum of sample W008 to determine the nitrogen concentrations in the sample. This sample contains 17.2 ppm of A-centres and 13.5 ppm of B-centres.

Appendix B

Detector construction

```
// EXPERIMENTALL HALL (world volume)
G4double expHall_x = 150*cm;
G4double expHall_y = 150*cm;
G4double expHall_z = 300*cm;

G4Box* experimentalHall_box
= new G4Box("experimentalHall_box",expHall_x,expHall_y,expHall_z);
//logical volume
logWorld = new G4LogicalVolume(experimentalHall_box, Vacuum,
"experimentalHall_log",0,0,0);
//physical volume
physWorld = new G4PVPlacement(0,G4ThreeVector(),logWorld,
"experimentalHall",0,false,0);
//SET VISUAL ATTRIBUTES
logWorld → SetVisAttributes (G4VisAttributes::Invisible);

//——— BEAM TUBE
G4double innerRadiusOfTheTube = 140*mm;
G4double outerRadiusOfTheTube = 170*mm;
```

*G4double hightOfTheTube = 100 *cm;*

*G4double startAngleOfTheTube = 0 *deg;*

*G4double spanningAngleOfTheTube = 360 *deg;*

G4Tubs beam_tube = new G4Tubs("beam_tube", innerRadiusOfTheTube,*

outerRadiusOfTheTube, hightOfTheTube,

startAngleOfTheTube, spanningAngleOfTheTube);

//logical volume

beam_tube_log = new G4LogicalVolume(beam_tube,Al,"beam_tube_log",0,0,0);

//physical volume

beam_tube_phys

= new G4PVPlacement(0,G4ThreeVector(), beam_tube_log,"beam_tube", logWorld, false,

0);

//SET VISUAL ATTRIBUTES

beam_tube_log→SetVisAttributes(new G4VisAttributes(G4Colour(1,0,0)));

//————————-BEAM STOP

*G4double innerRadiusOfTheTube = 0*mm;*

*G4double outerRadiusOfTheTube = 170*mm;*

*G4double hightOfTheTube = 1 *cm;*

*G4double startAngleOfTheTube = 0 *deg;*

*G4double spanningAngleOfTheTube = 360 *deg;*

G4Tubs beam_stop = new G4Tubs("beam_stop", innerRadiusOfTheTube,*

outerRadiusOfTheTube, hightOfTheTube,

startAngleOfTheTube, spanningAngleOfTheTube);

//logical volume

beam_stop_log = new G4LogicalVolume(beam_stop,Al,"beam_stop_log",0,0,0);

//physical volume

beam_stop_phys

*= new G4PVPlacement(0,G4ThreeVector(0,0,-100.0*cm), beam_stop_log,"beam_stop",*

logWorld, false, 0);

//SET VISUAL ATTRIBUTES

beam_stop_log→SetVisAttributes(new G4VisAttributes(G4Colour(1,0,1)));

Bibliography

[1] Van de Walle, C. G. and J. Neugebauer. Nature, 423:626–628, 2003.

[2] Ri, S., H. Watanabe, M. Ogura, D. Takeuchi, M. Hasegawa, H. Okushi, K. Shimomura. Diamond Relat. Mater., 13:709–712, 2004.

[3] Machi, I. Z., S. H. Connell, M. Baker, J. P. F. Sellschop, K. Bharuth-Ram, C. G. Fischer, R. W. Nilen, S. F. J. Cox and J. E. Butler. Physica B, 289 - 290:507–510, 2000.

[4] Miyazaki, T., H. Okushi and T. Uda. Phys. Rev. Lett., 88(6), 2002.

[5] Sque, S. J., R. Jones, J. P. Goss and P. R. Briddon. Phys. Rev. Lett., 92(1), 2004.

[6] Isberg, J., J. Hammersberg, D. J. Twitchen and A. J. Whitehead . Diamond Relat. Mater, 13:320–324, 2004.

[7] Isberg, J., J. Hammersberg, E. Johansson, T. Wikström, D. J. Twitchen, A. J. Whitehead, S. E. Coe and G. A. Scarsbrook. Science, 297:1670–1672, 2002.

[8] G. Davies. Physica B, 273 - 274:15–23, 1999.

[9] J. F. Prins. Semicond. Sci. Technol., 16:L50–L52, 2001.

[10] Katagiri, M., J. Isoya, S. Koizumi and H. Kanda. phys. stat. sol. (a), 201:2451–2456, 2004.

[11] Katagiri, M., J. Isoya, S. Koizumi and H. Kanda. Appl. Phys. Lett., 85:6365–6367, 2004.

[12] Collins, A. T. Diamond Relat. Mater., 8:1455–1462, 1999.

[13] Eaton, Sally C., Alfred B. Anderson, John C. Angus, Yulia E. Evstefeeva and Yuri V. Pleskov. Electrochem. Solid-State Lett., 5:G65–G68, 2002.

[14] Segev, D. and Su-Huai Wei. Phys. Rev. Lett., 91, 2003.

[15] Teukam, Z., J. Chevallier, C. Saguy, R. Kalish, D. Ballutaud, M. Barbe, F. Jomard, A. Troson-Carli, C. Cytermann, J. E. Butler, M. Bernard, C. Baron and A. Deneuville. Nat. Mater., 2:482–486, 2003.

[16] Goss, J. P., P. R. Briddon, R. Jones and S. Sque. Diamond Relat. Mater., 13:684–690, 2004.

[17] Li Rong-Bin, Hu Xiao-Jun, Shen He-Sheng and He Xian-Chang. Journal of Materials Science, 39:1135–1137, 2004.

[18] A. M. Stoneham. Diamond: Recent advances in theory. In J. E. Field, editor, The Properties of Natural And Synthetic Diamond. Academic Press Limited, 1992.

[19] H. Kawarada. Surf. Sci. Rep., 26:205–259, 1996.

[20] Chevallier, J., B. Theys, A. Lusson, C. Grattepain, A. Deneuville and E. Gheeraert. Phys. Rev. B, 58(12):7966–7969, 1998.

[21] S. K. Estreicher. Mater. Sci. and Eng., R14:319–412, 1995.

[22] Luchsinger, R., P. F. Meier, N. Paschedag, H. U. Suter and Yu Zhou. Phil. Trans. R. Soc. Lond. A, 350:203–214, 1995.

[23] Wang, L. G. and A. Zunger. Phys. Rev. B, 66, 2002.

[24] Goss, J. P., R. Jones, M. I. Heggie, C. P. Ewels, P. R. Briddon and S. Öberg. Phys. Rev. B, 65:115207–1 – 115207–13, 2002.

[25] Machi, I. Z., J. E. Butler, S. H. Connell, B. P. Doyle, R. D. Maclear, J. P. F. Sellschop, E. Sideras-Haddad and D. B. Rebuli. Diamond Relat. Mater., 8:1611–1614, 1999.

[26] Machi, I. Z., S. H. Connell, M. Dalton, M. J. Sithole, K. Bharuth-Ram, S. F. J. Cox and C. Baines. Diamond Relat. Mater., 13:909–913, 2004.

[27] Saada, D., J. Adler and R. Kalish. Phys. Rev. B, 61(16):10711 – 10715, 2000.

[28] J. P. Goss. J. Phys. Condens. Matter, 15:R551–R580, 2003.

[29] Estle, T. L., S. Estreicher and D. S. Marynick . Phys. Rev. Lett., 58(15):1547–1550, 1987.

[30] Van de Walle, C. G. and P. E. Blöchl. Phys. Rev. B, 47(8):4244–4255, 1993.

[31] King, P. J. C., R. L. Lichti, S. P. Cottrell, I. Yonenaga and B. Hitti. J. Phys.:Condens. Matter, 17:4567–4578, 2005.

[32] Patterson, B. D., A. Hintermann, W. Kündig, P. F. Meier, F. Wadner, H. Graf, E. Recknagel, A. Weidinger and Th. Wicher. Phys. Rev. Lett., 40(20):1347–1350, 1978.

[33] Holzschuh, E., W. Kündig, P. F. Meier, B. D. Patterson, J. P. F. Sellschop, M. C. Stemmet and H. Appel . Phys. Rev. A, 25(3):1272–1286, 1982.

[34] Schneider, J. W., R. F. Kiefl, K. H. Chow, S. Johnson, J. Sonier, T. L. Estle, B. Hitti, R. L. Lichti, S. H. Connell, J. P. F. Sellschop, C. G. Smallman, T. R. Anthony and W. F. Banholzer. Phys. Rev. Lett., 71(4):557–559, 1993.

[35] Blundell, S. J. Contemp. Phys., 40(3):175–192, 1999.

[36] Storchak, V. G., D. G. Eshchenko and J. H. Brewer. J. Phys.: Condens. Matter, 16:S4761–S4778, 2004.

[37] Reichart, P., G. Datzmann, A. Hauptner, R. Hertenberger, C. Wild and G. Dollinger . SCIENCE, 306:1537–1540, 2004.

[38] Fuchs, F., C. Wild, K. Schwarz, W. Müller-Sebert, P. Koidl. App. Phys. Lett., 66(2):177–179, 1995.

[39] Glover, C., M. E. Newton, P. Martineau, D. J. Twitchen and J. M. Baker. Phys. Rev. Lett., 90(18):185507–1 – 185507–4, 2003.

[40] Dischler, B., C. Wild, W. Müller-Sebert and P. Koidl. Physica B, 185:217–221, 1993.

[41] W. Walukiewicz. Physica B, 302-303:123–134, 2001.

[42] R. Kalish. Diamond Relat. Mater., 10:1749–1755, 2001.

[43] G. F. Nenmark. Mat. Sci. and Engineering: R, 21(1):1–46, 1997.

[44] Joseph, M., H. Tabuta and T. Kawai . Jpn J. Appl. Phys., 38:L1205–L1207, 1999.

[45] Yan, Y., S. B. Zhang and S. Pantelides. Phys. Rev. Lett., 86(25), 2001.

[46] Kilic, C. and A. Zunger. Phys. Rev. Lett., 88, 2002.

[47] S. B. Zhang. J. Phys.: Condens. Matter, 14:R881–R903, 2002.

[48] Nielsen, K. B., B. Bech Nielsen, J. Hansen, E. Andersen and J. U. Andersen . Phys. Rev. B, 60(3):1716–1728, 1999.

[49] S. K. Estreicher. Phys. Rev. B, 36(17):9122–9128, 1987.

[50] Yang-Fang Chen. Chinese Journal of Physics, 29(3):245–251, 1991.

[51] Chevallier, J., A. Lusson, B. Theys, A. Deneuville and E. Gheeraert. Diamond Relat. Mater., 8:278–282, 1999.

[52] G. Popovici and M. A. Prelas. Diamond Relat. Mater., 4:1305–1310, 1995.

[53] Saada, D., J. Adler and R. Kalish. Appl. Phys. Lett., 77(6):878–879, 2000.

[54] Collins, A. T. and M. Stanley. J. Phys. D: Appl. Phys., 18:2537–2545, 1985.

[55] Mainwood, A. Phys. Rev. B, 49(12):7934–7940, 1994.

[56] Mainwood, A. phys. stat. sol. (a), 172:25–35, 199.

[57] Kaiser, W. and W. L. Bond. Phys. Rev., 115(4):857–863, 1959.

[58] Anderson, B., J. Payne and R. K. Mitchell. The spectroscope and gemmology. Robert Hale Limited, 1998.

[59] Konstantin Iakoubovskii. Optical Study of defects in diamond. PhD thesis, Katholieke University Leuven, 2000.

[60] Iakoubovskii, K. and A. Stesmans. J. Phys.: Condens. Matter, 14:R467–R499, 2002.

[61] Wikipedia, 2007. http://en.wikipedia.org/wiki/crystallographic_defects_in_diamond.

[62] Shiryaev, A., K. Dembo, Yu. Klyuev, A. Naletov and B. Feigelson . J. Appl. Cryst, 36:420–424, 2003.

[63] C. G. Smallman. Hydrogen and Muonium in diamond. PhD thesis, University of the Witwatersrand, 1997.

[64] Collins, A. T. . J. Phys.: Condens. Matter, 14:3743–3750, 2002.

[65] Kajihara, S. A., A. Antonelli, J. Bernholc and R. Car. Phys. Rev. Lett., 66(15):2010–2013, 1991.

[66] Sternschulte, H., K. thonke, R. Sauer and S. Koizumi. Phys. Rev. B, 59(20):12924–12927, 1999.

[67] J. F. Prins. Nucl. Instrum. Methods Phys. Res., Sect. A, 514:69–78, 2003.

[68] Denham, P., E. C. Lightowlers and P. J. Dean. Phys. Rev., 161:762–768, 1967.

[69] S. Koizumi. Phys. Status Solidi (a), 172:71–78, 1999.

[70] Koizumi, S., T. Teraji and H. Kanda. Diamond Relat. Mater., 9:935–940, 2000.

[71] Sakaguchi, I., M. N. Gamo, Y. Kikuchi, E. Yasu, H. Haneda, T. Suzuki and T. Ando. Phys. Rev. B, 60(4):R2139–R2141, 1999.

[72] Kalish, R., A. Reznik, C. Uzan-Saguy and C. Cytermann. Appl. Phys. Lett., 76(6):757–759, 2000.

[73] Albu, T. V., A. B. Anderson and J. C. Angus. J. Electrochem. Soc., 149(5):E143–E147, 2002.

[74] Nishimatsu, T., H. Katayama-Yoshida, and N. Orita. Physica B, 302-303:149–154, 2001.

[75] Miyazaki, T. and H. Okushi. Diamond Relat. Mater., 10:449–452, 2001.

[76] Weiser, K. Phys. Rev., 126:1427–1436, 1962.

[77] Resende, A., R. Jones, S. Öberg and P. R. Briddon. Phys. Rev. Lett., 82:2111–2114, 1999.

[78] Johnson, N. M., C. Herring and C. G. Van de Walle. Phys. Rev. Lett., 73:130–133, 1994.

[79] Seager, C. H., R. A. Anderson and S. K. Estreicher. Phys. Rev. Lett., 74, 1995.

[80] Hitti, B., S. R. Kreitzman, T. L. Estle, E. S. Bates, M. R. Dawdy, T. L. Head and R. L. Lichti. Phys. Rev. B, 59(7):4918–4924, 1999.

[81] Herring, C., N. M. Johnson and C. G. Van de Walle. Phys. Rev. B, 64:125209–1 – 125209–27, 2001.

[82] S. F. J. Cox. J. Phys.: Condens. Matter, 15:R1727–R1780, 2003.

[83] Budde, M., Bech Nielsen, P. Leary, J. Goss, R. Jones, P. R. Briddon, S. Öberg and S. Breuer. Phys. Rev. B, 57:4397–4412, 1998.

[84] Claxton, T. A., A. Evans and M. C. R. Symons. J. Chem. Soc., Faraday Trans. 2, 82(11):2031–2037, 1986.

[85] Briddon, P. R., R. Jones and G. M. S. Lister. J. Phys. C., 21:L1027–L1031, 1988.

[86] Goss, J. P., R. Jones, M. I. Heggie, C. P. Ewels, P. R. Briddon and S. Öberg. phys. stat. sol. (a), 186(2):263–268, 2001.

[87] Chevallier, J., A. Lusson, D. Ballutaud, B. Theys, F. Jomard, A. Deneuville, M. Bernard, E. Gheeraert and E. Bustarret. Diamond Relat. Mater., 10:399–404, 2001.

[88] Ogura, M., N. Mizuochi, S. Yamasaki and H. Okushi. Diamond & Related Materials, 14:2023–2026, 2005.

[89] Mizuochi, N., M. Ogura, J. Isoya, H. Okushi and S. Yamasaki. Physica B, 376-377:300–303, 2006.

[90] Saguy, C., C. Cytermann, B. Fizgeer, V. Richter, Y. Avigal, N. Moriya, R. Kalish, B. Mathieu and A. Deneuville. Diamond Relat. Mater., 12:623–631, 2003.

[91] Glover, C., M. E. Newton, P. Martineau, Samantha Quinn and D. J. Twitchen. Phys. Rev. Lett., 92(13):135502–1 – 135502–4, 2004.

[92] Ballutaud, D., F. Jomard, J. Le Duigou, B. Theys, J. Chevallier, A. Deneuville and F. Pruvost. Diamond Relat. Mater., 9:1171–1174, 2000.

[93] Liang, Z. N., C. Haas and L. Niesen. Phys. Rev. Lett., 72(12):1846–1849, 1994.

[94] Bech, Nielsen B., J. U. Andersen and S. J. Pearton. Phys. Rev. Lett., 60(4):321–324, 1988.

[95] Denteneer, P. J. H., C. G. Van de Walle and S. T. Pantelides. Phys. Rev. Lett., 62(16):1884–1887, 1989.

[96] Breuer, S. J. and P. R. Briddon. Phys. Rev. B, 49(15):10332–10336, 1994.

[97] Mehandru, S. P. and A. B. Anderson. J. Mater. Res., 9(2):383–395, 1994.

[98] Chevallier, J., Z. Teukam, C. Saguy, R. Kalish, C. Cytermann, F. Jomard, M. Barbé, T. Kociniewski, J. E. Butler, C. Baron, A. Deneuville. phys. stat. sol. (a), 201(11):2444–2450, 2004.

[99] Dai, Ying, Dadi Dai, Donghong Liu, Shenghao Han and Baibiao Huang. Appl. Phys. Lett., 84(11):1895–1897, 2004.

[100] Dai, Y., C. X. Yan, A. Y. Li, Y. Zhang and S. H. Han. Carbon, 43(5):1009–1014, 2005.

[101] Nesladek, M., K. Meykens, K. Haenen, L. M. Stals, T. Teraji and S. Koizumi. Phys. Rev. B, 59(23):14852–14855, 1999.

[102] Nishimatsu, T., H. Katayama-Yoshida, and N. Orita. Japan. J. Appl. Phys., 41:1952–1962, 2002.

[103] Chang, K. J. and D. J. Chadi. Phys. Rev. Lett., 60(14):1422–1425, 1988.

[104] Miyazaki, T., H. Okushi and T. Uda. Appl. Phys. Lett., 78(25):3977–3979, 2001.

[105] T. Miyazaki and H. Okushi. Diamond Relat. Mater., 11, 2002.

[106] Celio, M and P. F. Meier. Phys. Rev. B, 28(1):39–49, 1983.

[107] A. Schenck. Muon Spin Rotation Spectroscopy: Principles and Applications in Solid State Physics. Adam Hilger Ltd, 1985.

[108] Erik B. Karlsson. Solid State Phenomena. Oxford Science, 1995.

[109] Lord, J. S., S. F. J. Cox, H. V. Alberto, J. Piroto Duarte and R. C. Vilão. J. Phys.: Condens. Matter, 16:S4707–S4720, 2004.

[110] Gil, J. M., H. V. Alberto, R. C. Vilão, J. Piroto Duarte, P. J. Mendes, L. P. Ferreira, N. Ayres de Campos, A. Weidinger, J. Krauser, Ch. Niedermayer and S.F. J. Cox. Phys. Rev. Lett., 83(25):5294–5297, 1999.

[111] Gil, J. M., H. V. Alberto, R. C. Vilão, J. Piroto Duarte, N. Ayres de Campos, A. Weidinger, J. Krauser, E. A. Davis, S. P. Cottrell and S. F. J. Cox. Phys. Rev. B, 64:075205–1 – 075205–8, 2001.

[112] Cox, S. F. J., E. A. Davis, S. P. Cottrell, P. J. C. King, J. S. Lord, J. M. Gil, H. V. Alberto, R. C. Vilão, J. Piroto Duarte, N. Ayres de Campos, A. Weidinger, R. L. Lichti and S. J. C. Irvine . Phys. Rev. Lett., 86(12):2601–2604, 2001.

[113] Shimomura, K., K. Nishiyama and R. Kadono. Phys. Rev. Lett., 89(25):255505, 2002.

[114] Shimomura, K., R. Kadono, K. Ohishi, m. Mizuta, M. Saito, K. H. Chow, B. Hitti and R. L. Lichti . Phys. Rev. Lett., 92(13):135505–1 – 135505–4, 2004.

[115] Davis, E. A.,S. F. J. Cox, R. L. Lichti and C. G. Van de Walle. Appl. Phys. Lett., 82(4):592–594, 2003.

[116] Storchak, V. G., D. G. Eshchenko, R. L. Lichti and J. H. Brewer. Physica B, 326:164–166, 2003.

[117] Storchak, V. G., D. G. Eshchenko, R. L. Lichti and J. H. Brewer. Phys. Rev. B, 67:121201–1 – 121201–4, 2003.

[118] Alberto, H. V., R. C. Vilão, J. Piroto Duarte, N. Ayres de Campos, J. M. Gil, R. L. Lichti, E. A. Davis, S. P. Cottrell and S. F. J. Cox. Hyperfine Interact., 136-137:471–477, 2001.

[119] Bakule, P. and E. Morenzoni. Contemporary Physics, 45(3):203–225, 2004.

[120] Anderson, C. D. and S. H. Neddermeyer. Phys. Rev., 50, 1937.

[121] Anderson, C. D. and S. H. Neddermeyer. Phys. Rev., 51:884–886, 1937.

[122] Anderson, C. D. and S. H. Neddermeyer. Phys. Rev., 54, 1938.

[123] Street, J. C. and E. C. Stevenson . Phys. Rev, 52, 1937.

[124] I. Z. Machi. Hydrogen-Impurity-defect complexes in diamond. PhD thesis, University of the Witwatersrand, 2000.

[125] Günter Schatz and Alois Weidinger. Nuclear Condensed Matter Physics: Nuclear Methods and Applications. John Wiley & Sons, 1996.

[126] A. Amato. Rev. Mod. Phys., 69:31119–1174, 1997.

[127] B. D. Patterson. Rev. Mod. Phys., 60(1):69–159, 1988.

[128] G. Eaton. Muon facilities and experiments; now and in the new millennium. Lectures given at the Nato advanced Study Institute on Muon Science, August 1998. RAL Report(RAL-RT-98-019).

[129] G. H. Eaton and S. H. Kilcoyne. Muon production: past, present and future. In MUON SCIENCE: Muons in Physics, Chemistry and Materials, 1999.

[130] Garwin, R. L., L. M. Lederman and M. Weinrich. Phys. Rev., 105:1415–1417, 1957.

[131] Klaus P. Jungmann. Aspects of fundamental muon physics. In MUON SCIENCE: Muons in Physics, Chemistry and Materials, 1999.

[132] Gerald D. Morris. Muonium formation and diffusion in cryocrystals. PhD thesis, The University of British Columbia, 1998.

[133] J. H. Brewer and R. Cywinski. μsr: an introduction. In MUON SCIENCE: Muons in Physics, Chemistry and Materials, 1999.

[134] C. T. Kaiser. Diffusion, reorientation and small magnetic fields studied by μSR. PhD thesis, Delft University, 2001.

[135] Dale Richard Harshman. The interactions of muonium with silica surfaces. PhD thesis, The University of British Columbia, 1986.

[136] David C. Walker. Muon and muonium chemistry. Cambridge University Press, 1983.

[137] de Reotier, Dalmas P. and A. Yaouanc. J. Phys.:Condens. Matter, 9:9113–9166, 1997.

[138] Scheuermann, R., E. Roduner, G. Engelhardt, H. -H. Klauss and D. Herlach. Phys. Rev. B, 66:144429–1 – 144429–6, 2002.

[139] B. D Rainford. Aspects of data treatment for transverse μsr. In MUON SCIENCE: Muons in Physics, Chemistry and Materials, 1999.

[140] Lee S. L., S. H. Kilcoyne, and R. Cywinski, editors. Muon Science: Muons in physics, Chemistry and Materials, Proceedings of the 51st Scottish Universities Summer School in Physics, Bristol, August 1998. Scottish Universities Summer School in Physics & Institute of Physics. A NATO Advanced Study Institute.

[141] Kanetada Nagamine. Introductory Muon Science. Cambridge University Press, 2003.

[142] Brewer, J. H., K. M. Crowe, F. N. Gygax, R. F. Johnson and B. D. Patterson. Phys. Rev. Lett., 31(3):143–146, 1973.

[143] S.F.J. Cox. Solid State Nuclear Magnetic Resonance, pages 103–121, 1998.

[144] Cox, S. F. J. J. Phys. C: Solid State Phys., 20:3187–3319, 1987.

[145] Bakker, C. J. and E. Segré. Phys. Rev., 81(4):489–492, 1951.

[146] E. Segré. Nuclei and Particles. W. A. Benjamin, Inc, 1977.

[147] Jacques A. Chakhalian. Local Magnetic Susceptibility of the Positive Muon in Graphite and the Quasi 1D Spin-half Chain CPC. PhD thesis, University of British Columbia, 2003.

[148] Holzschuh, E., H. Graf, E. Recknagel, A. Weidinger, Th. Wichert and P. F. Meier. Phys. Rev. B, 20(11):4391–4396, 1979.

[149] Sahoo, N., K. C. Mishra and T. P. Das. Phys. Rev. Lett., 55(14):1506–1509, 1985.

[150] Chow, K. H., R. L. Lichti, R. F. Kiefl, S. Dunsiger, T. L. Estle, B. Hitti, R. Kadono, W. A. MacFarlane, J. W. Schneider, D. Schumann and M. Shelley. Phys. Rev. B, 50(12):8918–8921, 1994.

[151] T. L. Estle and R. F. Kiefl. Muon spin rotation and muon level-crossing resonance. In Hyperfine Interaction of Defects in Semiconductors, 1992.

[152] P. F. Meier. Phys. Rev. A, 25:1287–1294, 1982.

[153] Kiefl, R. F., J. W. Schneider, H. Keller, W. Kündig, W. Odermatt, B. D. Patterson, K. W. Blazey, T. L. Estle and S. L. Rudaz . Phys. Rev. B., 32:530–532, 1985.

[154] Sahoo, N., K. S. Mishra, K. C. Mishra, A. Coker, T. P. Das, C. K. Mitra and L. C. Snyder. Phys. Rev. Lett., 50(12):913–917, 1983.

[155] Shimizu, A., H. Tachikawa and M. Inagak. Solid State Ionics, 127:157–162, 2000.

[156] Cox, S. F. J. and M. C. R. Symons. Chem. Phys. Lett., 126, 1986.

[157] Blazey, K. W., T. L. Estle, E. Holzschuh, W. Odermatt and B. D. Patterson. Phys. Rev. B, 27(1):15–19, 1983.

[158] Odermatt, W., Hp. Baumeler, H. Keller, W. Kündig, B. D. Patterson, J. W. Schneider, J. P. F. Sellschop, M. C. Stemmet, S. H. Connell and D. P. Spencer. Phys. Rev. B, 38(7):4388–4393, 1988.

[159] M. C. R. Symons. Hyperfine Interact., 17-19, 1984.

[160] Kiefl, R. F., M. Celio, T. L. Estle, G. M. Luke, S. R. Kreitzman, J. H. Brewer, D. R. Noakes, E. J. Ansaldo and K. Nishiyama . Phys. Rev. Lett., 58(17):1780–1783, 1987.

[161] Kiefl, R. F., M. Celio, T. L. Estle, S. R. Kreitzman, G. M. Luke, T. M. Riseman and E. J. Ansaldo. Phys. Rev. Lett., 60(3):224–226, 1988.

[162] Weidinger, A., G. Balzer, H. Graf, E. Recknagel and Th. Wichert. Phys. Rev. B, 24(10):6185–6188, 1981.

[163] Patterson, B. D., A. Bosshard, U. Straumann, P. Truöl, A. Wüest and Th. Wichert. Phys. Rev. Lett., 52(11):938–941, 1984.

[164] S. F. J. Cox. Muonium states and dynamics. In MUON SCIENCE: Muons in Physics, Chemistry and Materials, 1999.

[165] Chu, C. H. and S. K. Estreicher. Phys. Rev. B, 42(15):9486–9495, 1990.

[166] Cox, S. F. J. and R. L. Lichti. J. Alloys and Compounds, 253-254:414–419, 1997.

[167] Storchak, V., S. F. J. Cox, S. P. Cottrell, J. H. Brewer, G. D. Morris, D. J. Arseneau and B. Hitti. Phys. Rev. Lett., 78(14):2835–2838, 1997.

[168] Kreitzman, S. R., B. Hitti, R. L. Lichti, T. L. Estle and K. H. Chow. Phys. Rev. B, 51(19):13117–13137, 1995.

[169] Spencer, D. P., D. G. Fleming and J. H. Brewer. Hyperfine Interact., 17-19:567, 1984.

[170] Bharuth-Ram, K., R. Scheuermann, I. Z. Machi, S. H. Connell, J. Major, J. P. F.Sellschop and A. Seege. Hyperfine Interact., 105:339–344, 1997.

[171] Smallman, C. G., S. H. Connell, K. Bharuth-Ram, J. P. F. Sellschop, R. W. N. Nilen, M. Hampele, J. Major, R. Scheuermann, A. seeger and T. Stammler. Hyperfine Interact., C1, 1996.

[172] Lawson, Simon C., David Fisher, Damian C. Hunt and Mark E. Newton. J. Phys.: Condens. Matter, 10:6171–6180, 1998.

[173] Loubser, J. H. N. and J. A. van Wyk. Rep. Prog. Phys., 41:1203–1248, 1978.

[174] J. A. Van Wyk. J. Phys. C: Solid State Phys., 15:L981–L983, 1982.

[175] Welbourn, C. M., M. Cooper and P. M. Spear. Gems Gemol., 32:56, 1996.

[176] De Weerdt, Filip and Jef Van Royen. Diamond Relat. Mater., 10:474–479, 2001.

[177] John Coates. Interpretation of infrared spectra, a practical approach. In Encyclopedia of Analytical Chemistry, 2000.

[178] McNamara, Karen M. Appl. Phys. Lett., 83(7):1325–1327, 2003.

[179] Felix V. Kamisky and Galina K. Khachatryan. The Canadian Mineralogist, 39:1733–1745, 2001.

[180] Kiflawi, I., A. E. Mayer, P. M. Spear, J. A. van Wyk and G. S. Woods. Philosophical Magazine B, 69(6):1141–1147, 1994.

[181] Boyd, S. R., I. Kiflawi and G. S. Woods. Philosophical Magazine B, 69(6):1149–1153, 1994.

[182] Boyd, S. R., I. Kiflawi and G. S. Woods. Philosophical Magazine B, 72(3):351–361, 1995.

[183] David Fisher, 2002. IRspec-CAXBD97.XLS: Diamond Trading Company (Pty) Ltd.

[184] Terbanche, Cornelius, J. and Edward C. Reynhardt. Chemical Physics Letters, 322:273–279, 2000.

[185] Terbanche, Cornelius, J., Edward C. Reynhardt and Jan A. van Wyk. Solid State Nuclear Magnetic Resonance, 20:1–22, 2001.

[186] R. Fedaruk. Rev. Adv. Mater. Sci., 12:84–89, 2006.

[187] Van Wyk, J. A., J. H. N. Loubser, M. E. Newton and J. M. Baker. J. Phys.: Condens. Matter, 4:2651–2662, 1992.

[188] Shcherbakova, M. Ya., E. V. Sobolev, V. A. Nadolinnyi and V. K. Aksenov. Sov. Phys. Dokl., 20(11):725–728, 1975.

[189] Newton, M. E. and J. M. Baker. J. Phys.: Condens. Matter, 1:9801–9803, 1989.

[190] John E. Wertz and James R. Bolton. ELECTRON SPIN RESONANCE: Elementary Theory and Practical Applications. McGraw-Hill, Inc., 1972.

[191] Charles P. Jr Poole. Electron Spin Resonance: A Comprehensive Treatise on Experimental Techniques. John Wiley and Sons, 1983.

[192] Rutherford Appleton Laboratory ISIS Facility, 2006. The EMU User Guide: http://www.isis.rl.ac.uk/Muons/emu/index.htm.

[193] Lynch, M. C., S. P. Cottrell, P. J. C. King and G. H. Eaton. Physica B, 326:270–274, 2003.

[194] Sean Giblin, 2005. ISIS Reflector furnace manual.

[195] Agostinelli, S., J. Allison, K. Amako et al. Nucl. Instr. & Methods in Phys. Res. A, 506:250–303, 2003.

[196] F. L. Pratt. Physica B, 289-290:710–714, 2000.

[197] Leon, M. Hyperfine Interact., 87(1):1123–1127, 1994.

[198] J. S. Lord, 2005. Personal Communication.

[199] A. Singh. Journal of Materials Science, 31:1991–1996, 1996.

[200] Ryosuke Kadono. Current Opinion in Solid State and Materials Science, 6:141–146, 2002.

[201] Storchak, V. G., D. G. Eshchenko and J. H. Brewer. Physica B, 374-375:347–350, 2006.

[202] Gxawu, D., I. Z. Machi, S. H. Connell, K. Bharuth-Ram, M. J. Sithole and S. F. J. Cox. Diamond & Related Materials, 14:375–379, 2005.

[203] Machi, I. Z., S. H. Connell, J. P. F. Sellschop and K. Bharuth-Ram. Hyperfine Interactions, 136-137(3-8):727–730, 2001.

[204] Odermatt, W., Hp. Baumeler, H. Keller, W. Kündig, B. D. Patterson, J. W. Schneider, J. P. F. Sellschop, M. C. Stemmet and S. Connell. Hyperfine Interactions, 32:583–588, 1986.

[205] Allen M. Moore. Soil Biol. Biochem., 18(4), 1986.

[206] Kaneko, Junichi, Chushiro Yonezawa, Yoshimi Kasugai, Hitoshi Sumiya and Takeo Nishitani. Diamond and Related Materials, 9:2019–2023, 2000.

[207] Sumiya, H., N. Toda, Y. Nishibayashi and S. Satoh. Journal of Crystal Growth, 178:485–494, 1997.